PhD Thesis

Majorana Bound States in Semiconductor-Superconductor Hybrid Devices

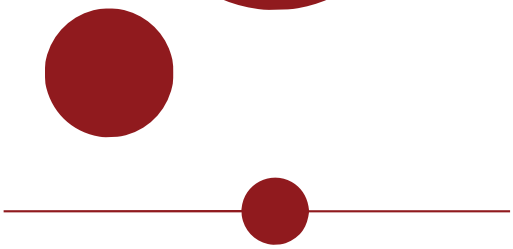

UNIVERSITY OF COPENHAGEN

Esben Bork Hansen

"I may not have gone where I intended to go, but I think I have ended up where I needed to be."

- *The Long Dark Tea-Time of the Soul*, Douglas Adams, 1952-2001

Colophon

This thesis was set with LaTeX 2$_\varepsilon$ using the memoir class. The font is Libertine on normal A4 paper.

Graphics created using Matplotlib[Hunter, 2007] under Python 3.6, Graph and Inkscape.

Chapterstyles courtesy CP3 and CØ.

Majorana Bound States in Semiconductor-Superconductor Hybrid Devices

Author Esben Bork Hansen
Advisor Karsten Flensberg

Center for Quantum Devices

Niels Bohr Institute

Faculty of Science
University of Copenhagen

July, 2018

Abstract

This thesis presents the results of theoretical studies of superconductor-semiconductor (SC-SM) hybrid nanowire systems with the focus on detecting Majorana bound states (MBSs) by methods using electron tunneling spectroscopy.

We model the SC-SM nanowire using three Hamiltonian models: the first is the 1D spinless p-wave SC, and the other two are a 1D SM nanowire with Rashba spin-orbit interaction, Zeeman field, and induced s-wave superconductivity, where the superconductivity is either modeled as a constant gap or an energy-dependent self-energy term. Electron tunneling spectroscopy will be simulated in the grounded nanowire setup using the scattering formalism and in the charged island setup using a master equation model.

We will present and discuss the results of five projects in this thesis. In the first project, we study a SC-normal-SC nanowire setup and simulate differential conductance measured at the end of the nanowire. We find that there exist 2 or 4 MBSs in the topological regime, depending on the phase difference between the two SCs. This phase dependence gives rise to distinctive 2π period features in the differential conductance, which are absent in the trivial phase and may be used to identify MBSs.

The second project is centered around modeling the experimental setup of a quantum dot coupled to the end of a SC-SM nanowire and understanding the observed differential conductance data. The experimental data is consistent with our model where the nanowire hosts MBSs and the levels in the quantum dot can be tuned in and out of resonance with the nanowire. We find that the observed energy splitting upon resonance with a dot level is due to the MBS wavefunction leaking into the quantum dot.

In the third project, we investigate the effect of the normal-conducting drain lead on the parent SC of the SC-SM nanowire. A below-gap density of states is induced into the parent SC at the normal-SC interface. Depending on the coherence length of the SC, this below-gap density of states may provide a leakage channel for the MBSs in the nanowire. This leakage may, depending on coherence length of the superconductor, result in a quenching of the energy oscillations and a suppression of the $2e^2/h$ quantized conductance usually associated with MBSs.

In the fourth project, we model quasiparticle poisoning in a charged SC-SM nanowire island and estimate the quasiparticle poisoning rate by comparing with experimental data.

In the final project, we find that the electron and hole components of the lowest-energy subgap state can be extracted from the ratio of consecutive conductance peaks measured at zero bias in a charged SC-SM nanowire island in the sequential tunneling regime. We study the correlation between this ratio and the energy splitting oscillations of the subgap state in case of MBSs and trivial Andreev bound states (ABSs). We find that certain kinds of trivial ABSs with MBS-like conductance features can be distinguished from true MBSs by comparing this ratio with energy splitting as function of magnetic field and chemical potential.

Although many indirect MBS signatures using electron spectroscopy do not provide unambiguous evidence of the presence of MBSs in SC-SM nanowire, they are still important in guiding the search for MBSs and developing a better understanding of quantum phenomena in SC-SM nanowires.

Dansk Resumé

I denne afhandling præsenteres resultaterne af en række teoretiske studier af superleder-halvleder-hybrid-nanotråd-systemer (SL-HL-nanotråde) med fokus på at detekterer lokaliserede Majorana kvantetilstande (LMKe) ved hjælp af elektron-spektroskopi-metoder.

Vi beskriver SL-HL-nanotrådene med tre Hamilton modeller: Den første er den endimensionelle spinløse p-bølge SL, og de to andre er en endimensionel HL-nanotråd med Rashba-spinbane-vekselvirkning, Zeeman felt, og induceret s-bølge superledning, hvor superledningen enten beskrives ved et konstant gab eller et energiafhængigt selvenergiled.

Vi præsenterer og diskuterer resultaterne af fem projekter i denne afhandling. I det første projekt vil vi studere et SL-normalleder-SL-system og simulere differentialkonduktansen, der måles ved enden af nanotråden. Vi finder, at der eksisterer enten 2 eller 4 LMKe i det topologiske regime afhængigt af faseforskellen mellem de to SLe. Denne faseafhængighed giver anledning til 2π-periodiske karakteristika i differentialkonduktansen, som er fraværende i det trivielle regime, og som kan bruges til at identificere LMKe.

Det andet projekt omhandler modellering af et eksperiment, hvor en kvanteprik er koblet til enden af en SL-HL-nanotråd og fortolkning af den observerede differentialkonduktans. Data fra eksperimentet er i overenstemmelse med vores teoretiske model, hvor to LMKe er tilstede i nanotråden og kvanteniveauerne i kvanteprikken kan justeres ind og ud af resonans med nanotråden. Vi finder, at den observerede energisplitning, når et kvanteniveau er resonant, skyldes, at bølgefunktionen af den LMK forskydes ind i kvanteprikken.

I det tredje projekt undersøger vi effekten af den normal-ledende afløbsleder på den inducerende SL i SL-HL-nanotråd-systemet. Der induceres en tilstandstæthed under SL-gabet i SLen ved overfladen mellem normal-lederen og SLen. Afhængig af kohærenslængden i SLen kan denne tilstandstæthed under gabet give anledning til lækage fra de LMKe i nanotråden. Denne lækage kan, afhængig af SLens kohærenslængde, resultere i en dæmpning af energisvingningerne og en undertrykkelse af den $2e^2/h$ kvantiserede konduktans, som normal ses forbundet med LMKe.

I the fjerde projekt modellerer vi kvasipartikel-forgiftning af en ladet SL-HL-nanotrådø og estimerer raten af kvasipartikel-forgiftning ved at sammenligne med data fra et eksperiment.

I det sidste projekt finder vi, at elektron- og hul-komponenterne af kvantetilstanden med lavest energi under det superledende gab kan estimeres fra forholdet mellem naboliggende konduktanstoppe, målt ved nul spændingsforskel, i en ladet SL-HL-nanotrådø i det sekventielle tunneleringsregime. Vi studerer korrelationen mellem dette forhold og svingningerne af energien af kvantetilstanden både, hvor tilstanden er en LMK og en triviel lokaliseret Andreev kvantetilstand (LAK). Vi finder, at man i vise tilfælde kan skelne trivielle LAKe med LMK-lignende konduktanskarakteristika fra sande LMKe ved at sammenligne dette forhold med tilstandens energi som funktion af styrken på det magnetiske felt og det kemiske potentiale.

Selvom mange af de forslåede indirekte signaturer for LKMe, som benytter sig af elektronspektroskopi, ikke er entydige beviser for tilstedeværelsen af LMKe i SL-HL-nanotråde, er de stadig vigtige for den videre forskning i LMKe og for bedre at forstå kvantefænomener i SL-HL-nanotråde.

Acknowledgments

The road to writing this thesis has been a exciting journey through solid state quantum physics. I am thankful for having been given the opportunity to study physics at this level and be part of the vibrant research community in the Condensed Matter Theory group and the Center for Quantum Devices. Along the way, many people have inspired me and enhanced my work, as well as helped and supported me in times of hardship. Without them, this thesis would not be half of what it is and for that, I would like to express my gratitude a bit more verbosely than what is customary for a Dane.

First and foremost, I thank my supervisor, Karsten Flensberg, for hiring me as a PhD student and providing great guidance through the years. He has a vast knowledge of condensed matter physics and quantum transport in particular, that he generously shares. For often spending hours of his time to discuss both intricate details of quantum states as well as sort out my confusion over more trivial calculations.

I thank Jeroen Danon for our great collaborations, through which I have learned many things that would have taken me twice as long to learn on my own. For hosting me in Trondhjem for one month.

The experimentalists of Qdev, Mingtang, Sven, Cliff, Eoin, and Fabrizio, for our close collaborations and many interesting discussions.

The people who have read and provided feedback on my thesis, Morten Ib Kjærgaard Munk and Gorm Ole Steffensen. I thank Pernille Saugmann and Roberta Hunt for making this thesis a lot more readable by correcting my English.

A thanks to the members of the CMT lunchclub through the years who have always provided a healthy Danish lunch and half an hour of interesting non-physics discussions.

I thank Reinhold Egger for hosting me for four months in Düsseldorf. Although our collaboration did not bear fruit, I still learned much from our discussions. I appreciate the warm welcome from the members of his group: Stephan, Matthias, Laura, Albert, Alex, Francesco, and Claudia.

I am grateful to Roberta Hunt for all her loving support, especially while I have been finishing this thesis. For sitting with me through many hours of writing and helping me stay motivated until the end.

The friends I have gained in the almost 10 years I have spend at Niels Bohr Institute. Although physics is the most interesting thing to do, it is the people who makes it fun too. Thanks to Arvad, Østfeldt, A9, Nina, Fysikrevyen™, rusvejledergruppen and Fysisk Fagråd.

My friends and family, who I at times may have neglected, I am grateful for your support.

Preface and Publications

The focus of this thesis is the theoretical study of Majorana bound states in superconductor-semiconductor hybrid nanowires systems and how they may be detected using electron tunneling spectroscopy. The results of the following scientific articles will be presented and discussed.

[Hansen *et al.*, 2016] E. B. Hansen, J. Danon, and K. Flensberg, "Phase-tunable Majorana bound states in a topological N-SNS junction," Physical Review B, **93**, 9, 094501 (2016).

[Deng *et al.*, 2016] M. T. Deng,, S. Vaitiekenas, E. B. Hansen, J. Danon, M. Leijnse, K. Flensberg, J. Nygård, P. Krogstrup, and C. M. Marcus, Science **354** (6319), 1557 (2016)

[Danon *et al.*, 2017] J. Danon, E. B. Hansen, and K. Flensberg, Physical Review B **96** (12), 125420 (2017)

[Albrecht *et al.*, 2017] S. M. Albrecht, E. B. Hansen, A. P .Higginbotham, F. Kuemmeth, T. S. Jespersen, J. Nygård, P. Krogstrup, J. Danon, K. Flensberg, and C. M. Marcus, Physical Review Letters **118** (13), 137701 (2017)

[Hansen *et al.*, 2018] E. B. Hansen, J. Danon, and K. Flensberg, Physical Review B, **97** (4), 041411 (2018)

Nomenclature

ABS	Andreev bound state
BCS	Bardeen–Cooper–Schrieffer
CB	Coulomb blockaded
CBMI	Coulomb blockaded Majorana island
ETS	Electron tunneling spectroscopy
MBS	Majorana bound state
MI	Majorana island
N-SNS	Normal-superconductor-normal-superconductor
NDC	Negative differential conductance
ps-ABS	Partially separated Andreev bound state
SC	Superconductor
SM	Semiconductor
ZBC	Zero bias conductance
ZBP	Zero bias peak

Contents

Part I

INTRODUCTION AND BACKGROUND

Chapter 1

Introduction

> “But what am I going to see?
> I don’t know. In a certain sense, it depends on you.
>
> Stanislaw Lem, Solaris

Topology

Topological phases are relatively new states of matter. It was believed for a long time that Landau theory could be used to classify all phases of matter by symmetries. However, the continuous discovery of new materials displaying a variety of different phases not separated by any symmetry breaking phase transitions, demonstrated the need for a new theory. The term ”topological” refers to the existence of a global characteristic quantity, a topological invariant, which only changes in quantized steps at topological phase transitions, and otherwise stays invariant under changes that respect the symmetries of the system. An analogy is often drawn to the topological classification of 2D surfaces embedded in 3D space by the number of holes in the surface. In this respect, a coffee cup is topologically equivalent to a donut and distinct from a sphere, since the cup can be smoothly deformed into a donut without changing the number of holes in the surface, but not into a sphere.

An example of a topological phase is the celebrated quantum Hall phase, which can exist in certain 2D semiconductor (SM) systems subjected to strong magnetic fields. At zero magnetic field, the system is in a conventional insulating phase, but as the field is increased a topological phase emerges. This phase is characterized by a quantized Hall conductance that changes in either integer or fractional steps of e^2/h as the electron density is varied. The quantization of the conductance does not depend on the details of the sample and is so exact that the ratio e^2/h has been determined to the precision of almost one part in a billion and is used as the standard unit of measure for electrical resistance. While the bulk of the SM is insulating, the Hall current is carried by gapless edge states and the Hall conductance is set by the number of filled edge channels. In the integer quantum Hall state, the number of edge states corresponds to the number of filled Landau levels, which can be labeled by a topological invariant called the Chern number. The Chern number can be calculated theoretically and the Hall conductance is thus a direct measurement of the topological invariant.

As the framework of topological materials was developed, many more exciting phases have been predicted and studied theoretically. In recent years, material science has made

rapid progress and it is now possible to study many of these topological phases experimentally. One system that has gained a lot of interest and will be the fulcrum of this thesis, is the superconductor-semiconductor (SC-SM) hybrid nanowire. It is anticipated that this system will, under the right conditions, exhibit a topological superconducting phase, which hosts exotic quasiparticle excitations, termed Majorana fermions. Before considering how this may be possible we provide a brief introduction of Majorana fermions in solid state physics.

Majorana Fermions

Initially conceived by Majorana [1937] as a solution to his real variant of Dirac's complex wave equation, Majorana fermions are neutrally charged fermions, which distinguish themselves from their charged Dirac fermion cousins by having real-valued field operators and by being their own anti-particles. Whether this mathematical construct exists as an elementary particle remains an open question (among the proposed candidates are neutrinos, super-symmetric partners, and dark matter particles), however it has been predicted that Majorana fermions may also emerge from collective excitations in exotic solid state systems. Here they have attracted much attention, as they are expected to behave as non-abelian anyons in 2D [Stern, 2010], and may serve as a useful basis for fault tolerant quantum computations[Kitaev, 2003; Nayak *et al.*, 2008].

Anyons are particles which obey different exchange statistics from ordinary fermions and bosons. Upon the exchange of two anyonic particles, the many body wavefunction is multiplied by a general phase factor which may be different from the usual -1 $(+1)$ for fermions (bosons). Non-abelian means that the exchange operations of different particles do not commute. A system hosting N pairs of Majorana fermions has a 2^N fold degenerate ground state manifold, which can be used to span the computational space of a quantum computer. The non-abelian anyonic nature of Majorana fermions makes it possible to perform logical operations by exchanging (or braiding) Majorana fermions.

It should be noted that when the term "Majorana fermion" is used in the context of solid state physics, any fermionic operator, in the language of second quatization, may be written as a superposition of two Majorana operators which are Hermitian. This simply amounts to splitting the fermion into its real and imaginary components. For ordinary fermions, the two Majorana fermions have wavefunctions that mostly coincide in space. Certain topological phases are however signified by hosting unusual fermionic states that consist of two spatially separated Majorana fermions and it is these states that the term "Majorana fermion" refers to in the context of condensed matter physics. To avoid confusion with the elementary particle Majorana fermion, the term Majorana bound state (MBS) will be used.

A fermionic state composed of two spatially separated Majorana operators is, in theory, protected from many types of decoherence, as it should be unchanged by local perturbations affecting only one of its constituting MBSs. These states are topological in nature and the hope is as such that they may be employed in topologically protected quantum computation schemes.

By now a myriad of different schemes have been proposed on how build and control Majorana based qubits and on how to make a scalable quantum computer. However, we have yet to realize a system where the presence of MBSs can be demonstrated unambiguously.

Majorana bound states in superconductors and nanowires

In the language of Fermi liquid theory, the notion of particles and anti-particles arises as electron and hole excitations in the Fermi sea ground state. They move and behave in many ways as free elementary particles, but their characteristics, such as mass, charge, g-factor,

and spin, may be renormalized due to interactions, which gives rise to a large variety of quasiparticles. Such interactions can lead to the emergence of superconducting phases, where electrons form a bosonic condensate by pairing up into Cooper pairs. The resulting quasiparticles are superpositions of both electrons and holes and therefore superconducting systems seem like promising places to search for Majorana-like particles.

The quasiparticles in ordinary s-wave superconductors are superpositions of an electron and a hole of opposite spin and are as such not their own anti-particle. Other kinds of superconductors with more interesting pairings do exist, although, they are not so easy to come by. One of these exotic superconductors is the p-wave superconductor with triplet pairing symmetry. In this case, the quasiparticles are superpositions of electrons and holes with the same spin. If there exists such a quasiparticle with zero energy and equal electron-hole components, its corresponding operator will be Hermitian and it would be a very strong candidate for a MBS. Indeed, the triplet superconductor accommodates a topological phase with MBSs as topological signatures.

In the 1D p-wave SC, MBSs are located at the two edges of the topological phase[Sengupta *et al.*, 2001; Kitaev, 2001], while in the 2D $p_x + ip_y$ SC, they are tied to the core of the vortices[Read and Green, 2000; Ivanov, 2001]. Intrinsic triplet pairing is, however, very sensitive to disorder, making it difficult to achieve experimentally because it requires very clean materials. Its existance was theorized in Sr_2RuO_4 by Das Sarma *et al.* [2006], but it remains to be observed experimentally.

About a decade ago, it was proposed by Fu and Kane [2008] that the surface states in a strong topological insulator in contact with an ordinary s-wave SC experience an effective triplet superconducting pairing. The mechanism behind this is the interplay between a strong spin-orbit coupling and the proximity induced s-wave pairing. Additionally, a Zeeman field has to be induced in order to lift the Kramer's degeneracy and effectively create a spin polarized band. It was soon thereafter realized that this may also be achieved by replacing the topological insulator by a SM with strong Rashba spin-orbit coupling[Sau *et al.*, 2010a; Alicea, 2010], enabling the use of a wide array of experimentally accessible materials.

One of the simplest setups, proposed by Oreg *et al.* [2010] and Lutchyn *et al.* [2010], is a 1D SM nanowire with strong Rasbha spin-orbit and superconducting s-wave pairing, subjected to a magnetic field. The s-wave pairing can be induced by proximity to a bulk s-wave SC, such as Al or NbTiN and Rashba spin-orbit coupling is generated by breaking inversion symmetry when placing the nanowire on an electrically gated surface. The interplay between the spin-orbit field and magnetic field results in a helical band, which effectively generates a superconducting p-wave pairing from the induced s-wave pairing.

Spectroscopic signatures of Majorana bound states

Despite the relative simplicity of this proposal, it requires very high quality materials as well as a high degree of experimental control, and involves counteracting factors, such as magnetic fields and superconductivity. Thus far, it has not been possible to realize a system where the non-abelian anyonic properties of MBS can put to the test. This field is still in the phase of refining experimental techniques and materials, as well at finding good setups for examining MBS braiding statistics. In order to guide experimental efforts, many indirect indicators have been proposed to test for the presence of MBSs. Among these indicators are: The $2e^2/h$ conductance at zero bias due to perfect Andreev reflection through the MBS[Law *et al.*, 2009; Linder *et al.*, 2010; Sengupta *et al.*, 2001; Flensberg, 2010; Akhmerov *et al.*, 2009; Wimmer *et al.*, 2011]. The 4π periodic Josephson effect[Kwon *et al.*, 2003; Fu and Kane, 2009; San-Jose *et al.*, 2012]. Exponentially suppressed energy splitting

of overlapping MBSs[Kitaev, 2001]. Oscillating energy splitting of overlapping MBSs as a function of chemical potential and magnetic field[Das Sarma *et al.*, 2012].

Many of these proposals involve using electron tunneling spectroscopy (ETS) to probe quantum states in the nanowire as a function of the applied source-drain bias. Experiments using this technique generally fall into one of two categories. One where a tunnel barrier is induced at the interface with the source lead and ETS is performed at one end only while the SC-SM nanowire is grounded by the drain lead. The second category is the Coulomb blockaded type, where tunnel barriers are induced at the interface of both the source and the drain lead, such that the SC-SM nanowire becomes a floating charged island with a tunable number of electrons.

One-end ETS experiments have mainly been focused on finding supporting evidence for MBSs by measuring $2e^2/h$ quantized zero bias conductance. The first zero bias peaks (ZBPs) in SC-SM nanowire devices were reported by Mourik *et al.* [2012] (shown in Fig. 1.1), Das *et al.* [2012], and Churchill *et al.* [2013]. These observations sparked a lot of excitement despite the conductance peaks being considerably smaller than $2e^2/h$. Other experiments have since reported similar findings, but the value of a non-quantized ZBP as a MBS signature has been questioned, since trivial Andreev bound states (ABS) may also be responsible[Liu *et al.*, 2012; Pikulin *et al.*, 2012; Liu *et al.*, 2017b]. A ZBP originating from a trivial ABS can take any value between 0 and $4e^2/h$, while one caused by a MBS should not surpass $2e^2/h$. Hence there was still the possibiity that the ZBP could be a MBS signature and a lot of effort was put into improving experiments to see whether the observed ZBP would saturate at $2e^2/h$ or surpass it. $2e^2/h$ quantized ZBPs in conductance have been reported by Nichele *et al.* [2017] and Zhang *et al.* [2018] as shown in Fig. 1.2. It was nevertheless recently shown by Moore *et al.* [2018b] and Vuik *et al.* [2018] that partially separated ABS (ps-ABS) might give rise to a persistent and $2e^2/h$ quantized ZBP, once more casting doubt on the potential of this being a MBS signature.

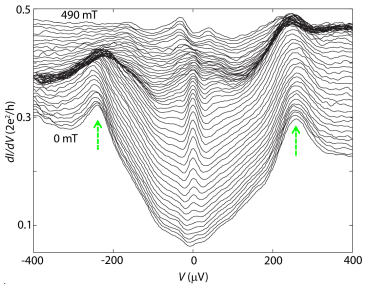

Figure 1.1: Measurement of one of the first zero bias peak from Mourik *et al.* [2012].

In the second category of experiments, the Coulomb blockaded ETS, the exponential suppression of energy splitting with nanowire length was reported by Albrecht *et al.* [2016]. Data from the experiments is shown in Fig. 1.3, where the energy splitting of the possibly MBS is obtained from the distance between the measured zero bias conductance peaks. Even though the data seem to support the existence of MBSs, it also showed discrepancies, such as MBS energy oscillations decreasing in amplitude instead of growing. Whether these observations speak in favor or against the presence of MBSs is still debated[Rainis *et al.*, 2013; van Heck *et al.*, 2016; Chiu *et al.*, 2017; Reeg *et al.*, 2017; Domínguez *et al.*, 2017; Escribano *et al.*, 2017; Reeg *et al.*, 2018].

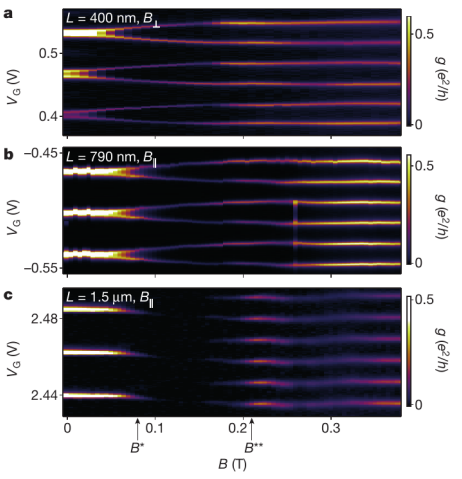

Figure 1.3: Measurement of zero bias conductance as a function of magnetic field and gate voltage, reported by Albrecht *et al.* [2016]. Energy splitting of the possible MBS is calculated from the distance between conductance peaks. The amplitude of the splitting decays exponentially with the length of the nanowire.

At the current state of the field, the presence of MBSs in SC-SM nanowires remains an open question, which in the end can only be answered by experimental observations. However,

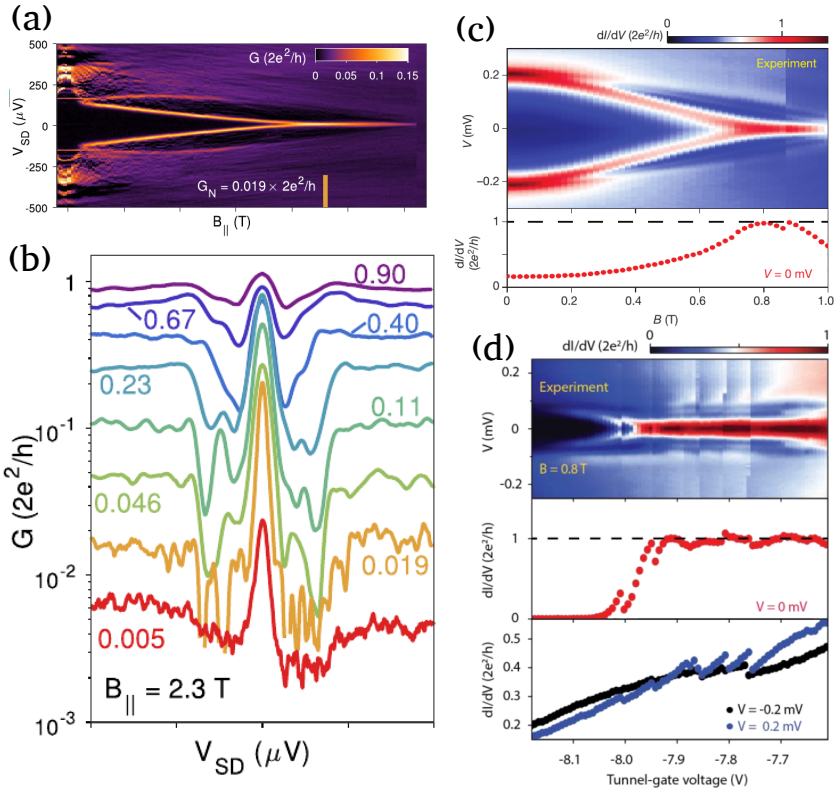

Figure 1.2: Measurements of $2e^2/h$ quantized ZBP reported by Nichele *et al.* [2017], (a) and (b), and by Zhang *et al.* [2018], (c) and (d). (a) and (c) show conductance measured as a function of magnetic field and source drain bias. (b) and (d) show conductance as a function of source drain bias for increasing transmission and a saturation of the ZBP at $2e^2/h$.

theoretical work dealing with interpreting experimental data, finding new ways to identify MBSs, and understanding the experimental setups is important in guiding experimental efforts and scrutinizing experimental findings. Time will tell whether the tremendous effort put into the study of these SC-SM nanowire devices will ultimately result in the realization of a topological quantum computer or not. Nonetheless, it will hopefully lead to a better understanding of quantum mechanical phenomena in these systems as well as great advancements in the materials used.

Structure of thesis

This thesis is devoted to the study of the MBS in SC-SM nanowires and how they may be discerned using ETS. The thesis is structured into three parts as follows:

In the remainder of this part, we will go through three microscopic models that are widely used to describe SC-SM-nanowires: The spinless p-wave SC, SC-SM nanowire Hamiltonian, and the SC-SM nanowire with energy-dependent gap.

The second part will be centered around studying one-end ETS of a grounded SC-SM nanowire. The differential conductance is computed using the scattering matrix formalism, taking a microscopic tight-binding version of one of the models introduced in the previous part as input. This transport model will be used in three projects: The first project is concerned with identifying features of MBSs in a Normal-Superconducting-Normal-Superconducting (N-SNS) setup[Hansen *et al.*, 2016]. The second project is a study of ETS through a quantum dot at the end of a SC-SM nanowire[Deng *et al.*, 2016]. We will focus on the theoretical modeling of the setup. In the third project, we investigate the effects that the

normal-conducting drain lead may have on the bulk SC in SC-SM nanowire setups[Danon *et al.*, 2017].

The third and last part of this thesis is devoted to studying SC-SM nanowires by ETS in a Coulomb blockade setup. A transport model based on the tunneling Hamiltonian formalism is used to calculate the two terminal current through the Coulomb blockaded nanowire by solving a set of steady state Pauli master equations. The nanowire is modeled as a superconducting island with a BCS density of states and a subgap state. We go present and discuss two projects where this transport model will be employed. In the first project, quasiparticle poisoning in a Coulomb blockaded nanowire island is studied and the transport model is used to obtain a quantitative estimate of the quasiparticle poisoning rate[Albrecht *et al.*, 2017]. In the second project, we study how the ratio of the heights of consecutive zero bias Coulomb peaks in the sequential tunneling regime can be used to measure the electron and hole components of the lowest-energy subgap state[Hansen *et al.*, 2018]. We discuss how this may be used to distinguish trivial ps-ABSs that exhibit MBS-like conductance features from real MBSs by comparing the conductance peak ratio with the energy splitting of the subgap state.

Chapter 2

Majorana Nanowires

> "The electron is a theory we use; it is so useful in understanding the way nature works that we can almost call it real.
>
> Richard Feynman

In this chapter we will introduce three microscopic models which exhibit topologically non-trivial phases with MBSs. First, the spinless p-wave superconductor, which is a cornerstone model of the theoretical study of MBSs and its relative simplicity allows for analytical results to be obtained. Second, the SM-SC nanowire Hamiltonian initially proposed by Oreg *et al.* [2010] and Lutchyn *et al.* [2010] to describe semiconducting nanowires with strong spin-orbit interactions, Zeeman fields and proximity induced s-wave superconductivity. Third, a Green's function model of the SC-SM hybrid nanowire where superconductivity is included through an energy-dependent self-energy, obtained by integrating out the electron degrees of freedom in the SC. The last two models will be employed to model SC-SM hybrid nanowire devices in the second and third parts of this thesis. The first model can be obtained as an approximation of the SC-SM nanowire Hamiltonian and will be used occasionally to achieve analytical results for further insights.

2.1 Classification of Topological phases

Before introducing the three models, we will briefly touch upon the classification scheme used to classify topological phases in insulators and superconductors. In general, most topological phases are strongly interacting systems where the ground state has long range entanglement. These systems fall outside the scope of this classification scheme, which is restricted to systems that can be described by an effective weakly interacting model that has a band gap in the electronic excitation spectrum. Systems of this type can be categorized into 10 symmetry classes introduced by Zirnbauer [1996] and Altland and Zirnbauer [1997]. The symmetry class is determined by the symmetries exhibited by the bulk single particle Hamiltonian. Depending on the dimensionality, each symmetry class may exhibit a different number of topologically distinct phases.

The distinct topological phases within each symmetry class are divided into trivial or non-trivial phases. The non-trivial phases are characterized by hosting topologically protected excitations, usually, in the form of gapless excitations on the boundary. Every symmetry class has one trivial phase which is topologically equivalent to vacuum, in the

sense that there do not exist gapless excitations on the boundary to vacuum. The number of topologically non-trivial phases depends on the dimensionality and are often just termed topological phases. The MBS is an example of a gapless excitation signifying a topological phase.

We will briefly review the topological classification scheme introduced by Zirnbauer [1996] and Altland and Zirnbauer [1997]. Consider a system of non-interacting fermions described by a Hamiltonian written in second quantization

$$H = \sum_{AB} \psi_A^\dagger \mathcal{H}_{A,B} \psi_B, \tag{2.1}$$

where $\psi_A^\dagger$ and ψ_B are fermionic creation and annihilation operators satisfying the usual anti-commutation relations. The subscripts A and B can be a set of indices labeling spins, lattice or continuous coordinates, orbitals and/or momenta. In BdG formalism, the sum can be written as a matrix product

$$H = \frac{1}{2} \Psi^\dagger \mathcal{H} \Psi, \tag{2.2}$$

where $\mathcal{H}_{A,B}$ are the matrix elements of the BdG-Hamiltonian $\mathcal{H}$ and $\Psi = (\psi, \psi^\dagger)^T$ is called the Nambu spinor. Hamiltonians of this form is classified according to three symmetry operators.

The Hamiltonian is said to possess particle-hole symmetry (PHS) if there exists an anti-unitary operator Υ such that $\Upsilon \mathcal{H} \Upsilon^{-1} = -\mathcal{H}$. An anti-unitary operator can in general be written as the product of a unitary operator and the complex conjugation operator. Secondly, the Hamiltonian is time-reversal symmetric (TRS) if there exists an anti-unitary operator Θ such that $\Theta \mathcal{H} \Theta^{-1} = \mathcal{H}$. The third kind of symmetry, called chiral (or sublattice) symmetry (SLS), may be present if either the Hamiltonian exhibits or lacks both time-reversal *and* particle-hole symmetry. The Hamiltonian is then classified according to its possessed symmetries and whether the corresponding anti-unitary operators square to +1 or −1.

		TRS	PHS	SLS	$d = 1$	2	3
Standard	A (unitary)	0	0	0	–	$\mathbb{Z}$	–
	AI (orthogonal)	+1	0	0	–	–	–
	AII (symplectic)	−1	0	0	–	$\mathbb{Z}_2$	$\mathbb{Z}_2$
Chiral	AIII (unitary)	0	0	1	$\mathbb{Z}$	–	$\mathbb{Z}$
	BDI (orthogonal)	+1	+1	1	$\mathbb{Z}$	–	–
	CII (symplectic)	−1	−1	1	$\mathbb{Z}$	–	$\mathbb{Z}_2$
BdG	D	0	−1	0	$\mathbb{Z}_2$	$\mathbb{Z}$	–
	C	0	−1	0	–	$\mathbb{Z}$	–
	DIII	−1	+1	1	$\mathbb{Z}_2$	$\mathbb{Z}_2$	$\mathbb{Z}$
	CI	+1	−1	1	–	–	$\mathbb{Z}$

Table 2.1: The 10 symmetry classes of single particle Hamiltonians classified according to the ten-fold way as presented by Schnyder *et al.* [2008]. The absence of a symmetry is denoted by "0" while ±1 denotes that the symmetry is present and the value of the square of the corresponding anti-unitary operator. The corresponding group of the topological invariant for the 10 symmetry classes in one to three dimensions are listed in the three rightmost columns.

The 10 resulting symmetry classes may each host 1, 2, or more topological phases depending on the dimensionality of the system [Schnyder *et al.*, 2008]. Systems with only 2 distinct topological phases are labeled by a $\mathbb{Z}_2$ invariant, while those with more are labeled by a $\mathbb{Z}$ invariant. The 10 symmetry classes are listed in Table 2.1 along with the group of their associated topological invariant in one to three dimensions.

2.2 Spinless p-wave superconductor

We will start by examining the 1D spinless p-wave superconductor, which is one of the simplest models exhibiting MBSs. It is possible to obtain some analytic results from which we gain some insights into the nature of MBSs that are useful when we consider more complicated models later on.

Consider a 1D system of spinless fermions with the unconventional p-wave superconducting pairing described by the Hamiltonian

$$H_{\text{pw}} = \frac{1}{2}\int \Psi^\dagger(x)\,\mathscr{H}_{\text{pw}}\Psi(x)\,\mathrm{d}x, \tag{2.3}$$

where $\Psi(x) = (\psi(x), \psi^\dagger(x))^T$ is a Nambu spinor with the operator $\psi^\dagger(x)$ creating a fermion at position x. The single particle BdG-Hamiltonian is

$$\mathscr{H}_{\text{pw}} = \left(-\frac{\hbar^2}{2m}\partial_x^2 - \mu\right)\tau_z - i\hbar\Delta\tau_x\partial_x \tag{2.4}$$

with the fermion mass m, the chemical potential μ, and the superconducting gap Δ which we assume to be real and positive. The Pauli matrices $\vec{\tau}$ act in particle-hole space. This Hamiltonian is both time-reversal symmetric and particle-hole symmetric since there exist two anti-unitary operators

$$\mathrm{Y} = \tau_x\mathcal{K} \qquad \text{and} \qquad \Theta = \mathcal{K}, \tag{2.5}$$

for which

$$\mathrm{Y}\,\mathscr{H}_{\text{pw}}\mathrm{Y}^{-1} = -\mathscr{H}_{\text{pw}} \qquad \text{and} \qquad \Theta\,\mathscr{H}_{\text{pw}}\Theta^{-1} = \mathscr{H}_{\text{pw}}. \tag{2.6}$$

The time-reversal operator Θ differs from the operator that is customarily denoted the time-reversal operator for fermions, $i\sigma_y\mathcal{K}$, and is therefore sometimes called a pseudo-time-reversal operator.

We straight forwardly get $\mathrm{Y}^2 = 1$ and $\Theta^2 = 1$, so according to Table 2.1, the p-wave Hamiltonian belongs to the BDI symmetry class. In general, the topological phases of a 1D system in the BDI symmetry class can be classified by a $\mathbb{Z}$ invariant. However, in the single channel bulk Hamiltonian we consider here there are two distinct topological phases: A trivial phase without MBSs and a topological phase with MBSs.

In the semi-infinite system, the topological phase hosts a MBS at the boundary, while in a finite system, there are one MBS at each boundary of the topological phase. The two MBSs are exponentially localized at the boundary, but always has a finite overlap. Hence it is only possible to realize MBSs that are exponentially close to true topological Majorana modes in a finite system.

We will not provide a rigorous proof for identifying the different topological phases, but instead use a winding number as a layman-proof of how to distinguish topological phases of the p-wave superconductor. To this end, we consider a translationally invariant system for which we write the Hamiltonian from Eq. (2.3) in terms of momentum eigenstate operators $c_p^\dagger$:

$$H_{\text{pw}} = \frac{1}{2}\sum_k \xi_k c_k^\dagger c_k + \Delta k c_k^\dagger c_{-k}^\dagger + \text{h.c.} \tag{2.7}$$

which has the energy spectrum

$$E_\pm(k) = \pm\sqrt{\xi_k^2 + \Delta^2 k^2}, \tag{2.8}$$

with $\xi_k = \frac{\hbar^2}{2m}k^2 - \mu$ where k is the wave number in the x-direction. The spectrum, which is shown in Fig. 2.1 for three different values of $\mu = \{-1, 0, 1\}$, is gapped for all values μ except $\mu = 0$ where the gap closes. Topological phase transitions are indicated by a gap closing in the bulk spectrum, but a gap closing is not necessarily a unique signature of a topological phase transition.

In order to identify different topological phases, we look for a topological invariant that is constant throughout each phase and changes at the transition between them[Tewari and Sau, 2012]. We consider the vector

$$\mathbf{v}_k = \frac{1}{\sqrt{\xi_k^2 + \Delta^2 k^2}} \begin{pmatrix} \xi_k \\ \Delta k \end{pmatrix} = \begin{pmatrix} \mathrm{Re}\, e^{i\phi(k)} \\ \mathrm{Im}\, e^{i\phi(k)} \end{pmatrix}, \tag{2.9}$$

with the phase given by $\tan\phi(k) = \frac{\Delta k}{\xi_k}$, and let the winding number W be the number of times the $\mathbf{v}_k$ rotates around the origin as k goes from $-\infty$ to $+\infty$:

$$W = \frac{1}{2\pi}\int_{-\infty}^{\infty} \phi(k)\ \mathrm{d}k. \tag{2.10}$$

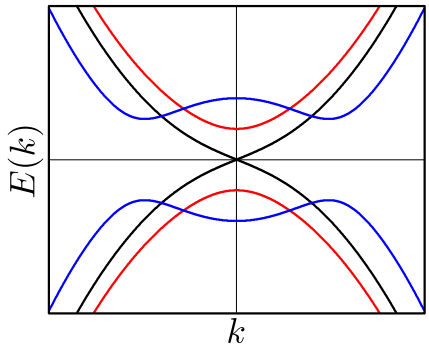

Figure 2.1: Spectrum resulting from Eq. (2.8) for $\mu < 0$ (red), $\mu = 0$ (black), and $\mu > 0$ (blue) as a function of wave number k.

The winding number is $W = 0$ for all $\mu < 0$ and $W = 1$ for all $\mu > 0$, and we take this as proof that these are two distinct topological phases separated by a phase transition at $\mu = 0$. In Fig. 2.2, we show examples of the evolution of the phase $\phi(k)$ across the k-space for different values of μ both in the trivial and topological phase.

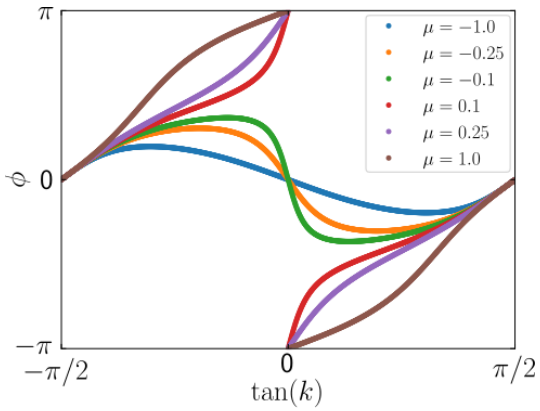

Figure 2.2: Plot of the phase $\phi(k)$ for different values of μ both in the trivial and topological phases. The y-axis is periodic, so lines ending at $\phi = \pi$ continue from $\phi = -\pi$ and k are mapped to $\tan k$ to show the whole k-space on a finite axis. In the three examples where $\mu > 0$, the phase winds 2π, while for the three with $\mu < 0$, the phase winds 0. Other parameters are $m/\hbar^2 = 1$ and $\Delta = 1$.

The phase with $W = 1$ hosts a state with energy below the gap that is exponentially localized at the edge and is therefore called the topologically non-trivial phase, or topological phase for short. The phase with $W = 0$ displays no such states and is called the topologically trivial phase or just trivial phase. The subgap state in the topological phase is a so called Majorana bound state (MBS). They always exist in pairs, since any real physical 1D system has two ends with one MBS located at each end. Each MBS also only constitutes half of an ordinary fermion and two are needed in superposition to form a whole ordinary fermion. The term "Majorana" is associated with these states because in the limit where the two MBSs are decoupled, it is possible to describe each of them by a Hermitian operator $\gamma = \gamma^\dagger$, also known as a Majorana operator. One way to theoretically obtain a true MBS is with a semi-infinite system where this state will be at zero energy. In a finite system, the two MBSs will in general acquire a non-zero energy that is exponentially small compared to the size of the system due to the overlap of their wavefunctions. We will work with a continuous model, but the corresponding tight-binding model, named the Kitaev toy

model[Kitaev, 2001], also provides a pedagogical introduction to the formation of MBSs in p-wave superconductors.

Wavefunction of the Majorana Bound State

We will be working a lot with real space wavefunctions throughout this thesis. We will therefore derive the wavefunction solution for the semi-infinite system with a hard wall condition at $x = 0$ and extending towards $x = +\infty$. We use a wavefunction ansatz of the form

$$\psi_{\mathrm{L}}(x) = \sum_n \begin{pmatrix} u_n \\ v_n \end{pmatrix} e^{-\lambda_n x} \tag{2.11}$$

where $\mathrm{Re}\,\lambda_n > 0$ so the wavefunction is localized at the left boundary. Acting with the Hamiltonian in Eq. (2.3) on the trial wavefunction we look for a $E = 0$ solution and get the secular equation

$$-\left(\frac{\hbar^2}{2m}\lambda_n^2 + \mu\right)^2 + \Delta^2\lambda_n^2 = 0 \qquad \Rightarrow \qquad \frac{\hbar^2}{2m}\lambda_n^2 + \mu - \nu\Delta\lambda_n = 0 \tag{2.12}$$

with the solution

$$\lambda_\pm = \frac{m\Delta}{\hbar^2}\left(\nu \pm \sqrt{1 - 2\frac{\hbar^2}{m\Delta^2}\mu}\right) \tag{2.13}$$

where $\nu = \pm 1$. Due to the constraint $\mathrm{Re}\,\lambda_n > 0$, only the case with $\nu = +1$ can be used. The $\nu = -1$ solution gives a wavefunction that decays in the other direction. The Schrödinger equation also gives the relation between the spinor components

$$i\Delta\lambda_\pm v_\pm = \left(-\frac{\hbar^2}{2m}\lambda_\pm^2 - \mu\right) u_\pm \tag{2.14}$$

which combined with the secular Eq. (2.12) gives

$$v_\pm = i u_\pm \tag{2.15}$$

and the wavefunction takes the form

$$\psi_{\mathrm{L}}(x) = \sum_{n=\pm} \begin{pmatrix} 1 \\ i \end{pmatrix} v_n e^{-\lambda_n x}. \tag{2.16}$$

The boundary condition $\psi(0) = 0$ gives $-v_- = v_+ \equiv C$ and the wavefunction of the MBS is then

$$\psi_{\mathrm{L}}(x) = \begin{pmatrix} 1 \\ i \end{pmatrix} C(e^{-\lambda_+ x} - e^{-\lambda_- x}), \tag{2.17}$$

where C is a normalization constant. The wavefunction is localized at the left boundary $x = 0$ and decays exponentially away from it. In the case of a finite system of length L there will be a corresponding bound state at the right end, but as long as $Lm\Delta/\hbar^2 \gg 1$ the wavefunction in Eq. (2.17) will be a good approximation of the MBS. The wavefunction of the state at the right end would have the form

$$\psi_{\mathrm{R}}(x) = \begin{pmatrix} 1 \\ -i \end{pmatrix} C(e^{\lambda_+ x} - e^{\lambda_- x}). \tag{2.18}$$

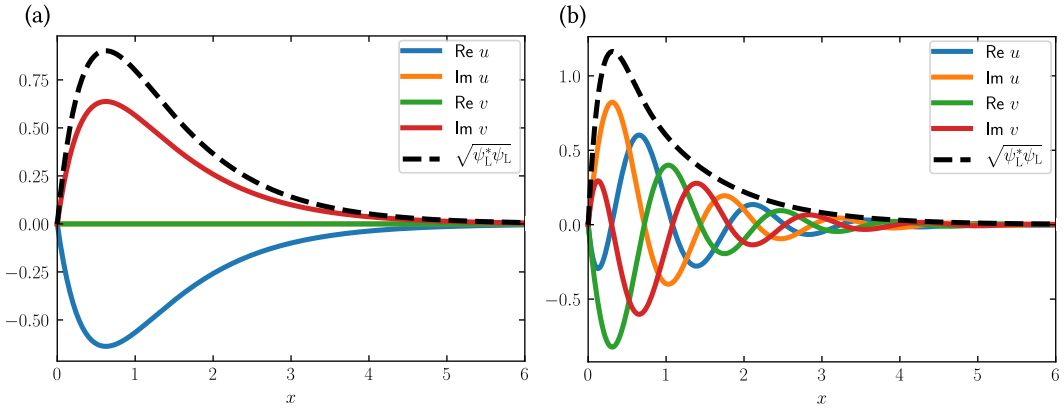

Figure 2.3: Components of the the MBS wavefunction in a semi-infinite p-wave superconductor given in Eq. (2.17) for parameters $m/\hbar^2 = 1$, $\Delta = 1$, and $\mu = 0.5$ in (a) and $\mu = 10$ in (b). u and v are the electron and hole components of the wavefunction. Note Im u = Re v = 0 in (a).

The electron and hole components u and v of ψ_L are plotted in Fig. 2.3 for a given set of parameters. For $\frac{2\hbar^2}{m\Delta^2}\mu < 1$, the wavefunction decays monotonically, while for $\frac{2\hbar^2}{m\Delta^2}\mu < 1$ it oscillates while decaying. In the first case, the localization length is given by λ_-. In the second case, the localization length is given by $\mathrm{Re}\,\lambda_\pm = m\Delta\hbar^{-2}$ and the wave length by $|\mathrm{Im}\,\lambda_\pm| = \frac{m\Delta}{\hbar^2}\sqrt{\frac{2\hbar^2}{m\Delta^2}\mu - 1}$. The wavefunction oscillates more rapidly as μ is increased. This can be understood as the localized MBS has support from states with wave numbers close to the Fermi wave number $k_F = \frac{\sqrt{2m\mu}}{\hbar}$, which grows as the chemical potential μ increases.

2.3 Superconductor-semiconductor hybrid nanowire Hamiltonian

The spinless p-wave SCs are not readily available in nature, but it is possible to generate a low-energy effective model with p-wave pairing from the interplay of Rashba spin-orbit coupling, a Zeeman field, and ordinary s-wave pairing. One such system that combines these ingredients is the SM nanowire, contacted with a s-wave SC, and subjected to a magnetic field. However, some of these factors counteract each other. For example, the large Zeeman field required to reach the topological phase is induced by applying a magnetic field, which at the same time becomes detrimental to the superconducting phase of the contacted parent SC. A very large g-factor in the SM is therefore desired in order to have a regime where the superconducting gap is of appreciable size when the topological phase is reached. In order to have a considerable and hard induced superconducting gap, the interface between the SM and the SC has to be good. Experiments have mainly used InAs and InSb nanowires due to their strong spin-orbit coupling, high electron mobility, and large Landé g-factor, while Al or NbTiN have been used as parent s-wave SCs. NbTiN has a larger superconducting gap, but the superconducting phase in Al is less susceptible to the applied magnetic field.

The 1D nanowires can be fabricated by growing nanowires by molecular epitaxy beam or by lithographically defining nanowire strips in a 2D quantum well heterostructure[Shabani *et al.*, 2016]. Previously, the parent SC was deposited on the nanowire after the nanowire had been exposed to oxygen making it necessary to remove an oxidized layer before deposition, which resulted in a soft induced superconducting gap due to a rough interface between the materials. Today, Al can be grown epitaxially on a nanowire or heterostructure[Krogstrup *et al.*, 2015; Zhang *et al.*, 2017] with a near perfect interface, yielding a hard induced superconducting gap[Chang *et al.*, 2015; Kjaergaard *et al.*, 2016; Gül *et al.*, 2017] in the SM nanowire. A good interface, however, also leads to a strong hybridization between the

SM and SC leading to a renormalization of the SM's parameters, such as a less effective g-factor. We will postpone a more accurate treatment of the parent SC to the next section and here introduce the SC-SM nanowire model, as we will denote it, where the induced s-wave pairing is described by a fixed potential.

We model the nanowire by the single channel Hamiltonian[Oreg *et al.*, 2010; Lutchyn *et al.*, 2010]

$$H = H_{\text{NW}} + H_{\text{SC}}, \tag{2.19}$$

where H_{NW} contains the kinetic part, the Rashba spin-orbit coupling, and the Zeeman field, while H_Δ contains the proximity induced superconductivity. Considering the first term

$$H_{\text{NW}} = \frac{1}{2}\int \Psi^\dagger(x)(\mathscr{H}_{\text{kin}} + \mathscr{H}_{\text{SOI}} + \mathscr{H}_{\text{Z}})\Psi(x)\,\mathrm{d}x, \tag{2.20}$$

with the Nambu spinor $\Psi(x) = (\psi_\uparrow(x), \psi_\downarrow(x), \psi_\downarrow^\dagger(x), -\psi_\uparrow^\dagger(x))^T$, where the operator $\psi_\sigma^\dagger(x)$ creates an electron of spin σ at position x. The Hamiltonian consists of three parts. The kinetic energy term

$$\mathscr{H}_{\text{kin}} = \left(-\frac{\hbar^2}{2m^*}\partial_z^2 - \mu\right)\tau_z, \tag{2.21}$$

where m^* is the effective mass of the electrons and μ is the chemical potential. The spin-orbit interaction term

$$\mathscr{H}_{\text{SOI}} = -i\alpha_{\text{R}}\partial_z\sigma_x\tau_z, \tag{2.22}$$

which is the Rashba type with α_{R} being the coupling strength. Lastly, the Zeeman field term

$$\mathscr{H}_{\text{Z}} = \frac{1}{2}g\mu_B\vec{\mathbf{B}}\cdot\vec{\boldsymbol{\sigma}} = \vec{V}_{\text{Z}}\cdot\vec{\boldsymbol{\sigma}}, \tag{2.23}$$

where g is the effective Landé g-factor and μ_{B} is the Bohr magneton. In general we will assume the Zeeman field to point along the wire and z-axis such that $\mathscr{H}_{\text{Z}} = V_{\text{Z}}\sigma_z$. The Pauli matrices $\vec{\boldsymbol{\sigma}}$ and $\vec{\boldsymbol{\tau}}$ act in spin and particle-hole space, respectively. The proximity induced superconductivity is described by the Hamiltonian

$$H_{\text{SC}} = \frac{1}{2}\int \Psi^\dagger(x)\,\mathscr{H}_{\text{SC}}\Psi(x)\,\mathrm{d}x = \frac{1}{2}\int \Psi^\dagger(x)\Delta_0\tau_x\Psi(x)\,\mathrm{d}x, \tag{2.24}$$

where Δ_0 is the induced superconducting gap.

The single particle Hamiltonian in momentum space is

$$\mathscr{H}^{(k)} = \mathscr{H}_{\text{NW}}^{(k)} + \mathscr{H}_{\text{SC}}^{(k)} = \begin{bmatrix} \xi_k + \alpha_{\text{R}}k\sigma_x + V_{\text{Z}}\sigma_z & \Delta_0 \\ \Delta_0 & -\xi_k - \alpha_{\text{R}}k\sigma_x + V_{\text{Z}}\sigma_z \end{bmatrix} \tag{2.25}$$

with the bulk spectrum

$$E_\pm^2(k) = V_{\text{Z}}^2 + \Delta^2 + \xi_k^2 + \alpha_{\text{R}}^2k^2 \pm 2\sqrt{V_{\text{Z}}^2\Delta^2 + V_{\text{Z}}^2\xi_k^2 + \alpha_{\text{R}}^2k^2\xi_k^2}. \tag{2.26}$$

The Hamiltonian is both time-reversal and particle-hole symmetric, with the same operators as the p-wave Hamiltonian, given in Eq. (2.5). It therefore also belongs in the BDI symmetry class and should exhibit MBSs if the system can be brought into a topologically non-trivial phase.

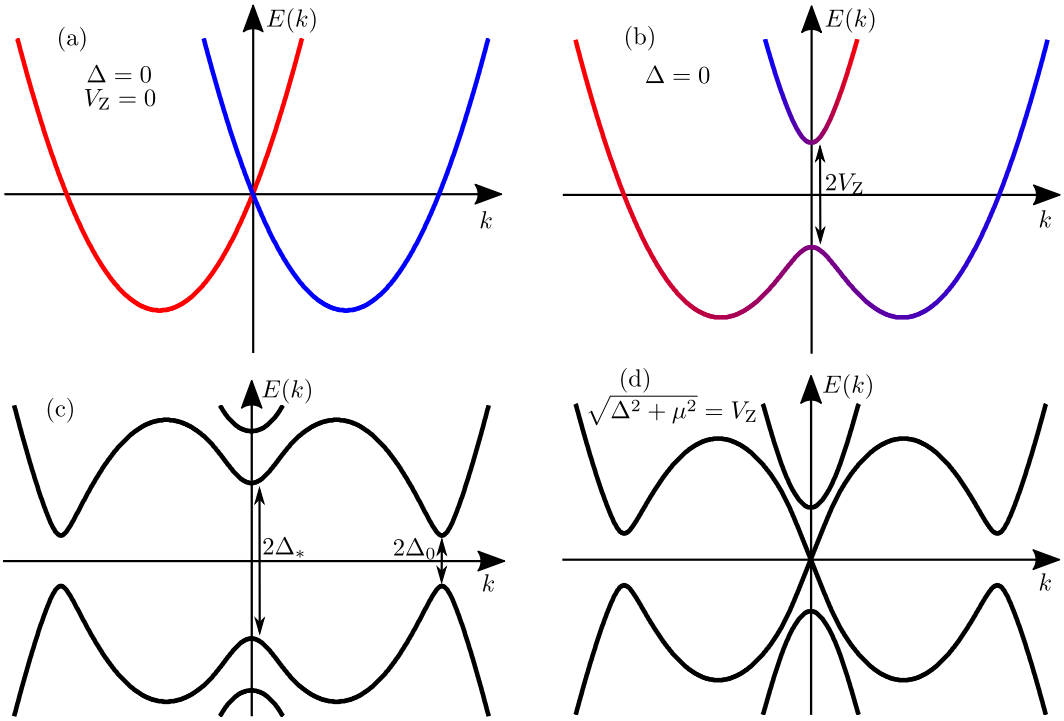

Figure 2.4: Bulk spectrum given by Eq. (2.26) for different parameters, all with $\mu = 0$. (a) and (b): The spin component along the spin-orbit field is shown by the line color. $\Delta_* = |V_Z - \sqrt{\Delta^2 + \mu^2}|$

In order to become familiar with this somewhat complex Hamiltonian and illustrate its connection to the p-wave Hamiltonian, we will discuss how the different parts of the Hamiltonian influence the bulk spectrum. For this discussion we set $\mu = 0$. We first consider the case with only spin orbit coupling present, so $V_Z = 0$ and $\Delta = 0$. The two parabolas are shifted due to the coupling of momentum and spin, as shown in Fig. 2.4 (a), where the direction of the spin is shown by the color of the parabola. Turning on V_Z opens up a gap at $k = 0$, as shown in Fig. 2.4 (b) and creates two helical bands where the spin changes direction as the momentum changes from negative to positive momentum. Lastly, when the superconducting s-wave pairing is included, a gap opens at the two Fermi points, as shown in Fig. 2.4 (c). The bulk spectrum is in general gapped for all parameters when $\Delta, \alpha_R \neq 0$, except at $V_{Z,c} = \sqrt{\Delta^2 + \mu^2}$, where the gap closes linearly at $k = 0$, as shown in Fig. 2.4 (d). This resembles the gap closing for the p-wave Hamiltonian and also signifies a topological phase transition in this case. Due to the Zeeman field, the spins at the Fermi points have a component pointing in the same direction, which results in an effective p-wave pairing.

To see how this comes about, we diagonalize the $\mathcal{H}_{NW}^{(k)}$ part of the Hamiltonian in Eq. (2.25), using the unitary operator $\mathcal{U} = \cos(\frac{\theta}{2})\sigma_0\tau_0 + i\sin(\frac{\theta}{2})\sigma_y\tau_z$ with $\sin(\theta) = \alpha_R k \kappa_k^{-1}$ and $\cos(\theta) = V_Z \kappa_k^{-1}$, where we have defined $\kappa_k = \sqrt{\alpha_R^2 k^2 + V_Z^2}$. After the transformation, the Hamiltonian has the form

$$\mathcal{U}^\dagger \mathcal{H}^{(k)} \mathcal{U} = \begin{bmatrix} \xi_k - \kappa_k & 0 & \frac{\Delta_0 V_Z}{\kappa_k} & -\frac{\alpha_R k \Delta_0}{\kappa_k} \\ 0 & \xi_k + \kappa_k & \frac{\alpha_R k \Delta_0}{\kappa_k} & \frac{\Delta_0 V_Z}{\kappa_k} \\ \frac{\Delta_0 V_Z}{\kappa_k} & \frac{\alpha_R k \Delta_0}{\kappa_k} & -\xi_k - \kappa_k & 0 \\ -\frac{\alpha_R p \Delta_0}{\kappa_k} & \frac{\Delta_0 V_Z}{\kappa_k} & 0 & -\xi_k + \kappa_k \end{bmatrix}, \tag{2.27}$$

where $\xi_k - \kappa_k$ and $\xi_k + \kappa_k$ correspond to the lower and upper band of the $\mathcal{H}_{NW}^{(k)}$ Hamiltonian, respectively. In this basis, it can be seen that the s-wave paring results in the inter-band

pairing $\Delta_0 V_Z \kappa^{-1}$ and intra-band pairing $\alpha_R k \Delta_0 \kappa^{-1}$ and that the latter is of the p-wave type. We perform an additional unitary transformation, which diagonalizes the inter-band pairing, but leaves the intra-band pairing unchanged:

$$\mathcal{W}^\dagger \mathcal{H}(k) \mathcal{W} = \begin{bmatrix} -\kappa_k + \rho_k & 0 & 0 & -\frac{\alpha_R k \Delta_0}{\kappa_k} \\ 0 & \kappa_k + \rho_k & \frac{\alpha_R k \Delta_0}{\kappa_k} & 0 \\ 0 & \frac{\alpha_R k \Delta_0}{\kappa_k} & -\kappa_k - \rho_k & 0 \\ -\frac{\alpha_R k \Delta_0}{\kappa_k} & 0 & 0 & \kappa_k - \rho_k \end{bmatrix}, \tag{2.28}$$

where $\rho_k = \sqrt{\xi_k^2 + \left(\frac{\Delta V_Z}{\kappa_k}\right)^2}$. The inter-band pairing lifts the degeneracy at $k = 0$ between the $\xi_k - \kappa_k$ and $-\xi_k - \kappa_k$ band, as seen in Fig. 2.5.

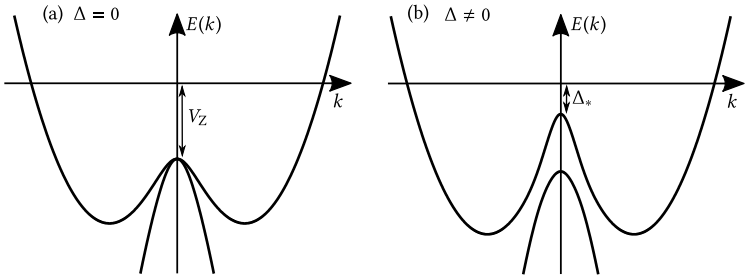

Figure 2.5: Energy spectrum of band $(-\kappa_k + \rho_k)$ and $(-\kappa_k - \rho_k)$. (a) For $\Delta = 0$ the two bands are degenerate at $k = 0$. (b) For $\Delta \neq 0$ a gap of $2\Delta_* = \left|\sqrt{\Delta_0^2 + \mu^2} - V_Z\right|$

Now the upper and lower band are decoupled and we consider just the lower energy (LE) band

$$\mathcal{H}_{\text{LE}}^{(k)} = (-\kappa_k + \rho_k)\tau_z - \frac{\alpha_R k \Delta_0}{\kappa_k}\tau_x. \tag{2.29}$$

It may not be obvious from this Hamiltonian that it is gapped for all $k \neq 0$ when $\Delta, \alpha_R, V_Z \neq 0$, so we will explore the spectrum a bit further. The band $-\kappa_k + \rho_k$ may have zeros at finite k, as seen in Fig. 2.5, but the off-diagonal term $\alpha_R k \Delta_0 \kappa_k^{-1} \tau_x$ couples the particle and hole band, opening a gap for all $k \neq 0$. So the only place where the spectrum can close is where this particle-hole pairing is zero, at $k = 0$, which then happens for $V_{Z,c} = \sqrt{\mu^2 + \Delta_0^2}$.

In the limit of $V_Z \gg \alpha_R k_F$ where $\kappa_k \approx V_Z$ we see that it has the form of the p-wave Hamiltonian in Eq. (2.4), although with a slightly different kinetic term

$$\mathcal{H}_{\text{LE}}^{(k)} \approx \left(\sqrt{\xi_k^2 + \Delta_0^2} - V_Z\right)\tau_z - \frac{\alpha_R k \Delta_0}{V_Z}\tau_x. \tag{2.30}$$

From here we also see that even though the Zeeman field drives the system into the topological phase, it also decreases the topological gap, $\frac{\alpha_R k \Delta_0}{V_Z}$, such that the topological phase only exists with a considerable gap for Zeeman fields of intermediate strength.

The exact wavefunction solutions for the MBS for this model cannot be found analytically in the general case, but certain limits are solvable[Klinovaja and Loss, 2012]. We will mainly focus on numerical studies of eigenenergies and wavefunctions and refer back to the p-wave Hamiltonian for analytic solutions when required.

Tight binding approximation and numerical computations

We will study the continuous models numerically by mapping to a lattice model, using the tight binding approximation,

$$k \to \frac{1}{a}\sin ka\,, \qquad\qquad k^2 \to \frac{4}{a^2}\sin\frac{ka}{2} = \frac{2}{a^2}(1-\cos ka), \tag{2.31}$$

where $a = L/N$ is the lattice constant, with L being the length of the nanowire and N the number of lattice sites.

After Fourier transforming from momentum space to lattice space and using the tight binding approximation, the non-superconducting part of the Hamiltonian in Eq. (2.19) takes the form

$$H_{\text{NW}} = \frac{1}{2}\sum_{i,j=1}^{N} \tilde{\mathbf{c}}_i^\dagger \mathscr{H}_{\text{NW}}^{(ij)} \tilde{\mathbf{c}}_j = \frac{1}{2}\sum_{i,j=1}^{N} \tilde{\mathbf{c}}_i^\dagger \left(\mathfrak{D}_{ij} + \mathfrak{T}_{ij}\right) \tilde{\mathbf{c}}_j, \tag{2.32}$$

where the sum is over the N lattice sites and $\tilde{\mathbf{c}}_j = (\tilde{c}_{j\uparrow}, \tilde{c}_{j\downarrow}, \tilde{c}_{j\downarrow}^\dagger, -\tilde{c}_{j\uparrow}^\dagger)^T$ is a Nambu spinor of electron lattice site operators $\tilde{c}_{j\sigma} = \sum_k e^{-ikR_j} c_{k\sigma}$ at position $R_j = ja$. The diagonal and off-diagonal parts of the lattice Hamiltonian are

$$\mathfrak{D}_{ij} = \left(\left(\frac{\hbar^2}{m^* a^2} - \mu\right)\tau_z + V_{\text{Z}}\sigma_z\right)\delta_{i,j}, \tag{2.33}$$

$$\mathfrak{T}_{ij} = \left(-\frac{\hbar^2}{2m^* a^2}(\delta_{i,j+1} + \delta_{i+1,j}) - \frac{i\alpha_{\text{R}}}{2a}\sigma_x(\delta_{i,j+1} - \delta_{i+1,j})\right)\tau_z. \tag{2.34}$$

and the superconducting part is

$$H_{\text{SC}} = \frac{1}{2}\sum_{i,j=1}^{N} \tilde{\mathbf{c}}_i^\dagger \Delta_0 \tau_x \delta_{i,j} \tilde{\mathbf{c}}_j, \tag{2.35}$$

We solve the eigenvalue equation of this discretized Hamiltonian in order to obtain the eigenenergies and eigenfunctions. Numerical computations are carried out in Python 3.6.5 using routines from the Numpy package[1]. The computations mainly involve obtaining eigenvalues and eigenvectors of a Hamiltonian represented as a matrix, inversion of matrices and solving linear sets of equations.

Majorana modes

Just as Kitaev [2001] wrote the fermionic operators of the Kitaev chain as a superposition of Hermitian Majorana operators, we can decompose the eigenfunctions of the discretized SC-SM Hamiltonian in a similar manner.

The eigenfunction with the corresponding eigenenergy ϵ has the form

$$\phi_\epsilon(i) = (u_{\epsilon\uparrow i}, u_{\epsilon\downarrow i}, v_{\epsilon\downarrow i}, -v_{\epsilon\uparrow i})^T, \tag{2.36}$$

where i is the site index on the chain of the discretized Hamiltonian. The creation operator corresponding to the state with energy ϵ can be written in terms of this eigenfunction and the electron creation and annihilation operators,

$$\psi_\epsilon^\dagger = \sum_i u_{\epsilon\uparrow i} c_{\uparrow i}^\dagger + u_{\epsilon\downarrow i} c_{\downarrow i}^\dagger + v_{\epsilon\downarrow i} c_{\downarrow i} - v_{\epsilon\uparrow i} c_{\uparrow i}. \tag{2.37}$$

1. Documentation can be found at https://docs.scipy.org/doc/

Due to particle-hole symmetry, the spectrum is symmetric around zero energy and the negative eigenfunction is related to the positive partner by

$$\phi_{-\epsilon}(i) = (-v^*_{\epsilon\uparrow i}, v^*_{\epsilon\downarrow i}, u^*_{\epsilon\downarrow i}, u^*_{\epsilon\uparrow i})^T. \tag{2.38}$$

From each pair of positive and negative eigenfunctions, we can construct linear combinations

$$\chi_{\epsilon A}(i) = \frac{1}{\sqrt{2}}\left[\phi_\epsilon(i) + \phi_{-\epsilon}(i)\right] = \left[\tilde{u}_{\epsilon A\uparrow i}, \tilde{u}_{\epsilon A\downarrow i}, \tilde{u}^*_{\epsilon A\downarrow i}, -\tilde{u}^*_{\epsilon A\uparrow i}\right], \tag{2.39}$$

$$\chi_{\epsilon B}(i) = \frac{i}{\sqrt{2}}\left[\phi_\epsilon(i) - \phi_{-\epsilon}(i)\right] = \left[\tilde{u}_{\epsilon B\uparrow i}, \tilde{u}_{\epsilon B\downarrow i}, \tilde{u}^*_{\epsilon B\downarrow i}, -\tilde{u}^*_{\epsilon B\uparrow i}\right], \tag{2.40}$$

with the corresponding operators

$$\gamma^\dagger_{\epsilon\alpha} = \sum_i \tilde{u}_{\epsilon\alpha\uparrow i} c^\dagger_{\uparrow i} + \tilde{u}_{\epsilon\alpha\downarrow i} c^\dagger_{\downarrow i} + \tilde{u}^*_{\epsilon\alpha\downarrow i} c_{\downarrow i} - \tilde{u}^*_{\epsilon\alpha\uparrow i} c_{\uparrow i}, \tag{2.41}$$

with $\alpha = A, B$. These linear combinations correspond to splitting each fermionic excitation $\psi^\dagger_\epsilon$ into a pair of Majorana operators, which satisfy $\gamma^\dagger_\alpha = \gamma_\alpha$. However, these linear combinations of eigenfunctions are not exact eigenstates of the Hamiltonian, but rather fulfill

$$\langle\chi_{\epsilon\alpha}|H|\chi_{\epsilon\alpha}\rangle = 0, \qquad \text{and} \qquad \langle\chi_{\epsilon A}|H|\chi_{\epsilon B}\rangle = i\epsilon, \tag{2.42}$$

corresponding to the overlap between the two Majorana states $|\chi_{\epsilon A}\rangle$ and $|\chi_{\epsilon B}\rangle$ that constitute the fermionic state $|\psi_\epsilon\rangle$. For most fermionic states, the two Majorana states have a large overlap in space, but for the MBS existing in the topological phase, the two Majorana states are exponentially localized at opposite ends of the nanowire.

Examples

We will now compute the eigenvalue spectrum as a function of parameters that can be tuned in experimental setups to see how the spectrum depends on model parameters. For a more detailed study we refer to the work by Mishmash *et al.* [2016].

In Fig. 2.6 we show several plots of the eigenvalue spectrum as a function of Zeeman field along the nanowire. Left and right columns compare a short ($L = 0.75\,\mu\text{m}$) and a long nanowire ($L = 1.5\,\mu\text{m}$) with different spin-orbit coupling strengths $\alpha_\text{R} = \{5, 10, 20, 50\}\,\mu\text{eV}\,\mu\text{m}$. With the chosen parameters $\Delta = 150\,\mu\text{eV}$ and $\mu = 0\,\mu\text{eV}$, the topological phase transition happens at $V_{\text{Z,c}} = 150\,\mu\text{eV}$, but it is seen that the bulk spectrum does not necessarily close and reopen as expected at a topological phase transition. This is due to finite size effects and strong spin-orbit interactions, which can make the level spacing large enough to push the bulk states out of the gap at the phase transition. The emerging MBS also does not reach zero energy at the bulk phase transition in these cases, but rather a slightly higher Zeeman field. The energy splitting oscillations of the MBS are larger in shorter wires and for small spin-orbit coupling. The topological gap after phase transition, on the other hand, grows with increasing spin-orbit coupling.

In Fig. 2.7, we see the two Majorana wavefunctions, calculated from the numerically obtained wavefunctions using Eq. (2.39) and (2.40), for three values of Zeeman field. One before the phase transition at $V_{\text{Z,c}} = 150\,\mu\text{eV}$ and two after. In the trivial phase, the two Majorana wavefunctions have a large overlap and they have a bulk-state profile extending over the whole nanowire. In the topological phase, the two Majorana wavefunctions are localized at opposite ends. They are more localized close to the phase transition, while at large V_Z, they become less localized and their overlap increases.

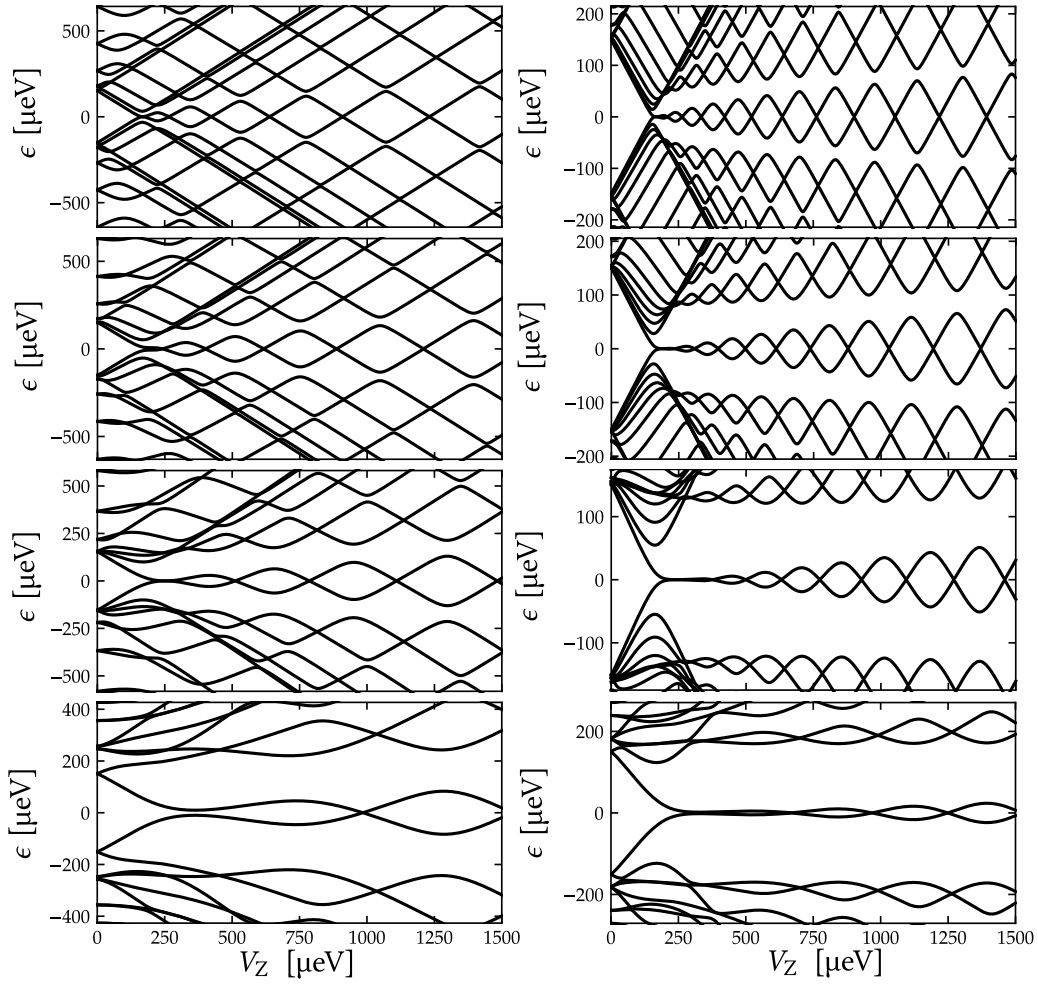

Figure 2.6: Eigenvalue spectrum as function of Zeeman field V_Z. Left: $L = 0.75\,\mu m$ Right: $L = 1.5\,\mu m$. Spin-orbit coupling is the same in each row. From top to bottom: $\alpha_R = 5\,\mu eV\,\mu m$, $10\,\mu eV\,\mu m$, $20\,\mu eV\,\mu m$ and $50\,\mu eV\,\mu m$. Other parameters are $m^* = 0.026\,m_e$, $\Delta_0 = 150\,\mu eV$, $\mu = 0\,\mu eV$, $N = 100$ sites

In Fig. 2.8, the eigenvalue spectrum is shown as a function of chemical potential for three different Zeeman fields. The top one is solely in the trivial phase, while the other two are in the topological phase for a finite region of chemical potential symmetric around $\mu = 0$. The topological phase transitions happen at $\mu_c = \pm\sqrt{V_Z^2 - \Delta^2}$. Energy splitting oscillations of the MBS also occur as a function of chemical potential, as can be seen at high Zeeman fields in the right plot.

A picture of the phase diagram as a function of Zeeman field and chemical potential can be constructed by computing the energy of the lowest-energy eigenstate, as shown in Fig. 2.9. The color-scale shows the energy of the state and the white dashed line indicates the topological phase transition with the topological phase to the right, inside the sideways parabola. In order to make the oscillations apparent, the color-scale saturates at the value of the induced superconducting gap Δ_0.

The striped pattern inside the topological phase is a generic feature in the case where the overlap of the Majorana modes located at each end is large enough to cause visible energy splitting. The spacing between the stripes becomes larger for increasing V_Z and μ indicating that energy splitting and the overlap of the end state Majorana modes becomes

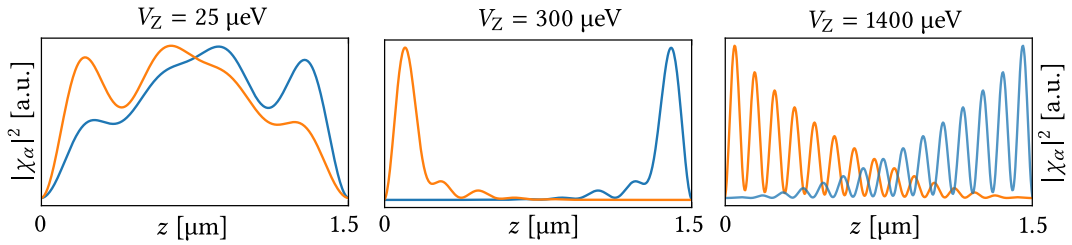

Figure 2.7: Majorana wavefunction for the lowest-energy state for three different values of Zeeman fields. Other parameters are $\alpha_R = 20\,\mu\text{eV}\,\mu\text{m}$, $m^* = 0.026\,m_e$, $\Delta_0 = 150\,\mu\text{eV}$, $\mu = 0\,\mu\text{eV}$, L =1.5 μm, $N = 400$ sites.

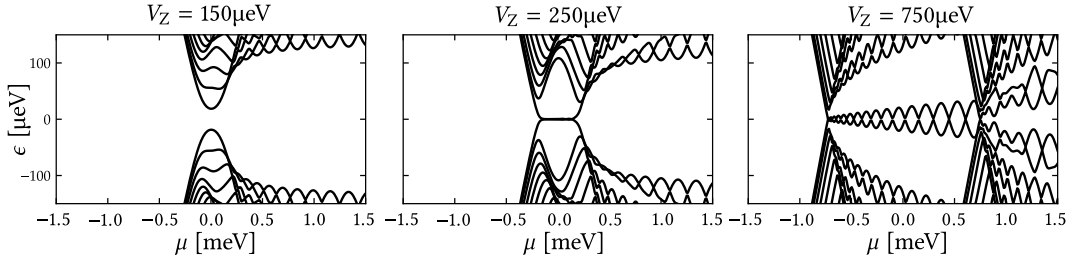

Figure 2.8: Eigenvalue spectrum as a function of chemical potential μ for three different Zeeman fields with values given in the figure. The energy scale (y-axis) is the same on all three plots. Other parameters are $L = 1.5$ μm, $m^* = 0.026\,m_e$, $\Delta_0 = 150$ μeV, $\mu = 0$μeV, $N = 100$ sites

larger. It is therefore preferable to enter the topological phase on the bottom side of the parabola at low μ if the goal is to have the smallest overlap between the Majorana modes.

The electron parity changes when the lowest-energy state crosses zero[Ben-Shach *et al.*, 2014]. From the bulk spectrum, given in Eq. (2.26), the trivial phase is expected to be fully gapped. However, due to finite size effects, there may exist states crossing zero outside the topological phase at high chemical potential in certain parameter regimes. An example of this is shown in Fig. 2.9, where the black rings outside the topological phase and at large μ are trivial states crossing zero energy. In the present situation of a uniform nanowire, these trivial states are fairly easy to distinguish from a MBS since they are not gapped from the bulk spectrum and they do not exhibit the same characteristic oscillations. However, in non-uniform nanowires and nanowires with non-superconducting segments at the end, it might be possible to find trivial states that oscillate in a similar manner to a MBS. We will return to this matter later in Chap. 9.

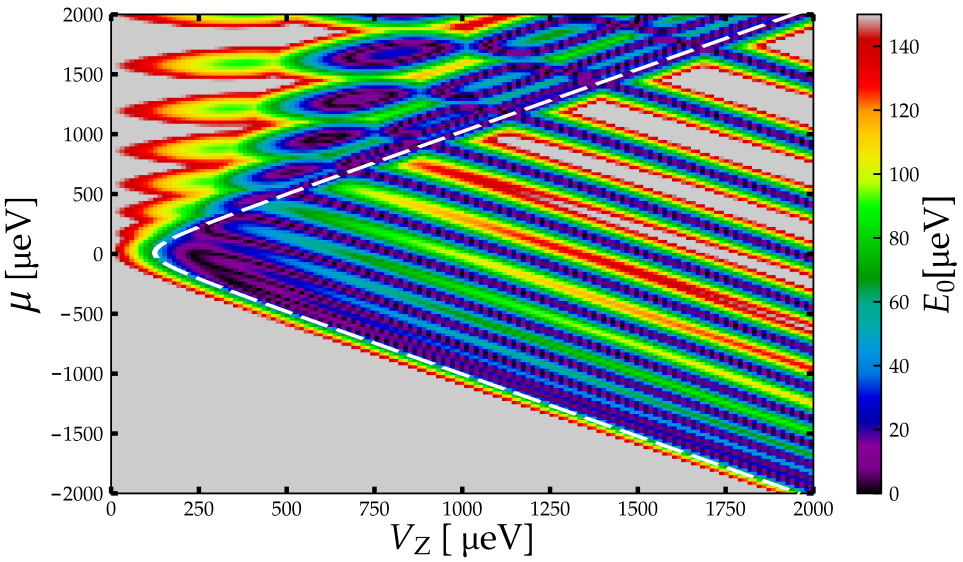

Figure 2.9: Energy of the lowest-energy eigenstate as a function of chemical potential μ and Zeeman field V_Z with the parameters: $L = 0.75$ μm, $m^* = 0.026\,m_e$, $\Delta_0 = 150$ μeV, $\alpha_R = 20$ μeV μm, $N = 200$ sites. Gray color indicates that the energy is larger than the gap Δ_0. The dashed white line given, by $V_Z - \sqrt{\mu^2 + \Delta_0^2} = 0$ μm, indicates where the topological phase transition occurs for an infinite size system.

2.4 SC-SM NANOWIRE SELF-ENERGY MODEL

In the previous section, we discussed the SC-SM nanowire Hamiltonian which despite being rather complex is still a non-interacting Hamiltonian and can be diagonalized numerically. However, it should be noted that the proximity induced gap only takes into account the zero frequency coupling to the parent superconductor and therefore best describes the limit of weak coupling between the superconductor and the nanowire. In order to construct a model that is valid at strong coupling, we use the tunneling Hamiltonian approach to calculate the quasiparticle Green's function of the nanowire by integrating out the electron's degrees of freedom in the parent superconductor. The resulting Green's function includes an energy-dependent self-energy that (i) describes the proximity effect, i.e. it introduces (superconducting) correlations between electrons and holes in the wire, and (ii) leads to a renormalization of all energy levels and quasi-particle weights in the wire. Both effects would not be captured fully by a model where the s-wave pairing is introduced phenomenologically as a constant pairing potential Stanescu *et al.* [2011]. Recent experiments in epitaxially grown SC-SM nanowires have showed a hard induced gap which is comparable in size to the gap in the parent superconductor Chang *et al.* [2015]. Especially in that case, retaining an energy-dependent self-energy can make a qualitative and important difference Peng *et al.* [2015].

We consider the Hamiltonian

$$H = H_{\mathrm{NW}} + H_{\mathrm{SC}} + H_{\mathrm{t}} \tag{2.43}$$

where the three parts describe the nanowire, the bulk superconductor, and the coupling between them, respectively. The nanowire Hamiltonian is the same as in the previous section

$$H_{\mathrm{NW}} = \sum_k \mathbf{c}_k^\dagger \mathcal{H}_{\mathrm{NW}} \mathbf{c}_k = \sum_k \mathbf{c}_k^\dagger \left[(\xi_k + \alpha_R k \sigma_x)\tau_z + V_Z \sigma_z \right] \mathbf{c}_k, \tag{2.44}$$

where $\mathbf{c}_k = (c_{\uparrow k}, c_{\downarrow k}, c^\dagger_{\downarrow k}, -c^\dagger_{\uparrow k})^T$ is a Nambu spinor of electron operators in momentum space. The Hamiltonian describing the superconductor is

$$H_{\text{SC}} = \sum_{\mathbf{p}} \mathbf{a}^\dagger_{\mathbf{p}} \left[\left(\frac{\hbar^2}{2m} p^2 - \mu_{\text{SC}} \right) \tau_z + \Delta \tau_x \right] \mathbf{a}_{\mathbf{p}}, \tag{2.45}$$

with the Nambu spinor of electron operators in the superconductor $\mathbf{a}_{\mathbf{p}} = (a_{\uparrow\mathbf{p}}, a_{\downarrow\mathbf{p}}, a^\dagger_{\downarrow\mathbf{p}}, -a^\dagger_{\uparrow\mathbf{p}})$, the superconducting gap Δ, and the chemical potential of the superconductor μ_{SC}. The Hamiltonian describing the tunneling between them is written in real space,

$$H_{\text{t}} = \sum_\sigma \int t(z, \mathbf{r}') \psi^\dagger_\sigma(z) \phi_\sigma(\mathbf{r}') + \text{h.c.} \;\; \mathrm{d}z \, \mathrm{d}\mathbf{r}' \tag{2.46}$$

where $\psi^\dagger_\sigma(z)$ creates an electron with spin σ in the nanowire at position z and $\phi^\dagger_\sigma(\mathbf{r}')$ creates an electron of spin σ in the superconductor at position $\mathbf{r}'$. The tunnel coupling is

$$t(z, \mathbf{r}') = \tilde{t} \delta(x') \delta(y') \delta(z' - z). \tag{2.47}$$

and is assumed to be real. We rewrite the tunnel Hamiltonian in momentum space

$$H_{\text{t}} = \sum_\sigma \int \tilde{t} \delta(x') \delta(y') \delta(z' - z) \frac{1}{\sqrt{\mathcal{L}_z}} \sum_k e^{-ikz} c^\dagger_{k\sigma} \frac{1}{\sqrt{\mathcal{V}}} \sum_{\mathbf{p}} e^{i\mathbf{p}\cdot\mathbf{r}'} a_{\mathbf{p}\sigma} + \text{h.c.} \;\; \mathrm{d}z \, \mathrm{d}\mathbf{r}' \tag{2.48}$$

$$= \frac{\tilde{t}}{\sqrt{\mathcal{L}_z \mathcal{V}}} \sum_{\sigma \mathbf{p} k} \int e^{-i(k - p_z)z} c^\dagger_{k\sigma} a_{\mathbf{p}\sigma} + \text{h.c.} \;\; \mathrm{d}z \tag{2.49}$$

$$= t \sum_{\sigma \mathbf{p} k} \delta_{k, p_z} c^\dagger_{k\sigma} a_{\mathbf{p}\sigma} + \text{h.c.} \tag{2.50}$$

$$= t \sum_{\mathbf{p} k} \delta_{k, p_z} \mathbf{c}^\dagger_k \tau_z \mathbf{a}_{\mathbf{p}}, \tag{2.51}$$

where we have defined $t = \frac{\tilde{t}}{\sqrt{\mathcal{L}_x \mathcal{L}_y}}$

We define a Nambu matrix structure for the imaginary time Green's functions we will be working with

$$\mathcal{G}(k, \tau) = \begin{bmatrix} \mathcal{G}^{\text{ee}} & \mathcal{G}^{\text{eh}} \\ \mathcal{G}^{\text{he}} & \mathcal{G}^{\text{hh}} \end{bmatrix}, \tag{2.52}$$

where we suppress the dependence on k and τ. There is also a spin structure to these Green's functions, which we define as

$$\mathcal{G}^{\text{ee}} = \begin{bmatrix} \mathcal{G}^{\text{ee}}_{\uparrow\uparrow} & \mathcal{G}^{\text{ee}}_{\uparrow\downarrow} \\ \mathcal{G}^{\text{ee}}_{\downarrow\uparrow} & \mathcal{G}^{\text{ee}}_{\downarrow\downarrow} \end{bmatrix} \quad , \qquad \mathcal{G}^{\text{eh}} = \begin{bmatrix} \mathcal{G}^{\text{eh}}_{\uparrow\downarrow} & -\mathcal{G}^{\text{eh}}_{\uparrow\uparrow} \\ \mathcal{G}^{\text{eh}}_{\downarrow\downarrow} & -\mathcal{G}^{\text{eh}}_{\downarrow\uparrow} \end{bmatrix} \tag{2.53}$$

$$\mathcal{G}^{\text{he}} = \begin{bmatrix} \mathcal{G}^{\text{he}}_{\downarrow\uparrow} & \mathcal{G}^{\text{he}}_{\downarrow\downarrow} \\ -\mathcal{G}^{\text{he}}_{\uparrow\uparrow} & -\mathcal{G}^{\text{he}}_{\uparrow\downarrow} \end{bmatrix} \quad , \qquad \mathcal{G}^{\text{hh}} = \begin{bmatrix} \mathcal{G}^{\text{hh}}_{\downarrow\downarrow} & -\mathcal{G}^{\text{hh}}_{\downarrow\uparrow} \\ -\mathcal{G}^{\text{hh}}_{\uparrow\downarrow} & \mathcal{G}^{\text{hh}}_{\uparrow\uparrow} \end{bmatrix}. \tag{2.54}$$

Of these Green's functions $\mathcal{G}^{\text{ee}}_{\sigma\sigma'}$ and $\mathcal{G}^{\text{hh}}_{\sigma\sigma'}$ are the usual electron and hole Green's functions, while $\mathcal{G}^{\text{eh}}_{\sigma\sigma'}$ and $\mathcal{G}^{\text{he}}_{\sigma\sigma'}$ are the anomalous Green's functions where a hole is turned into an electron or opposite through interactions with the superconductor. The single particle Green's functions we are working with are

$$\mathcal{G}^{\text{ee}}_{\sigma\sigma'}(k, \tau) = -\left\langle \hat{T}_\tau c_{k\sigma}(\tau) c^\dagger_{k\sigma'}(0) \right\rangle \quad , \qquad \mathcal{G}^{\text{eh}}_{\sigma\sigma'}(k, \tau) = -\left\langle \hat{T}_\tau c_{k\sigma}(\tau) c_{-k\sigma'}(0) \right\rangle \tag{2.55}$$

$$\mathcal{G}^{\text{he}}_{\sigma\sigma'}(k, \tau) = -\left\langle \hat{T}_\tau c^\dagger_{-k\sigma}(\tau) c^\dagger_{k\sigma'}(0) \right\rangle \quad , \qquad \mathcal{G}^{\text{hh}}_{\sigma\sigma'}(k, \tau) = -\left\langle \hat{T}_\tau c^\dagger_{-k\sigma}(\tau) c_{-k\sigma'}(0) \right\rangle. \tag{2.56}$$

We will let the above Green's function be the full imaginary time Green's functions of the nanowire, while the Green's functions of the nanowire and superconductor in the absence of coupling between them will be denoted by a subscript "0" and "SC".

We now write the full imaginary time Green's function as an expansion in the tunneling Hamiltonian and obtain a Dyson equation

$$\begin{aligned}\mathcal{G}(k,\tau) &= \mathcal{G}_0(k,\tau) + t^2\int_0^\beta \mathrm{d}\tau_1\,\mathrm{d}\tau_2 \mathcal{G}_0(k,\tau-\tau_1)\sum_{\mathbf{p}}\delta_{k,p_z}\mathcal{G}_{\mathrm{SC}}(\mathbf{p},\tau_1-\tau_2)\mathcal{G}_0(k,\tau_2)\\ &\quad + t^4\int_0^\beta \mathrm{d}\tau_1\ldots\,\mathrm{d}\tau_4 \mathcal{G}_0(k,\tau-\tau_1)\sum_{\mathbf{p}}\left\{\delta_{k,p_z}\mathcal{G}_{\mathrm{SC}}(\mathbf{p},\tau_1-\tau_2)\right\}\mathcal{G}_0(k,\tau_2-\tau_3)\\ &\quad \times\sum_{\mathbf{p}}\left\{\delta_{k,p_z}\mathcal{G}_{\mathrm{SC}}(\mathbf{p},\tau_3-\tau_4)\right\}\mathcal{G}_0(k,\tau_4)+\ldots \qquad (2.57)\\ &= \mathcal{G}_0(k,\tau) + \int_0^\beta \mathcal{G}_0(k,\tau-\tau_1)\Sigma_{\mathrm{SC}}(k,\tau_1-\tau_2)\mathcal{G}(k,\tau_2), \qquad (2.58)\end{aligned}$$

where we have defined the self-energy

$$\Sigma_{\mathrm{SC}}(k,\tau) = t^2\sum_{\mathbf{p}}\delta_{k,p_z}\mathcal{G}_{\mathrm{SC}}(\mathbf{p},\tau). \qquad (2.59)$$

The expansion only contains terms with even orders of the tunneling Hamiltonian since the electron has to start and end in the nanowire.

Converting the Green's functions to the frequency domain, we have

$$\begin{aligned}\mathcal{G}(k,i\omega_n) &= \int_0^\beta \mathrm{d}\tau\; e^{i\omega_n\tau}\mathcal{G}(k,\tau) \qquad (2.60)\\ &= \mathcal{G}_0(k,i\omega_n) + \mathcal{G}_0(k,i\omega_n)\Sigma_{\mathrm{SC}}(k,i\omega_n)\mathcal{G}(k,i\omega_n), \qquad (2.61)\end{aligned}$$

and we convert the sum over wave vectors into an integral over energy in the self-energy

$$\begin{aligned}\Sigma_{\mathrm{SC}}(k,i\omega_n) &= t^2\sum_{\mathbf{p}}\delta_{k,p_z}\mathcal{G}_{\mathrm{SC}}(\mathbf{p},i\omega_n) \qquad (2.62)\\ &= t^2\int \mathrm{d}\xi_{\mathbf{p}}\;\nu_2(\xi,k)\mathcal{G}_{\mathrm{SC}}(\xi,i\omega_n), \qquad (2.63)\end{aligned}$$

where $\nu_2(\xi,k) = \sum_{\mathbf{p}}\delta(\xi-\xi_{\mathbf{p}})\delta_{k,p_z}$ is the 2D density of states in the superconductor at energy ϵ and with wave vector k in the z-direction. The Green's function of the electrons and holes in the superconductor is [Bruus and Flensberg, 2004]

$$\begin{aligned}\mathcal{G}_{\mathrm{SC}}(\xi,i\omega_n) &= \frac{1}{\omega_n^2+\xi^2+|\Delta|^2}\begin{bmatrix}-i\omega_n-\xi & 0 & \Delta & 0\\ 0 & -i\omega_n-\xi & 0 & \Delta\\ \Delta & 0 & -i\omega_n+\xi & 0\\ 0 & \Delta & 0 & -i\omega_n+\xi\end{bmatrix}\\ &= \frac{-i\omega_n-\xi\tau_z+\Delta\tau_x}{\omega_n^2+\xi^2+|\Delta|^2}. \qquad (2.64)\end{aligned}$$

Assuming that $\Delta,\omega \ll \varepsilon_{\mathrm{F}}$ the effective density of states ν_2 is constant and we can perform the integral over ϵ and obtain the self-energy

$$\Sigma_{\mathrm{SC}}(k,i\omega_n) = \frac{\pi t^2\nu_2}{\sqrt{|\Delta|^2+\omega_n^2}}(-i\omega_n+\Delta\tau_x), \qquad (2.65)$$

and by analytic continuation, $i\omega_n \to \omega + i0^+$, the retarded self-energy

$$\Sigma^{\mathrm{R}}_{\mathrm{SC}}(k,\omega) = \frac{\gamma}{\sqrt{|\Delta|^2 - (\omega + i0^+)^2}}(-\omega + \Delta\tau_x), \tag{2.66}$$

where we have defined $\gamma = \pi t^2 \nu_2$.

We proceed to solve the Dyson equation in Eq. (2.61) to obtain the full Green's function containing the self-energy in Eq. (2.66) from which we construct the retarded Green's function by analytic continuation

$$G^{\mathrm{R}}(k,\omega) = \frac{1}{\left(G^{\mathrm{R}}_0(k,\omega)\right)^{-1} - \Sigma^{\mathrm{R}}_{\mathrm{SC}}(k,\omega) + i0^+} \tag{2.67}$$

$$= \frac{1}{\omega - \mathscr{H}^{(k)}_{\mathrm{NW}} - \Sigma^{\mathrm{R}}_{\mathrm{SC}}(k,\omega) + i0^+}, \tag{2.68}$$

with the single particle Hamiltonian of the nanowire given in Eq. (2.44).

Estimating parameters from experiments

This section includes results presented in the supplementary material of Deng et al. [2016].

In order to compare with experiments and extract model parameters, we derive some relations between observables in the energy spectrum and model parameters. For the remainder of this section we will assume that $\Delta = |\Delta|$ without loss of generality. At energies below the gap of the bulk superconductor Δ, the electronic spectrum is obtained by solving

$$0 = \det[\mathrm{Re}\,(G^{\mathrm{R}}(k,\omega))^{-1}] \tag{2.69}$$

$$= \omega^2\left(1 + \frac{\gamma}{\sqrt{\Delta^2-\omega^2}}\right)^2 - V_{\mathrm{Z}}^2 - \left(\frac{\gamma\Delta}{\sqrt{\Delta^2-\omega^2}}\right)^2 - \xi_k^2 - \alpha_{\mathrm{R}}^2 k^2 \pm 2\sqrt{V_{\mathrm{Z}}^2\left(\frac{\Delta\gamma}{\sqrt{\Delta^2-\omega^2}}\right)^2 + V_{\mathrm{Z}}^2\xi_k^2 + \alpha_{\mathrm{R}}^2 k^2 \xi_k^2}.. \tag{2.70}$$

One unknown parameter, is the coupling strength γ between the nanowire and the bulk superconductor. It can however be related to the lowest energy state (induced gap) at zero Zeeman field and zero chemical potential and the gap of the bulk superconductor. We define the induced gap Δ_{ind} in the nanowire as the lowest available energy, above a possible MBS. Setting $V_{\mathrm{Z}} = 0$ and $\mu = 0$, we find a relation between the γ, Δ_{ind}, and Δ, by solving $\det[\mathrm{Re}\,(G^{\mathrm{R}}(k=0,\omega=\Delta_{\mathrm{ind}}))^{-1}] = 0$:

$$\Delta_{\mathrm{ind}}\left(1 + \frac{\gamma}{\sqrt{\Delta^2 - \Delta_{\mathrm{ind}}^2}}\right) - \frac{\gamma\Delta}{\sqrt{\Delta^2 - \Delta_{\mathrm{ind}}^2}} = 0. \tag{2.71}$$

Solving for γ we obtain

$$\gamma = \Delta_{\mathrm{ind}}\sqrt{\frac{\Delta + \Delta_{\mathrm{ind}}}{\Delta - \Delta_{\mathrm{ind}}}}. \tag{2.72}$$

In the weak coupling limit $\Delta_{\mathrm{ind}} \ll \Delta$, we can approximate

$$\sqrt{\frac{\Delta - \Delta_{\mathrm{ind}}}{\Delta + \Delta_{\mathrm{ind}}}} = \sqrt{1 - 2\frac{\Delta_{\mathrm{ind}}}{\Delta + \Delta_{\mathrm{ind}}}} \approx 1 - \frac{\Delta_{\mathrm{ind}}}{\Delta + \Delta_{\mathrm{ind}}} = \frac{\Delta}{\Delta + \Delta_{\mathrm{ind}}} \tag{2.73}$$

and obtain an expression for the induced gap in terms of the coupling strength and parent superconductor gap

$$\Delta_{\text{ind}} \approx \frac{\gamma\Delta}{\gamma + \Delta}, \tag{2.74}$$

which is in agreement with the estimate by Stanescu *et al.* [2011]. In the strong coupling regime where $\Delta_{\text{ind}} \approx \Delta$ and $\gamma \gg \Delta$, we approximate

$$\sqrt{\frac{\Delta - \Delta_{\text{ind}}}{\Delta + \Delta_{\text{ind}}}} \approx \sqrt{\frac{\Delta - \Delta_{\text{ind}}}{2\Delta}}. \tag{2.75}$$

Inserting this in Eq. (2.72) and squaring, gives the equation

$$\gamma^2(\Delta - \Delta_{\text{ind}}) \approx 2\Delta_{\text{ind}}^2\Delta, \tag{2.76}$$

with the solutions

$$\Delta_{\text{ind}} \approx \frac{\gamma^2}{4\Delta}\left(-1 \pm \sqrt{1 + \frac{8\Delta^2}{\gamma^2}}\right). \tag{2.77}$$

We are looking for a solution with positive induced gap, so we pick the corresponding solution and expand the square root to second order in $\frac{8\Delta^2}{\gamma^2}$ to obtain

$$\Delta_{\text{ind}} \approx \Delta\left(1 - 2\frac{\Delta^2}{\gamma^2}\right). \tag{2.78}$$

Besides the induced superconducting pairing, the self energy also leads to a renormalization of the level spectrum below the gap of the bulk superconductor. As a result, the critical Zeeman field at which the topological phase transition occur is moved to a higher Zeeman field. We find the critical field by solving

$$\det[\text{Re}\,(G^{\text{R}}(k = 0, \omega = 0))^{-1}] = 0 \qquad \Rightarrow \qquad V_{\text{Z,c}}^2 = \gamma^2 + \mu^2. \tag{2.79}$$

Even though stronger coupling to the superconductor induces a larger gap in the nanowire, it also pushes the phase transition to higher fields, which might be difficult to obtain as it requires a very large magnetic field. The magnetic field will also eventually destroy the superconducting phase in the bulk superconductor, an effect that is not yet included.

This effect is included phenomenologically by letting the gap of the bulk superconductor depend on the applied magnetic field:

$$\Delta(\mathbf{B}) = \Delta(0)\left[1 - \left(\frac{\vec{\boldsymbol{B}} \cdot \vec{\boldsymbol{g}}_{\text{SC}}}{B_c}\right)^2\right], \tag{2.80}$$

where $\vec{\boldsymbol{g}}_{\text{SC}}$ is the Landé g-factor in the superconductor. In experiments, the critical magnetic field where the gap in the bulk superconductor closes depends on the direction of the magnetic field, which can be incorporated above by letting the g-factor in the superconductor be dependent on direction. For simplicity we will in general assume the g-factor to be the same in all directions. It will be explicitly specified in the text when this phenomenological gap closing model is included.

It is also possible to obtain an estimate of the coherence length ξ and the spin-orbit coupling strength α_{R} from the low energy spectrum at the topological phase transition. At

low energies $\omega \ll \Delta$ and for $\mu = 0$ and small k, the spectrum is approximately given by

$$\det[\mathrm{Re}\,(G^{\mathrm{R}}(k,\omega))^{-1}] \approx \omega^2 \left(1 + \frac{\gamma}{\Delta}\right)^2 - V_{\mathrm{Z}}^2 - \gamma^2 - \alpha_{\mathrm{R}}^2 k^2 - 2V_{\mathrm{Z}}\gamma \tag{2.81}$$

$$\Downarrow$$

$$\epsilon_k \approx \frac{\Delta}{\Delta + \gamma}\sqrt{(V_{\mathrm{Z}} - \gamma)^2 + k^2\alpha_{\mathrm{R}}^2}. \tag{2.82}$$

Close to the phase transition point $V_{\mathrm{Z,c}} = \gamma$ we then have

$$\epsilon_k \approx \frac{\Delta' |k| \alpha_{\mathrm{R}}}{\Delta' + \gamma}, \tag{2.83}$$

where Δ' is the gap of the parent superconductor at this point. Due to finite size effects, the induced gap does not close exactly at $V_{\mathrm{Z,c}}$, but at a slightly higher field. The gap at $V_{\mathrm{Z,c}}$ is given by the gap to the first excited state

$$\epsilon_1 \approx \frac{\Delta'}{\Delta' + \gamma}\frac{\pi\alpha_{\mathrm{R}}}{L}, \tag{2.84}$$

which was also shown by van Heck *et al.* [2016]. If we estimate the coherence length ξ near the phase transition as $\xi \approx \frac{\alpha_{\mathrm{R}}}{\Delta'}$, we have

$$\frac{\xi}{L} \approx \frac{\Delta' + \gamma}{\Delta'}\frac{\epsilon_1}{\pi\Delta'}, \tag{2.85}$$

and also from the previous equation an estimate of the spin-orbit coupling strength

$$\alpha_{\mathrm{R}} \approx \frac{\Delta' + \gamma}{\Delta'}\frac{L}{\pi}\epsilon_1. \tag{2.86}$$

Numerical computations

For numerical computations, we use a lattice version of Green's function, which is obtained using the tight binding approximation as in the previous section. Green's function from Eq. (2.68) in lattice space is

$$G^{\mathrm{R}}(i,j;\omega) = \frac{1}{\omega - \mathscr{H}_{\mathrm{NW}}^{(ij)} - \Sigma_{\mathrm{SC}}^{\mathrm{R}}(i,j;\omega) + i0^+}, \tag{2.87}$$

with the self-energy

$$\Sigma_{\mathrm{SC}}^{\mathrm{R}}(i,j;\omega) = \gamma\frac{-\omega + \Delta\tau_x}{\sqrt{|\Delta|^2 - (\omega + i0^+)^2}}\delta_{i,j}. \tag{2.88}$$

The differential conductance measured from a lead into any point in the grounded nanowire can be computed using the scattering matrix formalism that will be introduced in Chap. 3. We will here show a few plots of different tunnel coupling strengths to the bulk superconductor to see how the spectrum compares with the model in the previous section. The differential conductance, at the end of the nanowire as a function of Zeeman field along the wire and bias voltage, is shown in Fig. 2.10 for the different coupling strengths $\gamma = \{0.5, 1, 2, 4, 8\}\Delta$. Besides pushing the topological phase transition to higher Zeeman fields increasing γ also suppresses the MBS's energy splitting oscillations.

In Fig. 2.11 we show the differential conductance at the end of the nanowire as a function of Zeeman field and bias voltage where the gap of the bulk superconductor depends on the magnetic field as given in Eq. (2.80).

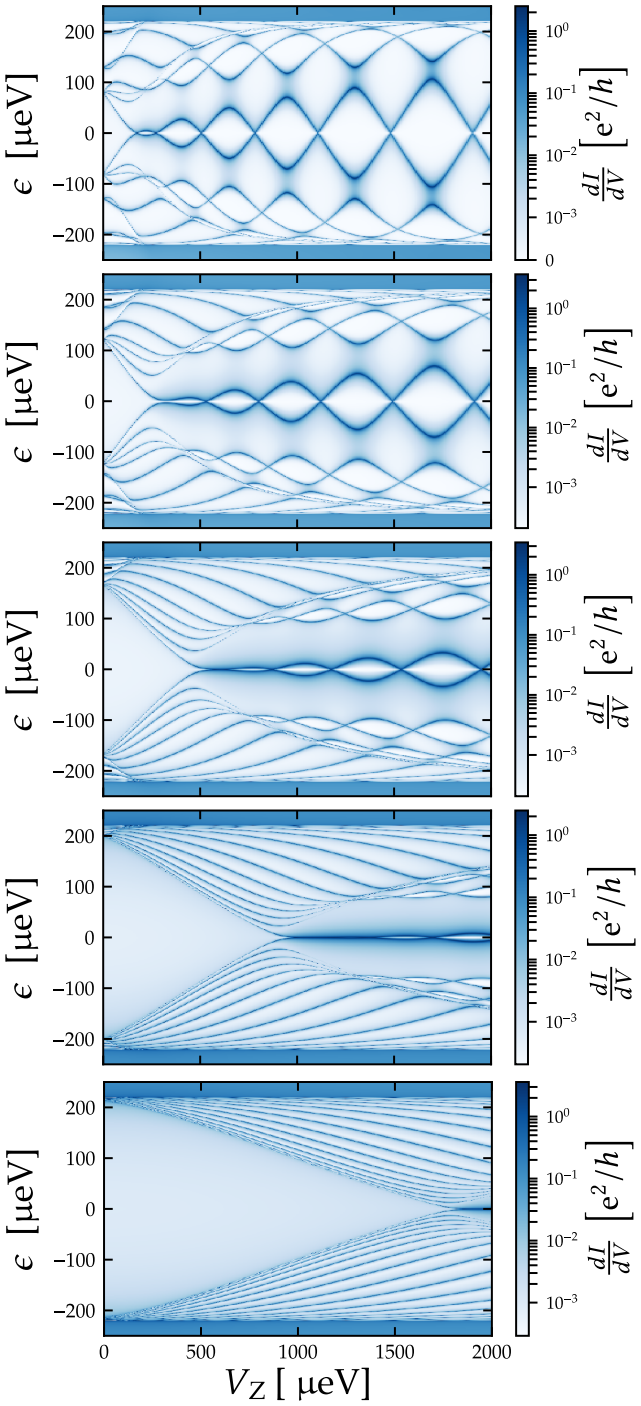

Figure 2.10: Differential conductance as a function of Zeeman field V_Z pointing along the nanowire for five different coupling strengths to the superconductor $\gamma = \{0.5, 1, 2, 4, 8\}\Delta$ from top to bottom. Other parameters are $L = 0.75\mu m$, $m^* = 0.026\, m_e$, $\Delta = 220\mu eV$, $\alpha_R = 20 pm\, eV$, $\mu = 0\mu eV$, $N = 100$ sites

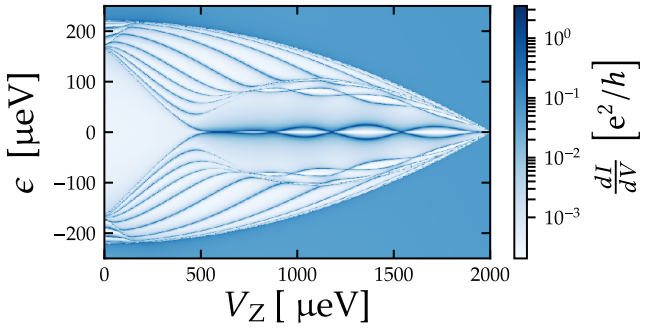

Figure 2.11: Differential conductance as a function of Zeeman field V_Z pointing along the nanowire with a Zeeman field dependent bulk superconductor gap, as given in Eq. (2.80) with $1/2\mu_B g_{SC} B_c = 2000\mu eV$. Other parameters are $\gamma = 2\Delta$, $L = 0.75\mu m$, $m^* = 0.026\, m_e$, $\Delta = 220\mu eV$, $\alpha_R = 20 pm\, eV$, $\mu = 0\mu eV$, $N = 100$ sites

2.5 Summary

In the first part of this thesis we have introduced and discussed three microscopic models that can exhibit a topologically non-trivial phase with MBSs. The SC-SM nanowire with the energy-dependent self-energy offers the best capability for accurately describing real experiment nanowire in the light of the hard induced superconducting gaps observed in experiments. However, it is also the most complex of the three models. When the goal is to understand a specific phenomenon, rather than reproducing experimental observations, the simpler SC-SM Hamiltonian with energy-independent induced superconducting gap may be more appropriate to use. The SC-SM Hamiltonian may be further approximated by the spinless p-wave superconductor, which are more tractable to deal with analytically. There are many other details of these models, but we have limited ourselves to providing an adequate overview that enables us to employ the models later on without further introduction.

Part II

GROUNDED NANOWIRE

Chapter 3

Scattering Matrix Formalism

> “If I were forced to sum up in one sentence what the Copenhagen interpretation says to me, it would be “Shut up and calculate!”
>
> David Mermin

This part of the thesis will revolve around studying grounded SC-SM nanowire devices by electron tunneling spectroscopy (ETS) at the end of the nanowire which is grounded. This will be carried out using the Landauer-Bütttiker formalism, which we will give a short introduction to in this chapter. First we will outline the starting point of the formalism in general terms and then focus on the practical problem at hand: Finding the current across a normal-superconductor interface. For a more detailed introduction, see *e.g.* Bruus and Flensberg [2004].

We consider the nanowire as a mesoscopic sample connected to two electron reservoirs through perfect leads, as pictured in Fig. 3.1. The reservoirs are macroscopic and their contacts to the leads are assumed to be reflectionless, such that any electrons incident on the reservoir from the leads will be fully absorbed and thermalized before being re-emitted. For simplicity we assume the leads $\alpha = \mathrm{L}, \mathrm{R}$ to be perfectly straight with a constant cross-section Ω and impenetrable boundary $\partial\Omega$, and we define the coordinate system such that x is parallel to the lead and $(y, z) = \mathbf{r}_\perp$ is the plane perpendicular to the lead. The Hamiltonians $\mathscr{H}_\alpha$ of the leads with the eigenstates $\phi^\pm_{\alpha\zeta nE}(x, \mathbf{r})$ with energy E are given by

$$\mathscr{H}_\alpha = -\frac{\hbar^2}{2m}\tau_z(\partial_x^2 + \partial_\perp^2), \qquad \text{for } \mathbf{r}_\perp \in \Omega, \text{ else } 0, \tag{3.1a}$$

$$\phi^\pm_{\alpha\zeta nE}(x, \mathbf{r}_\perp) = \frac{1}{\sqrt{k_n(E)}} v_\zeta \chi_n(\mathbf{r}_\perp) e^{\pm i k_n(E) x}, \qquad \zeta \in \{\mathrm{e}, \mathrm{h}\} \tag{3.1b}$$

$$-\frac{\hbar^2}{2m}\partial_\perp^2 \chi_n(\mathbf{r}_\perp) = \epsilon_n \chi_n(\mathbf{r}_\perp), \qquad n \in \mathbb{N}, \tag{3.1c}$$

$$\chi_n(\mathbf{r}_\perp) = 0, \qquad \text{for } \mathbf{r}_\perp \in \partial\Omega, \tag{3.1d}$$

$$\tau_z v_\zeta = \varsigma v_\zeta, \qquad \text{with } \varsigma = \pm 1, \tag{3.1e}$$

$$E = \varsigma\left(\frac{\hbar^2}{2m}k_n^2 + \epsilon_n\right). \tag{3.1f}$$

The quantum numbers ” + / − ” denote right/left moving states with wavenumbers $k_n(E)$ and χ_n is the eigenfunction of the transverse part of the Hamiltonian with the eigenenergie

ϵ_n. We have written the Hamiltonians in BdG form in order to accommodate so-called Andreev reflections, where an electron is reflected as a hole at the normal-superconductor interface[Blonder *et al.*, 1982]. The vector v_ζ is a spinor in electron-hole space where $v_\mathrm{e} = (1,0)^T$ and $v_\mathrm{h} = (0,1)^T$. The number of transverse eigenfunctions or channels, as we will call them, is in principle infinite, but we will in practice choose some cut-off value N and disregard higher states. The normalization of the wavefunctions have been chosen this way, such that they all carry the same absolute probability current in a given cross-section:

$$\int_\Omega \left(\phi^\pm_{\alpha\zeta nE}(x,\mathbf{r})\right)^* \overleftrightarrow{J_x}\,\tau_z \phi^\pm_{\alpha\zeta nE}(x,\mathbf{r})\,\mathrm{d}\mathbf{r}_\perp = \pm\frac{\varsigma\hbar}{m}, \qquad \overleftrightarrow{J_x} = \frac{\hbar}{2mi}\left(\overrightarrow{\partial}_x - \overleftarrow{\partial}_x\right), \tag{3.2}$$

where the arrows indicate which side the differential operator acts on and $\varsigma = \pm 1$ We will neglect spin for the purpose of this introduction, but it can easily be included by extension.

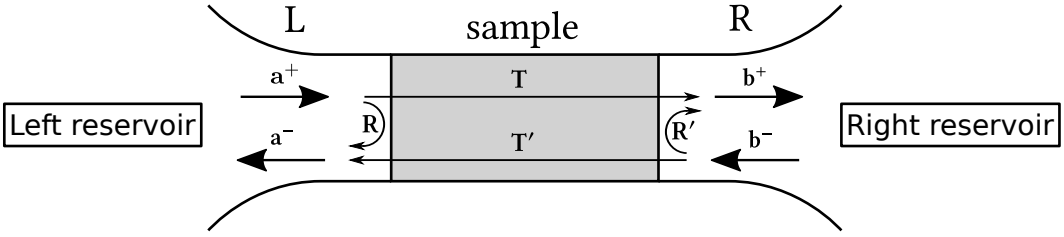

Figure 3.1: Setup considered, a superconducting mesoscopic sample connected by two reflectionless leads, each with N channels. Incoming and outgoing waves of electrons and holes are transmitted or reflected with amplitudes given by the S-matrix in Eq. (3.5).

Now we introduce the scattering matrix or S-matrix formalism in order to calculate the conductance without having to deal with the problem of finding the explicit wavefunctions of the sample. We start by considering an eigenstate with energy E and write its wavefunction in the three parts of the system as

$$\psi_{\zeta E}(x,\mathbf{r}_\perp) = \begin{cases} \sum_n a^+_{\zeta n}\phi^+_{\mathrm{L}\zeta nE}(x,\mathbf{r}_\perp) + \sum_n a^-_{\zeta n}\phi^-_{\mathrm{L}\zeta nE}(x,\mathbf{r}_\perp), & (x,\mathbf{r}_\perp)\in \mathrm{L}, \\ \psi_{\mathrm{M},\zeta E}(x,\mathbf{r}_\perp), & (x,\mathbf{r}_\perp)\in \mathrm{M}, \\ \sum_n b^+_{\zeta n}\phi^+_{\mathrm{R}\zeta nE}(x,\mathbf{r}_\perp) + \sum_n b^-_{\zeta n}\phi^-_{\mathrm{R}\zeta nE}(x,\mathbf{r}_\perp), & (x,\mathbf{r}_\perp)\in \mathrm{R}. \end{cases} \tag{3.3}$$

In the leads $\alpha = \mathrm{L},\mathrm{R}$, the wavefunction is a linear combination of incoming and outgoing waves $\phi^\pm_{\alpha\zeta nE}(x,\mathbf{r}_\perp)$, while in the sample region, it is some unknown wavefunction $\psi_{\mathrm{M},\zeta E}$. Using the usual boundary conditions: the wavefunction $\psi_{\zeta E}$ and its derivative must be continuous, we obtain $4\times 2N$ linearly independent equations that determine the amplitudes $a^\pm_{\zeta n}$ and $b^\pm_{\zeta n}$. Writing the amplitudes as vectors of the form $\mathbf{a}^+_\zeta = (a^+_{\zeta 1}, a^+_{\zeta 2}, \ldots)^T$, we can represent their linear dependence by the so-called scattering matrix or S-matrix:

$$\begin{pmatrix} \mathbf{a}^-_\mathrm{e} \\ \mathbf{a}^-_\mathrm{h} \\ \mathbf{b}^+_\mathrm{e} \\ \mathbf{b}^+_\mathrm{h} \end{pmatrix} = \begin{bmatrix} r_{\mathrm{ee}}(\epsilon,V) & r_{\mathrm{eh}}(\epsilon,V) & t'_{\mathrm{ee}}(\epsilon,V) & t'_{\mathrm{eh}}(\epsilon,V) \\ r_{\mathrm{he}}(\epsilon,V) & r_{\mathrm{hh}}(\epsilon,V) & t'_{\mathrm{he}}(\epsilon,V) & t'_{\mathrm{hh}}(\epsilon,V) \\ t_{\mathrm{ee}}(\epsilon,V) & t_{\mathrm{eh}}(\epsilon,V) & r'_{\mathrm{ee}}(\epsilon,V) & r'_{\mathrm{eh}}(\epsilon,V) \\ t_{\mathrm{he}}(\epsilon,V) & t_{\mathrm{hh}}(\epsilon,V) & r'_{\mathrm{he}}(\epsilon,V) & r'_{\mathrm{hh}}(\epsilon,V) \end{bmatrix} \begin{pmatrix} \mathbf{a}^+_\mathrm{e} \\ \mathbf{a}^+_\mathrm{h} \\ \mathbf{b}^-_\mathrm{e} \\ \mathbf{b}^-_\mathrm{h} \end{pmatrix} \tag{3.4}$$

$$= \begin{bmatrix} \mathbf{R}(\epsilon,V) & \mathbf{T}'(\epsilon,V) \\ \mathbf{T}(\epsilon,V) & \mathbf{R}'(\epsilon,V) \end{bmatrix} \begin{pmatrix} \mathbf{a}^+_\mathrm{e} \\ \mathbf{a}^+_\mathrm{h} \\ \mathbf{b}^-_\mathrm{e} \\ \mathbf{b}^-_\mathrm{h} \end{pmatrix}. \tag{3.5}$$

where the reflection matrices $r_{\zeta\zeta'}$ and $r'_{\zeta\zeta'}$ and the transmission matrices $t_{\zeta\zeta'}$ and $t'_{\zeta\zeta'}$ are of size $N\times N$. The normal reflection and transmission amplitudes of an incoming

wave in the left lead channel n' being reflected in the same lead or transmitted in the right lead channel n is represented by the matrix elements $(r_{ee})_{nn'}$ and $(t_{ee})_{nn'}$, respectively. Due to superconductivity, we also have Andreev reflection, where incoming electrons are reflected into holes, which is represented by the matrix elements $(r_{he})_{nn'}$[Blonder *et al.*, 1982]. Transmission and reflection amplitudes in the opposite direction are given by the elements of the primed matrices. A schematic representation of how the transmission and reflection matrices connect the incoming and outgoing waves is shown in Fig. 3.1.

We now turn to calculating the current through the sample and for this we define the so-called scattering states $\psi_{\alpha nE}$, these are states with an incoming wave in lead α in channel n. The conservation of current gives that, in steady state, the current is the same in both leads, and it will suffice to consider the scattering states in the left lead. We restrict our attention to the normal-superconductor interface of the left lead and the sample. In doing this, we assume the right lead to be far away from this interface. Across the NS-interface, the scattering of electrons impinging from the left lead can be described by just the reflection part of the S-matrix in Eq. (3.5):

$$\mathbf{R}(\epsilon, V) = \begin{bmatrix} r_{ee}(\epsilon, V) & r_{eh}(\epsilon, V) \\ r_{he}(\epsilon, V) & r_{hh}(\epsilon, V) \end{bmatrix}. \tag{3.6}$$

An incoming electron can either be scattered back from the NS interface as an electron by normal reflection (r_{ee}) or as a hole by Andreev reflection (r_{he}). In order to accommodate both processes, we define the scattering states originating from an incoming wave in the left lead to include both a reflected electron and a hole:

$$\psi_{\mathrm{L}nE}(x, \mathbf{r}_\perp) = \phi^+_{\mathrm{L}nE}(x, \mathbf{r}_\perp) + \sum_{n'\zeta'} (r_{\zeta'\mathrm{e}})_{n'n} \phi^-_{\mathrm{L}\zeta' n' E}(x, \mathbf{r}_\perp), \qquad (x, \mathbf{r}_\perp) \in \mathrm{L}. \tag{3.7}$$

We assumed that electrons entering the leads from the reservoirs are completely thermalized with a Fermi-Dirac energy distribution n_F of the given reservoir α, which is characterized by the chemical potential μ_α. Further, we assumed the leads to be perfectly transmitting, so in equilibrium, we take the scattering eigenstates to be stationary and their occupation set by the distribution function

$$f_\alpha(\epsilon) = n_\mathrm{F}(\epsilon - \mu_\alpha), \tag{3.8}$$

with the chemical potential set by the connected reservoir. We calculate the current contributions of the scattering states using

$$I_{\alpha\zeta nE} = \int_\Omega \left(\psi_{\alpha\zeta nE}(x, \mathbf{r})\right)^* \overleftrightarrow{J_x} \tau_z \psi_{\alpha\zeta nE}(x, \mathbf{r}) \, \mathrm{d}\mathbf{r}_\perp. \tag{3.9}$$

Considering only the scattering of incoming electrons, $\zeta = \mathrm{e}$, we use Eq. (3.2) and obtain

$$I_{\mathrm{L}nE} = \frac{\hbar}{m} \left[1 - (r^\dagger_{ee} r_{ee})_{nn} + (r^\dagger_{he} r_{he})_{nn}\right], \tag{3.10}$$

where $1 - (r^\dagger_{ee} r_{ee})_{nn}$ is the current contribution from transmitted electrons, while $(r^\dagger_{he} r_{he})_{nn}$ is the contribution from Andreev reflection.

Now we take the chemical potential of the right lead μ_R to be equal to the chemical potential of the sample μ, which we set to zero, and the chemical potential of the left lead to be shifted relative to this by $-eV$ due to the applied voltage bias. The current across the NS interface results from the difference in occupation of scattering states incident from the left and right reservoir, which is given by

$$f_\mathrm{L}(E) - f_\mathrm{R}(E) = n_\mathrm{F}(E + eV) - n_\mathrm{F}(E) \tag{3.11}$$

The electrical current is then obtained by multiplying the current contribution of each scattering with the difference in occupation, summing over all scattering states

$$I = -\frac{e}{2\pi\hbar}\sum_{kn} I_{\mathrm{L}nE}\left[n_{\mathrm{F}}(E+eV) - n_{\mathrm{F}}(E)\right]. \tag{3.12}$$

We transform the sum into an energy integral

$$I = -\frac{e}{2\pi\hbar}\int_0^\infty \sum_n \left[1 - (r_{\mathrm{ee}}^\dagger r_{\mathrm{ee}})_{nn} + (r_{\mathrm{he}}^\dagger r_{\mathrm{he}})_{nn}\right]\left[n_{\mathrm{F}}(E+eV) - n_{\mathrm{F}}(E)\right]\,\mathrm{d}E, \tag{3.13}$$

$$= \frac{1}{e}\int_0^\infty G_s(E,V)\left[n_F(E) - n_F(E+eV)\right]\,\mathrm{d}E, \tag{3.14}$$

where we have defined the spectral conductance

$$G_s(E,V) = \frac{e^2}{h}\mathrm{Tr}\left[1 - r_{\mathrm{ee}}^\dagger r_{\mathrm{ee}} + r_{\mathrm{he}}^\dagger r_{\mathrm{he}}\right], \tag{3.15}$$

with sum diagonal elements n written as the trace.

The differential conductance obtained by differentiating with respect to the voltage V is

$$\left.\frac{dI}{dV}\right|_V = \int -n_F'(E+eV)G_s(E,V) + \frac{1}{e}\left[n_F(\epsilon) - n_F(\epsilon+eV)\right]\frac{dG_s(E,V)}{dV}\,\mathrm{d}E. \tag{3.16}$$

This is for the general case, where the spectral conductance may depend on the applied bias voltage. Here we assume that the coupling to the leads is small enough that the spectral conductance is approximately independent of the voltage bias, so

$$\left.\frac{dI}{dV}\right|_V \approx \int -n_F'(\epsilon+eV)G_s(E)\,\mathrm{d}E, \tag{3.17}$$

which in the limit of zero temperature becomes

$$\left.\frac{dI}{dV}\right|_V \approx G_s(E) = \frac{e^2}{h}\mathrm{Tr}\left[1 - r_{\mathrm{ee}}^\dagger r_{\mathrm{ee}} + r_{\mathrm{he}}^\dagger r_{\mathrm{he}}\right]. \tag{3.18}$$

The reflection matrix needed to calculate the spectral conductance can be obtained from the Green's function of the sample using [Aleiner *et al.*, 2002; Beenakker, 2015]

$$\mathbf{R}(E) = 1 - 2i\pi W^\dagger\left\{\left[G^{\mathrm{R}}(E)\right]^{-1} + i\pi WW^\dagger\right\}^{-1}W, \tag{3.19}$$

where the matrix W describes the coupling between the sample and the lead. In lattice space we write it as

$$W = \sqrt{\gamma_W}(\mathbf{s}_n \otimes \mathbb{1}_4)^T, \tag{3.20}$$

where $\mathbf{s}_n = (0,\ldots,1,\ldots,0)$ is a vector of length N with a 1 in the n'th component and all other components being zero, $\mathbb{1}_4$ is a 4×4 identity matrix. The effective coupling parameter γ_W parametrizes the strength of the coupling to the lead. This $4N\times4$ matrix describes a coupling between one single mode in the lead and site n only. We see from Eq. (3.19) that $WW^\dagger$ plays the role of a self-energy for the particles in the wire, so γ_W can be seen as the electronic tunneling rate through the barrier between the wire and the lead. The Green's function of the nanowire is constructed by employing one of the microscopic models described in chapter 2.

This concludes the introduction of the framework we will use to compute the differential conductance for different setups.

Chapter 4

Phase-Tunable Majorana Bound States in a Topological N-SNS Junction

> “Those who are not shocked when they first come across quantum theory cannot possibly have understood it.
>
> Niels Bohr

This chapter is based on the work presented in [Hansen et al., 2016] with some changes in order to relate and conform to the notation used in the rest of this thesis. Some additional work has been added, which is pointed out in the text.

The motivation behind the work presented in this chapter is to propose a setup where MBSs may be identified using already well-established experimental techniques. We will investigate a superconductor-normal-superconductor (SNS) junction where two separate parts of the nanowire are coupled to two separate bulk superconductors, interconnected by a superconducting loop to control the phase difference between them (see the sketch in Fig. 4.1). Under the right circumstances there can emerge up to four low-energy MBSs (one at each NS boundary inside the wire), which are known to have very characteristic phase-dependent properties San-Jose *et al.* [2012]; Cayao *et al.* [2015]. It has previously been proposed to detect these features by measuring the Josephson current through the junction as a function of the voltage bias induced time-dependent phase difference [San-Jose *et al.*, 2012], or the supercurrent bias [San-Jose *et al.*, 2014].

Here we will investigate the normal-superconductor-normal-superconductor (N-SNS) junction by electron tunneling spectroscopy through the probe at the end of the nanowire. The presence of MBSs may be revealed by observing the phase dependence of the differential conductance due to the non-locality of the MBSs. The superconducting loop is introduced to create a controllable phase difference across the junction. Creating such a topological SNS junction is feasible with the current state of experimental techniques, and probing by means of tunneling spectroscopy is standard practice in this field.

The presence of MBSs reveal themselves by the low energy conductance being 2π periodic in the phase difference, both in the case of overlapping and well separated MBSs. In order to observe this, it is important that the entire nanowire is phase coherent and

achieving a gateable and disorder-free normal region in the SNS junction may pose an experimental challenge. It must however be noted that an experimental measurement with a local probe, such as tunnel conductance at just one end of the nanowire, cannot unequivocally probe a non-local phenomenon. It is however still an interesting experiment which may provide further evidence for the presence of MBSs in these systems.

Recently there have been proposals to measure the degree of non-locality of MBSs in nanowires, using a quantum dot at the end as a spectroscopic tool, by Prada *et al.* [2017] and Clarke [2017], which have shown to be in agreement with experimental observations by Deng *et al.* [2017]. We will turn to the setup of a coupled quantum dot nanowire system in the next chapter.

This chapter is structured as follows. In Sec. 4.1 we describe the setup we have in mind and present a Hamiltonian to model this system. We calculate the differential conductance using the S-matrix, as introduced in Sec. 3 and present the results in Sec. 4.2.

We examine the conductance of the wire for energies smaller than the superconducting gap, calculating the conductance spectrum as a function of applied magnetic field and of the phase difference between the two superconductors. We compare the spectra that result when the wire is in a topological phase and in a trivial phase, and we find that the conductance spectrum, when tunneling into one end of the wire, is only sensitive to the phase difference between the superconductors if the wire is in a topological phase.

Depending on the phase difference and the applied magnetic field, one to four low-energy subgap conductance peaks are visible: For zero phase difference, one strong zero-bias peak appears after entering the topological phase; at higher magnetic fields this peak splits and starts to oscillate due to the increasing overlap of the two MBSs at the ends of the wire. For a phase difference close to π we can see two more low-energy peaks, which we associate with the formation of two additional MBSs close to the central normal region of the SNS junction where the superconducting phase changes sign.

In section 4.3 we support our interpretation with a simple low-energy model based on a one-dimensional spinless p-wave superconductor with a phase discontinuity. This toy Hamiltonian reproduces all important qualitative features of our numerical results and provides insight into the structure of the "Majorana subspace" including the gradual gapping out of the central two Majorana states when the phase difference is reduced to zero.

We will also present some additional work that was not included in [Hansen *et al.*, 2016]. The investigation of the potential in the normal part of the SNS junction is extended to include the case where the potential forms a potential well. The phase difference between the two superconducting segments is controlled by threading a magnetic flux through a superconducting loop that connects the two segments. This may be accomplished experimentally by rotating the direction of the applied magnetic field. We investigate how a rotation of the magnetic field will affect the differential conductance spectrum.

4.1 Model

We consider a semiconducting nanowire proximity coupled to two s-wave superconductors, as illustrated in Fig. 4.1(a). The two superconductors are connected by a superconducting loop such that the phase difference ϕ between them can be tuned by threading a flux Φ through the loop. Further, the wire is assumed to have strong spin-orbit interaction and we include a magnetic field that initially only results in a Zeeman splitting of the electronic states inside the wire but does not add to the flux Φ. Later we consider how much the magnetic field needs to be rotated to thread a single flux quantum through the loop and how that rotation will affect the energy spectrum. At its left end, the wire is tunnel coupled

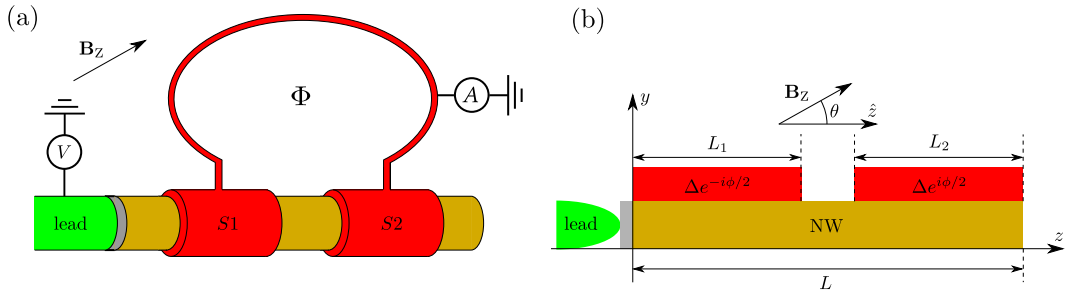

Figure 4.1: (a) Cartoon of the N-SNS setup we consider. A semiconducting nanowire with epitaxially grown s-wave superconductor covering two separate parts of the wire. The two superconductors $S1$ and $S2$ are connected by a grounded superconducting loop through which a flux Φ can be threaded, resulting in a phase difference between $S1$ and $S2$. An external magnetic field $\mathbf{B}_Z$ is applied that couples to the electronic spins inside the wire but does not add to Φ. The wire is tunnel coupled to a probe lead at the left end which can be used for tunneling spectroscopy by applying a bias voltage V to it while measuring the current A. (b) A more schematic view of the setup. The wire is oriented along the z-axis and $\mathbf{B}_Z$ lies in the yz-plane where the effective spin-orbit field is assumed to point along the y-axis.

to a normal-metal probe which can be used to measure the differential conductance of the system, as indicated in Fig. 4.1(a).

A more schematic picture of the setup is shown in Fig. 4.1(b). The nanowire of length L is oriented along the z-axis and it is proximity coupled to two bulk s-wave superconductors of length L_1 and L_2 which have the effective pairing potentials $\Delta e^{-i\phi/2}$ and $\Delta e^{i\phi/2}$ respectively. We assume the effective spin-orbit field to point along the y-axis and the Zeeman field to lie in the yz-plane, $\mathbf{B}_Z = B(\hat{z}\cos\theta + \hat{y}\sin\theta)$. By varying the direction of this field we can investigate both the topologically trivial state and non-trivial state of the system: The wire is in a trivial state when the Zeeman field is parallel to the spin-orbit field ($\theta = \pm\pi/2$) and can be in a topological state for non-parallel fields [Rex and Sudbø, 2014].

To describe this setup we will employ the model introduced in Sec. 2.4, but since it is not a uniform system, we will go through the details here. We use the Hamiltonian

$$H = H_{\mathrm{NW}} + H_1 + H_2 + H_{\mathrm{t}}, \tag{4.1}$$

where H_{NW}, H_1, and H_2 describe the electrons in the nanowire and the two superconductors respectively, and H_{t} accounts for the coupling between the different parts of the system.

Assuming that the wire is thin enough such that only the lowest electronic subband is occupied, we write a one-dimensional Hamiltonian in a Bogoliubov-de Gennes (BdG) form, $H_{\mathrm{NW}} = \frac{1}{2}\int dz\, \mathbf{\Psi}^\dagger(z)\, \mathscr{H}_{\mathrm{NW}} \mathbf{\Psi}(z)$, using the Nambu spinor $\mathbf{\Psi}(z) = \left[\Psi_\uparrow(z), \Psi_\downarrow(z), \Psi_\downarrow^\dagger(z), -\Psi_\uparrow^\dagger(z)\right]^T$, where the operator $\Psi_\sigma^\dagger(z)$ creates an electron with spin σ at position z in the nanowire. We use

$$\mathscr{H}_{\mathrm{NW}} = \left(-\frac{\hbar^2\partial_z^2}{2m^*} - \mu - i\alpha_{\mathrm{R}}\partial_z\sigma_y\right)\tau_z + \frac{1}{2}g\mu_{\mathrm{B}}\mathbf{B}_Z\cdot\sigma, \tag{4.2}$$

where the Pauli matrices τ and σ act in particle-hole space and spin space respectively. Further, m^* is the effective mass of the electrons in the wire, μ is the chemical potential, α_{R} is the Rashba spin-orbit strength, and g is the effective g-factor in the wire.

The Hamiltonians for the two superconductors read $H_n = \frac{1}{2}\int d\mathbf{r}\, \psi_n^\dagger(\mathbf{r})\, \mathscr{H}_n \psi_n(\mathbf{r})$, where the Nambu spinor $\psi_n(\mathbf{r})$ describes the electrons in superconductor n. The BdG Hamiltonian reads

$$\mathscr{H}_n = \left(\frac{p_n^2}{2m_{\mathrm{S}}^*} - \mu_{\mathrm{S}}\right)\tau_z + \Delta\left[\cos(\phi_n)\tau_x + \sin(\phi_n)\tau_y\right], \tag{4.3}$$

where p_n is the momentum operator for electrons in superconductor n, m_S^* is their effective mass, and μ_S is the chemical potential of the two superconductors. The superconducting phases are $\phi_1 = -\phi/2$ and $\phi_2 = \phi/2$, corresponding to a phase difference ϕ.

Finally, the tunnel coupling between the nanowire and the two superconductors is described by the tunneling Hamiltonian

$$H_t = \sum_{n,\sigma} \int d\mathbf{r}\, t_n(\mathbf{r}) \psi^\dagger_{n,\sigma}(\mathbf{r}) \Psi_\sigma(z) + \text{H.c.}, \tag{4.4}$$

using the functions $t_1(\mathbf{r}) = t\,\delta(x)\delta(y)\Theta(z)\Theta(L_1 - z)$ and $t_2(\mathbf{r}) = t\,\delta(x)\delta(y)\Theta(z - L + L_2)\Theta(L - z)$, with t parameterizing the coupling strength.

Our aim is to calculate the differential conductance of this system in a setup where one end of the wire is connected to a normal-metal tunnel probe (see Fig. 4.1). We will do this using the S-matrix formalism described in Chap. 3. To this end we need the retarded Green's function of the electrons and holes in the nanowire. We assume that the Fermi energy in the superconductor is by far the largest relevant energy scale in the problem, and proceed to integrate out the electron degrees of freedom in the two superconductors as described in Sec. 2.4. We then obtain an expression for the retarded Green's function $G^R(z, z', \epsilon)$ for the electrons and holes in the nanowire coupled to a bulk superconductor with pairing potential $\Delta e^{i\phi}$ as [Stanescu *et al.*, 2011; Sau *et al.*, 2010b; Danon and Flensberg, 2015]

$$\Sigma_S(\Delta, \phi; \epsilon) = \gamma \frac{-\epsilon + \Delta\left[\cos(\phi)\tau_x + \sin(\phi)\tau_y\right]}{\sqrt{\Delta^2 - (\epsilon + i0^+)^2}}, \tag{4.5}$$

where γ parametrizes the strength of the coupling to the superconductor (it is proportional to t^2 and to the normal-state density of states in the superconductor and corresponds roughly to the normal-state tunneling rate of electrons into the superconductor at the Fermi level) and 0^+ is a positive infinitesimal.

The self-energy (4.5) is diagonal in position space, and for our setup (involving two superconductors) we thus have the total self-energy

$$\Sigma(z, \epsilon) = \begin{cases} \Sigma_S(\Delta, -\phi/2; \epsilon) & \text{for } 0 < z < L_1, \\ \Sigma_S(\Delta, \phi/2; \epsilon) & \text{for } L - L_2 < z < L, \\ 0 & \text{otherwise.} \end{cases} \tag{4.6}$$

With this, we can write the Green function for the electrons and holes in the wire as

$$G^R(z, z', \epsilon) = \left[\frac{1}{\epsilon - H_{NW} - \Sigma(z, \epsilon)\delta(z - z') + i0^+}\right]_{z,z'}. \tag{4.7}$$

We then proceed to obtain the reflection matrix (part of the S-matrix) using Eq. (3.19) and calculate the differential conductance using Eq. (3.18). For our numerical calculations, we discretize the Hamiltonian H_{NW} on a one-dimensional lattice with N sites, and the Green function $G^R(\epsilon)$ is then found from inverting the $4N \times 4N$ matrix $[\epsilon - H_{NW} - \Sigma + i0^+]$.

We express all energies in terms of the spin-orbit energy $E_{SO} \equiv \alpha_R^2 m^*/2\hbar^2 \approx 68$ μeV, where the Rashba spin-orbit strength is set to $\alpha_R = 20$ μeV μm and the effective mass of the electrons in the nanowire is assumed to be $m^* = 0.026 m_e$, which is the value for bulk InAs at room temperature. Unless stated otherwise, the parameters we use in our simulations are as follows: The number of sites in the tight-binding model $N = 100$, the length of the wire $L = 1.5$ μm, the length of the two superconductors $L_1 = L_2 = 675$ nm, the bulk superconductor gap $\Delta = 2E_{SO}$, the wire's chemical potential $\mu = 0$, the coupling parameter

$\gamma = 2.5E_{\mathrm{SO}}$, and the coupling of the wire to the lead $\gamma_W = 25E_{\mathrm{SO}}$. This combination of parameters results in an effective hopping matrix element $t = \hbar^2/2m^*a^2 \approx 95E_{\mathrm{SO}}$, where $a = L/N$ is the lattice constant, and a spin-orbit-induced 'spin-flip' nearest-neighbor coupling of $s = \alpha_{\mathrm{R}}/2a \approx 9.8E_{\mathrm{SO}}$.

4.2 Results

In this section, we will present and discuss the results of the numerical model.

Trivial phase

We first investigate the differential conductance of the system in the topologically trivial phase, i.e. where the Zeeman field $\mathbf{B}_{\mathrm{Z}}$ is parallel to the spin-orbit field ($\theta = \pi/2$). In Fig. 4.2 we plot the differential conductance in units of e^2/h as a function of bias voltage V. Fig. 4.2 (a) shows the dependence on the strength of the Zeeman field $V_{\mathrm{Z}} = \frac{1}{2}g\mu_{\mathrm{B}}|\mathbf{B}_{\mathrm{Z}}|$, assuming no phase difference, $\phi = 0$. We see that conductance is high for energies larger than the bulk superconducting gap, $|eV| > \Delta$. Indeed, at these energies the superconductors have a finite single-particle density of states which allows for tunneling of electrons from the lead into the superconductors. For energies smaller than the bulk gap we see several sharp peaks in the conductance. These peaks are caused by Andreev bound states in the wire which can lead to Andreev reflection of electrons at the lead-wire interface, effectively resulting in the transfer of Cooper pairs from the lead into the superconductors. At $V_{\mathrm{Z}} = 0$, there is an induced gap in the wire of $\Delta_{\mathrm{ind}} \approx 1.2E_{\mathrm{SO}}$, which agrees quite well with the estimate $\Delta_{\mathrm{ind}} \sim \Delta\gamma/(\Delta+\gamma)$ from Eq. (2.74), even though this is in the intermediate coupling strength regime. When V_{Z} increases, the subgap states acquire a Zeeman splitting resulting in a closing of the induced gap at $V_{\mathrm{Z}} \approx 2.5E_{\mathrm{SO}}$, also in agreement with the estimate $V_{\mathrm{Z,c}} = \sqrt{\gamma^2+\mu^2}$ from Eq. (2.79). The gap does not reopen again, since the nanowire stays in the topologically trivial phase for $\theta = \pi/2$. The bending of the peaks for energies close to $\pm\Delta$ is due to the renormalization of the energy levels in the wire by the proximity of the superconductor. If we would have used a phenomenological (energy-independent) induced gap in the wire Hamiltonian, described in Sec. 2.3, this bending would have been absent.

We would like to point out that this Zeeman-induced subgap structure has qualitative features in common with the subgap spectrum in the topological regime. After the gap clos-

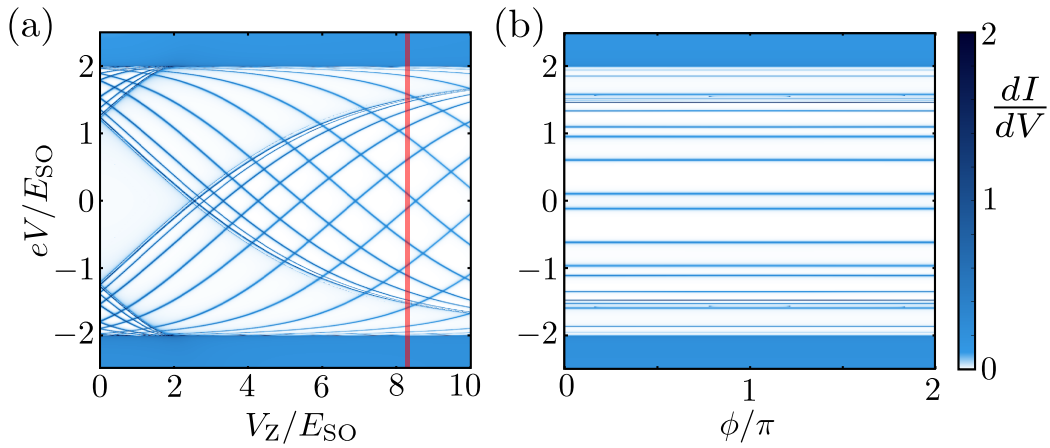

Figure 4.2: Differential conductance of the nanowire in units of e^2/h for $\theta = \pi/2$. With this orientation of the Zeeman field the system is always in the trivial regime. (a) Conductance as a function of bias voltage V and V_{Z} for $\phi = 0$. (b) Conductance as a function of V and ϕ for $VZ = 8.3E_{\mathrm{SO}}$, indicated by the red line in (a).

ing, the spacing between the conductance peaks at zero bias, $V = 0$, becomes proportional to $\sqrt{V_Z}$, which is the same as the expected V_Z-dependence of the period of the oscillations due to a finite overlap of the Majorana end states in the topological regime [Das Sarma *et al.*, 2012; Rainis *et al.*, 2013]. Also, the amplitude of the oscillations of the "splitting of the zero-bias peak" grows steadily with increasing V_Z, as it is expected to do in the Majorana case. Therefore, if one would focus only on the V_Z-dependence of the lowest-energy peaks in the conductance (for instance, when other features of the subgap structure are smeared by noise or finite temperature), then it could be hard to distinguish the topological from the trivial regime.

We now proceed by investigating the dependence of the conductance on the phase difference ϕ between the superconductors. In Fig. 4.2(b) we plot the differential conductance as a function of V and ϕ with fixed $V_Z = 8.3E_{SO}$, which is at the position of the red line in Fig. 4.2(a). We see that the positions of the peaks in the conductance do not depend significantly on ϕ. Indeed, in the trivial regime the Andreev bound states that are most strongly influenced by the phase difference between the two parts of the wire are expected to live mainly in the central normal region. The tunnel probe is attached to the left end of the wire and is thus predominantly coupled to the Zeeman-split subgap states in the left proximity-induced superconductor. We emphasize the importance of the weak coupling between the tunnel probe at the end of the wire and the Andreev states the middle of the wire for clearly distinguishing the topologically trivial and non-trivial phases in experiment. This requires to have the length of the wire covered by superconductor $S1$ longer than the coherence length of the resulting induced superconductivity. In experiment, one should verify this first by showing that, in the topologically trivial phase, the conductance has virtually no dependence on the phase difference between the superconductors.

Topological phase

Next we investigate the conductance of the wire when $\mathbf{B}_Z$ is oriented parallel to the wire, i.e. $\theta = 0$. In Fig. 4.3(a) we plot the differential conductance in units of e^2/h as a function of V and V_Z for the phase differences $\phi = 0$, $\pi/2$, and π (from top to bottom). We see that after the induced gap closes at $V_Z = V_c \approx 2.5E_{SO}$, it now reopens again, which signals a topological phase transition. For $\phi = 0$ (top plot) and $V_Z > V_c$ a strong zero-bias peak appears which at higher V_Z splits again and starts to oscillate. This zero-bias peak of conductance $2e^2/h$ as well as its splitting and the oscillations at higher field are consistent with the formation of Majorana end states at the boundaries of the topological regimes in the wire [Das Sarma *et al.*, 2012; Rainis *et al.*, 2013]. In our setup, one could in principle expect four Majorana states in the topological phase, as indicated in the cartoon inside the plot. The Majorana states labeled γ_2 and γ_3 are however strongly coupled through the central normal region, and thus will gap out to form a normal fermionic state. The two other Majorana modes (γ_1 and γ_4) are separated by L and both are localized on the scale of the coherence length ξ_M. This coherence length is a function of V_Z and the overlap of the two Majorana wave functions increases with increasing V_Z. This explains the splitting of the zero-bias peak into two, and the oscillations are due to the oscillatory form of the Majorana wave functions. In the case the two superconductors have opposite phases ($\phi = \pi$, bottom plot) the situation is different. The effective p-wave pairing term now changes sign across the central normal region, creating two *different* topological phases in the two halves of the wire (this induced p-wave superconductor falls in the BDI symmetry class). Since the Majorana modes γ_2 and γ_3 now belong to different phases, they cannot recombine into a normal fermionic mode and gap out, and we thus expect to have *four* low-energy Majorana

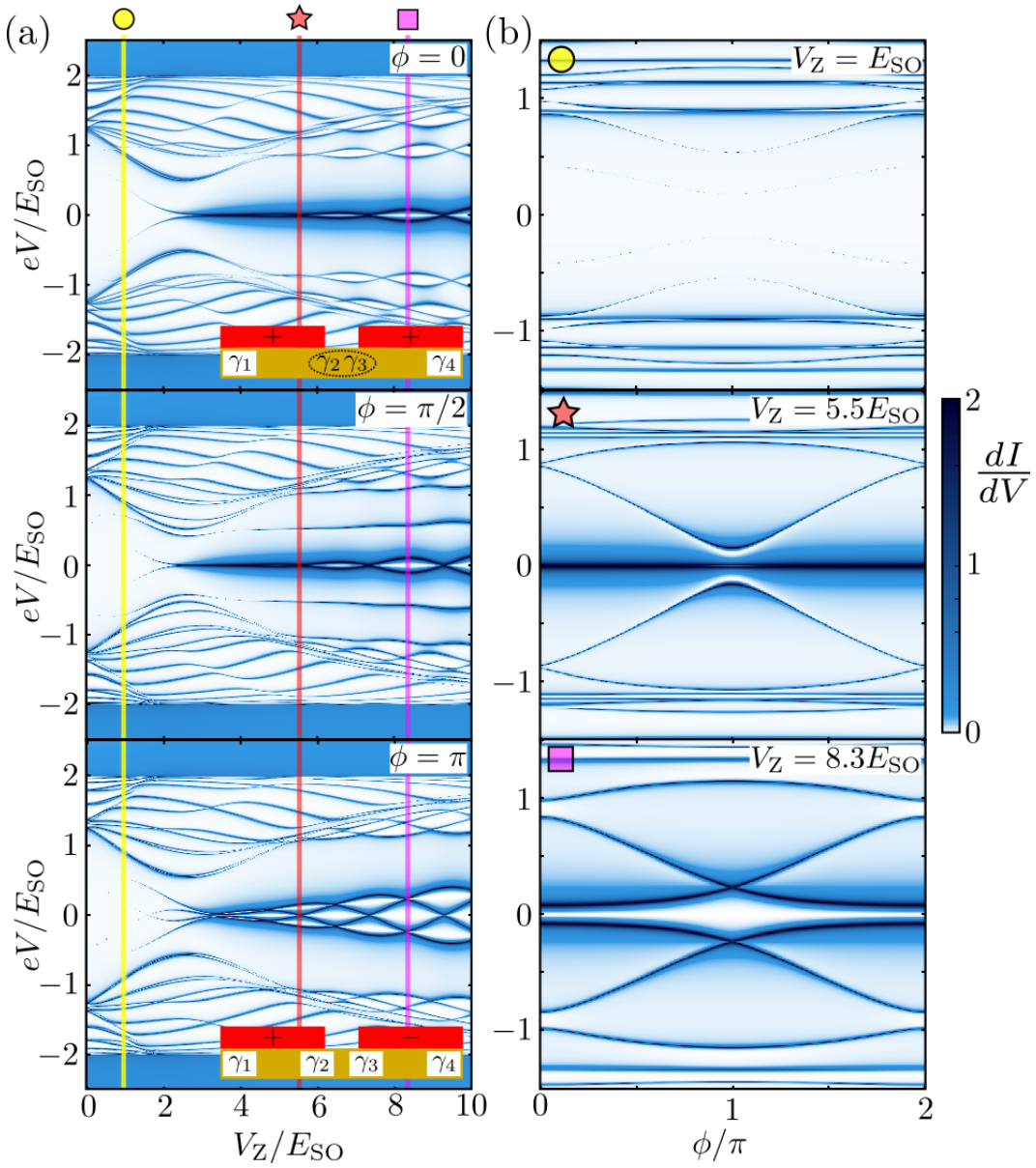

Figure 4.3: Differential conductance of the wire in units of e^2/h for $\theta = 0$. For this direction of magnetic field, the nanowire enters a topological phase when V_Z is larger than $V_{Z,c} = \sqrt{\gamma^2 + \mu^2}$. (a, left column) Conductance as a function of V and V_Z for $\phi = 0$, $\pi/2$, and π. (b, right column) Conductance as a function of V and ϕ for $V_Z = E_{SO}$, $5.5E_{SO}$, and $8.3E_{SO}$, indicated by the yellow circle, red star and purple square in the left column.

modes in the system [San-Jose *et al.*, 2012; Cayao *et al.*, 2015] [1], which will couple and split due to the finite size of the wire. The pair of Majorana states γ_1 and γ_2 (as well as the pair γ_3 and γ_4) still belong to the same topological phase. The states are separated by a distance of roughly $L/2$ and their energies will split when the two wave functions start to overlap significantly. We, indeed, see in our simulations two interlaced sets of oscillations which start at lower V_Z than those in the top plot and have both a larger period and amplitude. All these differences can be explained by the reduced separation of the overlapping Majorana

1. This situation is very similar to the case where the effective spin-orbit field changes sign along the wire. Such a sign change also leads to the formation of different topological phases in the wire and results in a pair of low-energy Majorana modes across the phase boundary[Ojanen, 2013]

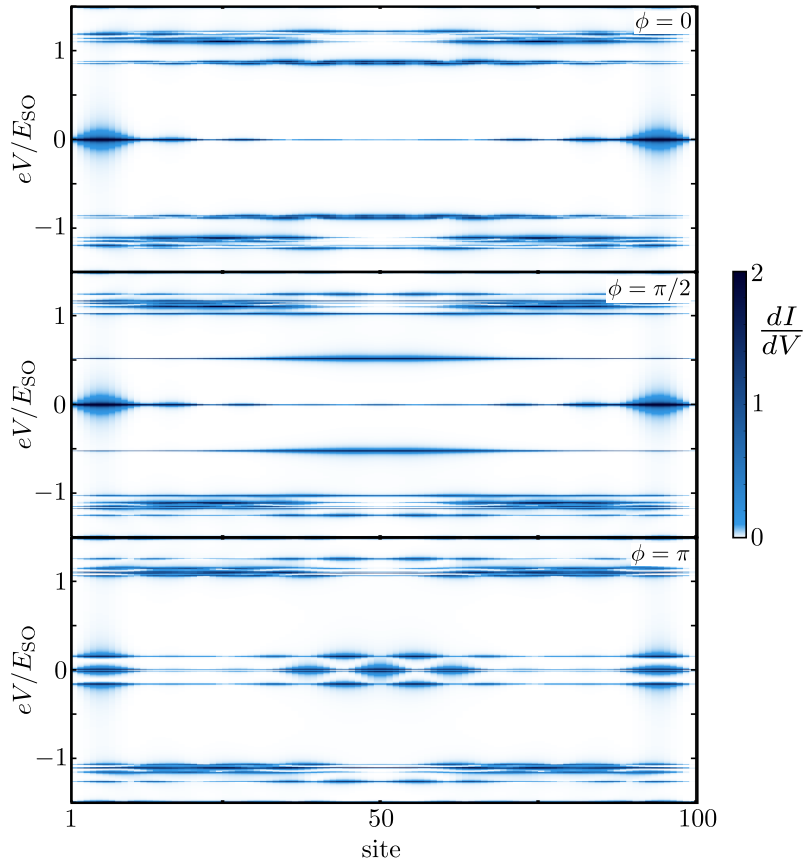

Figure 4.4: The differential conductivity of the wire in units of e^2/h as a function of V and position of the normal probe lead. We have set the phase difference to $\phi = 0$, $\pi/2$, and π (from top to bottom), the Zeeman energy to $V_Z = 5.5E_{SO}$, and the coupling strength to the lead to $\gamma_W = E_{SO}$.

states. The middle plot ($\phi = \pi/2$) shows an intermediate situation where the two central modes γ_2 and γ_3 are still coupled, but the coupling is not strong enough to push their energies outside of the induced gap.

In Fig. 4.3(b) we plot the differential conductance as a function of V and the phase difference ϕ, for three different Zeeman fields: $V_Z = E_{SO}$ (before the closing of the gap) and $V_Z = 5.5E_{SO}$ and $8.3E_{SO}$ (after the reopening of the gap), indicated by the red lines in the top left plot. In contrast to the topologically trivial case shown in Fig. 4.2(b), the low-energy conductance peaks now show a distinctive dependence on the phase difference. In the lower two plots we see how the peak due to the lowest excited state moves towards zero energy and increases in intensity when the phase difference goes from 0 to π. This is the gapped fermionic mode formed by the two central Majorana states gradually developing into two uncoupled low-energy Majorana modes with significant weight at the ends of the wire, cf. the spectra of Andreev bound states presented in Refs. San-Jose *et al.* [2012, 2014]; Cayao *et al.* [2015].

This picture is supported by plotting the local differential conductivity (where we vary the position of the probe lead along the wire, encoded in the matrix W), which maps out the local (tunneling) density of states in the wire. We show the result in Fig. 4.4 for $V_Z = 5.5E_{SO}$ and three different phase differences, $\phi = 0$, $\pi/2$, and π. The lowest excited state indeed develops from a bulk state with energy $\sim E_{SO}$ at $\phi = 0$ to a low-energy state localized at the boundaries of the topological regimes at $\phi = \pi$. This behavior is generally seen for all values of Zeeman fields in the topologically non-trivial phase.

The plots presented in Fig. 4.3 are the main results of the numerical work. They illustrate how the low-energy Majorana modes should manifest themselves as strong peaks in the differential conductance with a distinctive dependence on the phase difference ϕ, which is absent in the trivial case, see Fig. 4.2(b). The main feature that can be discerned is the gradual gapping out of the two central Majorana modes when ϕ is changed from π to 0. Below, in Sec. 4.3, we will investigate the phase-dependence of the low-energy part of the spectrum in more detail and present a simple model to analytically understand the level structure as a function of ϕ.

Unequal length of superconductors

However, before we move on to present our low-energy model, we will first investigate how deviations from the idealized system pictured in Fig. 4.1 would affect the conductance spectrum. Firstly, in an experimental setup it is unlikely that the two superconductors will be of exactly the same length. In Fig. 4.5(a,b) we show the differential conductance as a function of V and V_Z for $L_1 > L_2$ and $L_1 < L_2$ respectively. We see that when the two superconductors are of different lengths, the general structure can still be similar to that of Fig. 4.3(a, bottom plot), but now anti-crossings arise between some of the low-energy modes. In Fig. 4.5(a) where $L_1 > L_2$ we see that the "inner" modes show a higher conductance than the "outer" ones, and we see the opposite in Fig. 4.5(b) where $L_1 < L_2$. The tunneling lead is connected to the left end of the wire where it probes the local density of states. This signifies that the inner modes are localized mainly in the longer superconducting part of the wire and the outer modes mainly in the shorter part.

Dependence on potential in normal region

Another ingredient in an experimental setup could be a tunable potential barrier in the central normal region. We add this complication to our model as a constant potential of height V_m on all lattice sites where $\Sigma = 0$. Raising this barrier can deplete the wire in the normal region and gradually reduce the overlap of the two central Majorana modes. As the barrier becomes high enough this effectively cuts the wire into two uncoupled sections. In Fig. 4.5(c,d) we show the conductance spectrum as a function of V_m, again for $L_1 > L_2$ and $L_1 < L_2$ respectively, and for two phase differences $\phi = 0$ and π. We see that the two central Majorana modes that are gapped out at $V_m = 0$ and $\phi = 0$ (top plots) indeed move towards zero energy when the barrier is increased, due to their suppressed overlap. They hybridize with the original low-energy Majorana mode localized at the end of their section of the wire. At the right end of the plots in Fig. 4.5(c,d) the wire is effectively cut in two by the high barrier in the middle and the splitting of the two Majorana modes in the left section depends on both the length of the section and the Zeeman field (the shorter section will in general show a larger splitting due to a larger overlap between the MBSs). At $\phi = \pi$ the two central modes are always uncoupled and the dependence of the conductance spectrum on V_m is less pronounced (bottom plots). Since V_m could be easily tuned by adding an extra gate electrode to the sample, investigating the barrier- and phase-dependent conductance spectrum (such as in Fig. 4.5) could be used as an alternative direction in the search for signatures of Majorana physics in the wire.

The work presented in the rest of this section is not part of the work presented in [Hansen *et al.*, 2016], but is included for completeness. In Fig. 4.5 (c), it is shown how the differential conductance depends on the potential in the middle region, but only for positive potential, *i.e.* when the potential creates a barrier. In experiments, it might not be possible to control the potential in this region with a nearby gate or control is limited. It is therefore also relevant to consider the case where V_m is negative and the normal region behaves as a potential well between the two superconducting regions.

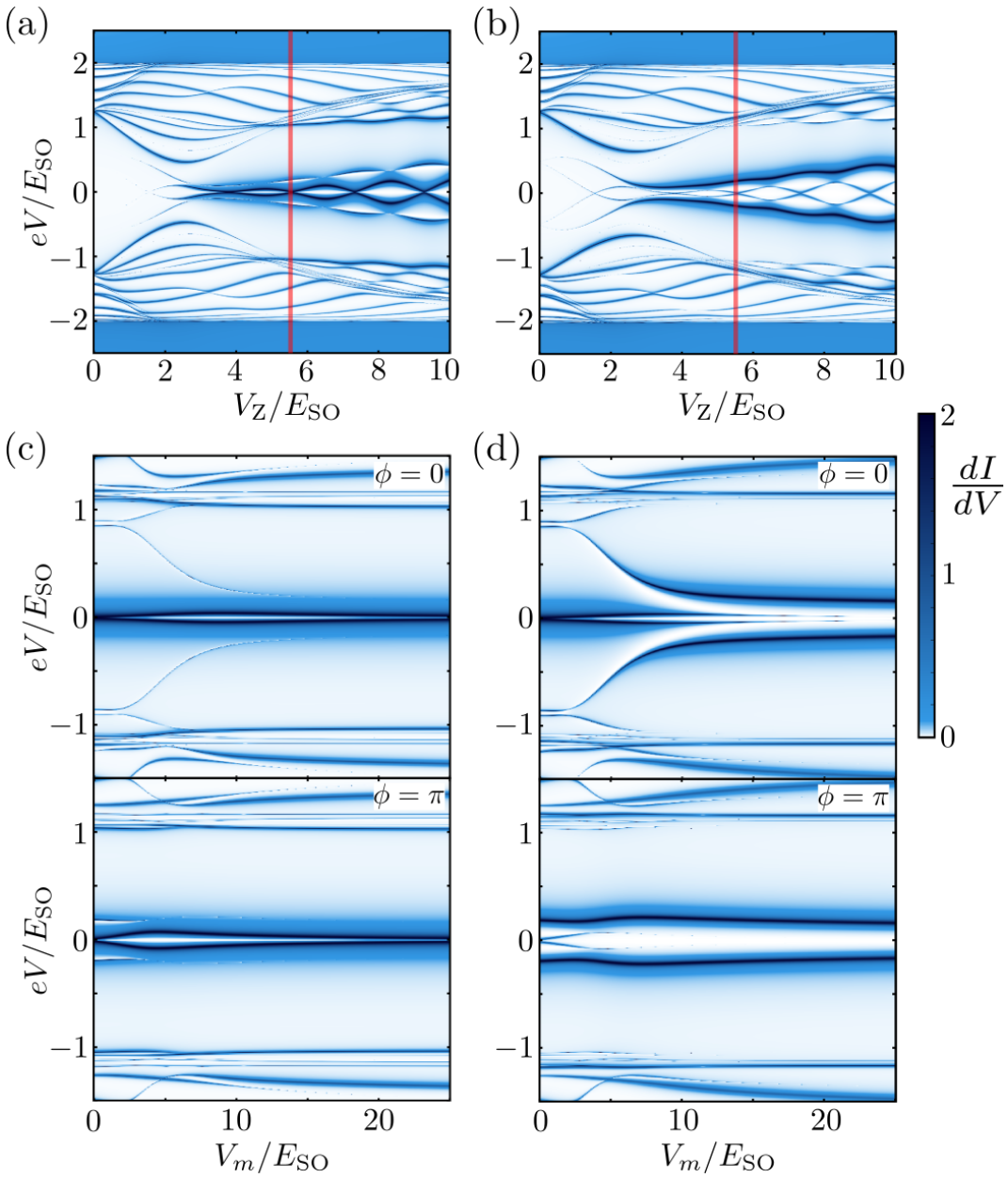

Figure 4.5: Differential conductance in units of e^2/h for the case that $L_1 \neq L_2$. We took $\theta = 0$ and $\phi = \pi$, and show dI/dV as a function of V and V_Z (a,b) and of V and the potential of the central normal region V_m (c,d). In (a,c) we have set $L_1 = 825$ nm and $L_2 = 525$ nm and in (b,d) we took the opposite, $L_1 = 525$ nm and $L_2 = 825$ nm. In (a,b) we did not include an extra potential offset in the central region, $V_m = 0$, and in (c,d) we fixed $V_Z = 5.5E_{SO}$, as indicated by the red lines in the top plots.

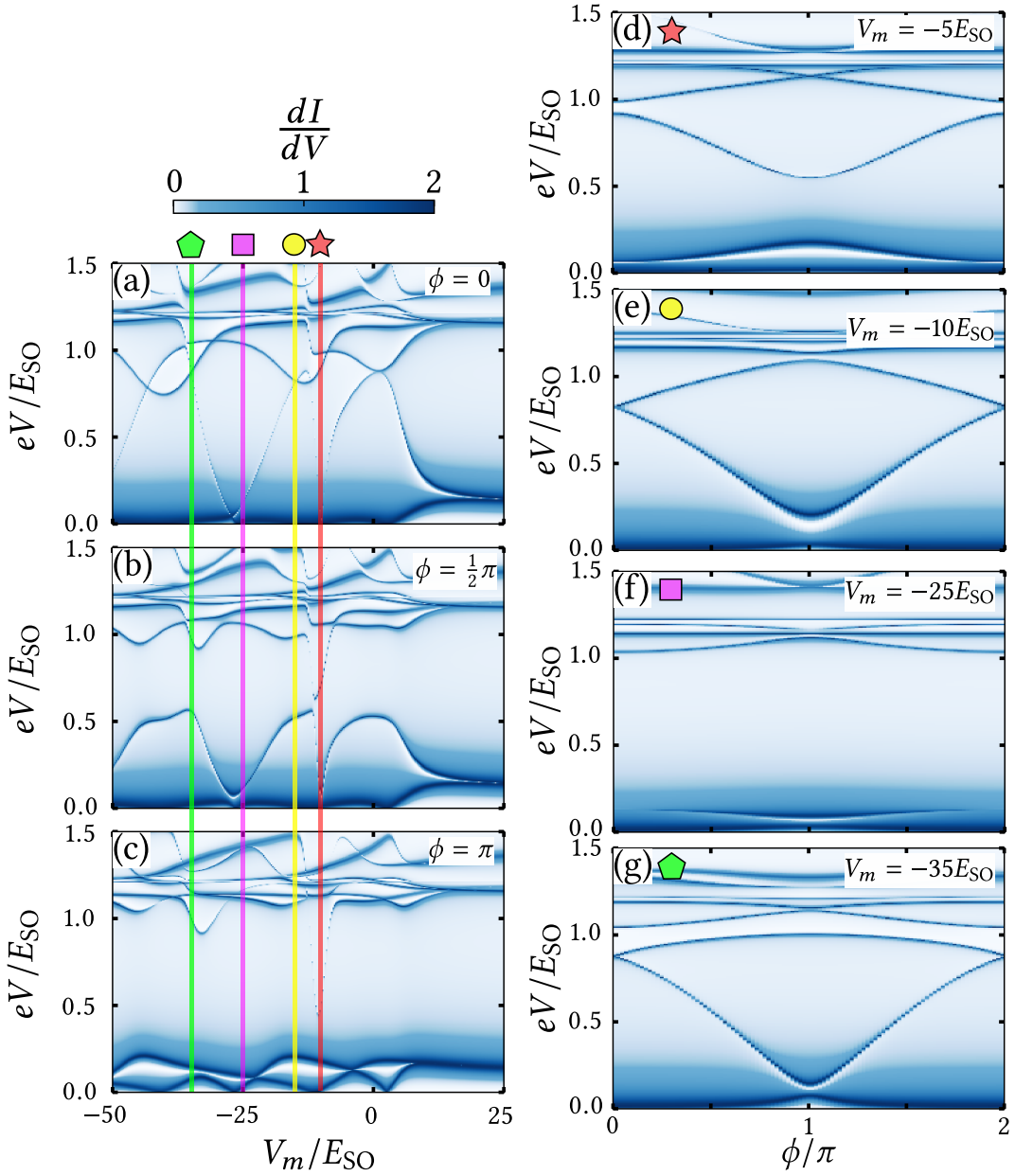

Figure 4.6: (a-c) Differential conductance in units of e^2/h as a function of bias voltage V and potential height in the normal region V_m for three different phase differences $\phi = \{0, 0.5, 1\}\pi$. (d-g) Differential conductance in units of e^2/h as a function of bias voltage V and phase difference ϕ for four different potential values $V_m = \{-5, -10, -25, -35\}E_{SO}$, indicated by the red star, yellow circle, purple square, and green pentagon in (a-c) . This is for a symmetric setup $L_1 = L_2 = 675$ nm and fixed $V_Z = 6E_{SO}$ and with $\gamma_W = 48E_{SO}$.

In Figs. 4.6(a-c) we show the differential conductance as a function of source-drain bias and potential in the normal region, for different phase differences $\phi = \{0, 0.5, 1\}\pi$. Note this is for a symmetric setup, $L_1 = L_2 = 675$ nm, and we only show the positive part of the spectrum, but the negative part is the same, just mirrored in the x-axis.

For $\phi = 0$, shown in Fig. (a), we see a differential conductance peak at high bias move down to low bias and up again repeatedly as the potential V_m is lowered while the Majorana ZBP is not affected much by this. At phase difference $\phi = \frac{1}{2}\pi$, as shown in Fig. (b), the peak does not go all the way to the gap at high bias, but rather moves between close to zero and

half way up to the gap. At $\Phi = \pi$, as shown in Fig. (c), there are two strong differential conductance peaks at low bias associated with the four MBSs in the system which oscillate in a seemingly unsystematic way as V_m is lowered.

Interestingly, lowering the potential V_m in the first two cases does not seem to effect the overlap of the two MBSs at the end of the wire, as the ZBPs in Figs. (a) and (b) are almost unchanged. Only when there are four MBSs, at $\phi = \pi$, is their overlap sensitive to changing V_m, as seen in the Fig. (c).

In order to illuminate how these three plots are connected, we compute the differential conductance as a function of bias voltage V and phase difference ϕ for different values of V_m, as shown in Figs. (d-g). The four chosen values of the potential $V_m = \{5, 10, 25, 35\}E_{\text{SO}}$ are indicated by the red star, yellow circle, purple square, and green pentagon in Figs. (a-c). We see that for certain values of V_m, there are no differential conductance peaks moving down to low bias from the gap. This happens when the second lowest state is already close to zero energy, around potential values $V_m = \{-5, -25\}$ in this case.

It is therefore important to have some ability to tune the potential in the normal region in order to ensure that it is not at a value where the differential conductance show little dependence on the phase difference.

Rotating the magnetic field

Another aspect of this setup that is relevant to consider is the effect of rotating the magnetic field. In the N-SNS setup under consideration, we propose to control the phase difference between the two superconductors by threading a magnetic flux through a superconducting loop that connects them. This superconducting loop will most likely be in plane with the nanowire, such that there is no flux through the loop when the magnetic field is applied along the nanowire. Let $\vec{\mathbf{v}}_{\perp-\text{loop}}$ be the normal vector to the plane of the superconducting loop for easy reference. In order to thread a flux through the loop, the magnetic field can be rotated towards $\vec{\mathbf{v}}_{\perp-\text{loop}}$. If this rotation is perpendicular to the spin-orbit field, it will not cause any change in the energy spectrum. However, the direction of the spin-orbit field may not be known and it will most likely not be perpendicular to both the nanowire and $\vec{\mathbf{v}}_{\perp-\text{loop}}$. A rotation of the magnetic field from the direction parallel to the nanowire towards $\vec{\mathbf{v}}_{\perp-\text{loop}}$ will therefore in general result in a larger component of the magnetic field pointing along the spin-field. If this component becomes too large, the topologically non-trivial phase will be destroyed.

We consider the worst case scenario where the spin-orbit field is parallel to $\vec{\mathbf{v}}_{\perp-\text{loop}}$, so the magnetic field is rotated directly towards the spin-orbit field. In Fig. 4.7, we plot the differential conductance as a function of bias voltage V and the angle of the magnetic field θ measured from the direction of the nanowire towards the spin-orbit vector for different Zeeman field strengths. At small Zeeman fields close to the phase transition, the field can be rotated to a larger angle before the topological gap is closed, while at higher fields the closing happens at a smaller angle and the spectrum changes more rapidly around $\theta = 0°$. There is therefore a trade-off between either increasing the magnetic field where it requires a smaller rotation of the field to generate a flux through the loop, but the spectrum is more sensitive to rotations, or maintaining lower fields where a larger rotation is required to generate the flux, but the spectrum is less sensitive.

In order to get an estimate of how many magnetic flux quanta can be threaded through the loop by rotating the magnetic field in a range where the spectrum is not affected too much, we consider some parameters comparable to what is observed in experiments. The zero bias peaks are observed to appear at magnetic fields in the range of $0.25 - 2.5\text{T}$ [Mourik *et al.*, 2012; Albrecht *et al.*, 2017; Nichele *et al.*, 2017; O'Farrell *et al.*, 2018]. We take a magnetic field of $|\mathbf{B}| = 0.5\text{T}$ and a superconducting loop of area $A = 0.25\mu\text{m}^2$ to get a conservative

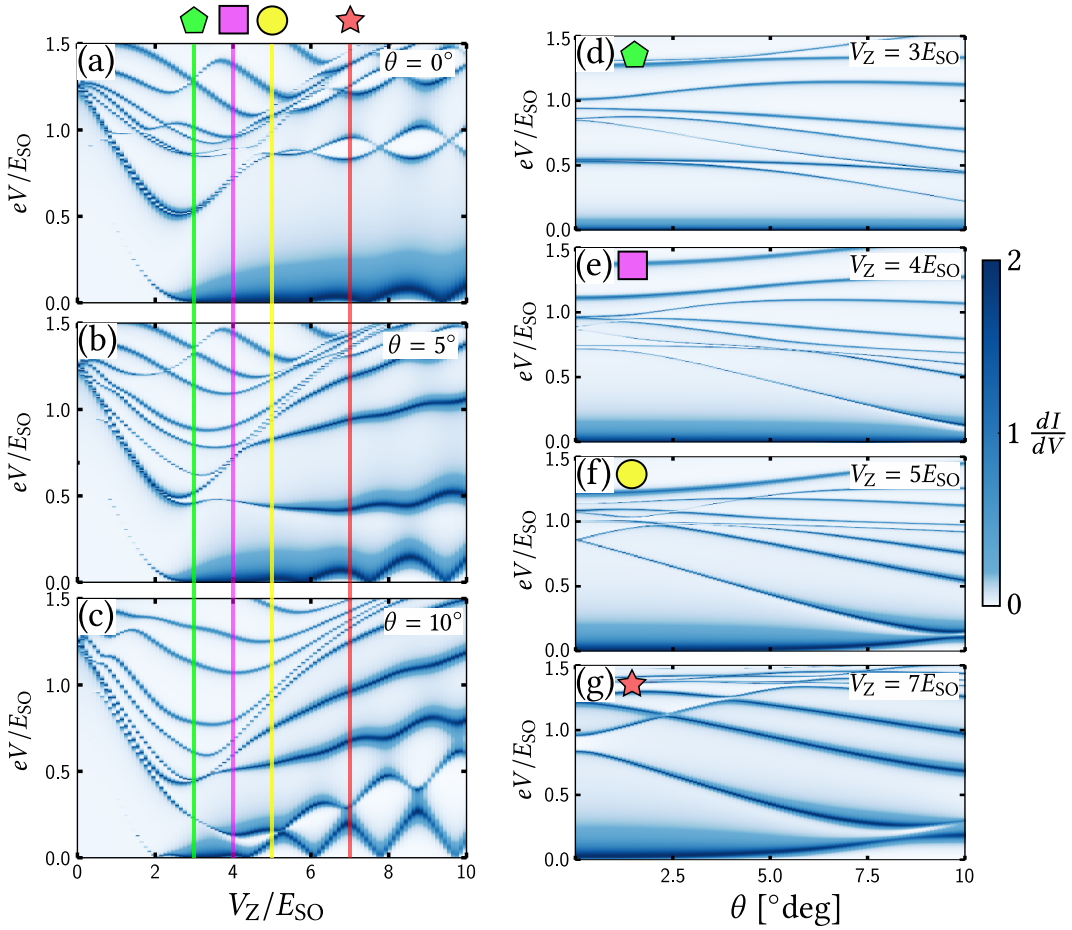

Figure 4.7: Differential conductance in units of e^2/h as a function of bias voltage V and either Zeeman field V_Z (a-c) or angle θ (d-g). In (a-c) plots are shown of three different angles $\theta = \{0°, 5°, 10°\}$. In (d-g) plots are shown of four different Zeeman fields $V_Z = \{3, 4, 5, 7\}E_{SO}$ indicated by the green pentagon, purple square, yellow circle, and red star in (a-c). This is for a symmetric setup $L_1 = L_2 = 675$ nm and fixed $\phi = 0$ and with $\gamma_W = 48E_{SO}$.

estimate. The flux through the loop is

$$\Phi(\theta) = A|\mathbf{B}|\sin(\theta) \tag{4.8}$$

For these parameters, rotations of 2.5° and 5° yield magnetic fluxes of $\Phi(2.5°) \approx 2.7\Phi_0$ and $\Phi(5°) \approx 5.3\Phi_0$ respectively through the superconducting loop. It should therefore be possible to tune the phase difference ϕ over a large enough range in this manner for systems with parameters comparable to what we have considered in this chapter.

4.3 Low-energy model

As presented in Sec. 4.2, our numerical calculations produced low-energy peaks in the differential conductance of a topological N-SNS junction and we showed that these peaks can be associated with states living on the boundaries between topologically trivial and non-trivial regions, all consistent with the interpretation of these states as being Majorana bound states. In this section we will provide further support for this picture by investigating a one-dimensional spinless p-wave superconductor with a phase discontinuity. We develop an effective model to describe the low-energy physics of this system and we show how it produces up to four Majorana bound states (at the ends of the system and at the phase

discontinuity). We then map the parameters in the p-wave Hamiltonian to those in the nanowire Hamiltonian (4.1) and show how this simple toy model produces qualitatively the same phase-dependent features as those found from our numerical simulations in Sec. 4.2.

We thus consider the one-dimensional p-wave superconductor that we discussed in Sec. 2.2 and describe with the Hamiltonian $H_p = \int dz\, \boldsymbol{\psi}^\dagger(z)\, \boldsymbol{\mathcal{H}}_p \boldsymbol{\psi}(z)$, where we use Nambu spinors in particle-hole space $\boldsymbol{\psi}(z) = [\psi(z), \psi^\dagger(z)]^T$. Now because the phase of the p-wave pairing potential has a spatial dependence, we have to write the Hamiltonian in a more general form as [Bernevig, 2013]

$$\boldsymbol{\mathcal{H}}_p = \begin{pmatrix} -\frac{\hbar^2\partial_z^2}{2m} - \mu & -\frac{i}{2}\{\Delta_p(z), \partial_z\} \\ -\frac{i}{2}\{\Delta_p^*(z), \partial_z\} & \frac{\hbar^2\partial_z^2}{2m} + \mu \end{pmatrix}, \tag{4.9}$$

where the pairing potential is position-dependent,

$$\Delta_p(z) = \begin{cases} \Delta_p e^{-i\phi/2} & \text{for } z < 0, \\ \Delta_p & \text{for } z = 0, \\ \Delta_p e^{i\phi/2} & \text{for } z > 0. \end{cases} \tag{4.10}$$

This Hamiltonian reduces to the form presented in Sec. 2.2 for $\phi = 0$. The superconductor is assumed to be of length L and the center of the wire corresponds to $z = 0$, see Fig. 4.8(a). As sketched in Fig. 4.8(b), the phase of the superconducting pairing potential $\Delta_p(z)$ jumps from $-\phi/2$ to $\phi/2$ at $z = 0$. As shown in Sec. 2.2, the p-wave superconductor is in the topologically non-trivial phase for $\mu > 0$, which is the only case we will consider in this section.

We expect this model to describe a situation similar to the one investigated in Sec. 4.2: For $\phi = 0$, the wire should have two Majorana bound states, one at each end, with an exponentially small energy splitting $\delta\epsilon \propto e^{-L/l_c}$ [Das Sarma *et al.*, 2012], where l_c is the coherence length of the superconductor. For $\phi \to \pi$ we expect two additional Majorana states to form close to the phase discontinuity at $z = 0$. We will now analyze the p-wave Hamiltonian (4.9) and try to derive an effective low-energy model to describe the physics of the four Majorana levels.

We try to solve the Schrödinger equation

$$(\boldsymbol{\mathcal{H}}_p - E)\psi(z) = 0, \tag{4.11}$$

using for $\psi(z)$ the Ansatz

$$\psi(z) = \sum_n e^{c_n z} \begin{pmatrix} u_n \\ v_n \end{pmatrix}. \tag{4.12}$$

This yields four solutions for (4.11) with

$$c_n = \pm\frac{1}{\xi}\sqrt{\tfrac{1}{2} - \tilde{\mu} \pm i\sqrt{\tilde{\mu} - \tilde{E}^2 - \tfrac{1}{4}}}, \tag{4.13}$$

where we used the coherence length $\xi = \hbar^2/2m\Delta_p$ and introduced the dimensionless $\tilde{E} = \xi E/\Delta_p$ and $\tilde{\mu} = \xi\mu/\Delta_p$, and we assumed that $\tilde{\mu} > \tilde{E}^2 + \frac{1}{4}$. In fact, we will take $\tilde{\mu} \gg 1$ which is deep in the topological regime and allows for several convenient simplifications. With (4.13) we find

$$v_n^\pm = i\frac{\tilde{c}_n^2 + \tilde{E} + \tilde{\mu}}{\tilde{c}_n e^{\pm i\phi/2}} u_n^\pm, \tag{4.14}$$

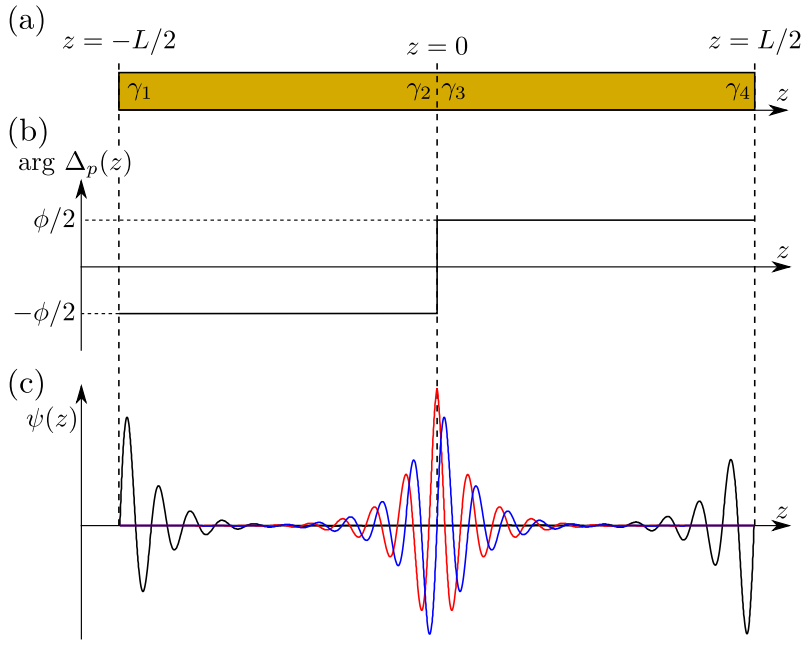

Figure 4.8: (a) Sketch of a one-dimensional p-wave superconductor centered around $z = 0$. We expect Majorana bound states to form at the ends of the wire and close to the phase jump at $z = 0$. (b) The phase of the pairing potential $\Delta_p(z)$ as a function of z. (c)

where the + applies to the right part of the wire, where $z > 0$, and the − to the left part, $z < 0$. We also used a normalized $\tilde{c}_n = \xi c_n$.

We expect the bound states to be localized close to $z = \pm L/2$ and $z = 0$ (depending on ϕ). In principle one should thus allow all four solutions for c_n in both the left and right part of the wire, and then find the explicit wave functions and energies from imposing the right boundary conditions and matching the solutions at $z = 0$.

Since we cannot solve this problem analytically, we construct approximate solutions by separating the problem into two parts. First we focus only on the bound states around $z = 0$, and we thus assume the wire to be infinitely long. Now we can only have decaying solutions for increasing $|z|$, which means that for $z > 0$ only the two c_n with Re $c_n < 0$ are allowed and for $z < 0$ only the two with Re $c_n > 0$. We then proceed as follows: (i) We match the wave functions at $z = 0$. (ii) Since the derivative can be discontinuous due to the δ-function resulting from the term $\partial_z \Delta_p(z)$ in the Hamiltonian, we impose

$$\lim_{\eta \to 0} \int_{-\eta}^{\eta} dz \, (\mathscr{H}_p - E)\psi(z) = 0. \tag{4.15}$$

(iii) We require normalized solutions, $\int dz \, |\psi(z)|^2 = 1$. This all together allows us to find explicit solutions for the eigenstates and eigenenergies for the two lowest levels. We make use of the assumption $\tilde{\mu} \gg 1$, and after a $\pi/2$-rotation along τ_x in particle-hole space we can finally write the Hamiltonian for this 2×2 subspace as

$$H_{23} = \frac{\Delta_p \sqrt{\tilde{\mu}}}{\xi} \cos(\tfrac{\phi}{2}) \tau_y, \tag{4.16}$$

and find the wave functions

$$\psi_2 = \sqrt{\frac{|\sin \frac{\phi}{2}|}{2}} e^{-\frac{1}{2\xi}|z \sin \frac{\phi}{2}|} \cos\left(\frac{\sqrt{\tilde{\mu}}}{\xi} z\right) \begin{pmatrix} i \\ -i \end{pmatrix}, \tag{4.17}$$

$$\psi_3 = \sqrt{\frac{|\sin\frac{\phi}{2}|}{2}} e^{-\frac{1}{2\xi}|z\sin\frac{\phi}{2}|} \sin\left(\frac{\sqrt{\tilde{\mu}}}{\xi}z\right)\begin{pmatrix} i \\ -i \end{pmatrix}, \tag{4.18}$$

cf. Ref. [Kwon *et al.*, 2003]. These two wave functions oscillate with period $\xi/\sqrt{\tilde{\mu}}$ and decay exponentially on a length scale $2\xi/|\sin\frac{\phi}{2}|$. The prefactor $(\frac{1}{2}|\sin\frac{\phi}{2}|)^{1/2}$ follows from normalization of the wave functions. We see that for $\phi = \pi$ the two states are strongly localized around $z = 0$ and their splitting is zero, whereas for $\phi \to 0$ the localization length diverges, their splitting becomes maximal, and the wave functions look more like bulk modes. This all is in agreement with the picture we presented in Sec. 4.1. In Fig. 4.8(c) we sketch the z-dependence of the two wave functions for $\phi = \pi$ and $\tilde{\mu} = 20$, showing the prefactor of the spinor $[i, -i]^T$ (blue and red curves in the central part of the plot).

We now turn to the bound states at the ends of the wire, at $z = \pm L/2$. As an approximation, we ignore the phase jump at $z = 0$: Terms in the wave function that decay for increasing z live almost entirely in the left part of the wire, and we assume that for these terms Eq. (4.14) applies with a minus sign for the whole extent of the wire, i.e. these terms are constructed taking $\Delta_p(z) = \Delta_p e^{-i\phi/2}$ throughout the wire. Similarly, we set $\Delta_p(z) = \Delta_p e^{i\phi/2}$ everywhere for all terms decaying with decreasing z. Using the boundary conditions $\psi(\pm L/2) = 0$ and the normalization constraint $\int dz\,|\psi(z)|^2 = 1$ we can again arrive at analytic expressions for the eigenstates and eigenenergies. In the limit of $\tilde{\mu} \gg 1$ and after an appropriate rotation in particle-hole space, we find for the two lowest levels the Hamiltonian

$$H_{14} = -2\frac{\Delta_p\sqrt{\tilde{\mu}}}{\xi}\cos(\tfrac{\phi}{2})\sin\left(\frac{\sqrt{\tilde{\mu}}}{\xi}L\right)e^{-\frac{L}{2\xi}}\tau_y, \tag{4.19}$$

and the wave functions

$$\psi_1 = \frac{e^{-\frac{1}{2\xi}(z+L/2)}}{\sqrt{2}}\sin\left(\frac{\sqrt{\tilde{\mu}}}{\xi}[z+\tfrac{L}{2}]\right)\begin{pmatrix} e^{i\pi/4-i\phi/4} \\ e^{-i\pi/4+i\phi/4} \end{pmatrix}, \tag{4.20}$$

$$\psi_4 = \frac{e^{\frac{1}{2\xi}(z-L/2)}}{\sqrt{2}}\sin\left(\frac{\sqrt{\tilde{\mu}}}{\xi}[z-\tfrac{L}{2}]\right)\begin{pmatrix} e^{-i\pi/4+i\phi/4} \\ e^{i\pi/4-i\phi/4} \end{pmatrix}. \tag{4.21}$$

These two wave functions oscillate with the same period $\xi/\sqrt{\tilde{\mu}}$ as $\psi_{2,3}$ found above, and always decay exponentially on a length scale ξ. The splitting between the states vanishes for $\phi = \pi$ and is maximal for $\phi = 0$, similar to the splitting between the central two states. However, since $\psi_{1,4}$ are always localized at the ends of the wire and never acquire a bulk character, their maximal splitting is reduced with a factor $e^{-L/2\xi}$. The black curves localized at $z = \pm L/2$ in Fig. 4.8(c) show the typical z-dependence of these solutions.

To complete our effective low-energy model, we have to include the coupling between the end states $\psi_{1,4}$ and the central states $\psi_{2,3}$. To that end we consider the two halves of the wire separately assuming that the main contribution to this overlap comes from the regions close to $z = \pm L/4$. The approximate wave functions derived above cannot be used to calculate the matrix elements directly (all leading-order terms in $\tilde{\mu}$ cancel), and we have to infer the splitting between the end states and the central states from the similarity of their wave functions.

We focus here on the matrix element between ψ_1 and ψ_3, all other elements follow from similar reasoning. We notice that ψ_3 and ψ_4 have a very similar structure, the differences being: (i) a renormalized ξ in the exponent in ψ_3, (ii) a different, ϕ-dependent prefactor in ψ_3, and (iii) a different orientation in particle-hole space. If we can understand the resulting differences in the matrix element between the two states, we can thus modify H_{14}

to describe the coupling between ψ_1 and ψ_3. The spinor structure of ψ_1 and ψ_3 together with the structure of the Hamiltonian guarantee that the matrix element has to be proportional to $(\cos\frac{\phi}{4}+\sin\frac{\phi}{4})$. This factor replaces the factor $\cos\frac{\phi}{2}$ in (4.19), which results in the same way from the spinor structure of ψ_1 and ψ_4. We assume that the renormalization of ξ in ψ_3 mainly results in a different exponential suppression: $e^{-L/2\xi}\to e^{-L(1+|\sin\frac{\phi}{2}|)/8\xi}$, where we used that the length of the segment we consider is now $L/2$. Including the extra prefactor $|\sin\frac{\phi}{2}|^{1/2}$, we thus infer the 2×2 coupling Hamiltonian

$$H_{13} = -2\frac{\Delta_p\sqrt{\tilde{\mu}}}{\xi}(\cos\frac{\phi}{4}+\sin\frac{\phi}{4})\sqrt{|\sin\tfrac{\phi}{2}|}\sin\left(\frac{\sqrt{\tilde{\mu}}}{2\xi}L\right)e^{-\frac{L}{8\xi}(1+|\sin\frac{\phi}{2}|)}\tau_y. \tag{4.22}$$

Exactly the same reasoning yields explicit expressions for the remaining seven matrix elements, and we finally arrive at the approximate low-energy Hamiltonian (cf. the low-energy Hamiltonian inferred from numerical calculations in the supplementary material in [Chiu *et al.*, 2015])

$$H_{\mathrm{M}} = 2\frac{\Delta_p\sqrt{\tilde{\mu}}}{\xi}\begin{pmatrix} 0 & if_c & if_s & i\cos(\frac{\phi}{2})\sin\left(\frac{\sqrt{\tilde{\mu}}}{\xi}L\right)e^{-L/2\xi} \\ -if_c & 0 & -\frac{i}{2}\cos(\frac{\phi}{2}) & if_c \\ -if_s & \frac{i}{2}\cos(\frac{\phi}{2}) & 0 & -if_s \\ -i\cos(\frac{\phi}{2})\sin\left(\frac{\sqrt{\tilde{\mu}}}{\xi}L\right)e^{-L/2\xi} & -if_c & if_s & 0 \end{pmatrix}, \tag{4.23}$$

where we used the functions

$$f_c = (\cos\tfrac{\phi}{4}+\sin\tfrac{\phi}{4})\sqrt{|\sin\tfrac{\phi}{2}|}\cos\left(\frac{\sqrt{\tilde{\mu}}}{2\xi}L\right)e^{-\frac{L}{8\xi}(1+|\sin\frac{\phi}{2}|)}, \tag{4.24}$$

$$f_s = (\cos\tfrac{\phi}{4}+\sin\tfrac{\phi}{4})\sqrt{|\sin\tfrac{\phi}{2}|}\sin\left(\frac{\sqrt{\tilde{\mu}}}{2\xi}L\right)e^{-\frac{L}{8\xi}(1+|\sin\frac{\phi}{2}|)}. \tag{4.25}$$

We would now like to connect this effective low-energy model for the p-wave Hamiltonian (4.9) to the results presented in Sec. 4.2, *i.e.* we would like to express the parameters $\sqrt{\tilde{\mu}}$ and ξ in terms of the parameters of the nanowire Hamiltonian (4.1). Using the result for $\phi=0$ and either small α_{R} or Δ_{ind} Das Sarma *et al.* [2012], we can identify

$$\frac{\sqrt{\tilde{\mu}}}{\xi}\equiv k_{\mathrm{F}}^* = \frac{\sqrt{2m^*}}{\hbar}\sqrt{\mu+\frac{m^*\alpha_{\mathrm{R}}^2}{\hbar^2}+\sqrt{\left(\mu+\frac{m^*\alpha_{\mathrm{R}}^2}{\hbar^2}\right)^2+V_{\mathrm{Z}}^2-\Delta_{\mathrm{ind}}^2-\mu^2}}, \tag{4.26}$$

$$\xi^{-1} = \frac{m^*}{\hbar^2}\frac{\alpha_{\mathrm{R}}\Delta_{\mathrm{ind}}}{\sqrt{\left(\mu+\frac{m^*\alpha_{\mathrm{R}}^2}{\hbar^2}\right)^2+V_{\mathrm{Z}}^2-\Delta_{\mathrm{ind}}^2-\mu^2}}, \tag{4.27}$$

where Δ_{ind} is the induced pairing potential in the wire, in this section for simplicity assumed to be constant. This yields for the energy scale $2\Delta_p\sqrt{\tilde{\mu}}/\xi=\hbar^2k_{\mathrm{F}}^*/m\xi$, which is consistent with the results of Das Sarma *et al.* [2012].

In Fig. 4.9 we plot the spectrum of H_{M}, using $\mu=0$ and $\Delta_{\mathrm{ind}}=4E_{\mathrm{SO}}$ and $L=20l_{\mathrm{SO}}$ where we define the spin-orbit length as $l_{\mathrm{SO}}=\hbar^2/m\alpha_{\mathrm{R}}$. Fig. 4.9(a) shows the energy levels as a function of V_{Z} for $\phi=0$ (top plot) and $\phi=\pi$ (bottom plot), to be compared with the top and bottom plots of Fig. 4.3(a). We see that for $\phi=0$ the two central states are again gapped out, their splitting being $\sim\hbar^2k_{\mathrm{F}}^*/m\xi$. The splitting of the two remaining low-energy states is suppressed by a factor $e^{-L/2\xi}$ and shows oscillations with a period of

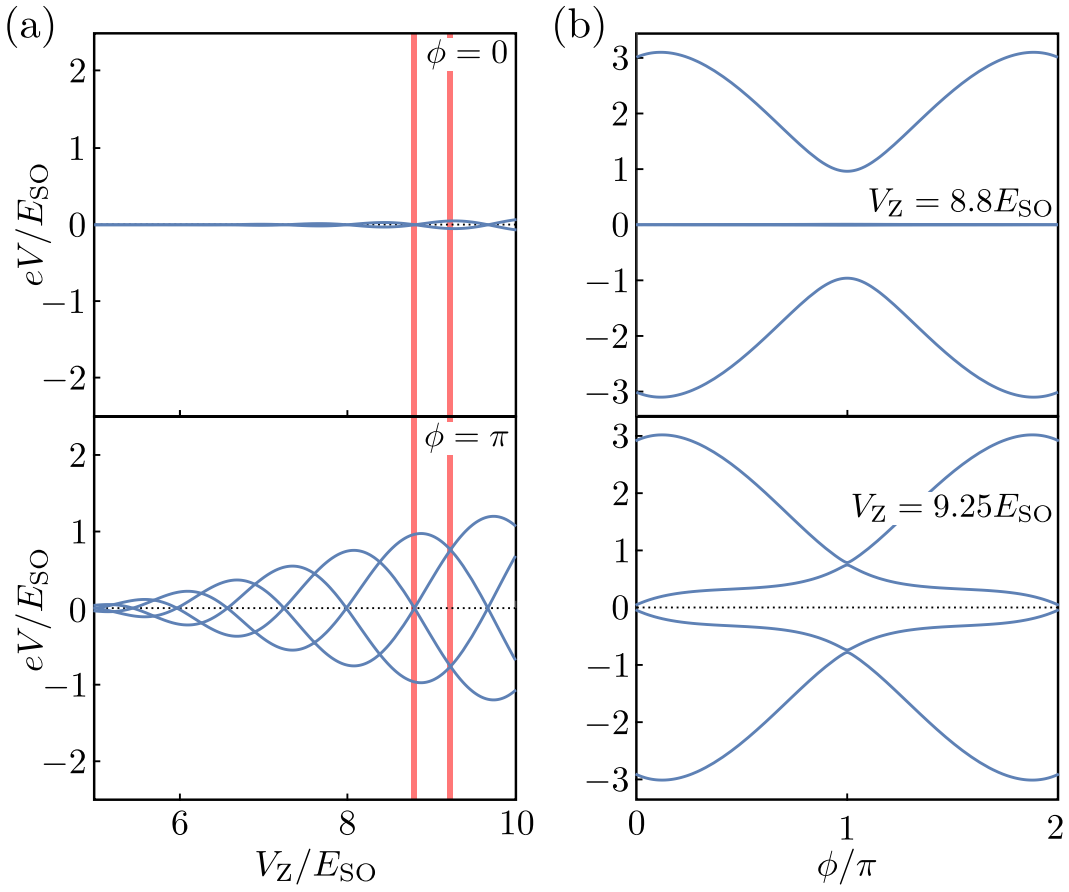

Figure 4.9: The spectrum of H_M for $\mu = 0$, $\Delta_{ind} = 4E_{SO}$, and $L = 20l_{SO}$. (a) Level structure as a function of V_Z for $\phi = 0$ (top) and $\phi = \pi$ (bottom). (b) Spectrum as a function of ϕ for $V_Z = 8.8E_{SO}$ (top) and $V_Z = 9.25E_{SO}$ (bottom), as indicated by the red lines in (a).

k_F^*. At $\phi = \pi$ the coupling between ψ_2 and ψ_3 vanishes, and all energies are suppressed by a factor $e^{-L/4\xi}$. In Fig. 4.9(b) we plot the spectrum as a function of ϕ, for $V_Z = 8.8E_{SO}$ (top plot) and $V_Z = 9.25E_{SO}$ (bottom plot), to be compared with the two lower two plots of Fig. 4.3(b). We see the same distinctive phase-dependence as in our numerical results: When the phase difference goes from 0 to π, the gapped fermionic mode formed by the two central Majorana states ψ_2 and ψ_3 gradually develops into two low-energy Majorana modes that are weakly coupled to ψ_1 and ψ_4. The slight bending of the levels close to $\phi = 0$ and $\phi = 2\pi$, which is absent in the numerical results presented in Fig. 4.3, is a consequence of including only four levels in the low-energy description: In the "full" numerical model of Sec. 4.2, two of the four low-energy states in fact merge with the above-gap states when ϕ approaches a multiple of 2π, and therefore we should not expect to find their correct energies with a low-energy model that does not include these above-gap states.

Finally, we only mention that it is straightforward to modify the Hamiltonian (4.23) in order to describe the case where the lengths of the two parts of the wire are different. The resulting spectrum (not shown here) indeed resembles the low-energy part of Fig. 4.5(a,b), reproducing the anti-crossings observed in the figure.

4.4 Summary

In this chapter, we investigated the phase-dependent conductance spectrum of a topological N-SNS junction in a semiconducting nanowire. Creating such a system is feasible with

the current state of experimental techniques, and we showed that it should in principle allow us to determine whether or not a measured low-bias peak in the differential conductance can be associated with non-local fermionic states formed by MBSs at the topological phase boundaries inside the wire. We presented numerical calculations of the conductance spectrum and indicated the phase-dependent features that could serve as a distinguishing signature of the formation of MBSs at the ends of the wire. We supported our interpretation with a simple low-energy model based on a one-dimensional spinless p-wave superconductor with a phase discontinuity. This toy Hamiltonian reproduced all important qualitative features of the numerical results and provides insight into the structure of the "Majorana subspace" including the gradual gapping out of the central two Majorana states when the phase difference is reduced to zero.

Chapter 5

Majorana Bound States in a Coupled Quantum-Dot Hybrid-Nanowire System

> "There are two possible outcomes: if the result confirms the hypothesis, then you've made a measurement. If the result is contrary to the hypothesis, then you've made a discovery
>
> Enrico Fermi

This chapter is based on work presented in [Deng et al., 2016] and the corresponding supplementary material.

One of the simplest setups for performing electron tunneling spectroscopy experiments on SC-SM nanowires is where the two ends of the nanowire are contacted by normal leads and with a single tunnel barrier at one end. Electrical gates of different sizes are deposited near the nanowire and used to change the electrostatic potential in different parts of the nanowire. One or two smaller gates at the end of the nanowire are used to create the tunnel barrier in a small segment of the nanowire close to where one of the leads is contacted. A voltage bias applied between the two contacts generates a current that may be used to probe quantum states in the nanowire. The fabrication of these nanowire devices is however not a fully controlled process, which occasionally results in the formation of a quantum dot in the tunnel barrier region. An example of such a device is shown in Fig. 5.1. The presence of such a quantum dot will inevitably influence the electron transport from the lead into the nanowire. It is therefore important to understand this influence when the goal is to probe other quantum states, such as the elusive MBS, that may also exist in the nanowire under the right circumstances.

In this chapter, we will present a theoretical model of a SC-SM nanowire where a small segment at the end is not coupled to the superconductor. In this normal segment, the potential well and the potential barrier emulate a quantum dot coupled to the end of a SC-SM nanowire. The model was developed as part of the work presented in [Deng *et al.*, 2016] and we will discuss how it was used to interpret the experimental data.

In the experiments, the energy spectrum of a grounded SC-SM nanowire coupled to a quantum dot at the end is investigated by ETS through the quantum dot. The system

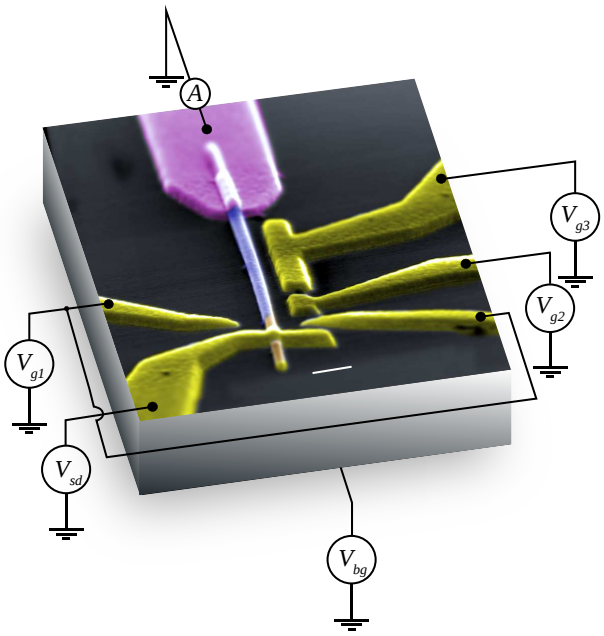

Figure 5.1: Scanning electron micrograph of device 1 in [Deng *et al.*, 2016], with false color representing different materials. The gates marked with voltage V_{g1} are used to create a tunnel barrier close to the lead with bias voltage V_{sd}, while those marked with V_{g2} and V_{g3} are used to tune the electrostatic potential in the nanowire. The current A is measured as a response to changing gate voltages, magnetic field, and voltage bias V_{sd} between the two leads, as a way of characterizing the quantum states in the SC-SM nanowire.

displays a rich spectrum of states below the superconducting gap and it is demonstrated that the electrostatic potential of the nanowire and the dot can be tuned separately. The evolution of the subgap spectrum is explored as a function of the applied magnetic field and gate voltages in cases where dot levels are on and off resonance with the Fermi levels of the nanowire. The conductance spectrum exhibits a ZBP in a regime that is compatible with the presence of MBSs. Bringing a dot level into resonance with the MBS ZBP leads to a splitting of the ZBP and an anti-crossing between the split ZBP and the dot level. Numerical simulations of the theoretical model are able to qualitatively reproduce the experimental data. These and further simulations are discussed in order to interpret and understand the hybridization between the MBS in the nanowire and the dot level.

In subsequent theoretical work by Prada *et al.* [2017] and Clarke [2017], a similar model is used to study the hybridization of the dot levels and the MBS in more detail and it is proposed that a quantum dot can be used as a spectroscopic tool to quantify the degree of non-locality of MBSs in the nanowire. In experiments reported by [Deng *et al.*, 2017], the observed MBS ZBP signatures are analyzed using the model of Prada *et al.* [2017]. A high degree of non-locality is found which is consistent with the interpretation of topological MBSs. We find similar features in our model, but will not go into a detailed comparison.

However, the presence of a dot at the end of the SC-SM nanowire may not only be a good thing with respect to identifying ZPB in conductance as a signature of topological MBS. In the theoretical work by Liu *et al.* [2017b], it is shown that strong hybridization between the nanowire and dot may lead to MBS-like ZBP features in conductance that are due to trivial ABSs. This happens in the regime of a very large chemical potential where localized ABSs with energies below the induced superconducting gap form at the ends of the nanowire. The non-superconducting segment at the end of the wire leads to the hybridization between these trivial ABSs, which in certain cases might result in

MBS-like ZBP features. In a similar theoretical model where the normal section constitutes an extended tunnel barrier [Moore *et al.*, 2018b], it is found that this trivial ABS may give rise to a persistent ZBP which is seemingly quantized at $2e^2/h$. Whether or not these models describe the experimental situation is debatable, and it is therefore important to develop methods for experimentally distinguishing these trivial ABSs from topological MBSs. This is however not the subject of the work presented in this chapter, so we will postpone this discussion until a later point.

5.1 Dot-nanowire model

We consider the setup of a SC-SM nanowire that is coupled to a lead through a tunnel barrier at the left end, as schematically pictured in Fig. 5.2 (a), though the lead and tunnel barrier are not considered as a part of the nanowire. The nanowire consists of three parts: a dot, a potential barrier, and a segment coupled to a bulk s-wave superconductor. The dot is the first segment from the left of length L_d, while the potential barrier is the next segment of length L_b. The right segment covered by the bulk superconductor is of length L and superconductivity is proximity induced in this part. Even though all three segments are part of the nanowire we will for the sake of easy reference refer to the right part as the nanowire. The potential profile throughout the whole nanowire is a stepwise changing profile, as shown in Fig. 5.2 (b), where the potential height in each segment can be tuned separately.

In order to obtain a picture of the local density of states throughout the wire, we model the connected tunneling lead as a movable tunneling probe that can be connected to any point along the nanowire, as shown in Fig. 5.2 (c).

The system will be described using the model introduced in Sec. 2.4, but with spatially dependent potentials. We will briefly recap the equations we need to describe the model and define the potentials. The Green's function of the electrons and holes in the nanowire is

$$G^{\mathrm{R}}(z,z';\omega) = \left[\frac{1}{\omega - \mathscr{H}_{\mathrm{NW}} - \Sigma^{\mathrm{R}}_{\mathrm{SC}}(\omega) + i0^+}\right]_{z,z'}, \tag{5.1}$$

with the position dependent self-energy

$$\Sigma^{\mathrm{R}}_{\mathrm{SC}}(z,z';\omega) = \gamma(z)\frac{-\omega + \Delta(B)\tau_x}{\sqrt{|\Delta(B)|^2 - (\omega + i0^+)^2}}\delta_{z,z'}, \tag{5.2}$$

where the superconducting gap of the parent superconductor $\Delta(B)$ depends on the applied magnetic field in the manner

$$\Delta(B) = \Delta(0)\left[1 - \left(\frac{B}{B_c}\right)^2\right], \tag{5.3}$$

such that the gap closes at $B = B_c$. The coupling between the nanowire and parent superconductor is parametrized by

$$\gamma(z) = \begin{cases} \gamma & \text{for } L_d + L_b < z < L_d + L_b + L, \\ 0 & \text{elsewhere.} \end{cases} \tag{5.4}$$

The BdG Hamiltonian of the nanowire is

$$\mathscr{H}_{\mathrm{NW}} = \left[-\frac{\hbar^2\partial_z}{2m^*} - i\alpha_{\mathrm{R}}\partial_z\sigma_y + V(z)\right]\tau_z + V_Z\sigma_z, \tag{5.5}$$

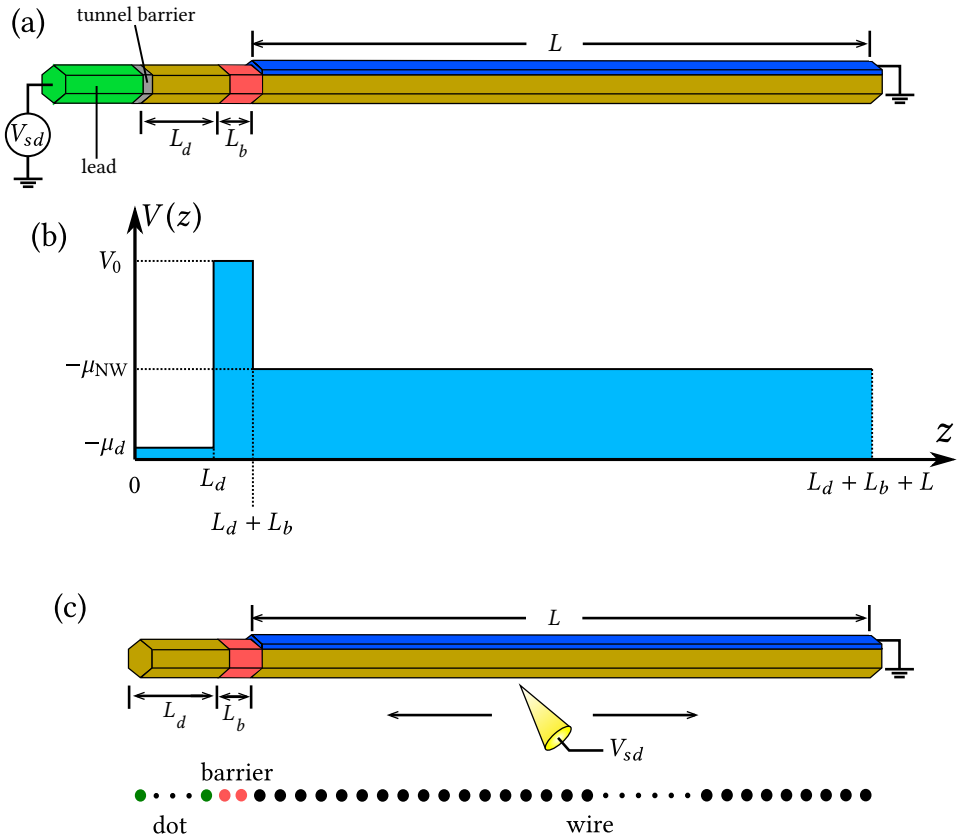

Figure 5.2: (a) Schematic drawing of the dot-nanowire setup. The nanowire is connected to a lead (green) through a tunneling barrier (grey) at the left end. The first segment of length L_d constitutes the quatum dot and the next segment of length L_b is the potential barrier (light red). The last segment of length L is partly covered by a superconducting shell and forms the topological part of the nanowire under the right conditions. The superconducting shell is connected to ground. (b) Profile of the potential $V(z)$ given in Eq. (5.6) without the phenomenological charging energy term $\frac{1}{2}E_C(\sigma_z + \mathbb{1}_2)$. (c) As in (a), but with a movable tunneling probe.

where m^* is the effective mass of the electrons, α_R is the spin-orbit coupling strength, $V_Z = \frac{1}{2}g\mu_B B$ is the Zeeman field induced by the magnetic field B pointing along the nanowire, with the g-facter g and the Bohr magneton μ_B. The potential is

$$V(z) = \begin{cases} -\mu_d + \frac{1}{2}E_C(\mathbb{1}_2 - \sigma_z) & \text{for } z < L_d, \\ V_0 & \text{for } L_d \le z \le L_d + L_b, \\ -\mu_{NW} & \text{elsewhere,} \end{cases} \tag{5.6}$$

so that μ_d is the chemical potential on the dot, V_0 is the height of the barrier, and μ_{NW} is the chemical potential on the proximitized part of the wire. Charging effects in the quantum dot are accounted for phenomenologically by the term E_C in $V(z)$. This term lifts the Kramers degeneracy in the dot states at $V_Z = 0$ by shifting the spin down state to a higher energy. This assumes a negative g-factor as is the case for the InAs nanowires under consideration. This qualitatively reproduces the results of a mean-field description of the Coulomb interactions at large magnetic field.

Using the methods described in Chap. 3, we compute the differential conductance measured by a tunnel probe connected to the system at position z_{probe} by

$$\left.\frac{dI}{dV}\right|_{V=V_{sd}} = \frac{e^2}{h}\mathrm{Tr}\left[1 - r_{ee}r_{ee}^\dagger + r_{he}r_{he}^\dagger\right] \tag{5.7}$$

where the reflection matrix is obtained by

$$\mathbf{R}(\epsilon) = \begin{bmatrix} r_{ee}(\epsilon) & r_{eh}(\epsilon) \\ r_{he}(\epsilon) & r_{hh}(\epsilon) \end{bmatrix} = 1 - 2i\pi W^\dagger \left\{ \left[G^R(\epsilon) \right]^{-1} + i\pi W W^\dagger \right\}^{-1} W. \tag{5.8}$$

For the purpose of numerical computations, the model described above is mapped to a tight binding model with N sites. The coupling to the tunnel probe is described by the matrix

$$W = \sqrt{\gamma_W} \left(\mathbf{s}_n \otimes \mathbb{1}_4 \right)^T \tag{5.9}$$

where γ_W parametrizes the coupling strength. The vector $\mathbf{s}_n = (0, 0, ..., 0, 1, 0, ...)$ has a single 1 located at the n'th entry and thereby encodes the position of the tunnel probe, $z_{\text{probe}} = nL/N$. The tunnel probe will in general be coupled to the left end of the wire, *i.e.* the first site, unless it is explicitly specified otherwise or we are computing the differential conductance as measured at points along the wire.

Model parameters

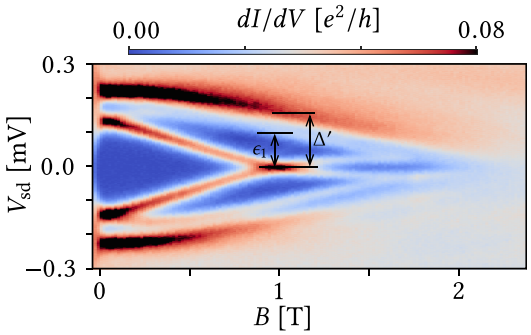

Figure 5.3: Experimental data of differential conductance as a function of magnetic field B and voltage bias V_{sd}. Data is from experiments presented in Fig. 3G in [Deng *et al.*, 2016] and a scanning electron micrograph of the device is shown in Fig. 5.4. The distance to the first excited state and the gap of the parent superconductor at the approximate point of the topological phase transition are indicated by ϵ_1 and Δ', respectively.

Some model parameters can be read off from the experimental data, such as the parent superconductor gap $\Delta(B)$ and the critical magnetic field where the parent superconducting gap closes B_c. Others can be estimated by the methods discussed in Sec. 2.4 and by comparing with similar experiments. In Fig. 5.3, we show a plot of the differential conductance as a function of magnetic field and voltage bias measured in the device we are modeling by Deng *et al.* [2016]. By reading off the gap of the parent superconductor $\Delta(0) \approx 220\mu\text{eV}$, and the induced gap $\Delta_{\text{ind}} \approx 130\mu\text{eV}$ at zero magnetic field from the data, we can estimate the effective coupling strength between the nanowire and parent superconductor γ by using Eq. (2.72):

$$\gamma = \Delta_{\text{ind}} \sqrt{\frac{\Delta + \Delta_{\text{ind}}}{\Delta - \Delta_{\text{ind}}}} \approx 256\mu\text{eV}. \tag{5.10}$$

The critical field where the parent superconductor gap closes is $B_c \approx 2.2\text{T}$.

We can also estimate the ratio of the effective distance between the MBSs, L, and the effective superconducting coherence length, ξ, near the topological phase transition using Eq. (2.85),

$$\frac{L}{\xi} \approx \frac{\Delta'}{\Delta' + \gamma} \frac{\pi \Delta'}{\epsilon_1}. \tag{5.11}$$

An estimate of γ was obtained above and we are able to read off the other parameters' values in Fig. 5.3: The energy distance to the first excited state $\epsilon_1 \approx 100\mu\text{eV}$ and the gap of the parent superconductor $\Delta' \approx 180\mu\text{eV}$ around the topological phase transition. From these parameters we obtain the estimate $\frac{L}{\xi} \approx 2.3$.

The model we employ assumes a clean disorder-free nanowire, but this is not the case for real world nanowires. The effective distance between MBSs, L, (to be used in the model) may therefore differ from the lithographic device length. If we take $\xi \approx 260\text{nm}$, which was estimated by Albrecht *et al.* [2016] from a fit of wire-length dependence in similar nanowires, we obtain and effective length of $L \approx 600\text{nm}$, which is shorter than the lithographic device length, as seen in Fig. 5.4. Using this effective length we can now estimate the spin-orbit coupling strength α_R using Eq. (2.86),

$$\alpha_\text{R} \approx \frac{\Delta' + \gamma}{\Delta'} \frac{L}{\pi} \epsilon_1 \approx 50 \text{ meV nm}, \tag{5.12}$$

which is rounded off to one significant digit. The remaining parameters are chosen such that the observed data in experiments is qualitatively reproduced or in accordance with what is widely used to model InAs nanowires.

To recap the model parameters we are using: Effective electron mass $m^* 0.026\text{m}_\text{e}$, spin-orbit coupling strength $\alpha_\text{R} = 50$ meV nm, g-factor $g = -18$, "Charging energy" $E_C = 5\text{meV}$, potential barrier height $V_0 = 8\text{meV}$, critical magnetic field for parent superconductor gap closing $B_c = 2.2\text{T}$, effective coupling strength between nanowire and parent superconductor $\gamma = 257\mu\text{eV}$, gap of parent superconductor at zero magnetic field $\Delta(0) = 220\mu\text{eV}$, length of dot $L_d = 60\text{nm}$, length of barrier $L_b = 12\text{nm}$, and length of superconductor covered part of the nanowire $L = 528\text{nm}$. The coupling strength to the lead will differ between plots and is given in the figure caption.

The rather large g-factor we have chosen should not be viewed as the "bare" wire g-factor, but rather as a phenomenological parameter, since we have not taken g-factor renormalization due to coupling to the parent superconductor into consideration. Obtaining an estimate of the g-factor by fitting to experimental data is also made difficult by the finite-size effect that makes it hard to read off the critical field of the topological phase transition.

5.2 Results

In this section, we will present the results of the numerical model along with some of the data from the experiments presented in [Deng *et al.*, 2016]. We will present and discuss some of the features observed in the experimental data, but refer to the article for a more in-depth discussion of the experimental details. Several nanowire devices were used in the experiment, but we will focus on the data from device 1 shown in Fig. 5.4.

In this device, a quantum dot was formed in the region indicated by the white bracket. The gates labeled with V_{g1} are connected to one voltage source and the gates labeled V_{g2} and V_{g3} to another. Besides these gates that are used to change the potential locally in the nanowire and quantum dot, a large back gate is used to tune the overall electron density in the nanowire.

The nanowire is covered by epitaxially grown Al superconductor on two of the six facets, resulting in a proximity-induced superconducting gap in the nanowire. The induced gap consists of two parts: A continuum of states which start at the gap of the parent superconductor and a discrete spectrum of Andreev bound states (ABSs) below the parent superconductor gap.

Depending on the back gate voltage, the nanowire may be tuned between a high density regime where there are many subgap ABSs present or a low density regime with no ABSs. In the intermediate density regime, a single ABS moves to zero energy and stays at zero over a range of magnetic field intensities. This regime is compatible with the existence of topological MBSs and the emergence of this ZBP is interpreted as a topological phase transition where the ABS transforms into a MBS.

The potential of the dot is then tuned to bring a dot level into resonance with the MBS. As the dot level comes into resonance, the MBS acquires a non-zero energy splitting and the dot level anti-cross with the MBS. This interpretation of the experimental data was developed in comparison with the numerical model introduced above, which simulates the situation of a topological nanowire with MBSs.

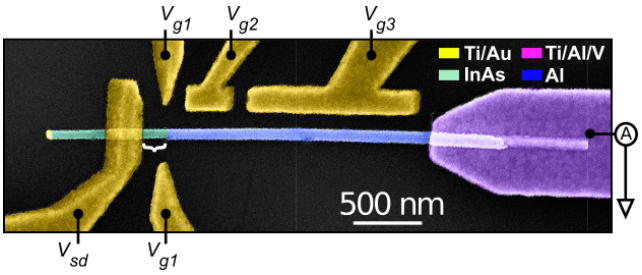

Figure 5.4: Top down view of the scanning electron micrograph of device 1 in [Deng *et al.*, 2016] with false color representing different materials, also shown in Fig. 5.1 from a different angle. The white brace indicates the location of a natively formed quantum dot. The gates marked with V_{g2} and V_{g3} are coupled to the same voltage source and are used to tune the electrostatic potential in the nanowire, while the gates labeled by voltage V_{g1} are used to create a tunneling barrier and tune the potential in the quantum dot.

5.2.1 Dot and nanowire states and their dependence on gates and magnetic field

First we compare with the experimental data presented in [Deng *et al.*, 2016] Fig. 2, reproduced in Fig. 5.5, where the differential conductance is measured as a function of the applied bias voltage V_{sd} and either the gate controlling the electrostatic potential in the dot V_{g1} or the magnetic field B. This is done at two different back gate voltages, corresponding to high density with many subgap states or low density with no subgap states. The data shows that a large degree of control over the quantum dot and the density in the wire is achieved by tuning the gates.

In Fig. 5.6, we show simulations reproducing most of the features observed in the experiment. Figs. (a-c) are in the high density regime with many subgap states and Figs. (d-f) are in the low density regime with almost no ABSs in the gap. In the low density regime with $\mu_{\text{NW}} = -1.1\,\text{meV}$, the nanowire stays in the topologically trivial phase for the whole range of magnetic fields. In the high density regime with $\mu_{\text{NW}} = 0.7\,\text{meV}$, the nanowire becomes topologically non-trivial with the formation of a pair of MBSs at the ends of the nanowire at the magnetic field where the lowest-energy state cross zero energy in Fig. (c). In the μ_d-sweep plots (a, b, d, e), we see two states crossing zero energy at $\mu_d \approx 2\,\text{meV}$ and 8 meV. These are the dot states of opposite spin where the distance between the two crossings corresponds to the charging energy in the dot plus the Zeeman splitting of the two spin states. In our model, we have chosen $E_C = 3.5\,\text{meV}$ such that the two spin states are well separated, but not so large that one of them coincides with higher energy dot states. The first and second zero energy crossing show a difference in peak intensity that is also seen in the experimental data in the high density regime, but not apparent in the low density regime.

The Zeeman splitting of the dot states is visible in the experimental data in Figs. 5.5 (a) and (d), but absent in our simulation. This is due to the way we have implemented charging effects in the dot, which gives an accurate description only when the Zeeman splitting of the dot levels is larger than the superconducting gap. This is also the regime where MBSs exist which is of interest to us here.

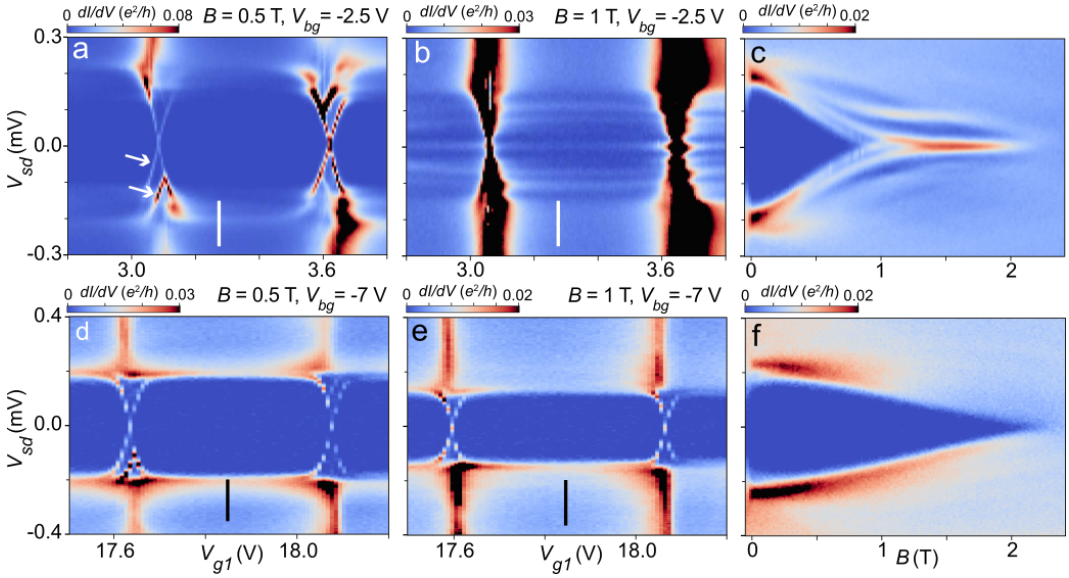

Figure 5.5: Reproduction of the experimental data presented in [Deng *et al.*, 2016] Fig. 2. Differential conductance measured as a function of the bias voltage V_{sd} and either gate voltage V_{g1} in (a, b, d, e) or the applied magnetic field B in (c, f). (a, b, c) correspond to the high density regime with many subgap states, while (d, e, f) correspond to low density regimes with no subgap states. The white/black line in (a) and (b), and (d) and (e) indicate the gate voltage where (c) and (f) are taken. (a) and (b), and (d) and (e) are taken at $B = 0.5, 1\,\mathrm{T}$, respectively. White arrows in (a) indicate the Zeeman splitting of the dot states.

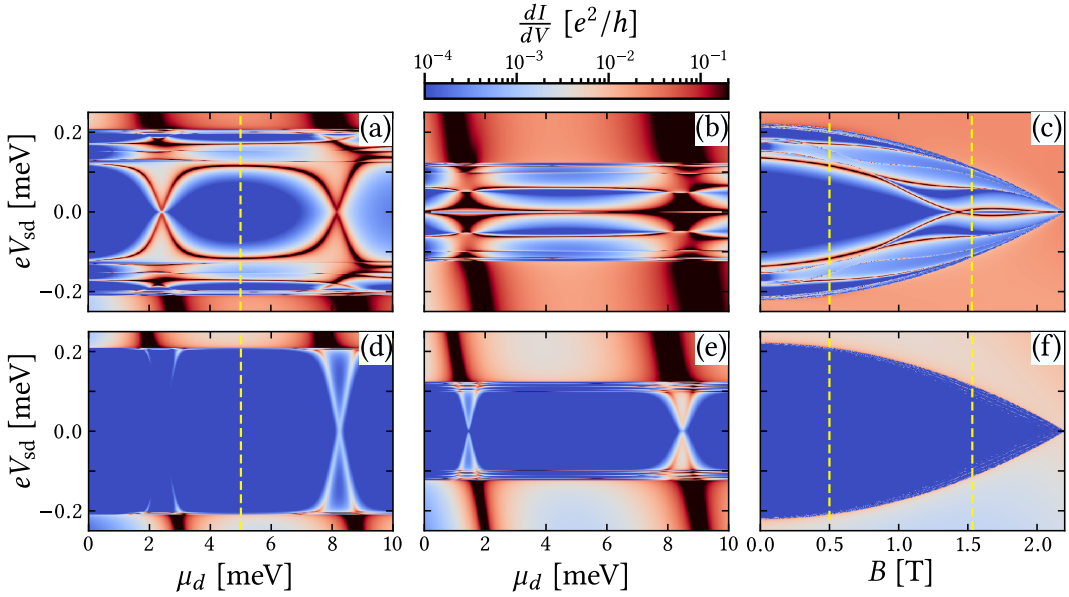

Figure 5.6: Simulated data corresponding to the experimental data shown in Fig. 5.5. Differential conductance as a function of bias voltage V_{sd} and either dot chemical potential μ_d (a, b, d, e) or magnetic field B (c, f). (a-c) are in the high density regime with $\mu_{\mathrm{NW}} = 0.7\,\mathrm{meV}$, while (d-f) are in the low density regime with $\mu_{\mathrm{NW}} = -1.1\mathrm{meV}$. The yellow dashed line in (a) and (d) at $\mu_d = 5\,\mathrm{meV}$ indicate the value of the dot chemical potential where (c) and (f) are taken. The two yellow dashed lines in (c) and (f) at $B = 0.5, 1.55\,\mathrm{T}$ indicate where (a) and (b), and (d) and (e) are taken, respectively. In all plots we have $\gamma_W = 2\,\mathrm{meV}$.

In Fig. 5.7 we see the data from [Deng *et al.*, 2016] Fig. 3. In experimental devices, gates are positioned close to parts of the setup in order to tune the local electrostatic potential by applying a voltage to the nearby gate. It is however often unavoidable that gates couple capacitively to more than just the one part of the setup. This is schematically shown in Fig. 5.7(a), where the gates g1 and g2, g3 couple to both the quantum dot and the nanowire. It is although possible to do a so-called smart sweep, where more than one gate voltage is swept together, in order to keep the potential in one region constant. How this works can be seen from the zero bias conductance plot shown in Fig. 5.7 (b). Zero bias conductance is measured as a function of gate voltages V_{g1} and $V_{g2,g3}$ to construct a so-called gate map. The high conductance lines indicated by the red arrows are dot levels and by performing a smart sweep parallel to these lines, the potential in the dot will be kept approximately constant while the potential in the nanowire is changed. This smart sweep is employed to measure the differential conductance as a function the nanowire potential, while the dot potential is kept constant, as shown in Fig. 5.7 (c-f). The data shows that the subgap spectrum has a strong dependence on the nanowire potential. At zero magnetic field in Fig. (c), the spectrum shows a single subgap state with a minimum[1] at a given gate voltage. At a small magnetic field in Fig. (d), the subgap state splits due to the Zeeman field and the minimum remains at the same gate voltage. At higher magnetic fields in Figs. (e) and (f), the subgap spectrum displays oscillating behavior as a function of gate voltage.

In Fig. 5.7 (g-i), differential conductance measured as a function of V_{sd} and magnetic field is shown for different gate voltages. Depending on the gate voltage, the subgap state may show different behaviors as it goes to zero energy. It may cross zero and split off from zero again, then at higher magnetic fields turn around and move towards zero again. Or it may go the zero energy and stick there as the magnetic field is increased. The point where the state goes to zero energy is around $B = 1\,\mathrm{T}$, but is also changed by the gate voltage. Whether the state crosses or sticks to zero energy is seen as reflecting the difference of an ABS and a MBS. The distinction is however not so clear cut, as an ABS evolves smoothly into a MBS through a transition where its wavefunction changes from having a bulk form, located throughout the nanowire, into a form localized at the ends of the wire. Even though the MBSs are localized at opposite ends of the wire, their wavefunctions decay exponentially into the wire. In shorter wires they have a notable overlap resulting in an observable energy splitting. This overlap is also sensitive to the potential in the wire and changing it will result in different magnetic field behaviors.

The simulated data, shown in Fig. 5.8, is able to reproduce many of the features observed in the experimental data described above. In Figs. (d-f), the nanowire enters the topological phase around the magnetic field strength where the lowest-energy subgap state goes to zero and becomes a MBS. There is a discrepancy between the simulation in Fig. (a) and the experimental data in Fig. 5.7(c), where the experiment shows that the subgap state at $B = 0$ has a minimum at a given gate voltage and moves towards the superconducting gap away from this point both for increasing and decreasing gate voltage. In the simulation, this happens only as μ_{NW} is lowered and the nanowire becomes depleted, but not for raising μ_{NW}. We have therefore chosen lower values of μ_{NW} instead of higher in Figs. (e) and (f) in order to have a situation where the subgap state at $B = 0$ moves towards the gap as seen in the experimental data in Fig. 5.7 (h) and (i). The difference between the theoretical model and experiment may be due to multiple transverse subbands being occupied in the experiment, whereas we only have a single subband in the model. In Figs. (d-f) we also see that the MBS oscillations are very sensitive to changing μ_{NW}. The field where the state cross zero is shifted and the number of visible oscillations change as μ_d is varied. This also happens for increasing μ_{NW} though it is not shown here.

1. minimum meaning minimum distance to zero bias voltage

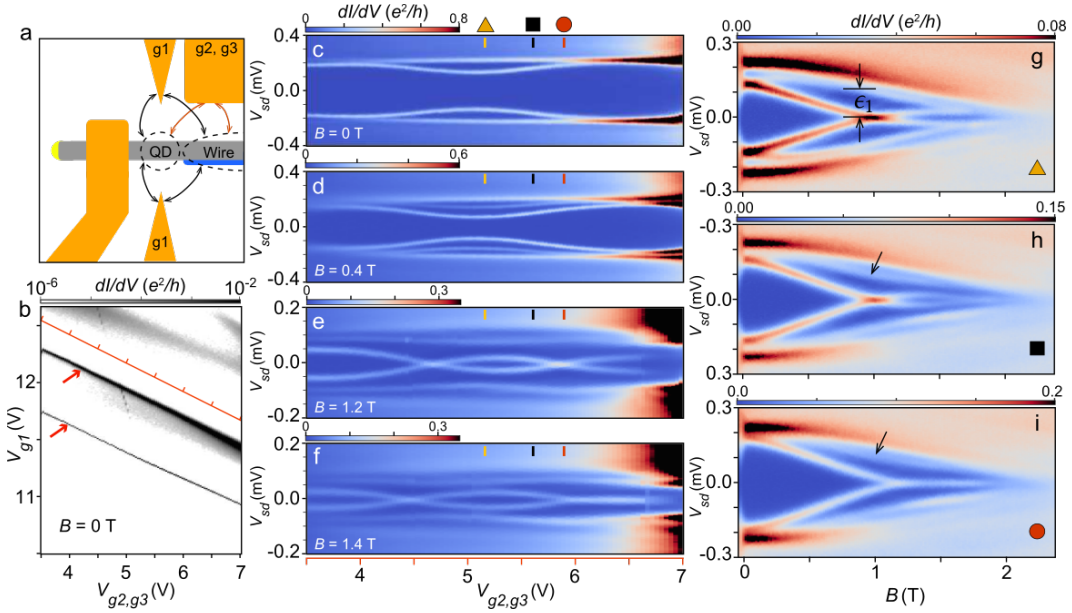

Figure 5.7: Reproduction of the experimental data presented in [Deng *et al.*, 2016] Fig. 3. (a) A schematic of device 1 with arrows indicating that both gates g1 and g2,g3 are capacitively coupled to both the dot and the nanowire. (b) Conductance measured at zero bias and $B = 0$, as a function of V_{g1} and $V_{g2,g3}$ (the gate map). Gate g2 and g3 are connected to the same voltage source. The high-conductance lines indicated by red arrows are the resonant levels in the end dot. (c-f) Differential conductance at intermediate density as a function of bias voltage and a combined sweep of V_{g1} and $V_{g2,g3}$ along the red line in (b) for different magnetic fields, noted in the figures. (g-h) Differential conductance as a function of bias voltage and magnetic field for different gate voltages of $V_{g2,g3}$ indicated by the triangle, square and circle symbols in (c-f). Arrows in (g-i) indicate the first excited state with energy ϵ_1.

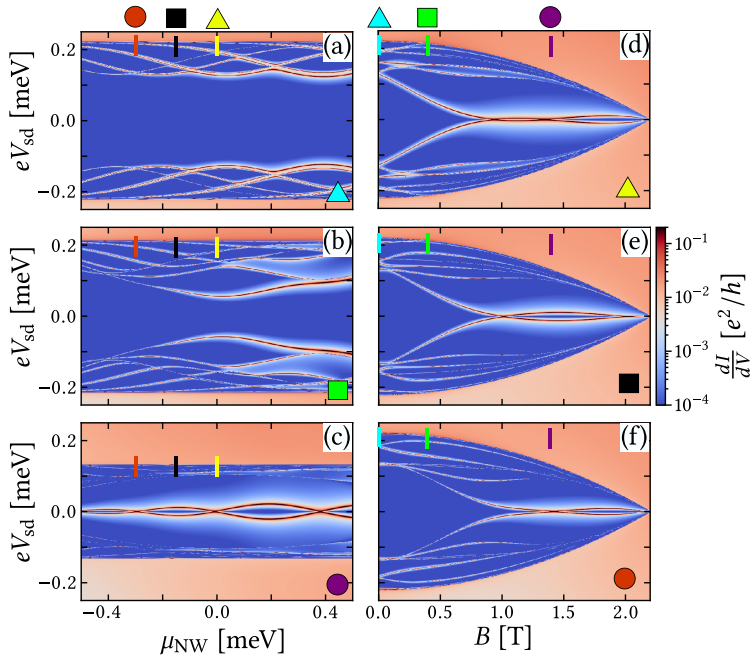

Figure 5.8: Simulated data corresponding to the experimental data shown in Fig. 5.7. Simulated differential conductance as a function of bias voltage V_{sd} and either nanowire chemical potential μ_{NW} (a-c) or magnetic field B (d-f). (a-c) are taken at different magnetic fields as indicated by the cyan triangle, green square and purple circle symbols. (d-f) are taken at different nanowire chemical potentials μ_{NW} as indicated by the yellow triangle, black square and red circle symbols. In all plots we have $\gamma_W = 2\mathrm{meV}$.

5.2.2 Hybridization of dot-levels and Majorana bound states

Next we consider the situation where a level in the dot becomes resonant with the Fermi level of the nanowire. The data from the experiment is shown in Fig. 5.9 (a-d). The gate map in Fig. (a) shows how the dot and wire states depend on the gate voltages V_{g1} and $V_{g2,g3}$. The blue and red dashed arrows indicate smart sweeps where either the dot potential or the wire potential is approximately constant. A smart sweep is performed along the red solid line, where a dot level crosses the Fermi level of the wire as potential in the nanowire is approximately constant. Differential conductance measurements as a function of the smart sweep gate voltage for different magnetic fields are shown in Figs. (b-c). In Fig. (b), the dot level simply cross zero energy. In Fig. (c), there is a single subgap state present below the induced gap. At resonance, a state moves down from the gap and anti-crosses with the subgap state, marked by the black dashed circle. The already present subgap state then proceeds to cross zero energy and moves back up to the same approximate energy as initially. In Fig. (d), a MBS initially at zero energy, splits off from zero when the dot level becomes resonant. The two anti-cross and the MBS returns to zero energy, resulting in a "diamond shaped" splitting pattern.

The simulated data is shown in Fig. 5.9 (e-i). In Fig. (e), we see the magnetic field dependence of the differential conductance at $\mu_{\mathrm{NW}} = 0$ meV. As the magnetic field is increased from zero, an ABS separates from the higher energy ABSs and moves toward zero. A MBS develops around $B = 1\,\mathrm{T}$ and performs two small oscillations close to zero before the bulk gap closes. The μ_d dependence of the spectrum is computed at four magnetic fields $B = 0, 0.4, 1.35, 1.8\,\mathrm{T}$. This is shown in Figs. (f-g), where Figs. (f-h) correspond to the experimental situations shown in Figs. (b-d), respectively. $B = 0$ and $0.4\,\mathrm{T}$ are in the trivial phase and $B = 1.35$ and $1.8\,\mathrm{T}$ are in the topological phase. The large range of μ_d is chosen to show the case of both dot spin states crossing the nanowire levels. Here we see that there are some differences between the two spin states coming into resonance. In general, the first state exhibits a lower peak intensity and a smaller anti-crossing compared to the second. At $B = 0$ in Fig. (f), both dot levels move down from the induced gap and cross zero in the same way. At finite magnetic fields in Figs. (g-i), where there is a nanowire single state present below the induced gap, the dot levels form an anti-crossing with the subgap state upon resonance. Depending on whether the subgap state is initially at a non-zero or close to zero energy when the dot levels are not resonant, the subgap state displays two different behaviors when a dot level becomes resonant. If the subgap state is initially at a non-zero energy, it will form a "bowtie" crossing, as seen in Figs. (g) and (i). If the subgap state is initially close to zero energy, it will split off from zero as the dot level comes into resonance and moves back to zero again after the resonance is passed, forming an eye-like or "diamond" shape, as seen in Fig. (h). In Fig. (h), the MBS shows a larger energy splitting when the second state becomes resonant compared to the first. In Fig. (g), there is an apparent asymmetry in the two anti-crossings by the first state, while the second state has a more symmetric anti-crossing, but still slightly asymmetric in the opposite direction. In Fig. (i), both zero crossings are shifted to the right of the center of the resonance, while in Fig. (g), the first is shifted right and the second to the left.

The difference in peak intensity and width of the anti-crossing indicates that the two dot spin states hybridize differently with the MBS, with the second state (spin down state) being more strongly hybridized with the MBS. In Fig. (g), the nanowire is still in the trivial regime, but the ABS is a precursor to a MBS and will have acquired some MBS character at this point.

In a similar model considered by Prada *et al.* [2017], the details of the bowtie and diamond shaped resonances are investigated as well as the differences between the resonances of the two different dot spin states. It was found that the MBSs at each end of the nanowire have

different spin cantings. The MBS closest to the dot has a larger spin down component and therefore hybridizes more strongly with the spin down dot state. The spin canting angle of the MBS may be extracted by comparing the size of the diamond shaped MBS splitting and the width of the anti-crossings of the two different dot spin levels. It is likely that the differences between the two dot spin level resonances we see in our model here are due to similar effects. We will however not pursue this matter further and instead turn our focus towards why the MBS energy splitting is affected by the dot level resonance.

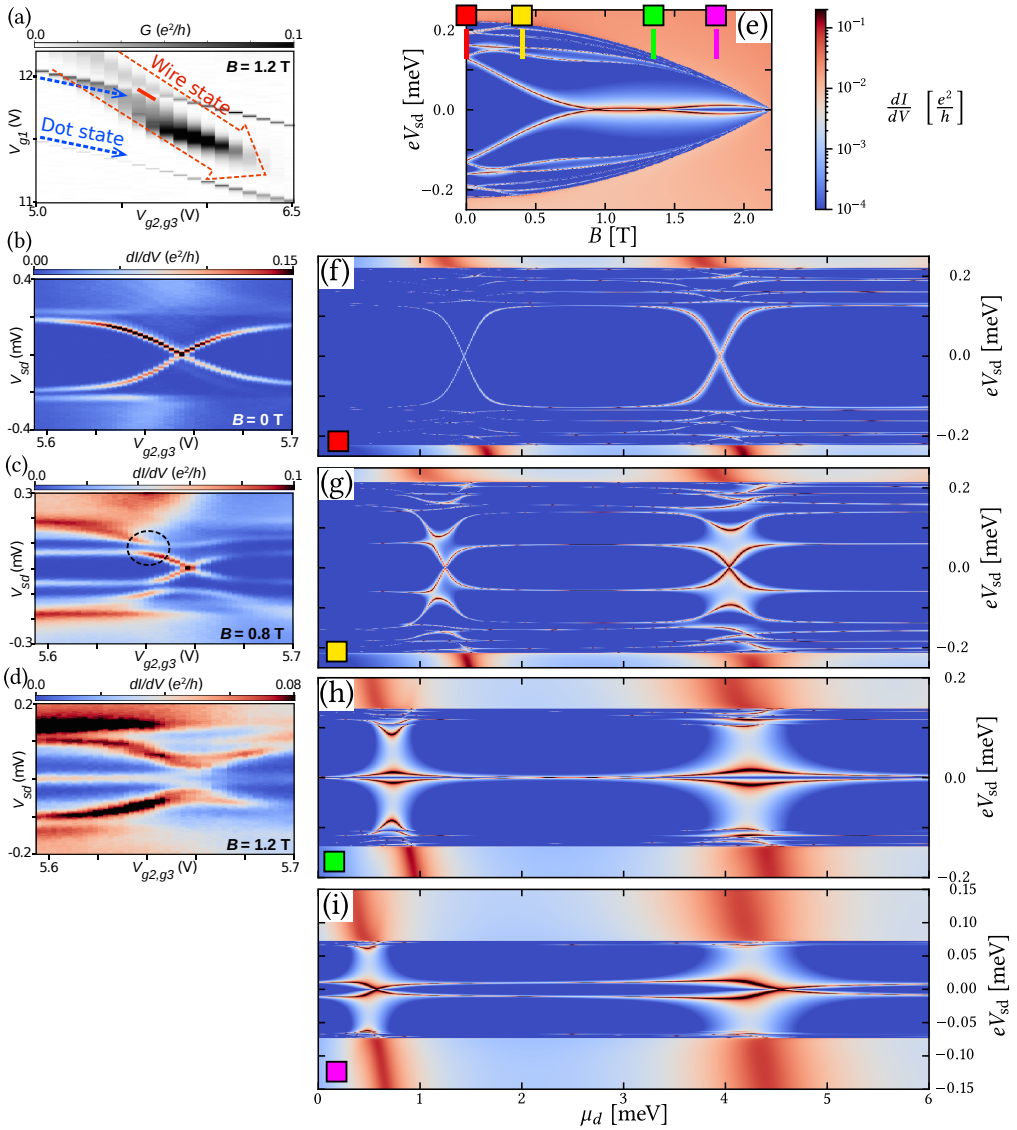

Figure 5.9: (a-d) Reproduction of the experimental data presented in [Deng *et al.*, 2016] Fig. 4. (a) A gate map of the zero bias conductance as a function of gate voltages V_{g1} and $V_{g2,g3}$ at $B = 1.2$ T similar to Fig. 5.7 (a). Blue dashed arrows denote the dot isopotential sweeping direction, and the red dashed arrow denotes the wire isopotential sweeping direction. (b-d) Differential conductance for different magnetic fields $B = 0$, 0.8 and 1.2 T as a function of V_{sd} and smart sweep of gate voltages along the line indicated by the solid red line in (a), where a dot level becomes resonant with the nanowire. (e-i) Data from simulations at chemical potential $\mu_{\mathrm{NW}} = 0$ meV corresponding to the intermediate density regime in the experimental data shown in (a-d). (e) Differential conductance as a function of V_{sd} and B and with $\mu_d = 2.5$ meV and $\gamma_W = 2$ meV. (f-i) Differential conductance as a function of V_{sd} and μ_d at different magnetic field strengths B =0, 0.4, 1.35 and 1.8 T as indicated by the colored squares in (e) and with $\gamma_W = 0.2$ meV.

Spatial profile of MBSs and dot level wavefunctions

The diamond shaped splitting of the MBS seen in Fig. 5.9 (h) is interpreted as a hybridization between the near-zero energy MBS and a dot level. The MBS partly leaks into the dot, which causes the effective overlap of the two end-state wavefunctions to change. In a finite nanowire, the actual splitting between the two MBSs is very sensitive to the details of their wavefunctions. A slight change in the wavefunctions on resonance can cause a significant change to the splitting. In order to explore this effect in more detail, we will in the following simulate a system with slightly different parameters, but where the observations still apply to the previous case.

The parameters that have changed from the simulation above are: The spin orbit coupling strength $\alpha_R = 20\,\text{meV nm}$, the height of the potential barrier $V_0 = 30\,\text{meV}$, the length of the dot $L_d = 80\,\text{nm}$, the length of the potential barrier $L_b = 16\,\text{nm}$, the length of the nanowire $L = 704\,\text{nm}$, The coupling to the parent superconductor $\gamma = 560\,\mu\text{eV}$, and the parent superconductor gap $\Delta(B) = 140\,\mu\text{eV}$ which we will take to be independent of the magnetic field in this case.

In Fig. 5.10, we investigate the spatial profile of the MBS wavefunction in the vicinity of a dot level resonance by simulating the differential conductance measured by a tunneling probe that is moved along the nanowire. In Fig. (a), the spectrum as a function of Zeeman field is shown, where the induced gap closes at $V_Z \approx 0.6\,\text{meV}$ and the topological phase emerges along with a MBS ZBP. The gap reopens at higher fields and the MBS oscillations increase in amplitude. In Fig. (b), we show the differential conductance as μ_d is varied in a range where the spin down dot level comes into resonance with the levels in the nanowire, at a Zeeman field $V_Z = 1415\,\mu\text{eV}$ that is well inside the topological phase and where the MBS splitting is close to zero when the dot level is not resonant. As the dot level comes into resonance, the MBS splits in a diamond-like shape, as was also shown in Fig. 5.9 (h). In Figs. (c-e), the differential conductance measured by a tunnel probe moved along the dot-barrier-nanowire setup is shown for three different values of dot potential corresponding to before, in the center of, and after resonance with the dot level. In the first and last case, the MBSs close to zero energy are located predominantly at the ends of the nanowire, which spans the setup from $z = 96$ to 800 nm. When the dot level is resonant, there are four subgap peaks (counting both positive and negative). These correspond to the hybridized dot level and the now split MBS where we see the wavefunction weight of the MBS has leaked into the dot and the dot leaked into the nanowire. We interpret the simultaneous shift of the MBS wavefunction and the increased MBS energy splitting as the shift of the wavefunction causes a change in the overlap between the MBSs.

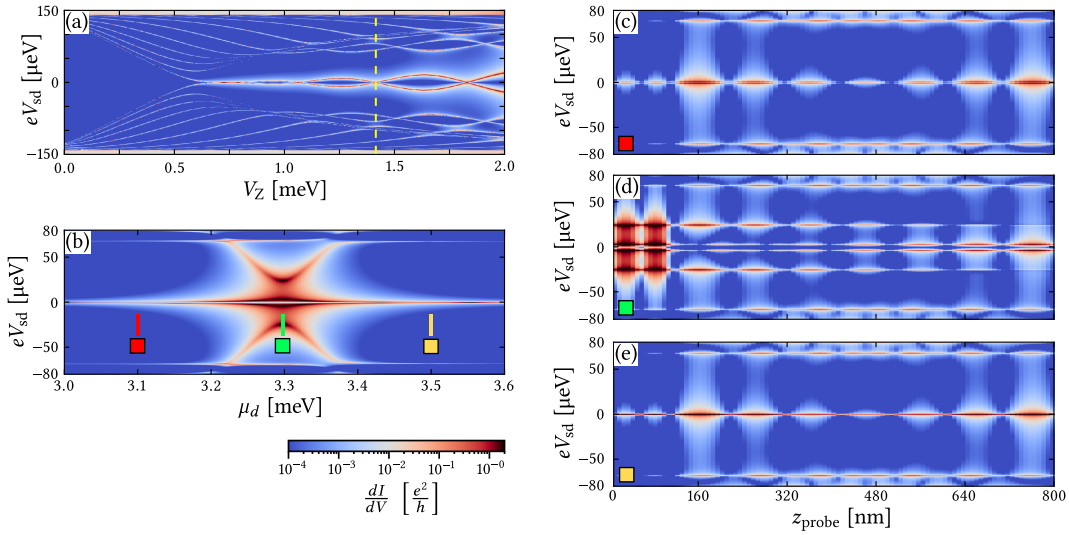

Figure 5.10: (a) Differential conductance as function of V_{sd} and Zeeman field V_Z measured by the tunneling probe connected at $z_{probe} = 96$nm, right where the barrier ends and the nanowire begins. The induced gap closes around $V_Z \approx 0.6$ meV where a MBS is formed at zero bias. The dashed yellow line indicates the value of V_Z where (b-e) are taken. The gap reopens at higher fields and the MBS energy oscillations increase in amplitude. Other parameters are $\gamma_W = 2$meV, $\mu_d = 2.5$meV. (b) Differential conductance as a function of V_{sd} and μ_d at $V_Z = 1415\,\mu$eV as measured by a tunneling probe connected at $z_{probe} = 0$ nm with coupling strength $\gamma_W = 0.1$ meV. In this range of μ_d the spin down dot level comes into resonance with the nanowire. The three colored squares indicate the values of μ_d where (c-e) are taken. (c-e) Differential conductance as the tunneling probe is moved along the dot-barrier-nanowire setup, for three different values of the dot potential $\mu_d = 3.1, 3.3$, and 3.5 meV corresponding to before, in the middle of, and after resonance with the dot level. Tunnel coupling to the probe is $\gamma_W = 0.03$ meV.

Hybridization dependence on MBSs overlap

In order to further support this interpretation, we consider cases where the MBSs have different degrees of overlap. The overlap of the MBSs depends on the Zeeman field and is smallest just after the topological phase transition, while it becomes larger as the Zeeman field is increased, hence the increasing energy splitting oscillations[2]. In the limit of a large Zeeman field, the MBS localization length is given by $\xi \approx \frac{\hbar^2 V_Z}{m\alpha_R \Delta_0}$ [Klinovaja and Loss, 2012; Das Sarma *et al.*, 2012], which sets the exponential decay length of the wavefunction envelope of each MBS away from the ends of the nanowire. Although the overlap of the two MBS wavefunctions grows with increasing Zeeman field, the MBSs energy splitting does not grow monotonically, but rather oscillates around zero with increasing amplitude. This is due to the different components of the two MBS wavefunctions oscillating in and out of phase with each other. At specific Zeeman fields where the components of the MBSs wavefunctions are completely out of phase, the energy splitting goes to zero, even though the wavefunctions still overlap in space. These points are fine tuned and small changes to their wavefunction will result in a non-zero energy splitting. The greater the overlap, the greater the splitting generated by a small change of the wavefunctions. However, the splitting is still bounded by the overlap of the wavefunctions, which is exponentially suppressed by the localization length and the distance between the MBSs. So by being able to make this bound smaller, the need to fine tune to zero energy splitting goes away.

In Fig. 5.11 we investigate the effect of increasing the MBS overlap. We choose four values of Zeeman field where the energy splitting of the MBSs vanishes, indicated by the colored squares in Fig. (a) and consider the energy splitting of each of them when a dot level comes into resonance with the MBS. In Figs. (b-e), we see that larger V_Z result in a larger diamond shaped splitting of the MBSs when the dot level becomes resonant, in agreement with the discussion above.

2. The MBSs wavefunctions also depend on all other model parameters, but we focus on the dependence on Zeeman field here.

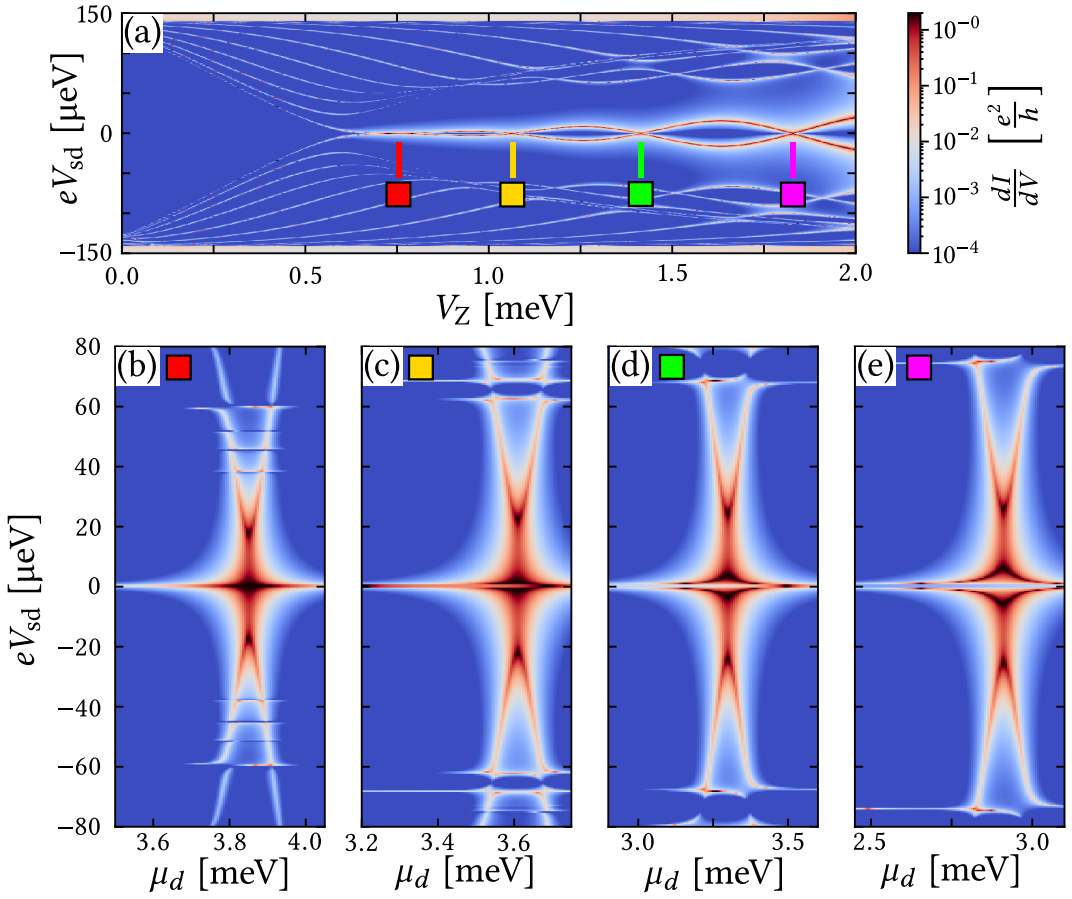

Figure 5.11: (a) Same as in Fig. 5.10(a), see details there. The colored squares mark the values of V_Z where (b-e) are taken. (b-e) Differential conductance as function of V_{sd} and μ_d for the values V_Z = 755, 1065, 1415 and 1830 T in the range of μ_d where the spin down dot level is resonant with the nanowire. The tunnel coupling to the lead is $\gamma_W = 0.1$ meV and the probe connected at $z_{probe} = 0$ nm.

Hybridization dependence on potential barrier height

Lastly, we investigate how changing the potential barrier height affects the diamond shaped splitting when the dot level is resonant. In Fig. 5.12 (a-d), we see the differential conductance as μ_d is varied across the resonance with the dot spin down state for different potential barrier heights. As the height of the barrier becomes lower, the hybridization of the dot level and the MBS becomes stronger, seen as the width of the anti-crossing between the dot level and the MBS becomes larger. The maximum energy splitting of the MBSs on resonance also becomes larger as the barrier height becomes smaller. In the case of no barrier $V_0 = 0$, we see a very different behavior. In Fig. (e), the spectrum for a wider range of μ_d is shown. In the case of no potential barrier between the nanowire and the dot, there is nothing to confine the wavefunctions in the nanowire. The MBS wavefunction is always leaking into the dot and is affected continuously as μ_d is changed. The MBS energy splitting is mainly around the value set by the overlap of the wavefunction, occasionally crossing zero energy when μ_d reaches a value where another bound state is accommodated in the dot and the parity of the dot-nanowire system changes parity. In the case of no potential barrier, the notion of separating the system into a dot and a nanowire part does not really make sense and the two should rather be viewed as a nanowire with a non-superconducting segment at the end. Even though this situation does not seem to apply to the observed dot behavior in the experiment above, it is relevant to consider, as it may host trivial low-energy ABS states that give rise to MBS-like features in the differential conductance. We will return to this case in Chap. 9.

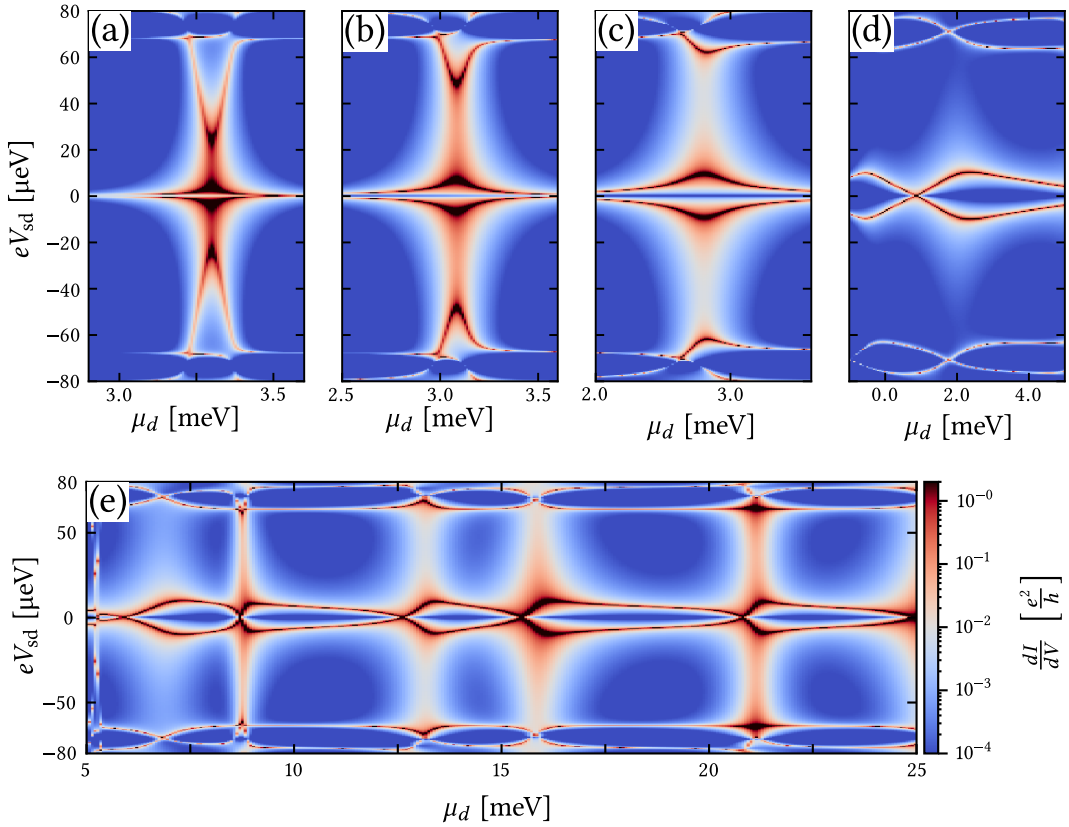

Figure 5.12: Differential conductance as a function of V_{sd} and μ_d in a range where the dot spin down state is resonant with the nanowire. (a-d) uses different heights of the potential barrier V_0 = 30, 15, 7.5 and 0 meV and Zeeman fields V_Z = 1415, 1405, 1385 and 1300 μeV. (e) Same as (d) but for a different range of μ_d. The coupling strength to the lead is $\gamma_W = 0.1\,\text{meV}$.

5.3 Summary

In this chapter, we have introduced a theoretical model of a quantum dot-potential barrier-nanowire setup and discussed its ability to explain the experimental observations in [Deng *et al.*, 2016]. Model parameters were extracted from the experiment and the numerical simulations showed a large degree of qualitative agreement with the experimental data. The observed diamond shaped energy splitting of the MBS which occurred when a dot level became resonant with a non-split MBS was reproduced by the simulation. By further studying the numerical model, it was found that the splitting of the MBS upon resonance with a dot level is due to a change in the MBS wavefunction resulting in the MBS leaking into the dot when the dot level is resonant. It was found that the size of the energy splitting depends on the coupling strength between the resonant dot level and the MBS, but is bounded by the energy splitting set by the overlap of the MBSs wavefunctions.

Chapter 6

Conductance Spectroscopy on Majorana Wires and the Inverse Proximity Effect

> “Not only is the Universe stranger than we think, it is stranger than we can think.
>
> Werner Heisenberg, *Across the Frontiers*

This chapter is almost entirely a reproduction of the work presented in [Danon et al., 2017] with minor changes in order to relate and conform to the rest of the thesis.

As was mentioned in the introduction in Chap. 1, the pioneering experiments using electron tunneling spectroscopy into one end of SC-SM hybrid nanowires have reported observations that speak both in favor and against the presence of Majorana bound states in the nanowires. Although a field-dependent zero-bias anomaly in the conductance was a commonly observed phenomenon at high enough magnetic fields [Mourik *et al.*, 2012; Deng *et al.*, 2012; Das *et al.*, 2012; Churchill *et al.*, 2013], several other observations were less compatible with an interpretation in terms of an emerging topological phase. These “inconsistencies” included the zero-bias peak in the differential conductance being much smaller than the predicted value of $2e^2/h$ and the absence of a clear gap closing at the phase transition.

A wave of theoretical work aimed at understanding the discrepancies followed in the wake of the experiments. Explanations that were consistent with having Majorana-like modes at the ends of the wire [Prada *et al.*, 2012; Rainis *et al.*, 2013; Mishmash *et al.*, 2016] as well as alternative “trivial” interpretations of the observed zero-bias features [Liu *et al.*, 2012; Kells *et al.*, 2012; Lee *et al.*, 2012] were put forward. In parallel, other “smoking-gun” features in the conductance spectrum were identified that could evidence a transition to a topological phase, a good candidate being the splitting of the zero-bias peak and subsequent characteristic oscillations of the low-energy modes as a function of magnetic field, due to finite-size effects [Das Sarma *et al.*, 2012; Rainis *et al.*, 2013].

In the years that followed, the quality of the experiments has steadily improved, mainly driven by advances in growth and fabrication techniques [Krogstrup *et al.*, 2015]. Today,

state-of-the-art experiments [Albrecht *et al.*, 2016; Deng *et al.*, 2016; Gül *et al.*, 2017] show quite compelling evidence for the existence of Majorana modes in these hybrid nanowires, but a few annoying discrepancies persist: (i) It is still very hard to measure a zero-bias peak that approaches $2e^2/h$ over a significant range of magnetic fields. (ii) In most experiments the expected "Majorana oscillations" as a function of magnetic field are absent. Recent experiments in the Coulomb-blockaded regime showed some oscillations [Albrecht *et al.*, 2016], but several of their characteristics do not fit current theory very well. (iii) The zero-bias peak is usually much broader than expected, often filling most of the (quite soft) topological gap.

Several recent theoretical works addressed these points and investigated many effects in detail, including the occupation of multiple subbands in the wire, finite temperature, the existence of low-energy Andreev bound states in the wire [Chiu *et al.*, 2017; Liu *et al.*, 2017b], electrostatic interactions between the electrons in the wire and the substrate [Domínguez *et al.*, 2017], a finite subgap density of states in the proximitizing superconductor [Stenger and Stanescu, 2017; Liu *et al.*, 2017a], and the presence of interfacial tunnel barriers and dissipation [Liu *et al.*, 2017c]. A general trend is that the more ingredients are added to the model the better the theory can be made to resemble the experimental observations.

In this chapter, we focus on one particular ingredient present in many experiments, which has been addressed only indirectly so far. Inspired by the difference in behavior of the wires in the Coulomb-blockaded regime (where Majorana-like oscillations were observed) and in the transport regime (where the oscillations are mostly absent), we propose that the presence of a second normal metal contact, usually connected as a drain lead to the superconductor, is a part of the setup that should be taken seriously. Depending on the strength of the coupling to this drain (weak in the blockaded regime, stronger in a transport setup), it can induce a finite subgap normal density of states in the hybrid wire, a phenomenon known as the inverse proximity effect. The bound states in the wire, including the low-energy Majorana modes, can thus acquire a finite life time which can be expected to affect the appearance of the measured conductance spectrum. A crude way to account for the "leakage" into the normal drain is to add an imaginary part to the electronic energies in the superconductor, resulting in a broadening of all levels [Liu *et al.*, 2017a; Stenger and Stanescu, 2017; Das Sarma *et al.*, 2016]. Although this does produce a finite subgap density of states in the system, it does not provide a straightforward way to investigate any details related to the device geometry or the nature of the coupling between the drain and the wire.

Below, we present a detailed theoretical investigation of the effects of such a drain contact and we show how the results can indeed differ qualitatively depending on the geometry of the device and on the coherence properties of the superconductor. The setup we will mainly have in mind is shown in Fig. 6.1 (a): A semiconducting nanowire is proximitized by an epitaxially grown thin layer of superconductor, shown in blue. A tunnel barrier (gray) in an uncovered part of the wire at the left end connects the proximitized region to a tunnel probe (the source contact 'S'). A second normal lead (marked 'D') is directly deposited onto the superconducting layer and serves as drain for transport measurements.

We model electronic transport in the superconductor (and in the drain lead) as being diffusive. Although the actual mean free path in the superconductor (the distance between impurity scattering events) is probably not much shorter than all relevant device dimensions in most experiments, the surface of the superconductor on the outside (which usually forms an interface with an oxide layer) is known to be rough and can be expected to randomize the electrons' momentum each time they scatter off this surface. We thus assume that we can use the thickness of the superconductor (typically 5–20 nm) as effective mean free path, which can justify employing a diffusion approximation.

The rest of this chapter is organized as follows: We will first present a numerical

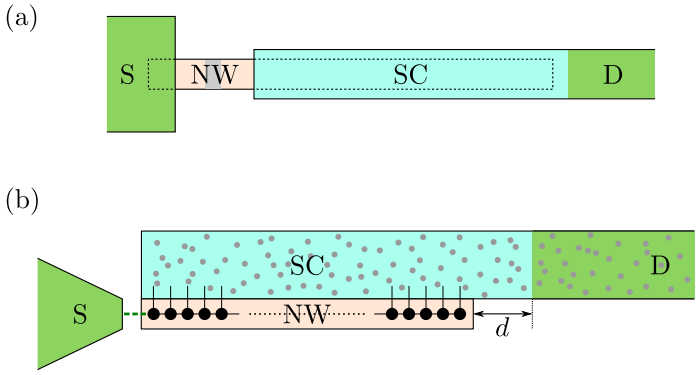

Figure 6.1: (a) Schematic of a commonly used setup for conductance spectroscopy experiments. The nanowire (marked 'NW') is contacted on one side by a tunnel probe (marked 'S') and is (partly) covered by an epitaxially grown *s*-wave superconductor layer (marked 'SC'), which proximitizes part of the wire. This superconducting layer is connected to a normal metal drain lead (marked 'D') through which the conductance is measured. (b) Sketch of the tight-binding model used for numerical calculations. The electron dynamics in the wire are discretized on a finite chain and the presence of the superconductor is included by adding a self-energy term in the electronic Green function. We treat the superconductor as being part of a diffusive SN-junction, where the junction interface is located a distance d away from the nanowire.

study of the conductance spectrum of the system, where we treat the superconductor and the drain lead together as one diffusive SN-junction. We will show how an efficient SN-coupling can be responsible for a quenching of the Majorana oscillations in the conductance spectrum. The result is either a persistent zero-bias peak approaching $2e^2/h$ throughout the topological phase or a gradual suppression and smearing out of all features in the spectrum, depending on the ratio of the coherence length in the superconductor to the length of the proximitized region in the wire. We also investigate the apparent hardness of the gap on both sides of the phase transition and find that a strong influence of the normal drain tends to soften the gap in the topological regime. We then present a toy model where we only focus on the dynamics of the two low-lying (Majorana) modes. We assume the modes to be coupled to each other and also include an effective coupling of both modes to the states in the source and drain leads. From this simple model we derive an analytic expression for the differential conductance from source to drain. We show how this result allows to qualitatively reproduce the main findings from our numerical calculations and we explain how it provides more insight in the underlying physics.

6.1 Numerical tight-binding simulations

We perform numerical tight-binding simulations of the conductance spectrum, using the S-matrix formalism described in Chap. 3. The nanowire is described using the model from Sec. 2.4, but with a modified self-energy term due to the parent superconductor being diffusive and the presence of the normal drain lead. The parent superconductor is treated as being part of a diffusive SN-junction and we use approximate expressions for the semi-classical regular and anomalous Green functions in this junction [Belzig *et al.*, 1996] to derive an effective self-energy for the electrons in the nanowire. With this approach, the self-energy itself produces a finite subgap density of states and thus allows for leakage out of the wire into the normal part of the junction.

We model the system as sketched in Fig. 6.1(b). The nanowire (light red region marked 'NW') is described by a one-dimensional Bogoliubov-de Gennes Hamiltonian, $H_{\mathrm{NW}} =$

$\frac{1}{2}\int dx\, \mathbf{\Psi}^\dagger(x)\, \mathscr{H}_{\rm NW} \mathbf{\Psi}(x)$, written in terms of the Nambu spinors $\mathbf{\Psi}(x) = [\Psi_\uparrow(x), \Psi_\downarrow(x), \Psi_\downarrow^\dagger(x), -\Psi_\uparrow^\dagger(x)]^T$, where the field operator $\Psi_\sigma^\dagger(x)$ creates an electron with spin σ at position x. Explicitly, we use the Hamiltonian

$$\mathscr{H}_{\rm NW} = \left(-\frac{\hbar^2}{2m^*}\partial_x^2 - \mu - i\alpha_{\rm R}\partial_x\sigma_y\right)\tau_z + V_{\rm Z}\sigma_z, \tag{6.1}$$

where the Pauli matrices $\boldsymbol{\sigma}$ and $\boldsymbol{\tau}$ act in spin space and particle-hole space respectively. Furthermore, m^* is the effective mass of the electrons in the wire, μ is their chemical potential, $\alpha_{\rm R}$ is the Rashba spin-orbit strength, and $V_{\rm Z}$ is the magnitude of the Zeeman splitting in the wire.

We discretize this Hamiltonian on $N = 100$ lattice sites and write for the retarded electronic Green function on this chain

$$G^R(n, m; \epsilon) = \left[\frac{1}{\epsilon - \mathscr{H}_{\rm NW} - \Sigma_{\rm SC}^R(\epsilon) + i0^+}\right]_{n,m}, \tag{6.2}$$

where 0^+ is a positive infinitesimal and $\Sigma_{\rm SC}^R(\epsilon)$ is the self-energy due to the coupling to the superconductor, which we will derive below. The differential conductance is then calculated using the method described in Chap. 3. From this Green function we calculate the reflection matrix of the hybrid wire,

$$\begin{aligned} R(\epsilon) &= \begin{bmatrix} r_{\rm ee}(\epsilon) & r_{\rm eh}(\epsilon) \\ r_{\rm he}(\epsilon) & r_{\rm hh}(\epsilon) \end{bmatrix} \\ &= 1 - 2i\pi W^\dagger \left\{\left[G^R(\epsilon)\right]^{-1} + i\pi W W^\dagger\right\}^{-1} W, \end{aligned} \tag{6.3}$$

where the amplitudes $r_{\rm ee(hh)}$ describe normal electron(hole) reflection and the off-diagonal amplitudes $r_{\rm eh,he}$ describe Andreev reflection. The matrix

$$W = \sqrt{\gamma_W}\,(\mathbf{s}_1 \otimes \mathbb{1}_4)^T, \tag{6.4}$$

models the coupling between the probe lead and the first site of the chain. Here, γ_W parametrizes the coupling strength, $\mathbb{1}_4$ is a 4×4 unit matrix, and the N-dimensional vector $\mathbf{s}_1 = (1, 0, 0, 0, \dots)$ specifies the position of the probe along the chain. The resulting reflection matrix allows us to calculate the differential conductance as

$$\frac{dI}{dV} = \frac{e^2}{h}\mathrm{Tr}\left[1 - r_{\rm ee}(\epsilon)^\dagger r_{\rm ee}(\epsilon) + r_{\rm eh}(\epsilon)^\dagger r_{\rm eh}(\epsilon)\right], \tag{6.5}$$

where we set $\epsilon = eV$, in terms of the bias voltage V on the tunnel probe.

The task left is to find a suitable self-energy $\Sigma_{\rm SC}^R(\epsilon)$ that accounts for the diffusive nature of the superconductor as well as the presence of a normal drain lead. We assume the Fermi wavelength inside the superconductor to be by far the shortest length scale in the problem, which allows us to use a local self-energy

$$\Sigma_{\rm SC}^R(x; \epsilon) = \tilde{t}^2 G_{\rm SC}^R(x, x; \epsilon), \tag{6.6}$$

in terms of the electronic Green function inside the superconductor $G_{\rm SC}^R$ that connects the point x at the superconductor-wire interface with itself (for simplicity we assume the coupling parameter $\tilde{t}$ to be real and constant along the wire). The elements of $\Sigma_{\rm SC}^R$ thus follow straightforwardly from the electron, hole, and anomalous Green functions in the superconductor.

To find these Green functions, we assume that the SN-junction is in the dirty (diffusive) limit and that we can describe the relevant electron dynamics in the junction using a semi-classical approximation, i.e., we assume that both the electronic mean free path and the Fermi wave length in the junction are much smaller than all relevant length scales in the wire. The semi-classical Green functions then obey the Usadel equation [Eilenberger, 1968; Usadel, 1970], which one can solve for the SN-junction, assuming no interface barrier and setting the order parameter $\Delta(\mathbf{r})$ to a constant $-i\Delta$ inside the superconductor and to zero in the normal metal [Kuprianov and Lukichev, 1988; Belzig *et al.*, 1996]. By doing so, one ignores the requirement for self-consistency of $\Delta(\mathbf{r})$, and in that sense the result must be seen as a lowest-order approximation, which is expected to introduce quantitative errors but not to affect the result in a serious qualitative way.

The solution for the semi-classical electronic and anomalous Matsubara Green functions presented in Ref. [Belzig *et al.*, 1996] uses the angular parametrization

$$g^{\mathrm{ee}}(x,\epsilon) = \cos\theta(x,\epsilon), \tag{6.7}$$

$$f^{\mathrm{eh}}(x,\epsilon) = \sin\theta(x,\epsilon), \tag{6.8}$$

where the position-dependent angle θ reads explicitly

$$\theta(x,\epsilon) = \begin{cases} 4\arctan\left\{e^{-(x/\xi_{\mathrm{N}})\sqrt{-i\epsilon/\Delta}}\tan\left(\frac{1}{2}\arctan\beta\right)\right\} & \text{for } x > 0, \\ -\arctan\frac{\Delta}{i\epsilon} + 4\arctan\left\{e^{(x/\xi_{\mathrm{S}})\sqrt[4]{1-(\epsilon/\Delta)^2}}\right. & \\ \quad \left.\times\tan\left(\frac{1}{2}\arctan\beta + \frac{1}{4}\arctan\frac{\Delta}{i\epsilon}\right)\right\} & \text{for } x \le 0, \end{cases} \tag{6.9}$$

assuming that the SN-interface is at $x = 0$ with the superconducting region at $x \le 0$. We used the notation

$$\beta = -\sin\left(\frac{1}{2}\arctan\frac{\Delta}{i\epsilon}\right)\left[\kappa\frac{\sqrt{-i\epsilon}}{\sqrt[4]{\Delta^2-\epsilon^2}} + \cos\left(\frac{1}{2}\arctan\frac{\Delta}{i\epsilon}\right)\right]^{-1}, \tag{6.10}$$

and introduced the quantities

$$\xi_{\mathrm{N,S}} = \sqrt{\hbar D_{\mathrm{N,S}}/2\Delta}, \tag{6.11}$$

$$\kappa = \sigma_{\mathrm{N}}\xi_{\mathrm{S}}/\sigma_{\mathrm{S}}\xi_{\mathrm{N}}, \tag{6.12}$$

with $D = \frac{1}{3}v_{\mathrm{F}}l_e$ the electronic diffusion constant in terms of the electronic mean free path l_e, and σ the normal-state conductivity, which both can be different in the normal and superconducting regions. For a detailed derivation, see App. A.

This allows us to derive straightforwardly a (position-dependent) self-energy for the electrons in the wire due to the proximity of the SN junction:

$$\Sigma^R_{\mathrm{SC}}(x,\epsilon) = \zeta\Big[\sin\theta(x,\epsilon)\tau_y - i\cos\theta(x,\epsilon)\Big], \tag{6.13}$$

where the parameter ζ characterizes the coupling between the wire and the junction. (Note that this self-energy is diagonal in the coordinate basis.) The energy ϵ could be given a finite imaginary part $\epsilon \to \epsilon + i\Gamma_{\mathrm{in}}$ in to account for inelastic scattering processes in the diffusive junction, which would introduce an extra broadening that smears out all features in the conductance spectrum. In all of the following, however, we disregard these processes and we set $\Gamma_{\mathrm{in}} = 0^+$.

Setting $\kappa \to 0$ corresponds to setting the conductivity of the normal part of the junction to zero. This should effectively remove the inverse proximity effect caused by the normal part, and make the self-energy reduce to that of a bulk superconductor. One can check that in

the limit of $\kappa \to 0$ we have $\arctan(\Delta/i\epsilon) = 2\arctan\beta$, which yields $\theta(x,\epsilon) = \arctan(\Delta/i\epsilon)$. This indeed produces a position-independent self-energy $\Sigma^R_{\mathrm{SC}}(\epsilon)$ identical to the self-energy one finds for a clean bulk superconductor [Stanescu *et al.*, 2011; Hansen *et al.*, 2016]. The further κ increases, the more the self-energy deviates from this "clean" self-energy.

We note that also in the limit $|x/\xi_{\mathrm{S}}| \gg 1$ the self-energy reduces to that of the clean bulk superconductor: The coherence length ξ_{S} thus determines how far from the SN interface the normal-metal part still has a significant influence on the electron dynamics inside the superconductor. To illustrate this, we calculate the position-dependent density of states in the junction, $\nu(x,\epsilon) = \nu_{\mathrm{N}} \operatorname{Re}[g^{\mathrm{ee}}(x,\epsilon)]$, obtained from analytically continuing the Green function (6.7), where ν_{N} is the density of states at the Fermi level in the normal state (assumed the same in the whole junction). In Fig. 6.2 we show the result at $\epsilon = \Delta/2$ for three different coupling parameters: $\kappa = 0.2$ (green), $\kappa = 1$ (red), and $\kappa = 5$ (blue). The inverse proximity effect clearly weakens with decreasing κ, but becomes always exponentially suppressed when x exceeds the coherence length ξ_{S}.

We can now calculate the differential conductance of the system using Eqs. (6.3)–(6.5), where the self-energy matrix is defined by $\left[\Sigma^R_{\mathrm{SC}}(\epsilon)\right]_{n,m} = \Sigma^R_{\mathrm{SC}}(x_n,\epsilon)\delta_{n,m}$ at position x_n, corresponding to the location of site n on the chain of the tight-binding discretization.

In all numerical simulations in this section we use $m^* = 0.026 m_e$, corresponding to the value for bulk InAs at room temperature, $\mu = 0$, $\alpha_{\mathrm{R}} = 10$ μeV μm, $\Delta = 180$ μeV, $\zeta = 720$ μeV, and $\gamma_W = 890$ μeV. The length of the wire is set to $L = 0.9$ μm, resulting with $N = 100$ in a lattice constant $a = 9$ nm, which is used to derive the tight-binding hopping matrix element $t = \hbar^2/2m^*a^2$ and spin-orbit-induced "spin-flip" nearest-neighbor coupling $s = \alpha_{\mathrm{R}}/2a$.

For simplicity we set the distance d between the SN-interface and the right end of the nanowire to zero. In this case we could expect different behavior depending on the parameter ξ_{S}/L: When $\xi_{\mathrm{S}} \lesssim L$ the drain will mainly affect the right end of the wire, and thus primarily couple to the right Majorana mode (when in the topological regime). If, however, $\xi_{\mathrm{S}} \gtrsim L$ then we expect a stronger, more homogeneous effect which will affect both Majorana modes more equally [1]. For a typical experimental setup, we make the following

1. This limit will also more closely resemble a situation where the superconductor is not epitaxially grown but rather deposited in bulk onto the nanowire. In this case the influence of the normal drain is not necessarily expected to be stronger on one particular side of the wire. Such a geometry was more common in the first generation of experiments.

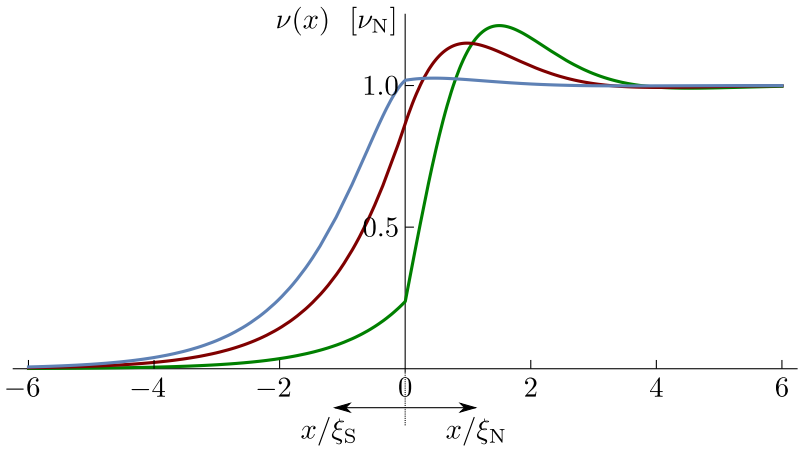

Figure 6.2: The position-dependent density of states $\nu(x,\epsilon)$ at energy $\epsilon = \Delta/2$ in a diffusive SN-junction, calculated from the electronic Green function (6.7). We used $\kappa = 0.2$ (green), $\kappa = 1$ (red), and $\kappa = 5$ (blue).

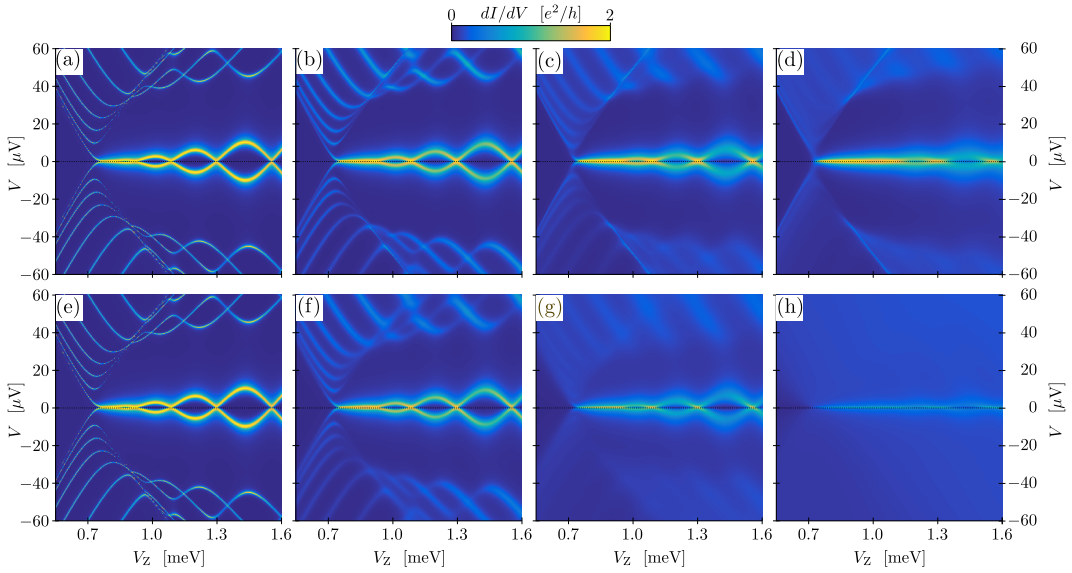

Figure 6.3: Calculated differential conductance as a function of Zeeman energy V_Z and applied bias voltage V on the probe lead, using a self-energy that includes the effect of a (diffusive) normal metal drain coupled to the (diffusive) superconductor. We assumed a setup as sketched in Fig. 6.1 where we set $d = 0$; all other parameters are given in the text. (a–d) With $L = 0.9\ \mu$m and $\xi_S = 0.1L$, we vary the coupling parameter κ: (a) $\kappa = 0$, (b) $\kappa = 0.2$, (c) $\kappa = 1$, and (d) $\kappa = 5$. (e–h) We keep $L = 0.9\ \mu$m and now set $\xi_S = L$, varying again the coupling parameter κ: (a) $\kappa = 0$, (b) $\kappa = 0.05$, (c) $\kappa = 0.2$, and (d) $\kappa = 1$.

very rough estimate: We assume the superconductor to be epitaxial aluminum and to have a thickness of ~ 10 nm. Setting $l_e = 10$ nm (assuming that the surfaces of the epitaxial layer are rough enough to randomize the electronic momentum after scattering from the surface) and using $v_F = 2 \cdot 10^6$ m/s and $\Delta = 180\ \mu$eV, we find $\xi_S \approx 100$ nm, which typically corresponds to $\xi_S/L \sim 0.1$. In case the superconductor would be clean and much thicker, effectively yielding $l_e \gtrsim L$, one should rather treat it as a ballistic medium. The presence of the normal drain lead can then still induce a finite subgap density of states inside the superconductor, but now the length scale over which this inverse proximity effect decays is probably set by the "clean" coherence length $\xi_0 \sim \hbar v_F/\Delta$. Then, depending on the ratio ξ_0/L one can still be in either of the regimes mentioned above and we can expect similar effects as in the diffusive case.

In Fig. 6.3 we show the calculated differential conductance, as a function of applied Zeeman field V_Z and bias voltage V, for two different coherence lengths ξ_S. In the first four plots (a–d) we set $\xi_S = 0.1L$ and we vary the coupling parameter κ: (a) $\kappa = 0$, (b) $\kappa = 0.2$, (c) $\kappa = 1$, and (d) $\kappa = 5$. In plots (e–h) we take a longer coherence length, $\xi_S = L$, and again vary the coupling κ: (e) $\kappa = 0$, (f) $\kappa = 0.05$, (g) $\kappa = 0.2$, and (h) $\kappa = 1$.

Roughly speaking, we see the following behavior: (i) For small ξ_S (small compared to L)—where the drain is expected to couple mainly to states living at the right end of the wire—the amplitude of the Majorana oscillations is suppressed with increasing κ, and they tend to collapse to a single zero-bias peak, which then approaches $2e^2/h$ again. (ii) For larger ξ_S—where the effective coupling to the drain is more uniform across the wire—the oscillations are again quenched, but now all features get smeared out and the conductance approaches $2e^2/h$ nowhere. (iii) In general the gap seems to be softer at higher fields (associated with the topological regime) than in the trivial regime; this effect appears more prominent for more uniform coupling (larger ξ_S).

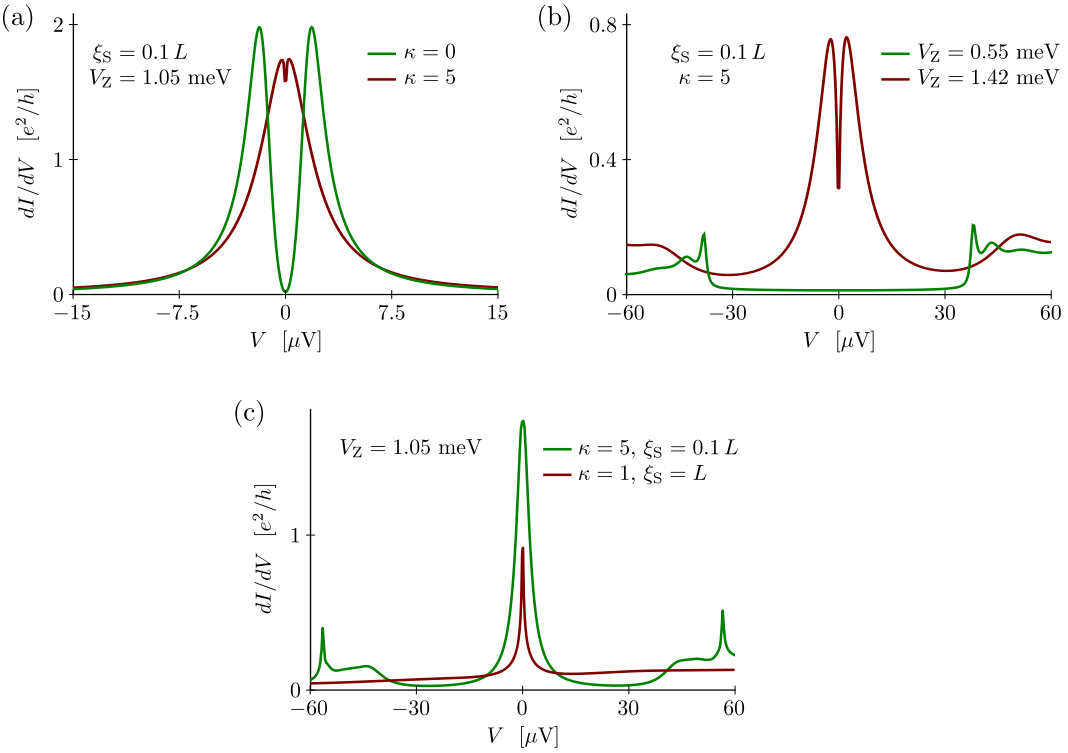

Figure 6.4: Line cuts from the differential conductance shown in Fig. 6.3. All choices of parameters are indicated in the plots.

We illustrate this in more detail in Fig. 6.4, where we present line cuts of the data of Fig. 6.3. In Fig. 6.4(a) we illustrate how the Majorana oscillations become suppressed and collapse to a zero-bias peak: We used $\xi_S = 0.1\,L$ (as in the upper row in Fig. 6.3), fixed $V_Z = 1.05$ meV (where the peak is clearly split at weak coupling), and show the differential conductance for $\kappa = 0$ (green) and $\kappa = 5$ (red). At strong coupling the splitting is indeed reduced, but the peak height is still close to $2e^2/h$. In Fig. 6.4(b), we show how the hardness of the gap can look different on opposite sides of the phase transition, when the coupling is strong: We have set $\xi_S = 0.1\,L$ and $\kappa = 5$, and show the conductance at $V_Z = 0.55$ meV (green, corresponding to the trivial phase) and $V_Z = 1.42$ meV (red, corresponding to the topological phase). The gap is clearly less hard in the high-field case, where the zero-bias feature has a width of the same order of magnitude as the gap. Finally, in Fig. 6.4(c) we compare the peak heights in the strong-coupling limit for $\xi_S = 0.1\,L$ (green) and $\xi_S = L$ (red), both at $V_Z = 1.05$ meV. This confirms that for longer ξ_S (a more homogeneous influence of the normal drain) not only the oscillations become quenched, but also the actual peak heights are suppressed.

6.2 Analytic toy model

We will now try to develop a better understanding of the results presented in the previous section. To this end, we will use a simple toy model to describe the spectroscopy setup, including the influence of a normal lead connected to the proximitizing superconductor, and we will focus on the low-energy features in the spectrum (the zero-bias peak and the Majorana oscillations).

The model we will use is sketched in Fig. 6.5: We assume that the nanowire is in the topological regime and that the gap separating the lowest-lying modes from all other states

is much larger than all energy scales relevant for the dynamics of these modes. In this case, we can project our description to this low-energy subspace and treat the hybrid wire (the blue region marked 'TS') as an effective two-level system of localized Majorana modes (indicated by the two $\hat{\gamma}$'s). The probe lead is tunnel coupled to the left Majorana mode, and also has a finite but weaker coupling to the right mode, due to the finite length of the wire. The normal metal contact connected to the superconductor is modeled as a second lead which is tunnel coupled to both Majorana modes and is assumed to be at the same chemical potential as the superconductor.

To calculate the differential conductance dI/dV of this system, we proceed along the same lines as in Ref. [Flensberg, 2010]. We first write an effective Hamiltonian

$$\hat{H} = \sum_{\alpha=S,D} (\hat{H}_\alpha + \hat{H}_{T,\alpha}) + \hat{H}_M, \tag{6.14}$$

where

$$\hat{H}_\alpha = \sum_{k,\sigma} \xi_{\alpha k\sigma} \hat{c}^\dagger_{\alpha k\sigma} \hat{c}_{\alpha k\sigma}, \tag{6.15}$$

describes the electrons in lead α,

$$\hat{H}_M = \frac{i}{2} \sum_{i,j=1,2} t_{ij} \hat{\gamma}_i \hat{\gamma}_j, \tag{6.16}$$

accounts for the coupling between the two Majorana modes, and

$$\hat{H}_{T,\alpha} = \sum_{k,\sigma,i} \left(V^*_{\alpha k\sigma i} \hat{c}^\dagger_{\alpha k\sigma} - V_{\alpha k\sigma i} \hat{c}_{\alpha k\sigma} \right) \hat{\gamma}_i, \tag{6.17}$$

describes the coupling between the Majorana modes and the electrons in lead α. The current from lead 'S' into the wire can then be expressed as

$$I = \frac{e}{\hbar} \sum_{k,\sigma,i} \left[V^*_{Sk\sigma i} G^<_{i,Sk\sigma}(0) - V_{Sk\sigma i} G^<_{Sk\sigma,i}(0) \right], \tag{6.18}$$

in terms of the mixed lead-wire lesser Green functions

$$G^<_{i,\alpha k\sigma}(t) = i\langle \hat{c}^\dagger_{\alpha k\sigma}(0) \hat{\gamma}_i(t) \rangle, \tag{6.19}$$

$$G^<_{\alpha k\sigma,i}(t) = i\langle \hat{\gamma}_i(0) \hat{c}_{\alpha k\sigma}(t) \rangle. \tag{6.20}$$

A lengthy but straightforward calculation then results in

$$\frac{dI}{dV} = \frac{2e^2}{h} \int d\omega\, M(\omega) \left[-n'_{\mathrm{F}}(\omega - eV) \right], \tag{6.21}$$

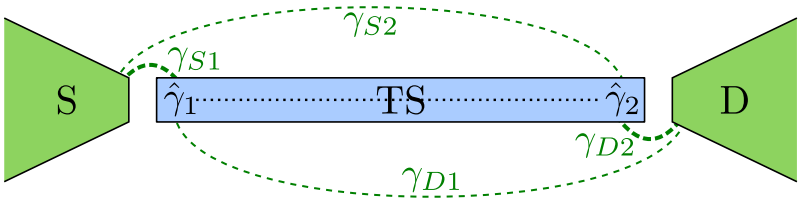

Figure 6.5: A toy model to include the effect of a (normal) drain lead connected to the superconductor proximitizing the nanowire. The hybrid nanowire is described in terms of a single low-energy fermionic bound state, which is split into two Majorana modes localized close to the ends of the wire.

where $n'_{\rm F}(x) = dn_{\rm F}(x)/dx$ is the derivative of the Fermi function, V is the voltage on the probe, and the spectral density $M(\omega) = A_{SS}(\omega) + \frac{1}{2}A_{DS}(\omega) + \frac{1}{2}T_{DS}(\omega)$, with

$$A_{\beta\alpha}(\omega) = \mathrm{Tr}\Big\{\mathbf{G}^R_\omega \mathbf{\Gamma}_\beta(-\omega)^* \mathbf{G}^A_\omega \mathbf{\Gamma}_\alpha(\omega)\Big\}, \tag{6.22}$$

$$T_{\beta\alpha}(\omega) = \mathrm{Tr}\Big\{\mathbf{G}^R_\omega \mathbf{\Gamma}_\beta(\omega) \mathbf{G}^A_\omega \mathbf{\Gamma}_\alpha(\omega)\Big\}, \tag{6.23}$$

describing respectively the probabilities of Andreev reflection and normal reflection, from lead α to lead β at energy ω. These probabilities are expressed in terms of the Majorana-lead coupling matrices

$$\Big[\mathbf{\Gamma}_\alpha(\omega)\Big]_{ij} = 2\pi \sum_{k\sigma} V_{\alpha k\sigma i} V^*_{\alpha k\sigma j} \delta(\omega - \xi_{\alpha k\sigma}), \tag{6.24}$$

and the Green function of the Majorana modes,

$$\mathbf{G}^R_\omega = \frac{2}{\omega - 2i\mathbf{t} + i[\mathbf{\Gamma}_\omega + \mathbf{\Gamma}^*_{-\omega}] - 2[\mathbf{\Lambda}_\omega - \mathbf{\Lambda}^*_{-\omega}]}, \tag{6.25}$$

where $\mathbf{t}$ is the Majorana coupling matrix and we used the notation $\mathbf{\Gamma}_\omega = \mathbf{\Gamma}_S(\omega) + \mathbf{\Gamma}_D(\omega)$ and introduced the matrix $\mathbf{\Lambda}_\omega = \mathbf{\Lambda}_S(\omega) + \mathbf{\Lambda}_D(\omega)$ with

$$\Big[\mathbf{\Lambda}_\alpha(\omega)\Big]_{ij} = \mathcal{P} \int \frac{dz}{2\pi} \frac{\Big[\mathbf{\Gamma}_\alpha(\omega)\Big]_{ij}}{\omega - z}. \tag{6.26}$$

For simplicity we now assume that we can neglect, over the range of all relevant energies, all energy- and spin-dependence of both the coupling elements $V_{\alpha k\sigma i}$ and the densities of states of the leads. This allows us to (i) simplify $[\mathbf{\Gamma}_\alpha]_{ij} = 2\pi V_{\alpha i} V^*_{\alpha j} \nu_\alpha$, where ν_α is the density of states at the Fermi level of lead α, and (ii) set $\mathbf{\Lambda}_\alpha(\omega) = 0$. If we furthermore assume that the lead-mediated Majorana-Majorana coupling will be dominated by the overlap-induced couplings t_{ij}, then the coupling matrices are real and diagonal,

$$\mathbf{\Gamma}_S = \begin{pmatrix} \gamma_{S1} & 0 \\ 0 & \gamma_{S2} \end{pmatrix} \quad \text{and} \quad \mathbf{\Gamma}_D = \begin{pmatrix} \gamma_{D1} & 0 \\ 0 & \gamma_{D2} \end{pmatrix}, \tag{6.27}$$

where $\gamma_{\alpha i}$ thus parametrizes the decay rate of Majorana mode i into lead α. For a not too short wire one usually has $\gamma_{S2} < \gamma_{S1}$. The magnitude of the "leakage" rates γ_{Di} to the drain as well as their ratio γ_{D1}/γ_{D2} depend on the actual geometry of the experimental setup, e.g. on how far from the wire the superconductor is contacted by a normal lead, but also on the detailed electronic dynamics inside the superconductor and the normal contact. We emphasize here that at this point these leakage rates γ_{Di} have turned into phenomenological parameters, which do not necessarily originate from the proximity of a normal drain lead: Leakage to any localized subgap state in the superconductor to which the two Majorana modes are coupled with (possibly) different strengths can be described using these model parameters.

Setting $\mathbf{t} = -i\sigma_y t_0/2$ we can now find an explicit expression for the spectral density,

$$M(\omega) = \frac{4G_{12}\omega^2 + 4G_{21}(t_0^2 + 4\Gamma_1\Gamma_2)}{\omega^4 - 2\Big(t_0^2 - 2[\Gamma_1^2 + \Gamma_2^2]\Big)\omega^2 + (t_0^2 + 4\Gamma_1\Gamma_2)^2}, \tag{6.28}$$

with $G_{ij} = \Gamma_1\gamma_{Si} + \Gamma_2\gamma_{Sj}$, and using the total Majorana decay rates $\Gamma_i = \gamma_{Si} + \gamma_{Di}$.

In the limit of zero temperature (which we will assume from now on for simplicity) the differential conductance thus reads

$$\frac{dI}{dV} = \frac{2e^2}{h} M(eV), \tag{6.29}$$

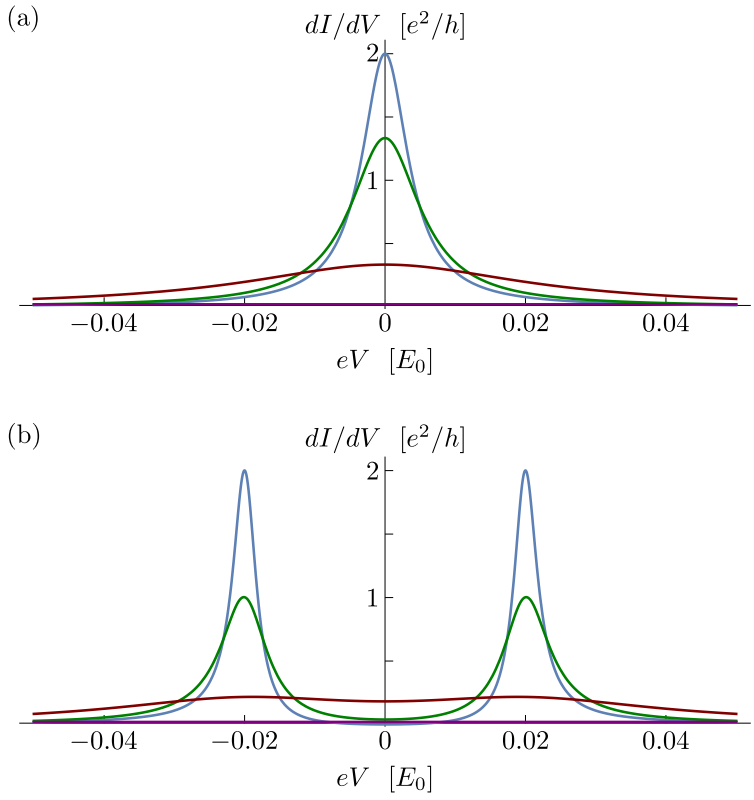

Figure 6.6: Differential conductance calculated using Eq. (6.29) with $\gamma_{S1} = 0.002\,E_0$ and $\gamma_{S2} = 0$, for (a) $t_0 = 0$ and (b) $t_0 = 0.02\,E_0$. We have set $\gamma_{D1} = \gamma_{D2} \equiv \gamma$ and we show the resulting conductance for $\gamma = 0$ (blue), $\gamma = 0.001\,E_0$ (green), $\gamma = 0.01\,E_0$ (red), and $\gamma = 0.2\,E_0$ (purple).

with $M(\omega)$ as given in Eq. (6.28).

Let us first investigate this result in the ideal case of a wire that is long enough so that t_0 and γ_{S2} can be neglected. In that limit the differential conductance,

$$\frac{dI}{dV} = \frac{2e^2}{h}\frac{4\gamma_{S1}\Gamma_1}{4\Gamma_1^2 + (eV)^2}, \tag{6.30}$$

acquires a Lorentzian line shape with a full width half maximum of $4\Gamma_1$ and a maximum conductance of $(2e^2/h)(\gamma_{S1}/\Gamma_1)$ at $V = 0$. We see that this zero-bias peak has a height of $2e^2/h$ as long as $\gamma_{D1} = 0$, i.e., as long as Majorana mode 1 (which is completely decoupled from mode 2) does not have a second normal channel into which it can decay. When γ_{D1} becomes finite, e.g. due to a superconductor-mediated coupling to a normal drain lead, the peak height is suppressed by a factor γ_{S1}/Γ_1. We illustrate this in Fig. 6.6(a), where we plot the differential conductance as given by (6.29) with $t_0 = 0$, $\gamma_{S2} = 0$, and $\gamma_{S1} = 0.002\,E_0$, in terms of the (arbitrary) energy scale E_0. We varied the coupling of Majorana mode 1 to the drain lead as $\gamma_{D1} = 0$ (blue), $\gamma_{D1} = 0.001\,E_0$ (green), $\gamma_{D2} = 0.01\,E_0$ (red), and $\gamma_{D1} = 0.2\,E_0$ (purple).

Another idealized limit is where the wire is short enough that t_0 cannot be neglected, but the probe lead is still coupled to mode 1 only and there is no effective leakage to a second normal contact at all, i.e. $\gamma_{S2} = \gamma_{D1} = \gamma_{D2} = 0$. In that case, Eq. (6.29) gives

$$\frac{dI}{dV} = \frac{2e^2}{h}\frac{4\gamma_{S1}^2(eV)^2}{t_0^4 - 2(t_0^2 - 2\gamma_{S1}^2)(eV)^2 + (eV)^4}, \tag{6.31}$$

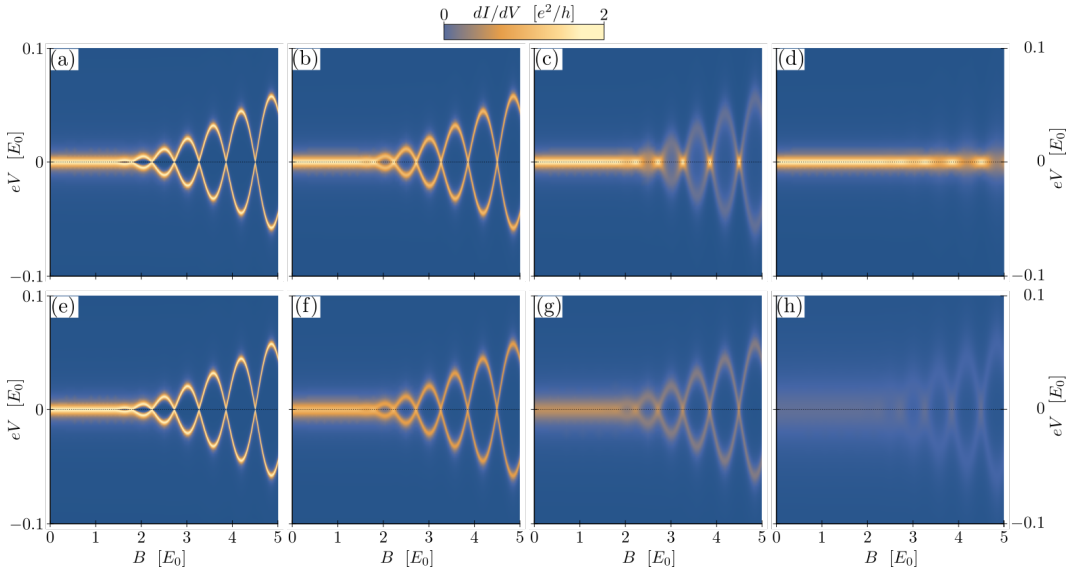

Figure 6.7: Differential conductance as a function of the bias voltage V and the applied magnetic field B, calculated using Eqs. (6.29) and (6.28) and using a B-dependent Majorana coupling energy $t_0(B)$ as given in Eq. (6.33). In all plots we have set $\gamma_{S1} = 0.002\,E_0$ and $\gamma_{S2} = 0$. (a–d) We set $\gamma_{D1} = 0$ and vary the coupling of the Majorana mode 2 to drain: (a) $\gamma_{D2} = 0$, (b) $\gamma_{D2} = 0.001\,E_0$, (c) $\gamma_{D2} = 0.01\,E_0$, and (d) $\gamma_{D2} = 0.2\,E_0$. (e–h) We set $\gamma_{D1} = \gamma_{D2} \equiv \gamma$ and vary this uniform coupling parameter: (a) $\gamma = 0$, (b) $\gamma = 0.001\,E_0$, (c) $\gamma = 0.003\,E_0$, and (d) $\gamma = 0.01\,E_0$.

which yields zero conductance at $V = 0$ and produces two peaks at $V = \pm t_0/e$ with a height of $2e^2/h$ and full width half maximum of $2\gamma_{S1}$, as expected. If we now add a finite coupling to the drain, the double-peak structure gets suppressed. This is illustrated in Fig. 6.6(b), where we again set $\gamma_{S1} = 0.002\,E_0$ and $\gamma_{S2} = 0$, but now use $t_0 = 0.02\,E_0$. The leakage rates to the drain are set equal, $\gamma_{D1} = \gamma_{D2} \equiv \gamma$, and are gradually increased from $\gamma = 0$ (blue), $\gamma = 0.001\,E_0$ (green), $\gamma = 0.01\,E_0$ (red), to $\gamma = 0.2\,E_0$ (purple).

In general, the function $M(eV)$ can have a single- or double-peak structure, depending on the relative magnitude of the Majorana coupling energy t_0 and the decay rates $\gamma_{\alpha i}$. For a given set of parameters, we find a single peak at $V = 0$ when

$$t_0^2 < t_c^2 \equiv 4\frac{\Gamma_1^3\gamma_{S2} + \Gamma_2^3\gamma_{S1}}{\Gamma_1(\gamma_{S1} + 2\gamma_{S2}) + \Gamma_2(2\gamma_{S1} + \gamma_{S2})}, \tag{6.32}$$

and the peak splits into two when $t_0^2 > t_c^2$. We see that t_c being non-zero depends on having a finite decay rate of Majorana mode 2: as long as $\Gamma_2 = 0$, which implies that $\gamma_{S2} = \gamma_{D2} = 0$, we have $t_c = 0$. From Eq. (6.32) it is thus clear how the effective coupling of the Majorana modes to normal metal leads—either to the tunnel probe itself or to a normal drain connected to the superconductor—can quench the split-peak behavior of the conductance at finite t_0. In the case of a proximitized semiconductor nanowire, where the effective coupling between the two low-energy modes is expected to oscillate as a function of the applied magnetic field, leakage to a drain lead can thus obscure the corresponding oscillatory pattern in the differential conductance.

To connect to the numerical results presented in Fig. 6.3, we show in Fig. 6.7 the conductance spectrum, as calculated from Eq. (6.29), as a function of both the bias voltage V and applied Zeeman field B. The effect of the field is implemented phenomenologically

by setting

$$t_0(B) = \frac{E_0}{\sqrt{b}} e^{-l/2b} \cos\left(l\sqrt{b}\right), \tag{6.33}$$

which corresponds to the coupling between the two Majorana modes due to the finite overlap of their wave functions, assuming for simplicity the large-B limit [Das Sarma *et al.*, 2012; Rainis *et al.*, 2013]. In this expression the Zeeman field $b = B/E_0$ is expressed in units of the (arbitrary) energy scale E_0 and the parameter l characterizes the length of the wire. By setting $l = L\sqrt{2mE_0}/\hbar$ (with L the actual length of the wire) and $E_0 = (2m\alpha^2\Delta^2/\hbar^2)^{1/3}$ (with $\alpha/\hbar$ the spin-orbit velocity and Δ the induced superconducting gap) one could connect these parameters to those used in more detailed models describing a semiconducting spin-orbit coupled nanowire in proximity to a superconductor [Das Sarma *et al.*, 2012]. We further assume that the wire is long enough so that we can neglect γ_{S2} and we investigate again the two different situations corresponding to the two rows in Fig. 6.3 (different coherence length ξ_S).

In Fig. 6.7(a–d) we set $\gamma_{D1} = 0$ and vary the coupling γ_{D2} of the right Majorana mode to the drain lead. This situation is expected to be more close to that of the top row of Fig. 6.3, where the coherence length $\xi_S = 0.1\,L$ was significantly smaller than the wire length, and the normal drain thus mainly affected states with most of their weight close to the right end of the wire.

We used (a) $\gamma_{D2} = 0$, (b) $\gamma_{D2} = 0.001\,E_0$, (c) $\gamma_{D2} = 0.01\,E_0$, and (d) $\gamma_{D2} = 0.2\,E_0$, and we see that increasing γ_{D2} again affects the appearance of the Majorana oscillations: For intermediate γ_{D2} the split-peak structure gets smeared out, and for large γ_{D2} ultimately all oscillatory behavior gets quenched and the conductance spectrum shows a single zero-bias peak that approaches $2e^2/h$, in a way very similar to what we found numerically in Fig. 6.3(a–d). To check, we evaluate from (6.32) the corresponding values for the critical Majorana coupling t_c, and find (a) $t_c = 0$, (b) $t_c = 0.001\,E_0$, (c) $t_c \approx 0.013\,E_0$, and (d) $t_c \approx 0.28\,E_0$. These values are indeed consistent with the global behavior seen in Fig. 6.7: The regions in Fig. 6.7(b–d,f–h) where $t_0(B) < t_c$, i.e., where the original splitting observed in Fig. 6.7(a,e) is smaller than t_c, indeed seem to be the regions where we see a single zero-bias peak instead of a split peak.

We can understand the behavior observed in Fig. 6.7(a–d) as follows: If Majorana mode 2 is the only mode coupled to the drain lead and the corresponding decay rate presents the largest energy scale in the model, then this rapid decay will prevent the two Majorana modes from hybridizing: All coherence built up between the two modes (which happens on the time scale $\hbar/t_0$) decays before it becomes significant (the decay happens on the time scale $1/\gamma_{D2}$). The Majorana modes thus become decoupled from each other if the decay is fast enough, and this brings us effectively to the situation where t_0 is zero and each Majorana mode is only coupled to the nearest lead. This explains why a single zero-bias peak of height $2e^2/h$ is recovered in Fig. 6.7(a–d) in the regime where $\gamma_{D2} \gtrsim t_0$.

An apparent difference between the numerical and analytical results is that the results in Figs. 6.3 (a-d) seem to show a gradual reduction of the amplitude of the oscillations with increasing coupling, whereas the analytic results in Figs. 6.7 (a-d) show a "fade out" of the oscillations without a reduction of their amplitude. We cannot say which detailed combination of ingredients reduces the apparent amplitude in Figs. 6.3 (a-d), but one important contribution is given by the energy dependence of the subgap normal density of states produced by Eqs. (6.7)-(6.10): there is always a dip in $\nu(x, \epsilon)$ on the superconducting side around $\epsilon = 0$ (cf. Fig. 3 in [Belzig *et al.*, 1996]), which yields a dip in the wire's conductance whenever the Majorana states are split. In a situation where the oscillations are almost fully faded out but the zero-bias peak is somewhat suppressed [e.g. comparable

to $B = 5E_0$ in Fig. 6.7 (d)], this extra dip at zero energy will indeed make the conductance peak look split, but with a smaller amplitude.

In Fig. 6.7(e–h) we try to reproduce the situation of the lower row of Fig. 6.3, where a longer coherence length $\xi_S = L$ resulted in a more homogeneous influence of the drain lead. To mimic this, we make the two couplings to the drain equal, $\gamma_{D1} = \gamma_{D2} \equiv \gamma$, and vary the parameter γ, using (e) $\gamma = 0$, (f) $\gamma = 0.001\,E_0$, (g) $\gamma = 0.003\,E_0$, and (h) $\gamma = 0.01\,E_0$. The results now indeed resemble more those shown in the lower row of Fig. 6.3: Increasing γ not only quenches the Majorana oscillations, but also suppresses the height of all conductance features. This results from Majorana mode 1 (the one probed by the source) now also being coupled to the drain and thus acquiring an effective life-time broadening.

In conclusion, our simple low-energy toy model thus shows how a finite leakage rate from the Majorana modes can quench the Majorana oscillations in the conductance spectrum. The result is either a persistent zero-bias peak or an overall broadening and suppression of all features in the spectrum, depending on the ratio of the leakage rates of the two modes. Similar phenomena are indeed commonly observed in experiments, even in very recent high-quality spectroscopy experiments [Deng *et al.*, 2016; Gül *et al.*, 2017]. The unexpected softness of the induced topological gap—another phenomenon often observed—is of course not captured here, since all dynamics on the energy scale of the gap and higher have been disregarded in this low-energy model.

6.3 Summary

Tunneling spectroscopy experiments on proximitized semiconducting nanowires, aimed at the detection of convincing signatures of Majorana modes, ultimately always involve a normal drain lead connected to the hybrid system. In this paper, we reported a detailed theoretical investigation of the effects on the conductance spectrum of the system if the contact to this normal lead is close enough to the nanowire to cause significant leakage from the low-energy modes in the wire.

We first presented numerical results, where we treated the proximitizing superconductor and the drain lead together as one diffusive SN junction. This yielded two qualitatively distinct types of behavior, depending on the relative strength of the leakage to the drain from the two ends of the wire: If leakage is only significant from one end of the wire, then increasing the coupling to the drain quenches the Majorana oscillations in the conductance spectrum and results in a prolonged zero-bias peak of almost $2e^2/h$. If, on the otherhand, leakage is equally strong from both ends, then increasing the coupling smears out and suppresses all features in the spectrum. We supported these results with the investigation of a simple toy model, which allowed us to derive analytic expressions for the conductance through the low-energy modes in the topological regime. These analytic results reproduced qualitatively all our main numerical findings and thereby provided more insight in the physics underlying the observed phenomena.

We thus conclude that several "inconsistencies" between experimental results and theoretical predictions, such as the commonly observed absence of Majorana oscillations in combination with a persisting zero-bias peak at higher magnetic fields, could, at least partly, be explained in terms of such leakage. The fact that the measured zero-bias peak usually is significantly lower than $2e^2/h$ is not necessarily inconsistent with our theory since we did not include finite temperature in our calculations [Nichele *et al.*, 2017]. The mechanisms described in this paper could indeed be expected to play an important role when the proximitizing superconductor is grown epitaxially on the wire and directly contacted by a normal lead [Deng *et al.*, 2016], and might be less significant if the superconductor is large and contacted by a normal lead far away from the wire [Zhang *et al.*, 2017]. We emphasize,

however, that any mechanism causing leakage from the bound states at the ends of the wire, irrespective of its detailed origin, will produce similar effects

This concludes the second part of this thesis, which revolved around studying MBSs in grounded SC-SM hybrid nanowires by simulating differential conductance measurements at the end of nanowire. This was done using the S-matrix formalism described in Chap. 3. The next and last part of the thesis will also be focused on electron transport in SC-SM nanowire, but in a Coulomb blockaged setup where charging effects are important. We therefore start the next part by developing another transport model in order to study these systems.

Part III

COULOMB BLOCKADE NANOWIRE ISLAND

Chapter 7

Coulomb Blockade Nanowire Island and the Master Equation

> “ Some people juggle geese!
>
> Wash
>
> - *Firefly*, Joss Whedon

The third and last part of this thesis will be centered around SC-SM nanowires in a Coulomb blockaded setup. For this purpose, we will develop a transport model, based on a similar model used by Higginbotham *et al.* [2015], to study electron transport in a two terminal setup, as pictured in Fig. 7.1. We assume that the tunnel couplings to the leads are weak, so the nanowire island has time to equilibrate between tunneling events. The tunneling Hamiltonian formalism is then used to build a set of master equations in order to study electron current as a function of the applied source-drain bias voltage. The nanowire is modeled as a superconducting island with a BCS-like continuum of states and a single subgap state, and charging effects are included through a constant interaction model. The number of charges on the nanowire island is restricted by the charging energy and controlled by the voltage V_G of a capacitively coupled gate. We will calculate the current to the first order in the tunneling Hamiltonian so the model is applicable in the sequential tunneling regime.

We start by defining the Hamiltonians of the leads, the nanowire island, and the coupling between them

$$H = H_{\text{leads}} + H_D + H_T. \tag{7.1}$$

The leads are described by the Hamiltonian

$$H_{\text{leads}} = \sum_{i,\nu,\sigma} (\epsilon_{i\nu} - \mu_i) c^\dagger_{i\nu\sigma} c_{i\nu\sigma}, \tag{7.2}$$

where the operator $c^\dagger_{i\nu\sigma}$ creates an electron with energy $\epsilon_{i\nu}$ in lead $i \in \{L, R\}$, with orbital index ν and spin $\sigma \in \{\uparrow, \downarrow\}$. We let the lead L act as the source and lead R as the drain and

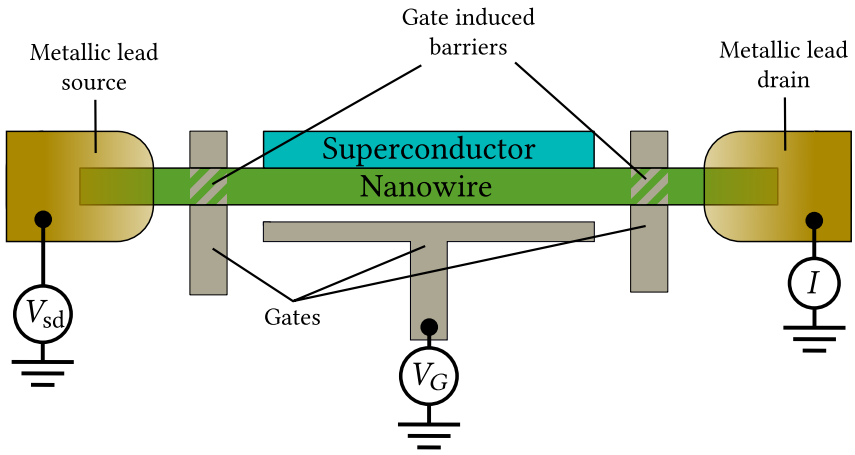

Figure 7.1: A semiconductor nanowire (green) with a epitaxially grown superconductor (blue) on part of the nanowire. Metallic leads are connected at the ends of the nanowire and two gates are used to create tunnel barriers towards both leads, creating a superconducting island in the middle of the nanowire. Another gate is capacitively coupled to the island and is used to control the number of charges on the island by changing the gate voltage V_G. Current I is measured as a function of the applied source-drain bias voltage V_{SD} and the gate voltage V_G.

define their chemical potentials by $\mu_L = -\mu_R = V_{\mathrm{sd}}/2$ where V_{sd} is a symmetrically applied bias voltage. The density of states in the leads is assumed to be constant in the energy range under consideration.

We describe the superconducting island containing N electrons by the Hamiltonian

$$H_{\mathrm{D}} = \sum_{\sigma} \left\{ \sum_{n} E_n \gamma_{n\sigma}^{\dagger} \gamma_{n\sigma} + E_{0\sigma} \gamma_{0\sigma}^{\dagger} \gamma_{0\sigma} \right\} + E_{\mathrm{el}}(N), \tag{7.3}$$

where the first term contains the energy of the quasiparticles and the second term models the electrostatic energy. For simplicty, we take the BCS continuum to be purely s-wave and neglect the effects of spin-orbit interactions and the magnetic field on the BCS states. The operator $\gamma_{n\sigma}$ corresponds to the states in the BCS continuum and $\gamma_{0\sigma}$ to the subgap state. The quasiparticle operator $\gamma_{n\sigma}^{\dagger}$ creates a quasiparticle excitation on the island which is a superposition of electron ($d_{n\sigma}^{\dagger}$) and hole ($d_{-n\bar{\sigma}}$), where the hole creation is accompanied by the addition of a Cooper pair, thereby ensuring that both terms carry the charge of an electron. The operator $d_{n\sigma}^{\dagger}$ creates an electron on the island with spin σ and orbital label n. The quasiparticle operators written in terms of electron operators are

$$\gamma_{n\sigma} = u_n d_{n\sigma} - \sigma v_n d_{-n\bar{\sigma}}^{\dagger} e^{-i\hat{\phi}}, \tag{7.4}$$

$$\gamma_{n\sigma}^{\dagger} = u_n^{*} d_{n\sigma}^{\dagger} - \sigma v_n^{*} e^{i\hat{\phi}} d_{-n\bar{\sigma}}, \tag{7.5}$$

where $e^{\pm i\hat{\phi}}$ shifts the number of Cooper pairs on the island by ± 1. Likewise, the electron operators, written in terms of the quasiparticle operators, are

$$d_{n\sigma} = u_n^{*} \gamma_{n\sigma} + \sigma v_n \gamma_{-n\bar{\sigma}}^{\dagger} e^{-i\hat{\phi}}, \tag{7.6}$$

$$d_{n\sigma}^{\dagger} = u_n \gamma_{n\sigma}^{\dagger} + \sigma v_n^{*} \gamma_{-n\bar{\sigma}} e^{i\hat{\phi}}, \tag{7.7}$$

The state $-n\bar{\sigma}$ is the time-reversed partner of $n\sigma$. For the energies of the quasiparticles and the coherence factors on the island we use

$$E_n = \sqrt{\epsilon_n^2 + \Delta^2}\,, \quad |u_n|^2 = \frac{1}{2}\left(1 + \frac{\epsilon_n}{E_n}\right), \quad |v_n|^2 = \frac{1}{2}\left(1 - \frac{\epsilon_n}{E_n}\right), \tag{7.8}$$

where ϵ_n is the electron energy measured from the chemical potential of the island and Δ is the effective superconducting gap on the island.

In general, the subgap state may be spinful and we allow for the coherence factors to be different at the two ends of the nanowire. We write the quasiparticle annihilation operator corresponding to the subgap state with energy $E_{0\sigma}$ as

$$\gamma_{0\sigma} = \sum_{i\sigma'} u_{0\sigma i\sigma'} d_{0\sigma'} - \sigma' v_{0\sigma i\sigma'} d^\dagger_{0\bar{\sigma}'} e^{-i\hat{\phi}}, \tag{7.9}$$

where $u_{0\sigma i\sigma'}$ and $v_{0\sigma i\sigma'}$ are the electron and hole coherence factors at the position where lead i is tunnel coupled.

The second term $E_{\mathrm{el}}(N)$ in Eq. (7.3) models the electrostatic energy of the island,

$$E_{\mathrm{el}}(N) = E_{\mathrm{C}}(N - N_{\mathrm{G}})^2 \,, \qquad \text{where} \quad N = \sum_{n\sigma} d^\dagger_{n\sigma} d_{n\sigma} + \sum_{\sigma} d^\dagger_{0\sigma} d_{0\sigma} \tag{7.10}$$

is the number of charges on the island, and $E_{\mathrm{C}} = \mathrm{e}^2/C_\Sigma$ is the charging energy of the nanowire island with total capacitance C_Σ. The dimensionless gate-induced charge number $N_{\mathrm{G}} = C_{\mathrm{G}} V_{\mathrm{G}}/\mathrm{e}$ is proportional to the gate voltage V_{G} and the capacitance between the island and the gate C_{G}.

Lastly, expressed in terms of the quasiparticle operators the tunneling Hamiltonian reads

$$\begin{aligned} H_{\mathrm{T}} = \sum_{i,\nu,\sigma} \Bigg\{ \sum_{\sigma'} \Big[& t_{0i} c^\dagger_{i\nu\sigma} (u^*_{0\sigma' i\sigma} \gamma_{0\sigma'} + \sigma v_{0\sigma' i\sigma} \gamma^\dagger_{0\bar{\sigma}'} e^{-i\hat{\phi}}) \\ & + t^*_{0i} (u_{0\sigma' i\sigma} \gamma^\dagger_{0\sigma'} + \sigma v^*_{0\sigma' i\sigma} \gamma_{0\bar{\sigma}'} e^{i\hat{\phi}}) c_{i\nu\sigma} \Big] \\ & + \sum_n \Big[t_i c^\dagger_{i\nu\sigma} (u^*_n \gamma_{n\sigma} + \sigma v_n \gamma^\dagger_{-n\bar{\sigma}} e^{-i\hat{\phi}}) \\ & + t^*_i (u_n \gamma^\dagger_{n\sigma} + \sigma v^*_n \gamma_{-n\bar{\sigma}} e^{i\hat{\phi}}) c_{i\nu\sigma} \Big] \Bigg\}, \end{aligned} \tag{7.11}$$

where we assume that the tunnel coupling elements t_i between the electronic states in lead i and the quasiparticle states on the island do not depend on energy. We allow for different coupling strengths to the subgap state t_{0i} and the continuum states t_i. Due to the island being superconducting, electrons can be added to the island by either creating a quasiparticle or annihilating a quasiparticle and creating a Cooper pair, as seen in the tunneling Hamiltonian. This gives rise to a characteristic odd-even effect between coulomb diamonds of odd and even ground state.

7.1 Thermodynamics of the odd/even parity effect

In order to calculate the current at finite temperature, we need to know the thermodynamics of quasiparticles in a BCS superconductor. A superconductor with a fixed number of electrons has two distinct ground states depending on whether the number of electrons is even or odd, due to the electron's ability to form Cooper pairs[Tuominen *et al.*, 1992; Lafarge *et al.*, 1993]. In the even case, all electrons can form pairs and leave a ground state with no quasiparticles, while the odd case ground state has a single quasiparticle left with none other to pair with. At finite temperatures, thermal fluctuations cause Cooper pairs to split, but the overall parity of the superconductor is preserved since quasiparticles can only be created in pairs this way. We will need the distribution function of quasiparticles in each parity sector in order to calculate the transition rates involving states in the BCS

continuum. The distribution functions in each parity sector can be related to each other by a difference in free energy. In this section, we will restrict ourselves to presenting the results of the calculation, which can be found in App. B.

The starting point for the derivation is the partition function for odd (o) and even (e) parity states at the inverse temperature $\beta = 1/k_B T$ that can be written as

$$2Z_p = \prod_n (1 + e^{-\beta E_n}) \mp \prod_n (1 - e^{-\beta E_n}), \tag{7.12}$$

where $p \in \{\mathrm{o}, \mathrm{e}\}$, $\bar{p}$ denotes the opposite of p, E_n is given in Eq. (7.8) and the $-$ $(+)$ applies to the odd (even) case.

In the limit of $\beta\Delta \gg 1$, which is the regime we are considering, we obtain the thermal distribution function as

$$f_p(E) = \frac{1}{e^{\beta(E \pm \delta F)} + 1}, \tag{7.13}$$

where the $-$ $(+)$ applies to the odd (even) case and we have defined the free energy difference between the odd and even parity sector

$$\delta F = F_\mathrm{o} - F_\mathrm{e} = -\frac{1}{\beta} \ln\left(\frac{Z_\mathrm{o}}{Z_\mathrm{e}}\right). \tag{7.14}$$

Using Eq. (7.12), the free energy difference may be calculated as

$$\delta F_\mathrm{BCS} \approx -\frac{1}{\beta} \ln\tanh \int_\Delta^\infty dE \rho_\mathrm{BCS}(E) \ln\coth\left(\frac{\beta E}{2}\right) \tag{7.15}$$

where

$$\rho_\mathrm{BCS}(E) = \frac{\rho_D E}{\sqrt{E^2 - \Delta^2}}, \tag{7.16}$$

is the BCS density of states with $\rho_D = \rho_\mathrm{Al}\mathcal{V}$ being the normal density of states at the Fermi level of the island including spin. ρ_Al is the aluminum density of states per volume and $\mathcal{V}$ is the volume of the island. This is the expression we will use to calculate the free energy difference for numerical calculations later on. In Fig. 7.2, we show the temperature dependence of δF_BCS for typical experimental parameters. For low temperatures $\beta\Delta \gg 1$ we can approximate

$$\begin{aligned} \ln\coth\left(\frac{\beta E}{2}\right) &\approx \coth\left(\frac{\beta E}{2}\right) - 1 \\ &\approx 2e^{-\beta E} \end{aligned} \tag{7.17}$$

which in the same limit lets us approximate the free energy difference as

$$\delta F_\mathrm{BCS} \approx -\frac{1}{\beta} \ln\tanh\left[2\int_\Delta^\infty dE \rho_\mathrm{BCS}(E) e^{-\beta E}\right] = -\frac{1}{\beta} \ln\tanh[N_\mathrm{eff} e^{-\beta\Delta}] \tag{7.18}$$

$$\approx \Delta - \frac{\ln(N_\mathrm{eff})}{\beta}, \tag{7.19}$$

with

$$N_\mathrm{eff} = 2\int_\Delta^\infty \rho_\mathrm{BCS}(E) e^{-\beta(E-\Delta)}\, \mathrm{d}E = 2\rho_\mathrm{D}\Delta e^{\beta\Delta} K_1(\beta\Delta), \tag{7.20}$$

where $K_\nu(x)$ is the modified Bessel function of the second kind and N_{eff} is an effective quasi-particle number.

In Fig. 7.2 we see the free energy difference between the odd and even parity states as a function of temperature. As the temperature is increased, Cooper pairs can be broken apart by thermal energy and the number of quasiparticles in both parity sectors increases. As the number of quasiparticles in each parity sector becomes $\gg 1$ the difference between even and odd parity goes away, and the free energy difference goes to zero.

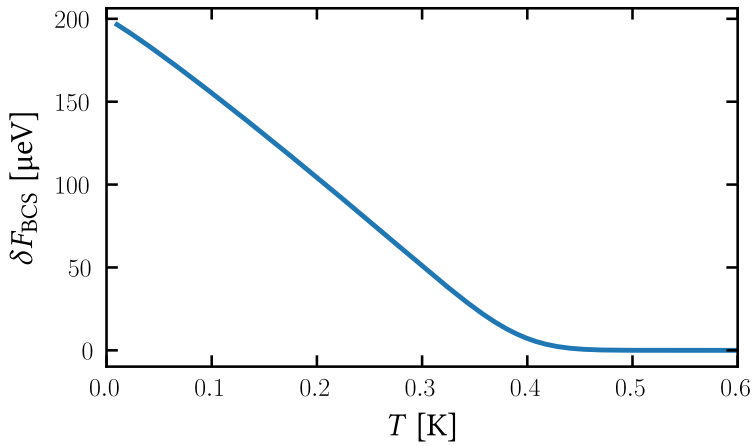

Figure 7.2: The free energy difference as a function of temperature calculated using Eq. (7.15) in the regime of higher temperatures, $\beta\Delta < 10$, and Eq. (7.18) for low temperatures, $\beta\Delta \geq 10$, with the parameters $\Delta = 200\,\mu\text{eV}$ and $\rho_D = 1.7\,\mu\text{eV}^{-1}$.

Number of Quasiparticles in the BCS Continuum

We use the distribution function derived above to calculate the number of quasiparticles in each parity sector, in the absence of a subgap state. In the low temperature limit, where the free energy difference is given in Eq. (7.19), the distribution function takes the form

$$f_{\text{e}} = \frac{1}{1 + e^{\beta(E+\delta F_{\text{BCS}})}} \approx N_{\text{eff}} e^{-\beta(E+\Delta)}, \tag{7.21}$$

$$f_{\text{o}} = \frac{1}{1 + e^{\beta(E-\delta F_{\text{BCS}})}} \approx \frac{e^{-\beta(E-\Delta)}}{N_{\text{eff}}}, \tag{7.22}$$

where N_{eff} is given in Eq. (7.20). We calculate the number of quasiparticles in each parity sector using

$$N_p = 2\int_\Delta^\infty \rho_{\text{BCS}}(E) f_p(E)\, \mathrm{d}E. \tag{7.23}$$

In the odd parity case, we find approximately one quasiparticle,

$$N_{\text{o}} = 2\int_\Delta^\infty \rho_{\text{BCS}}(E) f_{\text{o}}(E)\, \mathrm{d}E \approx \frac{2\int_\Delta^\infty \rho_{\text{BCS}}(E) e^{-\beta(E-\Delta)}\, \mathrm{d}E}{N_{\text{eff}}} = 1, \tag{7.24}$$

as expected. For the even case we have

$$N_{\text{e}} = 2\int_\Delta^\infty \rho_{\text{BCS}}(E) f_{\text{e}}(E)\, \mathrm{d}E \approx 2\int_\Delta^\infty \rho_{\text{BCS}}(E) e^{-\beta(E+\Delta)} N_{\text{eff}}\, \mathrm{d}E = (N_{\text{eff}} e^{-\beta\Delta})^2. \tag{7.25}$$

Since the quasiparticles can only be created in pairs at energy above the superconducting gap Δ, the number of quasiparticles is suppressed by the exponential factor $e^{-2\beta\Delta}$ in the even parity sector.

7.2 Master Equation

Now we will turn towards setting up the master equation for calculating the current through the nanowire island, where we assume that transport is dominated by incoherent sequential tunneling processes, *i.e.* temperature, Tk_B, is larger than the coupling to the leads $\Gamma_{L,R}, \Gamma_{0L,R}$. The time between tunneling events is long enough that the number of quasiparticles in the BCS continuum relaxes to the distribution function of the given parity, which we derived in the previous section. However, the time is not so long that a quasiparticle in the continuum will always relax into the subgap state. Instead we include a relaxation rate for the quasiparticle from the BCS continuum into the subgap state with the characteristic time τ_r, which has been estimated to be of order $\sim 0.1\,\mu$s in experiments conducted by Higginbotham *et al.* [2015].

We label the many body state of the nanowire island in terms of the number of charges on the island N, the number of quasiparticle excitations in the BCS continuum N_Δ and the occupation of the subgap state N_0. The equilibrium probability density function $P_{(N,N_\Delta,N_0)}$ is found by solving the master equation

$$\begin{aligned}\frac{d}{dt}P_{(N,N_\Delta,N_0)} &= \sum_{N',N'_\Delta,N'_0}\Big\{\Gamma_{(N,N_\Delta,N_0)\leftarrow(N',N'_\Delta,N'_0)}P_{(N',N'_\Delta,N'_0)} \\ &\qquad - \Gamma_{(N',N'_\Delta,N'_0)\leftarrow(N,N_\Delta,N_0)}P_{(N,N_\Delta,N_0)}\Big\} \\ &= 0,\end{aligned} \tag{7.26}$$

together with the normalization condition

$$\sum_{N,N_\Delta,N_0} P_{(N,N_\Delta,N_0)} = 1, \tag{7.27}$$

where $\Gamma_{(N',N'_\Delta,N'_0)\leftarrow(N,N_\Delta,N_0)}$ is the transition rate from the state (N,N_Δ,N_0) to (N',N'_Δ,N'_0).

Rates with $N \neq N'$ involve tunneling of charges to and from the leads, and these rates thus include contributions from both leads. Only focusing on (lowest-order) single-particle tunneling, this means that we can write

$$\Gamma_{(N\pm1,N'_\Delta,N'_0)\leftarrow(N,N_\Delta,N_0)} = \sum_{i\in\{L,R\}}\Gamma^{(i)}_{(N\pm1,N'_\Delta,N'_0)\leftarrow(N,N_\Delta,N_0)}, \tag{7.28}$$

where the superscript i indicates which lead the charge is tunneling to or from. The current resulting from sequential tunneling is then obtained as

$$I = (-e)\sum_{N,N_\Delta,N'_\Delta}\left\{\Gamma^{(L)}_{(N+1,N'_\Delta,N'_0)\leftarrow(N,N_\Delta,N_0)} - \Gamma^{(L)}_{(N-1,N'_\Delta,N'_0)\leftarrow(N,N_\Delta,N_0)}\right\}P_{(N,N_\Delta,N_0)}. \tag{7.29}$$

In order to calculate the current explicitly, the only task left is to find all relevant transition rates $\Gamma_{(N',N'_\Delta,N'_0)\leftarrow(N,N_\Delta,N_0)}$. In our model we include (i) tunneling of charges to and from the leads resulting in the creation or annihilation of a quasiparticle excitation in the BCS continuum, $\Gamma^{(L,R)}_{(N\pm1,N'_\Delta,N_0)\leftarrow(N,N_\Delta,N_0)}$, (ii) tunneling to and from the leads combined with a change of the occupation of the subgap mode $\Gamma^{(L,R)}_{(N\pm1,N_\Delta,N'_0)\leftarrow(N,N_\Delta,N_0)}$, and (iii) we add internal relaxation processes on the island $\Gamma_{(N,N'_\Delta,N'_0)\leftarrow(N,N_\Delta,N_0)}$. In the following subsections we will discuss these three types of transitions in more detail.

7.3 Transition Rates

We calculate the incoherent tunneling rates between the leads and the nanowire island using Fermi's golden rule,

$$\Gamma_{\beta\leftarrow\alpha} = 2\pi \sum_{f_\beta, i_\alpha} |\langle f_\beta|H_T|i_\alpha\rangle|^2 W_{i_\alpha} \delta(E_{f_\beta} - E_{i_\alpha}), \tag{7.30}$$

where $\alpha = (N, N_\Delta, N_0)$ is the initial state, $\beta = (N', N'_\Delta, N'_0)$ is the final state, and we set $\hbar = 1$. The sum goes over all the configurations of internal degrees of freedom of the initial state i_α and final state f_β weighted by the corresponding thermal distribution function $W_{i\alpha}$. We divide the transition rates into two categories depending on whether the process involves the creation or annihilation of a quasiparticle excitation in either (a) the BCS continuum or (b) the subgap states. We also include a third category of internal relaxation processes with no electrons tunneling in or out of the nanowire island, but the value of these rates are obtained from experiments rather than calculations.

7.3.1 Transition rates in and out of the BCS continuum

We first calculate the rates that involve the creation or annihilation of quasiparticles in the BCS continuum. There are four different rates, two where an electron is added to the island, and two where an electron is removed. We write up the relation and energy difference between the final and initial states:

$$|f_{N+1,N_\Delta+1}\rangle = \gamma^\dagger_{n\sigma} c_{i\nu\sigma} |i_{N,N_\Delta}\rangle, \qquad E_{f_{N+1,N_\Delta+1}} - E_{i_{N,N_\Delta}} = U_N + E_n - \epsilon_{i\nu}, \tag{7.31a}$$

$$|f_{N+1,N_\Delta-1}\rangle = e^{i\hat{\phi}} \gamma_{-n\bar{\sigma}} c_{i\nu\sigma} |i_{N,N_\Delta}\rangle, \qquad E_{f_{N+1,N_\Delta-1}} - E_{i_{N,N_\Delta}} = U_N - E_n - \epsilon_{i\nu}, \tag{7.31b}$$

$$|f_{N,N_\Delta}\rangle = c^\dagger_{i\nu\sigma} \gamma_{n\sigma} |i_{N+1,N_\Delta+1}\rangle, \qquad E_{f_{N,N_\Delta}} - E_{i_{N+1,N_\Delta+1}} = -U_N - E_n + \epsilon_{i\nu}, \tag{7.31c}$$

$$|f_{N,N_\Delta}\rangle = c^\dagger_{i\nu\sigma} \gamma^\dagger_{-n\bar{\sigma}} e^{-i\hat{\phi}} |i_{N+1,N_\Delta-1}\rangle, \qquad E_{f_{N,N_\Delta}} - E_{i_{N+1,N_\Delta-1}} = -U_N + E_n + \epsilon_{i\nu}, \tag{7.31d}$$

where we have suppresed the subgap state index N_0 and defined $U_N = E_{\rm el}(N+1) - E_{\rm el}(N) = E_C(2N - 2N_G + 1)$ as the difference in charging energy between a state with $N+1$ and N electrons.

As an example, we consider the two ways an electron can be added to the island. First, the final state in Eq. (7.31a) is created from the initial state $|i_N\rangle$ by removing an electron from lead i with energy $\epsilon_{i\nu}$ and creating an electron quasi-particle $\gamma^\dagger_{n\sigma}$ with energy E_n (given in eq. 7.8). The initial state has energy $E_c(N)$ while the final state has the energy $E_c(N+1) + E_n - \epsilon_{i\nu}$. Second, if a quasiparticle is already present on the island, the added electron can form a Cooper pair with it, as written in eq. 7.31b. This final state has a different energy than in the first case since the Cooper pair has to be at the Fermi energy of the island.

Due to the thermodynamics of the odd/even parity effect of the BCS density of states discussed in Sec. 7.1, both ways of adding (removing) an electron to the island should be included when calculating the transition rate. The distribution function $\langle \gamma^\dagger_{n\sigma}\gamma_{n\sigma}\rangle_p = f_p(E_n)$ given in Eq. (7.13) with the free energy difference δF given in Eq. (7.15) will take care of weighting each process appropriately for the given parity p of N_Δ. The transition rates of adding and removing an electron to the island follow from a straight forward calculation of Eq. (7.30) with the tunneling Hamiltonian given in Eq. (7.11),

$$\begin{aligned}\Gamma^{(i)}_{N+1\leftarrow N} = 2\pi \Bigg(&\sum_{i_N} W_{i_N} |\langle i_N| c^\dagger_{i\nu\sigma} \gamma_{n\sigma} t_i u^*_n \gamma^\dagger_{n\sigma} c_{i\nu\sigma} |i_N\rangle|^2 \delta(U_N + E_n - \epsilon_{i\nu}) \\ &+ \sum_{i_N} W_{i_N} |\langle i_N| c^\dagger_{i\nu\sigma} \gamma^\dagger_{-n\bar{\sigma}} e^{i\hat{\phi}} t^*_i v^*_n e^{-i\hat{\phi}} \gamma_{-n\bar{\sigma}} c_{i\nu\sigma} |i_N\rangle|^2 \delta(U_N - E_n - \epsilon_{i\nu}) \Bigg)\end{aligned}$$

$$
\begin{aligned}
&= \Gamma_i \int d\epsilon_i d\epsilon_n \Big\{ |u_n|^2 n_F(\epsilon_i - \mu_i)(1 - f_p(E_n))\delta(U_N + E_n - \epsilon_i) \\
&\qquad + |v_n|^2 n_F(\epsilon_i - \mu_i) f_p(E_n)\delta(U_N - E_n - \epsilon_i) \Big\} \\
&= \Gamma_i \int d\epsilon_n \Big\{ |u_n|^2 n_F(U_N + E_n - \mu_i)(1 - f_p(E_n)) \\
&\qquad + |v_n|^2 n_F(U_N - E_n - \mu_i) f_p(E_n) \Big\} \qquad (7.32)
\end{aligned}
$$

$$
\begin{aligned}
\Gamma^{(i)}_{N \leftarrow N+1} &= 2\pi \Bigg(\sum_{i_{N+1}} W_{i_{N+1}} |\langle i_{N+1}| \gamma^\dagger_{n\sigma,e} c_{iv\sigma} t_i u_n c^\dagger_{in\sigma} \gamma_{n\sigma,e} |i_{N+1}\rangle|^2 \delta(-U_N - E_n + \epsilon_{iv}) \\
&\qquad + \sum_{i_{N+1}} W_{i_{N+1}} |\langle i_{N+1}| \gamma_{-n\bar{\sigma},h} c_{iv\sigma} t_i v_n c^\dagger_{iv\sigma} \gamma^\dagger_{-n\bar{\sigma},h} |i_{N+1}\rangle|^2 \delta(-U_N + E_n + \epsilon_{iv}) \Bigg) \\
&= \Gamma_i \int d\epsilon_n \Big\{ |u_n|^2 f_p(E_n)(1 - n_F(U_N + E_n - \mu_i)) \\
&\qquad + |v_n|^2 (1 - n_F(U_N - E_n - \mu_i))(1 - f_p(E_n)) \Big\}, \qquad (7.33)
\end{aligned}
$$

where we have suppressed the index of the BCS continuum and subgap state occupation. The coupling strength $\Gamma_i = 2\pi\rho_D\rho_i|t_i|^2$ with ρ_D and ρ_i being the normal density of states of the island and lead, respectively, is related to the normal conductance $g_{\mathrm{Al}} = 2\pi(e^2/h)\Gamma_i$, which can be measured in spectroscopy experiments as the peak height at high bias voltage. These two transition rates cover both the case of even and odd numbers of electrons on the island. Terms containing u_n (v_n) correspond to adding (removing) a quasi-particle to (from) the island. For the sake of easy reference, we write the expression for u_n, v_n and E_n here:

$$
E_n = \sqrt{\epsilon_n^2 + \Delta^2}\,, \quad |u_n|^2 = \frac{1}{2}\left(1 + \frac{\epsilon_n}{E_n}\right), \quad |v_n|^2 = \frac{1}{2}\left(1 - \frac{\epsilon_n}{E_n}\right). \qquad (7.34)
$$

Both u_n and v_n contain a term $(\epsilon_n/2E_n)$ which is odd in ϵ_n and a term that is even $(1/2)$. Since the rest of the integrand (which is a function of E_n) is even in ϵ_n, integrating ϵ_n from $-\infty$ to ∞ gives zero for the odd part. We keep the even part and change integration variable to E_n using

$$
d\epsilon_n = \frac{d\epsilon_n}{dE_n} dE_n = \frac{E_n}{\sqrt{E_n^2 - \Delta^2}} dE_n. \qquad (7.35)
$$

We have then obtained the final expressions for the transition rates involving quasiparticles in the BCS continuum:

$$
\Gamma^{(i)}_{N+1 \leftarrow N} = \Gamma_i \int_\Delta^\infty dE_n \left\{ \frac{E_n}{\sqrt{E_n^2 - \Delta^2}} A_{\mathrm{in}}(E_n) \right\} \qquad (7.36a)
$$

$$
\Gamma^{(i)}_{N-1 \leftarrow N} = \Gamma_i \int_\Delta^\infty dE_n \left\{ \frac{E_n}{\sqrt{E_n^2 - \Delta^2}} A_{\mathrm{out}}(E_n) \right\} \qquad (7.36b)
$$

where

$$
A_{\mathrm{in}}(E_n) = n_F(U_N + E_n - \mu_i)(1 - f_p(E_n)) + n_F(U_N - E_n - \mu_i) f_p(E_n) \qquad (7.37a)
$$

$$
A_{\mathrm{out}}(E_n) = (1 - n_F(U_N + E_n - \mu_i)) f_p(E_n) + (1 - n_F(U_N - E_n - \mu_i))(1 - f_p(E_n)), \qquad (7.37b)
$$

and the integrals are calculated numerically.

Before moving on to the transition rates involving the subgap state, we will consider the case where there is no subgap state. The energy of the island is then

$$E(N, N_\Delta) = E_C(N - N_G)^2 + \Delta N_\Delta, \tag{7.38}$$

where we have approximated the energy of a quasiparticle by Δ. The low-energy spectrum is shown in Fig. 7.3 (a), where black (blue) parabolas correspond to the energy of even (odd) charge states with no (one) quasiparticle in the continuum. The odd parabolas are shifted up by the superconducting gap Δ, giving rise to a difference in the size of the Coulomb diamonds of even and odd charge states. This is seen in Fig. 7.3 (c), where the differential conductance as a function of induced gate charge N_G and source-drain bias voltage V_{sd} is shown. Peaks at zero bias correspond to ground state degeneracies where the black and blue parabolas cross each other in (a).

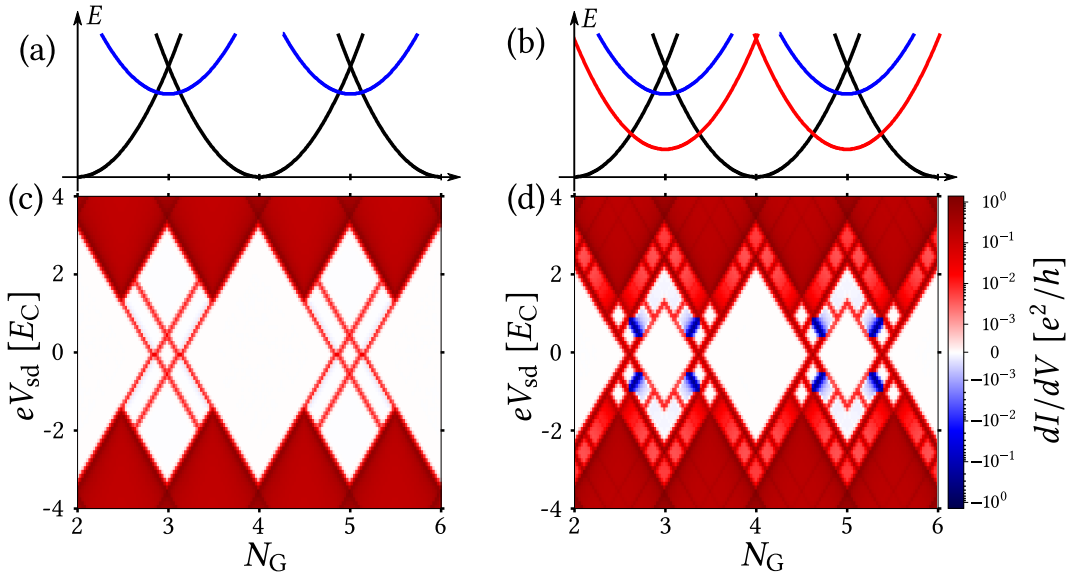

Figure 7.3: (a-b) Energy spectrum of the superconducting island without (a) and with (b) a subgap state. Black parabolas correspond to even charge states with no quasiparticles in either continuum or subgap states. Blue (red) parabolas correspond to odd charge states with one quasiparticle in the continuum (subgap state). (c-d) Differential conductance as a function of the induced gate charge N_G and the source-drain bias voltage V_{sd} obtained by solving the master equation numerically. Note the colorscale is logarithmic down/up to $|dI/dV| = 10^{-3}e^2/h$ and then linear across zero. (c) Only the BCS density of states are included and transition rates are calculated using Eq. (7.36), with parameters $\Delta = 75\,\mu\text{eV}$, $E_C = 100\,\mu\text{eV}$, $\rho_D = 2.25\,\mu\text{eV}^{-1}$, $\Gamma_{L,R} = 0.1\,\mu\text{eV}$, and $T = 20\,\text{mK}$. (d) Both the BCS density of states and a subgap state with energy $E_0 = 25\,\mu\text{eV}$ and coupling to leads $\Gamma^{\text{sub}}_{L,R} = 1\,\mu\text{eV}$. Other parameters are the same as in (c).

7.3.2 Transition rate in and out of the subgap state

We now calculate the transition rates that involve creating or annihilating quasiparticles in the subgap state. We consider the general case where the subgap state is spinful and allows for the two spin states to have different energies as well as coherence factors that may be different for each lead $i = \text{L}, \text{R}$,

$$\gamma_{0\sigma} = \sum_{i\sigma'} u_{0\sigma i\sigma'} d_{0\sigma'} - \sigma' v_{0\sigma i\sigma'} d^\dagger_{0\bar{\sigma}'} e^{-i\hat{\phi}}. \tag{7.39}$$

In this general case, the occupation of the subgap state can take the values $N_0 \in \{0, \uparrow, \downarrow, 2\}$ and we have to consider the following states

$$|f_{N+1,\sigma}\rangle = \gamma_{0\sigma}^\dagger c_{iv\sigma}|i_{N,0}\rangle, \qquad E_{f_{N+1,\sigma}} - E_{i_{N,0}} = U_N + E_{0\sigma} - \epsilon_{iv}, \tag{7.40a}$$

$$|f_{N+1,2}\rangle = \gamma_{0\bar{\sigma}}^\dagger c_{iv\bar{\sigma}}|i_{N,\sigma}\rangle, \qquad E_{f_{N+1,2}} - E_{i_{N,\sigma}} = U_N + E_{0\bar{\sigma}} - \epsilon_{iv}, \tag{7.40b}$$

$$|f_{N+1,0}\rangle = e^{i\hat{\phi}}\gamma_{0\sigma} c_{iv\bar{\sigma}}|i_{N,\sigma}\rangle, \qquad E_{f_{N+1,0}} - E_{i_{N,\sigma}} = U_N - E_{0\sigma} - \epsilon_{iv}, \tag{7.40c}$$

$$|f_{N+1,\sigma}\rangle = e^{i\hat{\phi}}\gamma_{0\bar{\sigma}} c_{iv\sigma}|i_{N,2}\rangle, \qquad E_{f_{N+1,\sigma}} - E_{i_{N,2}} = U_N - E_{0\bar{\sigma}} - \epsilon_{iv}, \tag{7.40d}$$

$$|f_{N,0}\rangle = \gamma_{0\sigma} c_{iv\sigma}^\dagger|i_{N+1,\sigma}\rangle, \qquad E_{f_{N,0}} - E_{i_{N+1,\sigma}} = -U_N - E_{0\sigma} + \epsilon_{iv}, \tag{7.40e}$$

$$|f_{N,\sigma}\rangle = \gamma_{0\bar{\sigma}} c_{iv\bar{\sigma}}^\dagger|i_{N+1,2}\rangle, \qquad E_{f_{N,\sigma}} - E_{i_{N+1,2}} = -U_N - E_{0\bar{\sigma}} + \epsilon_{iv}, \tag{7.40f}$$

$$|f_{N,\sigma}\rangle = e^{-i\hat{\phi}}\gamma_{0\sigma}^\dagger c_{iv\bar{\sigma}}^\dagger|i_{N+1,0}\rangle, \qquad E_{f_{N,\sigma}} - E_{i_{N+1,0}} = -U_N + E_{0\sigma} + \epsilon_{iv}, \tag{7.40g}$$

$$|f_{N,2}\rangle = e^{-i\hat{\phi}}\gamma_{0\bar{\sigma}}^\dagger c_{iv\sigma}^\dagger|i_{N+1,\sigma}\rangle, \qquad E_{f_{N,2}} - E_{i_{N+1,\sigma}} = -U_N + E_{0\bar{\sigma}} + \epsilon_{iv}, \tag{7.40h}$$

where the first (last) four states correspond to a process where an electron has been added to (removed from) the island. The calculation of the transition rates using Eq. (7.30) is similar to that involving the quasiparticles in the BCS continuum. In this case we have a discrete state instead of a continuum and the expectation value $\langle \gamma_{0\sigma}^\dagger \gamma_{0\sigma}\rangle$ just takes the value 0 or 1 depending on the occupation of the subgap state. The transition rates are

$$\Gamma^{(i)}_{N+1,\sigma\leftarrow N,0} = \Gamma_i^{\text{sub}}|u_{0\sigma i}|^2 n_F(U_N + E_{0\sigma} - \mu_i) \tag{7.41a}$$

$$\Gamma^{(i)}_{N+1,2\leftarrow N,\sigma} = \Gamma_i^{\text{sub}}|u_{0\bar{\sigma} i}|^2 n_F(U_N + E_{0\bar{\sigma}} - \mu_i) \tag{7.41b}$$

$$\Gamma^{(i)}_{N+1,0\leftarrow N,\sigma} = \Gamma_i^{\text{sub}}|v_{0\sigma i}|^2 n_F(U_N - E_{0\sigma} - \mu_i) \tag{7.41c}$$

$$\Gamma^{(i)}_{N+1,\sigma\leftarrow N,2} = \Gamma_i^{\text{sub}}|v_{0\bar{\sigma} i}|^2 n_F(U_N - E_{0\sigma} - \mu_i) \tag{7.41d}$$

$$\Gamma^{(i)}_{N,0\leftarrow N+1,\sigma} = \Gamma_i^{\text{sub}}|v_{0\sigma i}|^2 (1 - n_F(-U_N - E_{0\sigma} + \mu_i)) \tag{7.41e}$$

$$\Gamma^{(i)}_{N,\sigma\leftarrow N+1,2} = \Gamma_i^{\text{sub}}|v_{0\bar{\sigma} i}|^2 (1 - n_F(-U_N - E_{0\sigma} + \mu_i)) \tag{7.41f}$$

$$\Gamma^{(i)}_{N,\sigma\leftarrow N+1,0} = \Gamma_i^{\text{sub}}|u_{0\sigma i}|^2 (1 - n_F(-U_N + E_{0\sigma} + \mu_i) \tag{7.41g}$$

$$\Gamma^{(i)}_{N,2\leftarrow N+1,\sigma} = \Gamma_i^{\text{sub}}|u_{0\bar{\sigma} i}|^2 (1 - n_F(-U_N + E_{0\sigma} + \mu_i)) \tag{7.41h}$$

where we have suppressed the index of the BCS continuum occupation N_Δ and defined $|u_{0\sigma i}|^2 = \sum_{\sigma'} |u_{0\sigma i\sigma'}|^2$, $|v_{0\sigma i}|^2 = \sum_{\sigma'} |v_{0\sigma i\sigma'}|^2$. The estimated coupling strength to the subgap state $\Gamma_i^{\text{sub}} = 2\pi|t_{0i}|^2\rho_i$ is determined by fitting a zero-bias conductance peak to the functional form of a Breit-Wigner resonance with unequal tunnel barriers, see Supplement of Ref. Jørgensen *et al.* [2007].

Now with both the BCS continuum and the subgap state, the energy of the island is

$$E(N, N_\Delta, N_0) = E_C(N - N_G)^2 + \Delta N_\Delta E_0 N_0 \tag{7.42}$$

where we have assumed that the subgap state energy is the same for both spin directions and again approximated the energy of a quasiparticle in the continuum by Δ.

The low-energy spectrum is shown in Fig. 7.3 (b), where black parabolas correspond to the energy of even charge states with no quasiparticles and blue (red) parabolas to the energy of odd charge states with one quasiparticle in the continuum (subgap state). The idea is to let the subgap state act as a MBS on the island, so we assume the subgap state to be equal superposition of electron and hole, $|u_{0\sigma i}|^2 = |v_{0\sigma i}|^2 = \frac{1}{2}$, even though it is not at zero energy. Further, we assume that the couplings to the leads are greater than the continuum states (which is also seen in experiments), due to the state being localized at the ends of the nanowire. Since $E_0 < \Delta$, the ground state degeneracies are now at crossings

between black and red parabolas. There is still different spacing of the even and odd charge ground states at zero bias, as long as $E_0 \neq 0$.

The differential conductance spectrum is shown in Fig. 7.3 (d), where we also see new features at finite bias. The blue lines are negative differential conductance (NDC) which indicate the current getting blocked. This happens because the BCS continuum states are more weakly coupled to the leads than the subgap state. It occurs when the bias voltage becomes large enough so that electrons can enter the continuum. Here they become trapped for a much longer time compared to the subgap state which results in a blocking of current.

This current blocking effect can be used to estimate the relaxation rate of quasiparticles from the BCS continuum into the subgap state. This is important for knowing the lifetime of the parity of the subgap state and was done in experiments by Higginbotham *et al.* [2015].

7.3.3 Internal relaxation

The last type of transitions we include in the general description of the master equation model are transitions due to relaxation and excitation between states of the island where no electrons are exchanged with the leads.

The first type of relaxation process we consider, is where a quasiparticle from the BCS continuum relaxes down into the subgap state. The rate of this process was estimated by Higginbotham *et al.* [2015] in a SC-SM nanowire similar to those we will consider later. In these SC-SM nanowires, the subgap state is more strongly coupled to the leads than the BCS continuum states, *i.e.* $\gamma_i^{\text{sub}} > \gamma_i$. This leads to a current blocking effect when a quasiparticle enters the BCS continuum and becomes trapped there for a long time, due to the weaker coupling to the leads. The current blocking is observed as a NDC peak at finite bias.

However, the trapped quasiparticle may exit the island via a different process than directly tunneling to the leads. It can first relax into the subgap state, which is much more strongly coupled to the leads and thus facilitates fast subsequent tunneling out of a charge. The rate of relaxation from the BCS continuum into the subgap state can then be estimated from the heights of the positive and NDC peaks. A similar effect is seen in superconducting grains in the contunneling regime where current is blocked at finite bias when single electron tunneling becomes enabled Hekking *et al.* [1993].

We assume that the different relaxation processes involving a quasiparticle from the BCS continuum relaxing into the subgap to be approximately the same and define a common relaxation rate for all of them. These relaxation processes are:

$$\Gamma_{(N_\Delta-1,\sigma)\leftarrow(N_\Delta,0)} = \Gamma_{(N_\Delta-1,2)\leftarrow(N_\Delta,\sigma)} = \Gamma_{(N_\Delta-1,0)\leftarrow(N_\Delta,\sigma)} = \Gamma_{(N_\Delta-1,\sigma)\leftarrow(N_\Delta,2)} \equiv \Gamma_{\text{relax}}, \quad (7.43)$$

where we have suppressed the index of the number of charges on the island N as it does not change in these processes.

In terms of the schematics shown in Fig. 7.4: The first rate describes a transition from an initial state as pictured in (e) to a final state (d), the second rate corresponds to going from (c) to (b), and the third rate from (c) to (a). The last rate describes transitions from a state with three excitations (two in the subgap and one in the continuum) to (d). Relaxation processes like the third and the fourth one mentioned in eq. (7.43) include the recombination of a Cooper pair, which are allowed since translational invariance is broken in the system: momentum is not a good quantum number and Cooper pairs are not simply composed of opposite momentum quasiparticles. For simplicity we assume the same, energy-independent relaxation rate for all these transitions. The reverse thermal

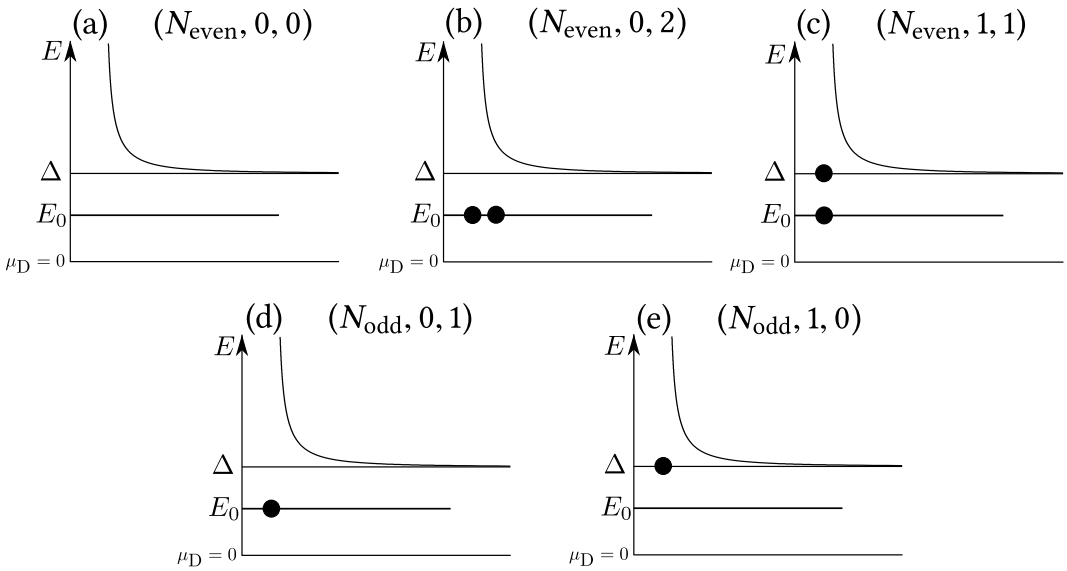

Figure 7.4: Schematic density of states of the island where the subgap state is assumed to be degenerate, $E_{0\sigma} = E_0$, for the sake of simplicity. (a–c) Assuming even N, the three lowest-energy states are (a) without any excitations, (b) a state with a doubly occupied subgap state, and (c) a state with a singly occupied subgap state and one quasiparticle excitation. (d,e) With odd N the lowest-energy state (d) has a singly occupied subgap mode and the first excited state (e) has one quasiparticle excitation.

excitation rates are also included and read

$$\Gamma_{(N,N_\Delta+1,0)\leftarrow(N,N_\Delta,\sigma)} = \Gamma_{\text{relax}} e^{-\beta(\Delta - E_{0\sigma})}, \tag{7.44}$$

$$\Gamma_{(N,N_\Delta+1,\sigma)\leftarrow(N,N_\Delta,2)} = \Gamma_{\text{relax}} e^{-\beta(\Delta - E_{0\bar{\sigma}})}, \tag{7.45}$$

$$\Gamma_{(N,N_\Delta+1,\sigma)\leftarrow(N,N_\Delta,0)} = \Gamma_{\text{relax}} e^{-\beta(\Delta + E_{0\sigma})}, \tag{7.46}$$

$$\Gamma_{(N,N_\Delta+1,2)\leftarrow(N,N_\Delta,\sigma)} = \Gamma_{\text{relax}} e^{-\beta(\Delta + E_{0\bar{\sigma}})}. \tag{7.47}$$

We also include the similar process of Cooper pair recombination(breaking) from(to) the doubly-occupied subgap state,

$$\Gamma_{(N,0,0)\leftarrow(N,0,2)} = \Gamma_{(N,1,0)\leftarrow(N,1,2)} = \Gamma_{\text{relax}}, \tag{7.48}$$

$$\Gamma_{(N,0,2)\leftarrow(N,0,0)} = \Gamma_{(N,1,2)\leftarrow(N,1,0)} = \Gamma_{\text{relax}} e^{-\beta(E_{0\uparrow} + E_{0\downarrow})}. \tag{7.49}$$

To see how these relaxation rates affect the current through the island, we simulate the differential conductance for different values of Γ_{relax}, shown in Fig. 7.5. We write the relaxation rate in terms of a relaxation time $\tau_{\text{relax}} = h/\Gamma_{\text{relax}}$, which is the lifetime of a quasiparticle in the continuum with respect to relaxing into the subgap state. For smaller τ_{relax} we see the NDC peak diminish and turn into a positive peak, while the peak marked with g' grows. The current blocking effect disappears since the quasiparticle remains trapped in the continuum for a shorter time as it can relax into the subgap state, from which it can exit into the drain subsequently. The relaxation time can be quantified by the relative conductance ratio

$$R = \frac{g' + g_{\text{NDC}}}{g' - g_{\text{NDC}}} \tag{7.50}$$

between the minimum of the NDC peak g_{NDC} and the growing peak g' [Higginbotham *et al.*, 2015]. The relaxation time is then estimated by fitting the model relaxation time to the one obtained experimentally.

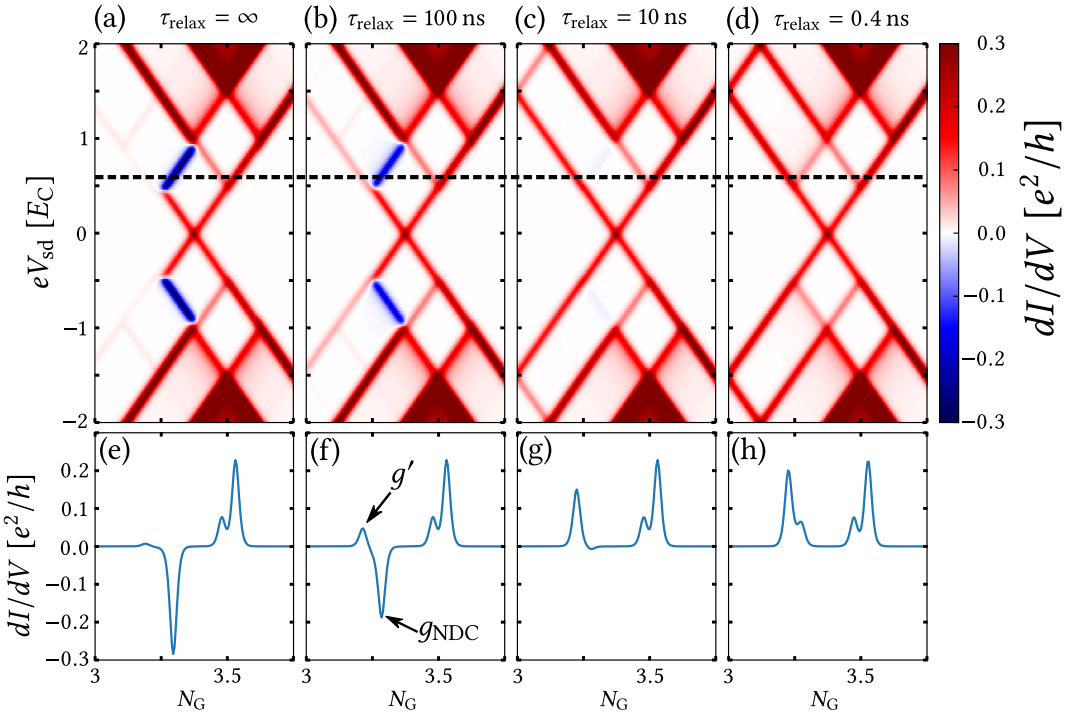

Figure 7.5: (a-d) Differential conductance as a function of the induced gate charge N_G and the source-drain bias voltage V_{sd} in the vicinity of odd to even charge state degeneracy for different values of relaxation times, written above each plot. The x-axis below (e-h) also applies to (a-d). (e-h) Cut along the dashed line in (a-d). The marked conductance peaks g' and $_{\text{NDC}}$ are used to estimate the relaxation time. Parameters are $\Delta = 75\,\mu\text{eV}$, $E_C = 100\,\mu\text{eV}$, $\rho_D = 2.25\,\mu\text{eV}^{-1}$, $\Gamma_{L,R} = 0.1\,\mu\text{eV}$, $E_0 = 25\,\mu\text{eV}$, and $\Gamma^{\text{sub}}_{L,R} = 1\,\mu\text{eV}$.

This concludes the introduction of the master equation model in its general form. Further details will be specified in the concrete cases of the following chapters.

Chapter 8

Transport Signatures of Quasiparticle Poisoning in a Majorana Island

> "Never's the word God listens for when he needs a laugh.
>
> Stephen King, The Dark Tower

This chapter is based on the work presented in [Albrecht et al., 2017].

In many Majorana-based qubit proposals, the quantum information is stored in the parity of the MBS. The MBSs are however not strictly topological due to their finite overlap [Bonderson and Nayak, 2013] and the information is susceptible to errors from quasiparticle poisoning. In recent papers by Plugge *et al.* [2017] and Karzig *et al.* [2017], it is proposed to implement the Majorana-based qubit in a Coulomb blockaded (CB) setup, where a large charging energy will help protect the quantum information. In order to find out if it is feasible to use CB superconducting nanowire islands in these schemes, it is important to know the parity life-time of the charge states in these islands.

In this chapter, we will analyze the data from a tunneling spectroscopy experiment on a CB SC-SM nanowire island, similar to the setup shown in Fig. 8.1. We use the master equation model introduced in Chap. 7 to determine the rate of quasiparticle poisoning of the island.

The setup consists of an InAs nanowire partially covered by epitaxially grown Al on two of the nanowires six facets. The Al covered segment constitutes the floating island and is created by tunnel gate induced barriers at the ends of the segment. The side gate labeled V_G is capacitively coupled to the island and controls the number of charges on the island.

Tunnel spectroscopy is performed by measuring the current I as a function of the applied source-drain bias voltage V_{SD} and either the gate voltage V_G or the magnetic field $B_\perp$. For further details on the experimental setup and more data, see [Albrecht *et al.*, 2017]. Zero bias differential conductance data (not included in this thesis) displays a low energy state, which oscillates as a function of $B_\perp$ in accordance with interpreting the state as a MBS [Albrecht *et al.*, 2016], while the island remains topologically trivial for magnetic field B_{tr}.

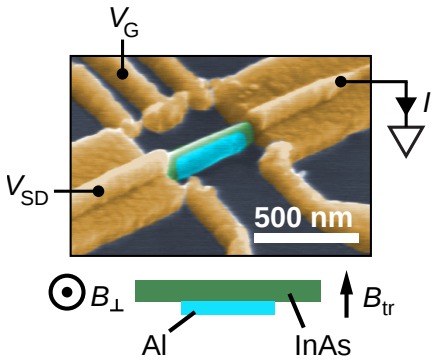

Figure 8.1: Top: Electron micrograph (false color) of a Majorana island device similar to the one used in this experiment. The applied bias voltage V_{SD}, gate voltage V_G, and measured current I are indicated. Bottom: Schematic top view of the InAs nanowire (green) with two-facet epitaxial Al shell (light blue), showing the direction of applied magnetic fields $B_\perp$ and B_{tr}.

8.1 Theoretical model

Before discussing the experimental results, we will briefly summarize the theoretical model, which was introduced in more detail in Chap. 7, in order to discuss the transport processes relevant for estimating the poisoning rate.

We consider the superconducting island to be a floating charged island with N charges. We assume that the density of states of the island can be described by a BCS density of states with superconducting gap Δ, and discrete subgap states at energies $E_{0\sigma}$. At finite magnetic field, the energy of the two spin directions of the subgap state are different, but the continuum is unaffected. We assume that the coherence factors of the subgap states are the same at both ends of the wire where the leads are attached and that the electron and hole components are equal, *i.e.* $|u_{0\sigma}|^2 = |v_{0\sigma}|^2 = \frac{1}{2}$.

The number of charges on the island is given by $N = 2N_{cp} + N_\Delta + N_0$, where N_{cp} is the number of Cooper pairs, N_Δ is the number of quasiparticles in the BCS continuum, and N_0 is the occupation of the discrete subgap states. The charging energy associated with having N charges on the island is

$$E_{el} = E_C(N - N_G)^2, \tag{8.1}$$

and may be controlled through the gate induced charge $N_G = C_G V_G/e$ by tuning the capacitively coupled gate V_G, where C_G is the capacitance between the gate and the island. The internal states of the island are labeled by (N, N_Δ, N_0), with $N \in \mathbb{N}$, $N_\Delta \in \{0, 1\}$, and $N_0 \in \{0, \uparrow, \downarrow, 2\}$ and the island is tunnel coupled to a source and a drain lead with a voltage bias V_{SD} applied between.

We assume that the time between tunneling events is long enough that the island has time to equilibrate. A set of master equations are solved to calculate the distribution functions of states of the island and the current as a function of the voltage bias V_{SD} and the gate voltage V_G. In this set of equations, we include only single electron tunneling transitions, which were calculated in Sec. 7.3, and the model is therefore only valid in the sequential tunneling regime.

For the sake of simplicity, we will in the following discussion restrict the occupation of the subgap state to $N_0 \in \{0, 1\}$, with the subgap state having energy E_0. This is enough to explain the concept behind estimating the quasiparticle poisoning rate, but in the numerical simulations we include the larger set of subgap state occupations given above since it is a more realistic representation of the experimental situation. We will return to how the energy splitting of the two subgap spin states is implemented later.

For the present, we take the energy of the island to be

$$E(N, N_\Delta, N_0) = E_C\,(N_G - N)^2 + N_\Delta \Delta + N_0 E_0. \tag{8.2}$$

In writing (8.2) we assume that if there is a BCS quasiparticle on the island, its energy can be approximated by Δ.

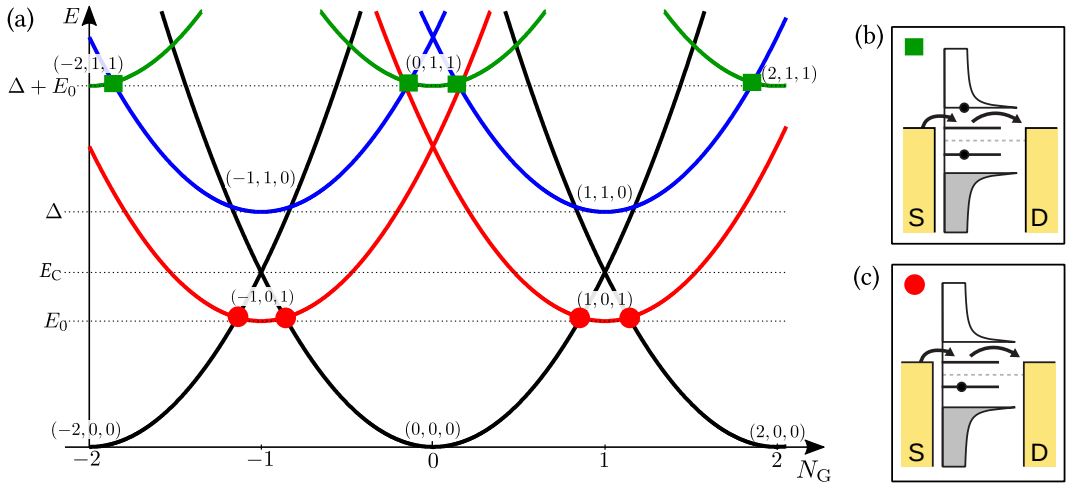

Figure 8.2: (a) Spectrum resulting from Eq. (8.2) for different states (N, N_Δ, N_0) as a function of the gate-induced charge N_G. Red circles mark degeneracies between different charge states $(N_{even}, 0, 0)$ and $(N_{odd}, 0, 1)$, in the ground state branch. Green squares mark degeneracies between different charge states $(N_{even}, 1, 1)$ and $(N_{odd}, 1, 0)$, in a branch of excited (poisoned) states. The plot is made to scale with the parameters extracted from the experimental data: $E_C = 105\,\mu eV$, $\Delta = 140\,\mu eV$, and $E_0 = 75\,\mu eV$. (b) and (c) Processes corresponding to poisoned (green square) and unpoisoned (red circle) transport through the subgap state.

The low-energy part of the resulting spectrum is plotted in Fig. 8.2 (a) as a function of the gate-induced charge N_G where the parameters are extracted from experimental data. Each parabola corresponds to the energy of state (N, N_Δ, N_0) with the labels included in the figure (note that N is to be understood modulo an arbitrary number of Cooper pairs on the hybrid island). For even N, the ground state is a pure BCS condensate without any excitations in the subgap state or in the BCS continuum (black curves in the plot). With this limited occupation space of the subgap state, the first excited state (solid green) has one excitation in the subgap state and one in the BCS continuum, resulting in an excitation energy of $\Delta + E_0$. For odd N, the ground state (solid red) has one excitation in the subgap state (energy E_0), and the first excited state (solid) has one excitation in the BCS continuum instead (energy Δ).

At low temperatures and ignoring quasiparticle poisoning for now, the island is expected to be mostly in its ground charge state, with transport occurring only at charge-state degeneracies, indicated by the red circles in Fig. 8.2 (a). At these points, an extra electron can be added to (removed from) the island without energy cost, changing the occupation of the subgap state. Transport cycles at these degeneracies, schematically shown in Fig. 8.2 (b), correspond to the processes,

$$(N_{even}, 0, 0) \rightleftarrows (N_{odd}, 0, 1). \tag{8.3}$$

The two degeneracies are symmetric about odd values of N_G, and produce a conductance peak pattern with unequal even and odd peak spacings, $S_e = 1 + E_0/E_C$ and $S_o = 1 - E_0/E_C$. The odd-even conductance peak spacing defined here relates to the dimensionless induced gate charge N_G, but it can be related to the gate voltage V_G through the gate lever arm (see

[Albrecht *et al.*, 2017] for details). The peak spacing difference thus gives the energy of the subgap state, [Higginbotham *et al.*, 2015]

$$E_0 = E_C \frac{S_e - S_o}{2}, \tag{8.4}$$

and can be used to track the subgap state in experiments.

Quasiparticle poisoning excites the system from its charge ground state to a state with $N_\Delta = 1$, corresponding to the green and blue parabolas in Fig. 8.2 (a). Due to the relatively weak coupling of the BCS continuum states to the leads, when compared to the subgap state, a quasiparticle may be trapped in the continuum long enough to facilitate observable transport in this excited branch at charge-state degeneracies, marked with green squares in Fig. 8.2 (a). The associated transport cycles, shown in Fig. 8.2 (c), correspond to

$$(N_{\text{odd}}, 1, 0) \rightleftarrows (N_{\text{even}}, 1, 1). \tag{8.5}$$

We include two types of quasiparticle poisoning processes,

$$(N, 0, N_0) \rightarrow (N \pm 1, 1, N_0). \tag{8.6}$$

The "+" corresponds to an electron entering the island from one of the leads, while the "-" corresponds to the breaking of a Cooper pair with one of the electrons exiting the island and the other staying behind as an excitation in the continuum. The processes are characterized by the poisoning rate $\Gamma_p = h/\tau_p$ and poisoning time τ_p. The model does not include poisoning events that populate the subgap state as they will tunnel out again on a time scale set by the large subgap state-lead coupling, $\Gamma^{\text{sub}}_{L,R}$, and thus does not contribute significantly to the shadow peak conductance. In the limit of a weakly coupled island, τ_p sets a lower bound on the parity lifetime of the island.

Processes that bring the island back to an unpoisoned state with $N_\Delta = 0$ include (i) Cooper pair recombination, $(N, 1, 1) \rightarrow (N, 0, 0)$ (made possible by the lack of translational invariance), (ii) quasiparticle relaxation into the subgap state, $(N, 1, 0) \rightarrow (N, 0, 1)$, and (iii) quasiparticle tunneling out to a lead, $(N, 1, N_0) \rightarrow (N - 1, 0, N_0)$. We discussed the relaxation processes in more detail in Sec. 7.3.3. Depending on the relative magnitude of the relaxation rates, the poisoning rate, and the coupling of the subgap state to the source and drain leads $\Gamma^{\text{sub}}_{L,R}$, the transport cycles in Eq. (3) can yield measurable conductance resonances. As evident from Fig. 8.2 (a), the conductance peaks in the poisoned state should occur with the same peak spacings as the unpoisoned state, $S_{e,o}$, but shifted by $1e$ in gate voltage. The conductance height of the poisoned peaks contains quantitative information about the quasiparticle poisoning and relaxation rates. The associated relaxation time was quantified as $\tau_{\text{relax}} = \Gamma^{-1}_{\text{relax}} = 0.1\ \mu$s in Ref. Higginbotham *et al.* [2015], where a similar SC-SM nanowire device was used. These relaxation processes are internal processes of the island and therefore should not depend on the coupling to the leads, so we will use the same relaxation time here.

Zeeman splitting of the subgap states

Applying a magnetic field to the island will split the energy of the subgap states by a Zeeman splitting, which is linear for small fields. Eventually, the state moving up in energy will merge with the (quasi-)continuum of BCS states, whereas the state moving down will evolve into a single low-energy mode (a Majorana mode in the limit of a long wire). We model this effect by including a linear splitting of the two subgap states,

$$E_{0\uparrow}(B) = \begin{cases} E_0 + V_Z & \text{for } 0 \le V_Z < \Delta - E_0, \\ \Delta & \text{for } V_Z \ge \Delta - E_0, \end{cases} \tag{8.7}$$

$$E_{0\downarrow}(B) = \begin{cases} E_0 - V_Z & \text{for } 0 \le V_Z < E_0, \\ 0 & \text{for } V_Z \ge E_0, \end{cases} \tag{8.8}$$

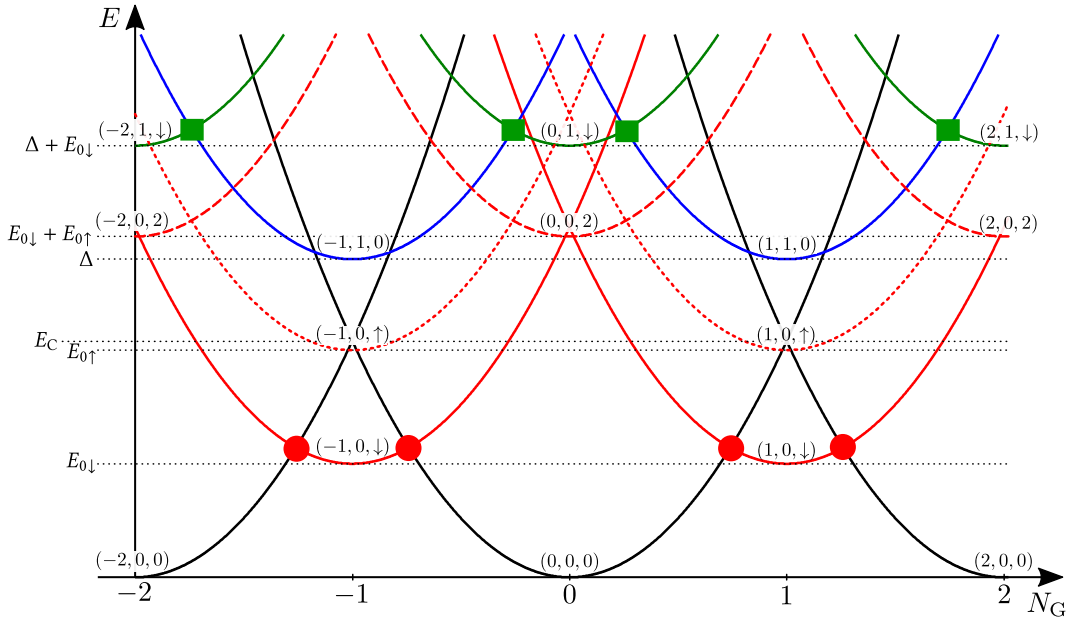

Figure 8.3: Spectrum as a function of the gate-induced charge N_G resulting from Eq. (8.2) with $E_{0\sigma}$ as given in Eqs. (8.7) and (8.8). Labels indicating the different states (N, N_Δ, N_0) are again included, and the plot is again made to scale with the parameters given in the main text: $E_C = 105\,\mu\text{eV}$, $\Delta = 140\,\mu\text{eV}$, and $E_0 = 75\,\mu\text{eV}$. We now also included a Zeeman energy of $E_Z = 25\,\mu\text{eV}$.

where $V_Z = \frac{1}{2} g \mu_B B$ with g the effective g-factor of the subgap state (taken to be positive here). When the state with $\sigma = \uparrow$ reaches the superconducting continuum it stays at the energy $E_{0\uparrow}(B) = \Delta$ for larger B, and when the state with $\sigma = \downarrow$ reaches zero it stays at $E_{0\downarrow}(B) = 0$ for larger B. We also include the effect of the decrease in coupling strength to the leads when the higher subgap state develops into a BCS continuum state in a phenomenological way, by making the coupling parameters spin- and field-dependent,

$$\Gamma^{\text{sub}}_{\alpha,\uparrow} = \Gamma^{\text{sub}}_{\alpha} \left(1 - \frac{E_{0\uparrow}(B) - E_0}{\Delta - E_0}\right) + \gamma_\alpha \frac{E_{0\uparrow}(B) - E_0}{\Delta - E_0}, \tag{8.9}$$

$$\Gamma^{\text{sub}}_{\alpha,\downarrow} = \Gamma^{\text{sub}}_{\alpha}. \tag{8.10}$$

For completeness, we show in Fig. 8.3 again the spectrum as a function of gate-induced charge (similar as in Fig. 8.2), but now including the effect of a finite Zeeman splitting where $E_{0\uparrow}, E_{0\downarrow} < E_C$.

8.2 Results

Spectroscopy of similar SC-SM nanowire islands in a CB setup reported by Higginbotham *et al.* [2015] and Albrecht *et al.* [2016] showed peaks at the unpoisoned resonances, Eq. (8.3), but no features associated with the poisoned transport cycles in Eq. (8.5). We present data here from the 400nm device that was also used in [Albrecht *et al.*, 2016] with barriers set to be more transparent. This increases the coupling of both the subgap state $\Gamma^{\text{sub}}_{L,R}$ and the continuum $\Gamma_{L,R}$, as well as the rate of quasiparticle poisoning from the leads, giving rise to measurable transport features associated with the poisoned resonances Eq. (8.5).

Fig. 8.4 (a) shows the differential conductance, $g = dI/dV_{SD}$ as a function of source-drain bias voltage V_{SD} and gate voltage V_G at zero magnetic field. The data shows a high-conductance Coulomb diamond pattern with large even-occupancy diamonds, small odd-occupancy diamonds, and negative differential conductance (NDC) at finite bias. The

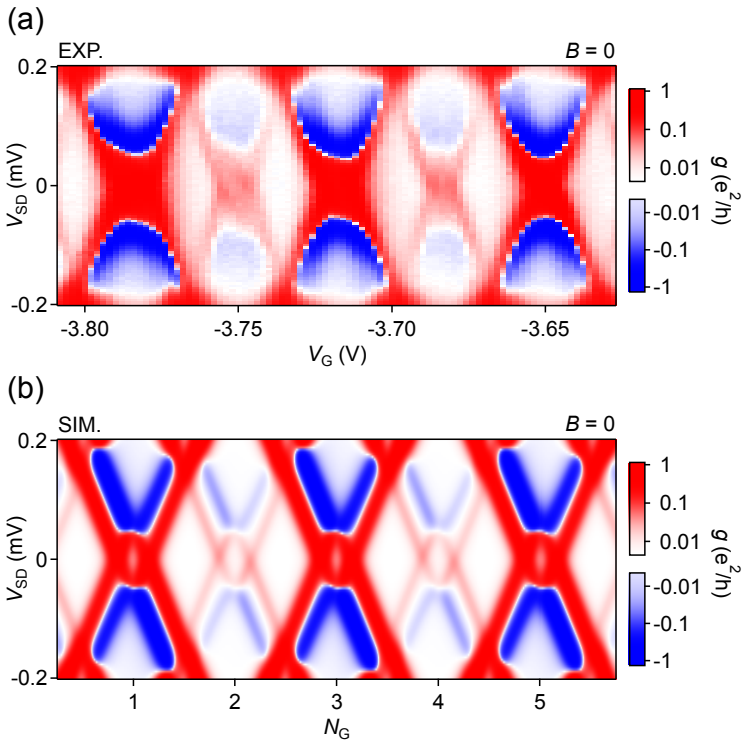

Figure 8.4: (a) Experimental differential conductance g as a function of gate voltage, V_G, and source-drain voltage, V_{SD},at zero magnetic field, showing a series of 2e-periodic Coulomb diamonds with a second set of weaker shadow diamonds offset from the main diamonds by 1e. (b) Numerically calculated differential conductance as a function of gate-induced charge N_G and source-drain voltage with poisoning time $\tau_p = 1.2\,\mu s$.

nearly vanishing odd diamond indicates that the subgap state energy E_0 is only slightly smaller than E_C.

In addition to the main Coulomb diamonds with peak conductance $g_m \approx 0.5e^2/h$ in Fig. 8.4 (a), a weaker set of "shadow" Coulomb diamonds centered on the valleys of the main diamonds, with peak conductance $g_s \approx 0.03e^2/h$. The shadow diamonds are similar to the main diamonds, including regions of NDC, though much lower in conductance and shifted by the equivalent of 1e in gate voltage. Similar shadowlike peaks were previously investigated in metallic superconductor islands by Hergenrother *et al.* [1994], in which case they were made visible by increasing temperature rather than island-lead coupling.

From the main Coulomb diamonds we extract the charging energy $E_C = 105\,\mu eV$ and the zero-field subgap state energy $E_0 = 75\,\mu eV$. Other extracted parameters are: The coupling of the subgap state to the leads, $\Gamma_L^{sub} \approx 4.14\,\mu eV$ and $\Gamma_R^{sub} \approx 24.84\,\mu eV$. The lead-continuum conductance, $g_{Al} \approx 0.7e^2/h$, from which the lead-continuum coupling can be obtained by $\Gamma_{L,R} = g_{Al}(2\pi(e^2/h))^{-1}$. The induced superconducting gap, $\Delta = 140\,\mu eV$, chosen to match the onset of NDC. The temperature in the simulation was $T = 80\,mK$. The relaxation time of quasiparticles from the continuum to the subgap state, previously measured to be $\tau_p \approx 0.1\,\mu s$ in similar devices [Higginbotham *et al.*, 2015].

In Fig. 8.4 (b) we show the simulated differential conductance g as a function of V_{SD} and induced gate charge N_G using the parameters above. The qualitative features of the experimental conductance data are reproduced and a poisoning time of $\tau_p = 1.2\,\mu s$ gives the best agreement with the observed ratio of main and shadow-peak conductance (see below for more details).

Fig. 8.5 (a) shows the measured zero-bias differential conductance as a function of V_G

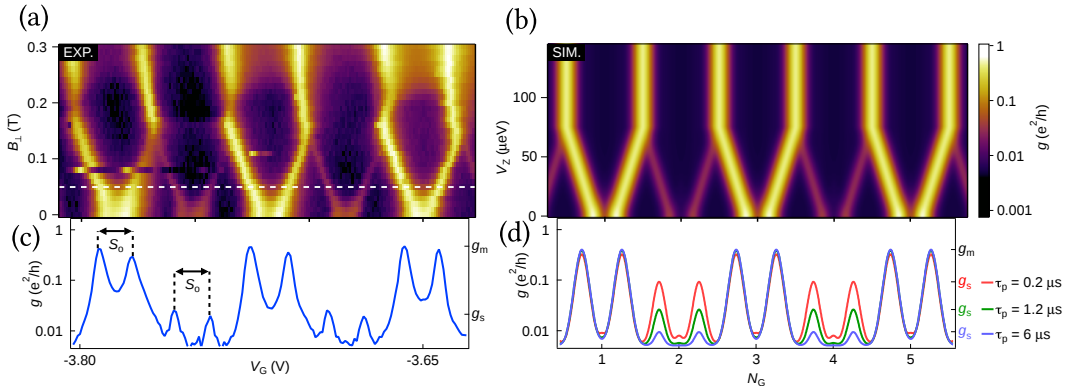

Figure 8.5: (a) Measured zero-bias differential conductance g as a function of perpendicular magnetic field, $B_\perp$, and gate voltage, V_G, showing a series of strong even-odd Coulomb peaks with weaker shadow peaks in the even valleys between main peaks. Both sets of peaks split with increasing field and merge at $B_\perp \approx 160\,\text{mT}$. (b) Simulated differential conductance as a function of Zeeman energy, V_Z, and dimensionless gate voltage (charge number), N_G with poisoning time $\tau_p = 1.2\,\mu\text{s}$. (c) Measured differential conductance vs V_G at $B_\perp = 50\,\text{mT}$ [white dashed line in (a)]. The average heights of the main and shadow peaks are indicated by g_m and g_s, respectively. (d) Simulated differential conductance as a function of N_G for poisoning times $\tau_p = 0.2$, 1.2, and 6 μs. Simulations show an increase in g_s and decrease in g_m for decreasing τ_p.

and perpendicular magnetic field $B_\perp$. The (initially small) odd Coulomb valley spacings increase with $B_\perp$ up to a field of $B_\perp \approx 160\,\text{mT}$, where the average peak spacings become uniform, $\langle S_e \rangle = \langle S_o \rangle$, indicating a zero-energy state $E_0 = 0$. For higher fields, the peak spacings oscillate as a function of magnetic field, as expected theoretically for hybridized Majorana modes [Hützen *et al.*, 2012; Das Sarma *et al.*, 2012; Stanescu *et al.*, 2013] and observed experimentally [Albrecht *et al.*, 2016; Sherman *et al.*, 2017]. Shadow peaks have the same magnetic-field dependence as the main peaks, shifted by $1e$ gate-induced charge. Above $B_\perp \approx 160\,\text{mT}$, where $E_0 \approx 0$, main and shadow peaks merge.

The Zeeman effect on the subgap state is included in the numerical model as described in the previous section. The resulting zero bias conductance g as a function of N_G and V_Z is shown in Fig. 8.5 (b). Using $\tau_p = 1.2\,\mu\text{s}$ as in Fig. 8.4 (b) reproduces the qualitative features of the data, including the splitting and merging of main and shadow peaks.

A cut of g vs V_G at $B_\perp = 50\,\text{mT}$ (where the overlap between adjacent peaks is minimal) is shown in Fig. 8.5 (c). Defining g_m and g_s as the average main and shadow peak conductance, we find $g_m/g_s \approx 18$ in the presented gate range. Model conductance curves for different poisoning times are shown in Fig. 8.5 (d), showing an increase in g_s and decrease in g_m for decreasing τ_p. The decrease in g_m, deemphasized by the logarithmic scale in Fig. 8.5 (d), matches the increase in g_s, reflecting that the island is either in a poisoned or in an unpoisoned state. For these parameters, the model yields the simple dependence,

$$\tau_p = a\frac{g_m}{g_s} + b, \tag{8.11}$$

with $a = 0.068\,\mu\text{s}$ and $b = -0.004\,\mu\text{s}$. From this relation and the observed ratio g_m/g_s, we infer $\tau_p = 1.2 \pm 1\,\mu\text{s}$.

The data presented here is not taken in an optimal tuning for long parity lifetimes. By estimating the maximum ratio g_m/g_s from the noise floor in more weakly coupled device tunings, where no shadow diamonds were observed [Albrecht *et al.*, 2016], a conservative estimate on the poisoning time of $\tau_p > 10\,\mu\text{s}$ can be made. In the limit of a fully decoupled island this time scale of $\sim 10\,\mu\text{s}$ sets a conservative bound on the lifetime of the parity state of the island.

8.3 Summary

In conclusion, we have observed and modeled shadow diamonds offset from the main Coulomb diamonds by $1e$, associated with quasiparticle poisoning of a SC-SM nanowire island, yielding estimates for poisoning times on a $\sim 1\,\mu s$ time scale. High-field measurements indicate a transition to the topological phase, with extracted Majorana mode hybridization energies consistent with previous measurements.

Chapter 9

Probing Electron-Hole Components of Subgap States in Coulomb Blockaded Majorana Islands

> "The most exciting phrase to hear in science, the one that heralds the most discoveries, is not "Eureka!" (I found it!) but "That's funny..."
>
> Isaac Asimov

This chapter is based on the work presented in [Hansen et al., 2018].

The hunt for MBSs has led to an extensive study of SC-SM hybrid nanowires along with a growing list of theoretically predicted features of MBSs. The list includes an exponential suppression of MBS energy with the length of the wire [Kitaev, 2001], a 4π-periodic Josephson effect [Kitaev, 2001], a $(2e^2/h)$-quantized ZBP in conductance [Law *et al.*, 2009; Sengupta *et al.*, 2001; Flensberg, 2010], and non-Abelian braiding statistics [Nayak *et al.*, 2008]. Since the first observations of a ZBP on the background of a soft superconducting gap [Mourik *et al.*, 2012], advancements in material growth have enhanced the quality and resolution of experiments to a point where the more detailed features of the possible MBSs can be subjected to further experimental tests. The clean interface between Al and InAs in epitaxial nanowires has been shown to induce a hard superconducting gap in the nanowire, close to the gap of Al [Chang *et al.*, 2015], which in turn enabled the observation of an exponential suppression of the oscillations of the lowest bound-state energy with increasing wire length in Coulomb blockaded Majorana islands (CBMIs) [Albrecht *et al.*, 2016] as well as, more recently, a quantized zero-bias conductance of $2e^2/h$ [Nichele *et al.*, 2017; Zhang *et al.*, 2017]

However, persistent ZBPs in conductance measurements are not conclusive evidence for the existence of MBSs since other (topologically trivial) phenomena might give rise to ZBPs as well. Trivial Andreev bound states (ABSs) with conductance features resembling MBSs might arise due to disorder [Liu *et al.*, 2012], smooth confinement [Kells *et al.*, 2012], and/or strongly coupled non-superconducting quantum dots at the ends of the nanowire [Liu *et al.*, 2017b]. In certain cases where a dot/normal segment is strongly coupled to the end

of the superconducting nanowire, these trivial ABSs may even result in a $2e^2/h$ quantized conductance peak at zero bias [Moore *et al.*, 2018b; Vuik *et al.*, 2018]. Braiding experiments would give a conclusive answer to whether the states associated with the observed ZBP are topological or trivial in nature, but since these are still outside the reach of current experiments, transport spectroscopy is currently among the best techniques for obtaining information about the low energy quantum states in SC-SM nanowires. It is therefore of great interest to the field to extract additional information about the state behind the ZBP from the currently accessible transport spectroscopy measurements.

Experiments with CBMIs have shown consistent behavior in tunnel conductance measurements over many Coulomb peaks [Albrecht *et al.*, 2016], indicating that transport happens through the same state and that the state is, to a large degree, unperturbed by the change in gate voltage. So far, analyses of the zero-bias conductance in these setups have mainly focused on the oscillations and intensity of individual peaks as a function of system parameters [Albrecht *et al.*, 2016; van Heck *et al.*, 2016; Das Sarma *et al.*, 2012].

In this chapter, we will discuss how zero-bias conductance (ZBC) measurements on CBMIs [see Fig. 7.1] can give information about the electron and hole components of the system's lowest-energy state, which in turn might help to discern whether this state is a MBS or a trivial ABS. We study the ZBC in the sequential tunneling regime with the assumption that the lowest-energy state is well separated from higher excited states on the scale of temperature and tunnel coupling. We find that, the ZBC at even-odd (odd-even) charge degeneracies is proportional to the electron (hole) component of the lowest-energy state, see Fig. 9.1. The ratio of consecutive ZBC peaks thus gives a direct measure of the ratio of the electron and hole components of the state, which can be compared with theoretical predictions.

In the case where the CBMI hosts a pair of MBSs, we find that this ratio will follow a similar beating pattern as that of the energy splitting. MBSs are localized exponentially at the ends of the SC-SM nanowire and the wave-function overlap of a pair of MBSs is exponentially suppressed by the distance between them. When the separation of MBSs is several times larger than the Majorana localization length, the MBSs are, to a good approximation, completely decoupled from each other and consist of an equal superposition of an electron and a hole at zero energy. In shorter nanowires where the overlap between MBSs is non-negligible, the MBSs acquire an energy splitting, which oscillates as a function of the magnetic field. The electron and hole components (u and v) of overlapping MBSs are in general unequal, and the ratio $(|u|^2 - |v|^2)/(|v|^2 + |u|^2)$ oscillates as a function of the magnetic field with the same period as the energy splitting but shifted such that the ratio differs from 0 when the splitting is zero and is ± 1 when the energy splitting is maximal.

This additional piece of information might serve to differentiate a trivial ABS with MBS-like conductance features from a true MBS. We show how this applies to an example case, similar to the setups considered in Refs. [Liu *et al.*, 2017b; Moore *et al.*, 2018a], where a Majorana nanowire with a non-superconducting region at the end hosts a trivial ABS that gives rise to a ZBP similar to what is seen in the experiment reported in Ref. [Deng *et al.*, 2016]. We find that trivial ABSs of this kind can be distinguished from topological MBSs by looking at the correlation between the ratio of conductance peaks and the energy splitting.

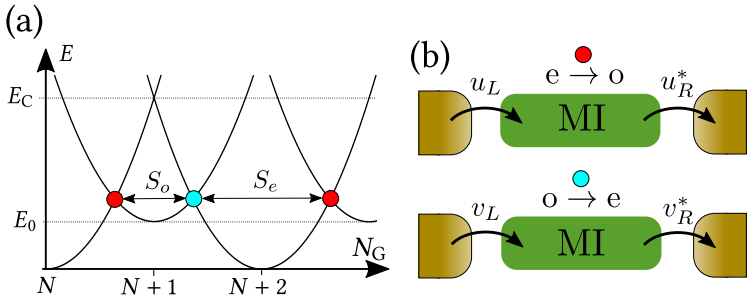

Figure 9.1: (a) Energy spectrum of the CBMI, given in Eq. (9.1), as a function of the dimensionless gate-induced charge N_G. (c) At even-to-odd (odd-to-even) charge-state degeneracies, indicated in (b), the sequential transport is governed by the value of the norm of the subgap state's electron (hole) coherence factor $|u|^2$ ($|v|^2$) at the end of the wire.

9.1 Model

We consider the setup of a CBMI as depicted in Fig. 7.1. It is assumed that the subgap eigenstate of the MI with lowest-energy E_0 is well separated from higher eigenstates on the scales of temperature and tunnel coupling to the leads. In the sequential-tunneling regime, the dominating contribution to conductance at zero bias is by transport through this state, and we will therefore include only this state in our master equation transport model. We label the states of the CBMI by the number of charges N and the occupation of the state at E_0, $N_0 = \{0, 1\}$. The number of charges include an even number of electrons that are condensed into Cooper pairs, and N can only be odd (even) when $N_0 = 1(0)$. The spectrum, shown in Fig. 9.1 (b), is given by

$$E(N, N_G, N_0) = E_C(N - N_G)^2 + N_0 E_0, \tag{9.1}$$

where the first term is the electrostatic energy due to Coulomb interaction with N_G being the dimensionless gate-induced charge proportional to the gate voltage V_G. At zero bias, conductance peaks appear when two charge states are degenerate which is indicated with red and cyan circles in Fig. 9.1 (a). The distance between these peaks is labeled S_o and S_e corresponding to odd or even ground states.

The master equation transport model we employ here was introduced in Chap. 7. In this chapter, we add some more structure to the subgap state as compared to the case in Chap. 8, where $|u|^2 = |v|^2 = 1/2$.

We consider the operator $\psi_\sigma^\dagger(x)$ that creates an electron of spin σ at position x in the SC-SM nanowire that constitutes the CBMI. Writing it in terms of the eigenstates of the CBMI γ_n it takes the form

$$\psi_\sigma^\dagger(x) = \sum_n \left[u_{n\sigma}(x)\gamma_n^\dagger + v_{n\sigma}^*(x)\gamma_n e^{i\hat{\phi}} \right], \tag{9.2}$$

where the sum is over all eigenstates of the MI and $e^{i\hat{\phi}}$ creates the charge equivalent of a Cooper pair on the island. The coherence factors u and v depend on the microscopic model of the MI, which we will return to later. Projecting the tunneling Hamiltonian onto the lowest bound state, with creation operator $\gamma_0^\dagger$, we write it as

$$H_T = \sum_{\sigma, i=L,R} t_{0i}(u_{0\sigma i}\gamma_0^\dagger + v_{0\sigma i}^*\gamma_0 e^{i\hat{\phi}})c_{iv\sigma} + \text{h.c.} \tag{9.3}$$

where $c_{iv\sigma}^\dagger$ is the electronic creation operator of electrons in lead i in state v. We assume a constant density of states in the metallic leads and energy-independent tunnel couplings.

The coherence factors $u_{0\sigma i}$ and $v_{0\sigma i}$ correspond to the coherence factors on the left ($x = 0$) and right ($x = L$) ends of the island for $i = L$ and R, respectively.

The zero-bias conductance can be calculated analytically in the vicinity of ground-state degeneracies by solving the master equation under the approximation that only the two degenerate states contribute to transport. The result is

$$G_{\mathrm{e}\to\mathrm{o}} = \frac{e^2}{h}\frac{\Gamma_L\Gamma_R|u_L u_R|^2}{4(\Gamma_L|u_L|^2+\Gamma_R|u_R|^2)}\frac{\beta}{\cosh^2\left[\frac{\beta}{2}(U_N+E_0)\right]}, \tag{9.4}$$

for the even-to-odd degeneracies, where $\Gamma_{L,R}$ are dimensionless parameters characterizing the coupling to the left and right lead and β is the inverse temperature. We have defined the electrostatic energy difference $U_N = E_{\mathrm{el}}(N+1) - E_{\mathrm{el}}(N)$ between charge states $N+1$ and N and the spin sum of the coherence factor $|u_i|^2 = \sum_\sigma |u_{\sigma i}|^2$. The conductance in the vicinity of the odd-to-even degeneracy is the same, but with $u_i \to v_i$ and $E_0 \to -E_0$:

$$G_{\mathrm{o}\to\mathrm{e}} = \frac{e^2}{h}\frac{\Gamma_L\Gamma_R|v_L v_R|^2}{4(\Gamma_L|v_L|^2+\Gamma_R|v_R|^2)}\frac{\beta}{\cosh^2\left[\frac{\beta}{2}(U_N-E_0)\right]}. \tag{9.5}$$

Assuming that the coherence factors u_i and v_i do not change between neighboring conductance peaks $G_{\mathrm{e}\to\mathrm{o}}$ and $G_{\mathrm{o}\to\mathrm{e}}$, we define the ratio

$$\Lambda = \frac{G_{\mathrm{e}\to\mathrm{o}} - G_{\mathrm{o}\to\mathrm{e}}}{G_{\mathrm{e}\to\mathrm{o}} + G_{\mathrm{o}\to\mathrm{e}}} = \frac{\frac{U_L U_R}{U_L+U_R} - \frac{V_L V_R}{V_L+V_R}}{\frac{U_L U_R}{U_L+U_R} + \frac{V_L V_R}{V_L+V_R}}, \tag{9.6}$$

where we have defined $U_i = \Gamma_i|u_i|^2$ and $V_i = \Gamma_i|v_i|^2$. This ratio is accessible experimentally and carries information about the relative size between electron and hole coherence factors of the subgap state. The ratio goes from -1 where the state is purely hole-like, to $+1$ for a purely electron-like state (at the end positions where the leads are attached). In the general case between these two limits, it might be difficult to disentangle the effective tunnel coupling to the leads, Γ_i, from the coherence factors, $|u_i|^2$ and $|v_i|^2$, which depend on the distribution of the subgap state wavefunction. We will here consider a couple of cases where it is possible.

When the coherence factors are the same where both leads are attached, $u_{L,R} = u$ and $v_{L,R} = v$, the couplings to the leads, $\Gamma_{L,R}$, cancel and the ratio Λ gives a direct measure of the ratio of the coherence factors

$$\Lambda_{\mathrm{uni}} = \frac{|u|^2 - |v|^2}{|u|^2 + |v|^2}. \tag{9.7}$$

This may correspond to a case where the island is made of a uniform SC-SM nanowire and it is an ideal case for determining the ratio of the electron and hole components of the subgap state.

In the limit of very asymmetric couplings to the leads, where $U_R \gg U_L$ and $V_L \gg V_R$, we get

$$\Lambda_{\Gamma_R\gg\Gamma_R} = \frac{|u_L|^2 - |v_L|^2}{|u_L|^2 + |v_L|^2}, \tag{9.8}$$

and the ratio gives a measure of the electron and hole components at the position of the most weakly coupled lead (in this case lead L). Having good experimental control of the couplings to the leads would then make it possible to probe the ratio of the electron and hole components at each lead position somewhat independently.

In the case of symmetric couplings to the leads, $\Gamma_L = \Gamma_R$, we have

$$\Lambda_{\Gamma_L=\Gamma_R} = \frac{\frac{|u_L|^2|u_R|^2}{|u_L|^2+|u_R|^2} - \frac{|v_L|^2|v_R|^2}{|v_L|^2+|v_R|^2}}{\frac{|u_L|^2|u_R|^2}{|u_L|^2+|u_R|^2} + \frac{|v_L|^2|v_R|^2}{|v_L|^2+|v_R|^2}}. \tag{9.9}$$

These results hold in general for any lowest-energy subgap state as long it is well separated from higher-energy states and sequential tunneling processes dominate the transport. The experimentally obtained ratio Λ can then be compared with a microscopic model of the subgap state in order to determine its nature.

We model the SC-SM nanowire that constitutes the CBMI by the single channel BdG Hamiltonian introduced in Sec. 2.3. Previously written details are left out and we only write the single particle Hamiltonian to refresh our memory:

$$\mathscr{H} = \left[-\frac{\hbar^2}{2m^*}\partial_z^2 - \mu - i\alpha_R\partial_z\sigma_x\right]\tau_z + V_Z\sigma_z + \Delta\tau_x, \tag{9.10}$$

where m^* is the effective mass of the electrons, μ is the chemical potential, α_R is the spin-orbit coupling strength, $V_Z = \frac{1}{2}g\mu_B B$ is the Zeeman energy due to the magnetic field B along the nanowire with Landé g-factor g and the Bohr magneton μ_B, and Δ is the induced superconducting gap. The Pauli matrices $\boldsymbol{\sigma}$ and $\boldsymbol{\tau}$ act on spin and particle-hole space, respectively.

The eigenenergies ϵ_n and the electron and hole components $u_{n\sigma}$ and $v_{n\sigma}$ are found by numerically diagonalizing a discretized version of the Hamiltonian obtained using the tight binding approximation on a chain of length L with N sites.

9.2 Results

We will consider both the case of the subgap state being a topological MBS and a trivial ABS, which displays a MBS-like conductance peak at low bias. The ratio Λ will be calculated using Eq. (9.6), rather than extracting it from simulating conductance measurements with the master equation model, but it has been checked that the results agree.

9.2.1 Uniform nanowire

We will first study the case where the nanowire island is a uniform SC-SM nanowire and consider both the topological phase (Zeeman field perpendicular to spin-orbit field) and the trivial phase (Zeeman field parallel to spin-orbit field).

Topologically non-trivial

We study the topological case to look for features that might be used to identify topological MBSs. We take the island to be a uniform SC-SM nanowire of length $L = 1\,\mu\text{m}$ and use $N = 100$ sites in the discretized model. We use symmetric coupling to the leads, $\Gamma_L = \Gamma_R$, although the results are independent of the lead couplings, cf. Eq. (9.7). The other parameters are the effective mass of the electrons in the nanowire $m^* = 0.026m_e$, spin-orbit coupling strength $\alpha_R = 30\,\mu\text{eV}\,\mu\text{m}$, chemical potential $\mu = 0\,\mu\text{eV}$, and superconducting gap $\Delta = 140\,\mu\text{eV}$.

In Fig. 9.2, we see a simulated example of how measured data from a CBMI might look for the parameters given above in the regime with topological MBSs. The ZBC is calculated using Eqs. (9.4) and (9.5), where the energy E_0 and the coherence factors at the end of the nanowire $u_{L,R}$ and $v_{L,R}$ are obtained numerically by diagonalizing the discretized Hamiltonian.

In an experimental data set, such as this, the ratio Λ defined in Eq. (9.6) can then be accessed directly using the heights of consecutive conductance peaks as shown in Fig. 9.2

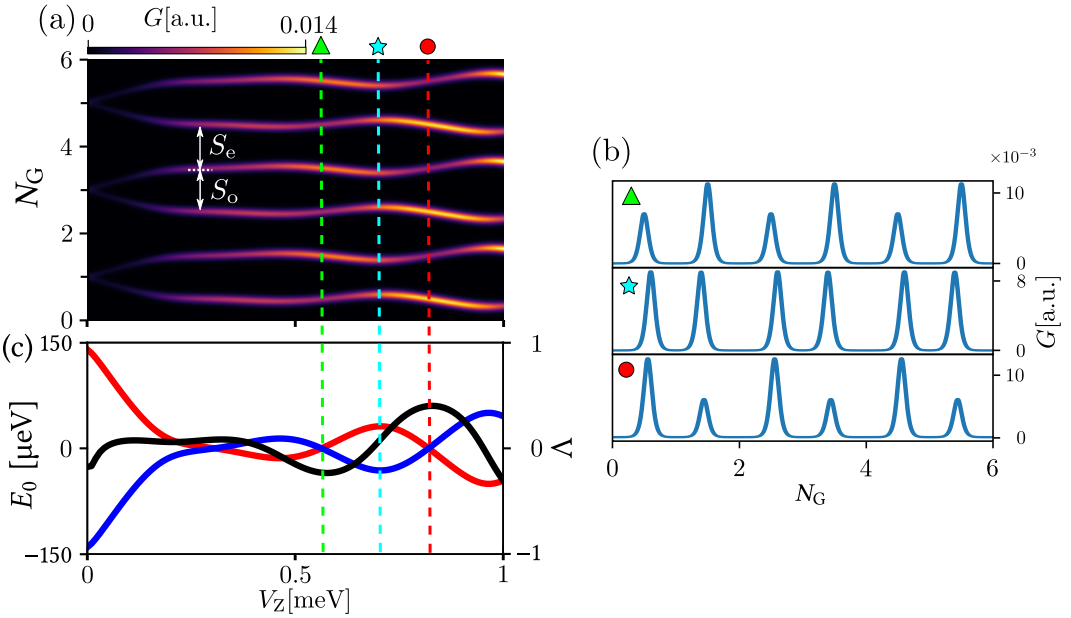

Figure 9.2: (a) Zero-bias conductance as a function of Zeeman-field V_Z and gate-induced charge N_G, calculated from Eqs. (9.4) and (9.5) with $T = 150$ mK, $E_C = 150$ μeV, and $\Gamma_{L,R} = 1$. The colored dashed lines indicate where cuts in (b) are taken and the x-axis is the same as in (c). (b) Cuts along the N_G axis of (a) at $V_Z = 570$ microeV (the green triangle), 685 μeV (the cyan star), and 820 μeV (the red circle). (c) Energy of the subgap state $\pm E_0$ (red and blue) on the left axis, and Λ (black) on the right axis.

(b). The energy of the subgap state can also be extracted from the size of the odd-even peak spacings through [Higginbotham *et al.*, 2015]

$$E_0 = E_C \frac{S_e - S_o}{2}, \tag{9.11}$$

where S_e and S_o are in units of the induced gate charge.

In Fig. 9.2 (c), we see $\pm E_0$ (red and blue), plotted along with the ratio Λ. The oscillating behavior of Λ, seen after the topological phase transition $V_{Z,c} \approx 140$ μeV, is a generic feature of MBSs. The oscillations follow the same period as the splitting between $\pm E_0$ but shifted so that $|\Lambda|$ is maximal when E_0 crosses zero. That is, the MBS is more electronlike/holelike when it is at zero energy and half-electron/half-hole when the energy splitting is maximal. This behavior is generic in the sense that Λ is correlated to the oscillations of E_0 such that, if parameters are changed, Λ will change accordingly to the change in E_0 .

The finite energy splitting and the non-zero Λ are due to the finite size effects, where the MBS at each end of the nanowire hybridize with each other. In longer nanowires, where the overlap between MBSs is smaller, both the energy splitting as well as Λ are smaller, as seen in Fig. 9.3 (a), where a nanowire of length $L = 2$ μm is considered. As the Zeeman field increases, the oscillations of Λ grow in a similar manner as the energy splitting oscillations, due to the increasing overlap of the MBSs.

In the limit of an infinitely long nanowire, both the energy splitting and Λ go to zero. However, this is also the expected behavior in the limit when the nanowire island becomes normal (non-superconducting). It is therefore important to determine if there still is a finite superconducting gap between the subgap state and higher excited states, *e.g.* by considering finite bias conductance.

In experiments, the superconducting gap will eventually be destroyed by the applied magnetic field. This effect is not included in our model, but it appears to be common in

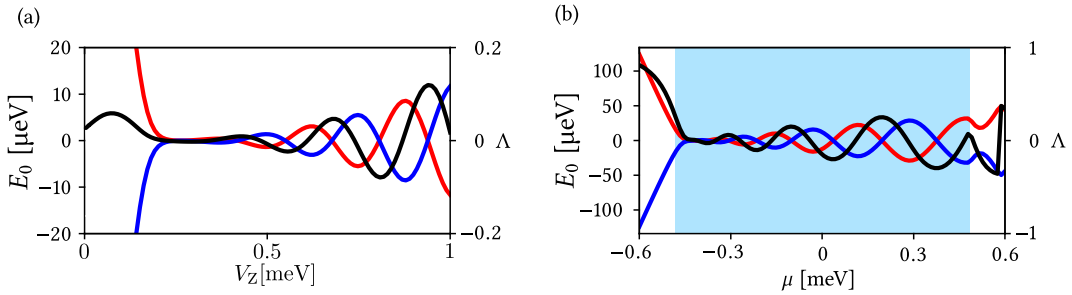

Figure 9.3: Energy of the subgap state $\pm E_0$ (red and blue) on the left axis, and Λ (black) on the right axis as a function of Zeeman field V_Z (a) and chemical potential μ (b). Parameters are the same as in Fig. 9.2, except $L = 2$ μm for (a) and $V_Z = 0.5$ meV in (b). The shaded blue area in (b) indicated the topological phase in the range $|\mu| < \sqrt{\Delta^2 + V_Z^2} \lesssim 520$ μeV.

current state of the art experiments to observe only one or two energy splitting oscillations as a function of magnetic field. It is therefore difficult to investigate the correlated behavior between the energy splitting and Λ discussed above as a function of magnetic field. However, the energy splitting and Λ is correlated in the same way as a function of chemical potential, as seen in Fig. 9.3 (b). Even when the Zeeman/magnetic field is tuned to the first maximum of the energy splitting oscillations as done here, the topological phase contains several oscillations as functions of μ. This makes the chemical potential a more attractive parameter to be able to tune in experiments when looking for correlations between the energy splitting and Λ and it was recently observed in experiments by O'Farrell *et al.* [2018].

The kinks in the curve of Λ at large μ are due to a crossing of the lowest and second lowest energy subgap state. Since the two states have different ratios of electron-hole components and we only include the lowest-energy subgap state in our model, Λ will jump when the lowest-energy state changes. Taking higher energy states into account is expected to smooth out the kinks of the curve where the lowest-energy state crosses the second lowest state, but not change Λ where there is a considerable gap between the lowest and second lowest-energy state. Including the effects of higher energy states should thus not affect the observed behavior inside the topological phase, since there is a considerable gap between these and the subgap state.

In this section, we considered the nanowire island to be a uniform SC-SM nanowire for which $|u_L|^2 = |u_R|^2$ and $|v_L|^2 = |v_R|^2$. The ratio Λ was thus given by Eq. (9.7) which is independent of the couplings to the leads $\Gamma_{L,R}$. Tuning the couplings to the leads may be used experimentally to study whether the nanowire island is uniform or at least uniform enough that the subgap state is coherent across the island. It would be signified by Λ being independent of tuning the couplings to the leads, assuming that tuning the coupling does not perturb the subgap state inside the nanowire significantly.

Topologically trivial case

Next we consider the situation where the Zeeman field is parallel to the spin-orbit field, such that the nanowire stays in the trivial phase. The energy of the lowest-energy state and Λ as a function of Zeeman field is shown in Fig. 9.4 (a). In this case there is no gap between the lowest-energy and second lowest-energy state, as seen in (b). Since both states will contribute to transport when they are approximately degenerate, we can not expect the picture in (a) to be completely accurate, but it still gives a qualitative picture of the correlation between the energy splitting and Λ.

The curve of Λ jumps when the lowest and second lowest-energy states cross each other. We expect, as in the previous section, that including the second lowest state in our

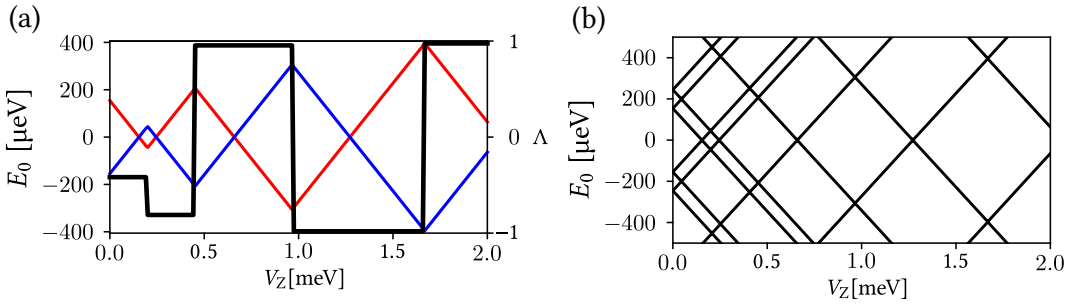

Figure 9.4: (a) Energy of the subgap state $\pm E_0$ (red and blue) on the left axis, and Λ (black) on the right axis and (b) eigenenergies as a function of Zeeman field V_Z for a Zeeman field parallel to the spin-orbit field. Parameters are the same as in Fig. 9.2, except $L = 0.4$ μm.

model will result in a smoothening of these jumps, but that the oscillating behavior will be left unchanged. The oscillations of Λ are hence correlated with the energy splitting oscillations in the same way as we saw in the topological case above. It might therefore be difficult to tell the two apart by only considering the energy splitting and Λ. This correlated behavior between Λ and the energy splitting should therefore be viewed as a signature of the nanowire island being uniform enough that the subgap state is coherent across the island, rather than a MBS signature. Under the right conditions, that is a considerable spin-orbit interaction and magnetic field perpendicular to the spin-orbit field, this state should turn into a MBS. Finite bias measurements can be used to align the magnetic field correctly and determine whether there is a gap between the lowest-energy state and higher energy states.

9.2.2 Dot-Nanowire system

We will now consider the case where the island is a non-uniform SC-SM nanowire. Occasionally, a quantum dot is formed in the nanowire at the position of a tunnel barrier, as in the experiment considered in Chap. 5.

Several theoretical studies of SC-SM nanowires with non-uniform potentials in a grounded nanowire setup have reported the existence of low-bias conductance features in the topologically trivial regime, which are similar to MBS features. Liu *et al.* [2017b] found that in the case of the dot being strongly coupled to the superconducting part of the nanowire (*i.e.* no potential barrier between the dot and nanowire), low-bias conductance features emerged in the topologically trivial regime, which were very similar to the features observed in the experiments by Deng *et al.* [2016].

In work by Moore *et al.* [2018a], it was found that non-uniform potentials or a non-superconducting segment at the end of the nanowire may give rise to low energy partially separated ABS (ps-ABS) in topologically trivial parts of parameter space. These ps-ABSs may exhibit conductance features similar to MBSs, such as a robust ZBP with $2e^2/h$ quantized conductance as a function of Zeeman field [Moore *et al.*, 2018b]. The ps-ABSs are mainly localised at only one end of the nanowire, as opposed to MBSs, which have equal and correlated parts at both ends. It was proposed to discern the ps-ABSs from MBSs by looking at the correlations between ETS conducted at both ends of the nanowire.

In this section, we will study such ps-ABSs in a non-uniform nanowire and see how they may be distinguished from MBSs in a coulomb blockaded setup. We take the island to be as SC-SM nanowire where a segment at the end of the nanowire is uncovered by the superconductor, as pictured in Fig. 9.5. The superconductor covers a part of the nanowire of length L_Δ and the uncovered part is of length L_{dot}. Although a more realistic setup would have a normal segment at both ends of the nanowire, we consider this setup for simplicity.

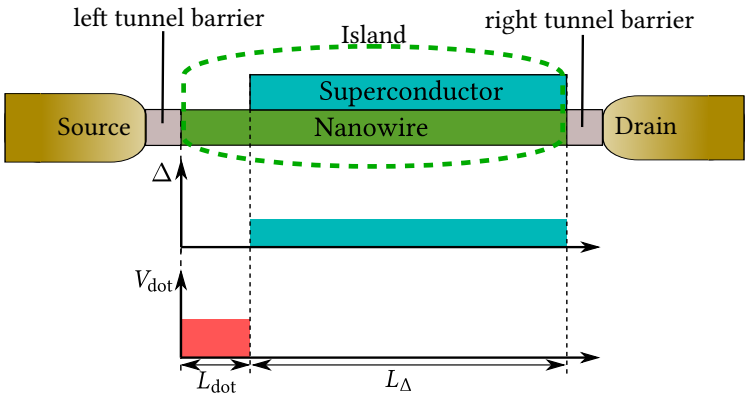

Figure 9.5: (top) Schematic picture of the Coulomb blockaded nanowire island setup and the spatial profile of the induced superconducting gap Δ (middle) and the potential in the dot V_{dot} (bottom).

Case	(A)	(B)
Induced superconducting gap:	$\Delta = 140\,\mu eV$	$\Delta = 250\,\mu eV$
Dot size:	$L_{dot} = 0.15\,\mu m$	$L_{dot} = 0.3\,\mu m$
Spin-orbit interaction:	$\alpha_R = 30\,\mu m\,\mu eV$	$\alpha_R = 40\,\mu m\,\mu eV$
Dot potential:	$V_{dot} = 1000\,\mu eV$	$V_{dot} = 750\,\mu eV$

Table 9.1:

We will refer to non-superconductor-covered segment as the ”dot” for easy reference even though it does not constitute a quantum dot. The Hamiltonian describing the island is still Eq. (9.10), but now with induced superconducting gap in only a part of the nanowire,

$$\Delta(z) = \begin{cases} 0 & \text{for } z < L_{dot}, \\ \Delta & \text{else}, \end{cases} \tag{9.12}$$

and a dot potential

$$V_{dot}(z) = \begin{cases} V_{dot}\tau_z & \text{for } z < L_{dot}, \\ 0 & \text{else}. \end{cases} \tag{9.13}$$

We simulate this setup with two sets of parameters. In Case (A), we will see a subgap state going to zero and oscillating around zero in a MBS-like manner. In case (B), we see a subgap state going to zero energy and forming a robust ZBP with constant conductance close to $2e^2/h$. The common parameters are the superconductor covered section $L_\Delta = 1\,\mu m$ and the effective mass of the electrons $m^* = 0.026m_e$, while the case specific ones are given in table 9.1. The remaining parameters are given in the captions of the figures.

In order to identify a parameter regime where these MBS-look-alike ps-ABSs exist, we simulate transport, where the right tunnel barrier is completely open and the island is grounded, using the S-matrix formalism introduced in Chap. 3.

In Fig. 9.6 (a) and (b), we see a subgap state starting at finite energy which moves to zero energy as a function of Zeeman field. In (a), it oscillates around zero energy in a way similar to a MBS while in (b) it remains zero for an extended range of the Zeeman field. However, the topological phase transition happens at $V_{Z,c} = \sqrt{\Delta^2 + \mu^2}$, which is $V_{Z,c}^{(A)} \approx 1550\,\mu eV$ and $V_{Z,c}^{(B)} \approx 1350\,\mu eV$ in the two cases, hence the ZBP is due to a trivial ABS. The zero-bias conductance shown in (c) is not quantized exactly at $2e^2/h$, but shows a plateau at $\approx 1.75e^2/h$.

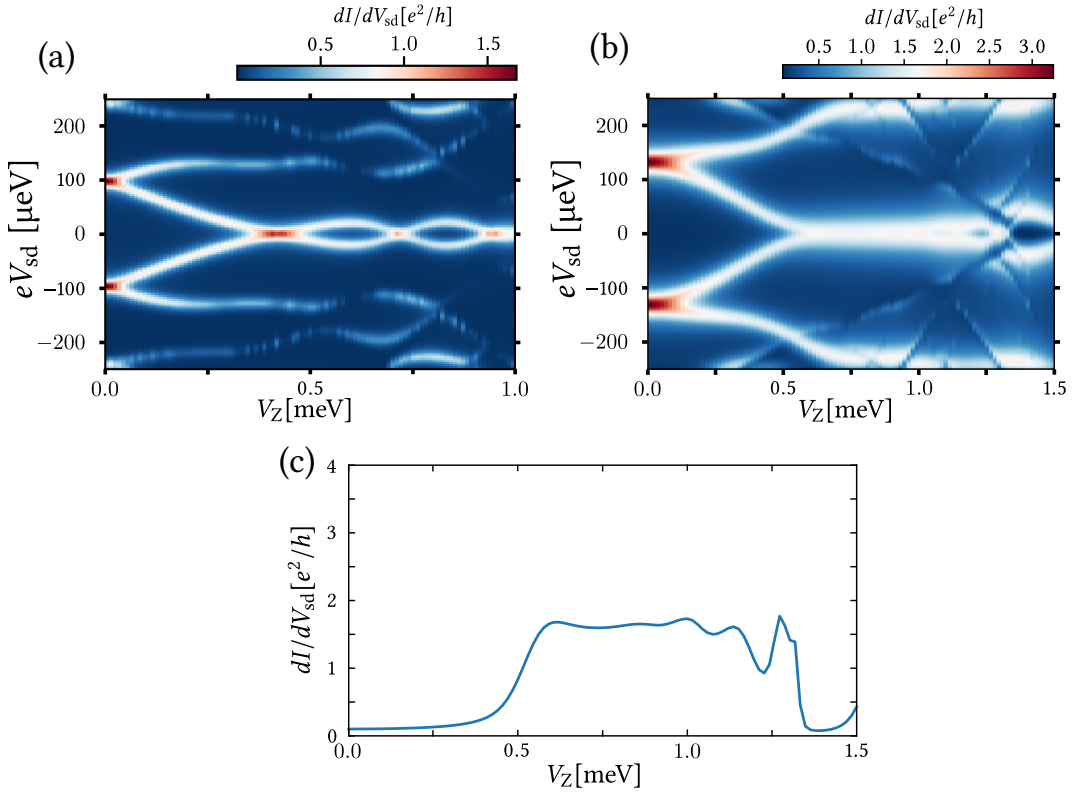

Figure 9.6: (a) and (b) Differential conductance as a function of source drain bias voltage V_{sd} and Zeeman field V_Z. (a) [(b)] correspond to case (A) [(b)] with $\mu = 1550\,\mu$eV [1320 μeV] and the effective tunnel coupling to source lead is $\gamma = 1\,$meV [4.5 meV]. (c) Zero-bias differential conductance as a function of Zeeman field V_Z.

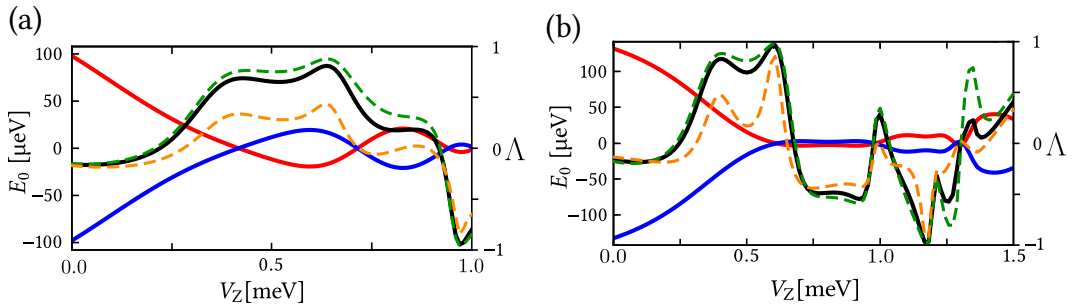

Figure 9.7: Energy of the subgap state $\pm E_0$ (red and blue) on the left axis, and Λ on the right axis for symmetric coupling to the source and drain leads $\Gamma_L = \Gamma_R$ (black) and for asymmetric couplings $\Gamma_L = 10\Gamma_R$ (dashed green) and $\Gamma_R = 10\Gamma_L$ (dashed orange). (a) correspond to case (A) with $\mu = 1550\,\mu$eV and (b) to case (B) with $\mu = 1320\,\mu$eV.

Since the chemical potential μ is not known in experiments and the g-factor is estimated from the slope of the subgap state, the critical magnetic field where the topological phase transition occurs is not known. In an infinite system, the phase transition is accompanied by a closing of the superconducting bulk gap, but it is not necessarily visible in finite systems [Stanescu *et al.*, 2012]. ZBPs such as these two examples may thus be mistaken as signatures of MBSs.

We proceed to the case where tunnel barriers are induced at both ends and the nanowire becomes a floating charged island. We assume that the low energy spectrum is not affected by the right tunnel barrier now being closed and extract the electron and hole coherence

factors of the lowest-energy state at the ends of the nanowire, as in the uniform case.

The evolution of E_0 and Λ as function of the Zeeman field in the two cases is shown in Fig. 9.7. In (a), corresponding to case (A), if the lowest-energy state were a MBS, we would expect Λ to oscillate in the same way as the energy splitting, but shifted so that $|\Lambda|$ has a local maximum when E_0 cross zero and $|\Lambda| \approx 0$ when $|E_0|$ has a local maximum. Instead we see Λ being mostly positive, corresponding to the state being mostly electron-like. Λ also shows some dependence on the relative strength between the couplings to the source and drain leads, as shown by the dashed orange and green curves being distinct from the black curve.

In (b), the oscillations of E_0 are very small over an extended range of Zeeman fields, so for a MBS we would expect the Λ to be close to 0 in this range. Instead we see Λ oscillating back and forth across 0 in a seemingly unsystematic manner and that Λ depends on the relative strength of the couplings to the leads for some values of V_Z.

In light of the correlation between Λ and E_0 in the case of uniform nanowires and MBSs, as discussed in Sec. 9.2.1, both cases discussed here exhibit very different behavior and can be discounted as MBS candidates.

Further details on trivial low-energy ABS

We will study these trivial ABSs a bit further in order find their origin and where they might be encountered.

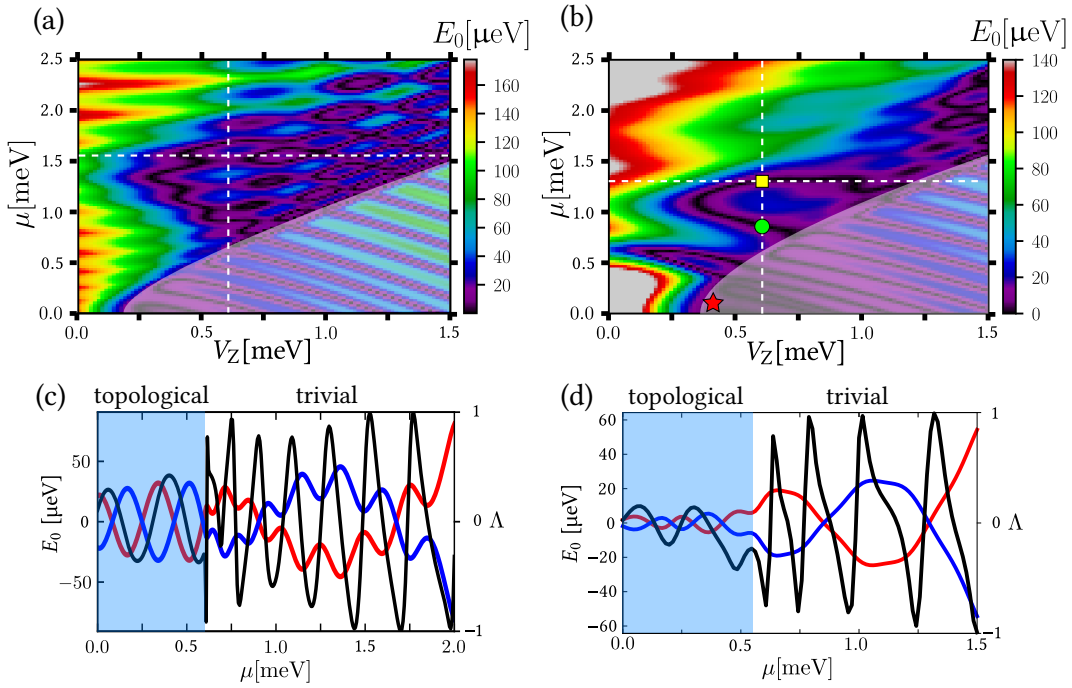

Figure 9.8: (a) and (b): Energy of the lowest-energy state as a function of Zeeman field and chemical potential for case (A) and (B) with parameters as given in the text. The horizontal white dashed lines indicate the value of μ where Fig. 9.7 (a) and (b) are taken, while the vertical white dashed lines indicate the value of V_Z where (c) and (d) in this figure are taken. The regime where the superconductor covered part of the nanowire is in the topological phase is indicated by the white-shaded region. The red star, green circle, and yellow square indicate values of V_Z and μ used in Fig. 9.9. (c) and (d): Energy of the subgap state $\pm E_0$ (red and blue) on the left axis, and Λ on the right axis (black) as a function of chemical potential (for $\Gamma_L = \Gamma_R$) with $V_Z = 600$ in both (c) and (d). The light-blue shaded region indicates the region where the superconductor covered part of the nanowire is topological.

In Fig. 9.8 (a) and (b), we see the energy of the lowest-energy state as a function of Zeeman field and chemical potential in cases (A) and (B), respectively. The consistent striped pattern seen in the topological regime (white shaded) is symptomatic of MBS oscillations. Outside the topological region there are regions with high chemical potential where the lowest-energy state cross zero energy (black color). Although these trivial low-energy states seem to be generic at large μ for a range of model parameters, the parameter configurations where the states behave in a MBS-like manner as function of the Zeeman field are fine-tuned points. We discussed two such cases (indicated by the horizontal white dashed lines in Fig. 9.8 (a) and (b)) in the section above. A slight change of μ alters the evolution of E_0 as a function of V_Z drastically. There is thus a clear difference between the systematic behavior in the topological phase and the more chaotic behavior in the trivial phase.

This is also seen in Fig. 9.8 (c) and (d), where we compare the splitting of the lowest-energy state (blue and red) with Λ (black) as a function of the chemical potential. In the topological regime (light blue shaded) we see the same correlated behavior between the energy splitting oscillations and Λ as in the case of the uniform nanowire. In the trivial regime we see two distinct behaviors, but both are different from the topological and uniform cases. In case (A) [Fig. 9.8 (c)], the energy splitting oscillates around zero, but Λ clearly oscillates with a different period than the energy splitting. In case (B) [Fig. 9.8 (d)], Λ oscillates with the same frequency as the small energy oscillations, but the energy oscillations are not centered around zero.

Both behaviors are different from that of the MBS in the topological regime, where we expect the energy splitting to oscillate around zero and Λ to oscillate with the same period, but shifted by $\pi/2$ relative to the energy splitting. It should therefore be possible to discern trivial ABSs of this kind from MBSs by looking at the correlation between the energy splitting and Λ as a function of the chemical potential.

Even in the case where it is possible to find a set of parameters in the trivial regime where the energy splitting and Λ are correlated as a MBS as a function of V_Z (μ), it would most likely be a very fine tuned point in parameter space, which should be revealed by tuning μ (V_Z).

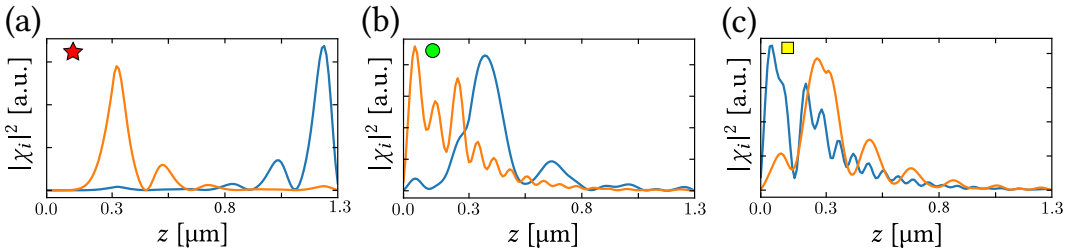

Figure 9.9: Spatial wavefunction of the two Majorana modes of the lowest-energy fermionic mode with energy E_0. (a, red star) MBS in the topological phase with $\mu = 100\,\mu$eV and $V_Z = 400\,\mu$eV. (b, green circle and c, yellow square) Trivial low-energy ABS with parameters $V_Z = 600\,\mu$eV and (b) $\mu = 880\,\mu$eV and (c) $\mu = 1320\,\mu$eV. The values of μ and V_Z are indicated by corresponding symbols in Fig. 9.8 (a). The remaining parameters are given in the text for case (A).

Lastly, we look at the spatial wavefunctions of the two Majorana modes that the lowest-energy fermionic mode can be decomposed into, using Eq. (2.39) and (2.39). This decomposition is not only tied to the MBS, but can be done for any fermionic mode, although for a MBS, the two constituting Majorana modes will be spatially separated, as we discussed in Sec. 2.3.

In Fig. 9.9 (a), we show the Majorana modes of a MBS in the topological regime, localized at the edges of the topological phase (superconductor covered part of nanowire). This is compared with two trivial low-energy ABSs in (b) and (c) where the two Majorana modes

are localized at the left end of the nanowire where the dot is situated. The Majorana modes of these trivial low-energy ABSs do not overlap completely, but rather are slightly separated, earning them the name partially-separated ABSs (ps-ABSs) as they have been termed by Moore *et al.* [2018a]. When the separation is so large that only one Majorana mode has weight at the left end, it may be impossible to tell this ps-ABS from a MBS using only ETS at the left end. However, since the ps-ABS is only located at one end of the nanowire, as opposed to the MBS, it should also be possible to discern from a MBS by looking at the correlation between the conducted ETS at both ends of the nanowire, as proposed by Moore *et al.* [2018a]. Here, we have discussed another way of discerning these ps-ABSs, by considering the correlation between the lowest-energy state splitting and Λ in Coulomb blockaded transport experiments in the sequential tunneling regime.

9.3 Summary and perspective

In this chapter, we have calculated the ZBC through a CBMI hosting a single isolated subgap state in the sequential tunneling regime. We found that the height of the ZBC peaks at the even-to-odd $G_{e\to o}$ (odd-to-even $G_{o\to e}$) charge state degeneracy is proportional to the electron (hole) components of the subgap state wavefunction at the position of the tunnel coupled leads. By considering the ratio of neighboring conductance peaks,

$$\Lambda = \frac{G_{e\to o} - G_{o\to e}}{G_{e\to o} + G_{o\to e}}, \tag{9.14}$$

it is possible to gain information about the relative size of the subgap state's electron and hole components.

We proceeded to study the correlated behavior between the ratio Λ and the energy of the subgap state for different microscopic models of the MI and subgap states. We considered the case of a uniform SC-SM nanowire both in the topological case with MBSs (Zeeman perpendicular to spin-orbit) and the trivial case (Zeeman parallel to spin-orbit).

In the topological case, Λ oscillates with the same frequency as the energy splitting of the MBS but shifted such that $\Lambda \approx 0$ when the energy splitting is maximal and $|\Lambda|$ is maximal when energy splitting is ≈ 0. This behavior is observed both as a function of Zeeman field and chemical potential. In the limit of a long nanowire where the MBSs are decoupled, the energy splitting and Λ goes to zero.

In the trivial case, we see the same correlated behavior between the energy splitting of the subgap state and Λ. The correlated oscillations between the energy splitting and Λ can therefore not be used as exclusive indicators of the presence of MBSs. It is rather indicating that the SC-SM nanowire constituting the MI is uniform and that the subgap state may evolve into a MBS under the right circumstances, *i.e.* Zeeman field perpendicular to spin-orbit field and strong spin-orbit interaction. It may also be used to discard certain trivial low-energy ABSs that behave similar to MBSs.

As an example, we considered the case of a non-uniform SC-SM nanowire where a segment at the left end of the nanowire was not covered by the superconductor. This case is known to exhibit trivial low-energy ABSs which give rise to MBS-like conductance features in one-end ETS in a grounded nanowire setup [Liu *et al.*, 2017b; Moore *et al.*, 2018a; Vuik *et al.*, 2018]. We considered two sets of parameters where a low-energy subgap state either oscillated around zero energy or formed a robust ZBP as a function of Zeeman field in a manner similar to what is expected for a MBS. In both cases, the correlations between the energy splitting and Λ was significantly different from the observed behavior in the uniform and topological case above which makes it possible to distinguish these trivial ABS states from MBSs.

It is nevertheless not possible to rule out the possibility of trivial ABSs where the energy splitting and Λ correlate in the same manner as MBSs. Further investigations of these trivial low-energy ABSs revealed that they seem to exhibit MBS-like behavior only at fine tuned points, which may be uncovered by tuning the chemical potential. It may hence be possible to distinguish these trivial ABSs from MBSs in general by looking at the correlations between the energy splitting and Λ both as a function of magnetic field and chemical potential.

We also looked at the wavefunctions of these trivial low-energy ABSs and found that they are located mainly in the non-superconducting segment at the left end of the nanowire, in contrast to MBSs that are located at both ends of the superconducting segment. Decomposing them into two Majorana modes showed that the ABS is what could be termed as a partially-separated ABS, where the two Majorana modes are not separated well enough to be considered real MBSs [Moore *et al.*, 2018a].

The kind of trivial low-energy ABSs we have studied here occur somewhat generically at large chemical potential, as seen in Fig. 9.8 (a) and (b). Their details depend strongly on the size and potential in the dot/normal segments as well as the strength of the spin-orbit interaction. Ongoing studies (not included in this thesis) seems to indicate that these ABSs can be avoided or made less frequent by having a short dot/normal segment ($\lesssim 100\,\mathrm{nm}$) and a larger potential (barrier).

9.3.1 Ideas for future work

Due to the constraints of time, some questions will have to be left open for future studies. We will here discuss a couple of ideas that might be natural to consider next.

Normal-superconductor-normal setup

In the non-uniform case above, we considered a SC-SM nanowire with a non-superconducting segment only at the left end. However, a more realistic setup in the Coulomb blockaded setup would be a normal-superconductor-normal (NSN) configuration since tunnel barriers are induced at both ends of the SC-covered nanowire. Although we will not be studying this setup here, we will argue that the results found above apply to the NSN setup in most cases.

In a Coulomb blockaded setup, the two tunnel barriers at the ends would in general not be identical, and we should thus consider a NSN setup with normal segments of different sizes and potentials. The MBSs live inside the superconducting region and are thus not very sensitive to changes in the N segments. We therefore expect the topological case to be very similar to the case we have discussed in this chapter. The ps-ABSs on the other hand are localized in the normal segments, and for a non-symmetric setup we expect the ps-ABS located in each normal segment to be different in general, except at some fine tuned points. We base this on the observed behavior of the ps-ABSs in this chapter where we found the ps-ABSs to depend very sensitively on the potentials. In particular, we expect the two ps-ABS in the NSN setup to have different electron and hole component. This should make it possible to distinguish them from MBSs by looking at the correlation between the energy splitting and Λ in the same way as discussed in this chapter.

Disorder

From our consideration of the uniform SC-SM nanowire, we concluded that the correlated behavior between the oscillations of the energy splitting and Λ cannot be used as an exclusive indicator of a MBS, since both the trivial and topological cases showed the same qualitative behavior. Rather, the correlated behavior is an indication that the SC-SM

nanowire that constitutes the MI is uniform or at least uniform enough that the electron and hole components of the subgap wavefunction are the same at both lead interfaces. It is thus natural to ask "what is uniform enough?", and study how non-uniform potentials and disorder potentials inside the superconducting segment affect the wavefunction of the subgap state both in the topological and trivial cases. This has already been done [Kells *et al.*, 2012; Brouwer *et al.*, 2011; Rainis *et al.*, 2013], and the focus should thus be made on how non-uniform potentials and disorder may affect the correlated behavior between the energy splitting and Λ in relation to what is observed in the uniform case.

Higher order transition rates

Our studies of the correlated behavior between Λ and the energy of the lowest-energy subgap state rely on the equations we derived for the conductance peak heights [Eq. (9.4) and (9.4)], which are valid in the sequential transport regime. This regime might not always be accessible experimentally, and it is thus relevant to investigate whether information about the electron-hole components also can be extracted in other transport regimes.

The cotunneling regime is a natural next case to consider. Although explicit calculations are needed in order to get quantitative answers, we will discuss some qualitative considerations of what may be expected using the intuition we have gained in this chapter.

In the case of $E_0 > E_C$, the odd charge state parabolas in Fig. 9.1 (a) will be shifted above the N and $N+2$ charge state degeneracies, and all ground states have even parity. At the charge state degeneracies between N and $N+2$, the Cooper pair tunneling process, where two electrons tunnel in (out) of the island by forming (breaking) a Cooper pair, is resonant. This process involves the combination of the two single electron tunneling processes we considered and will be proportional to $|u|^2|v|^2$. It will thus not be possible to probe the electron-hole components of the subgap state using this resonance.

Another process to consider is cotunneling, where an electron enters (exits) on one side of the island and exits (enters) on the other side. Depending on whether $E_0 > E_C$ or $E_0 < E_C$, there may be two or four relevant tunneling processes.

Starting with the case of $E_0 > E_C$, we may not be able to neglect the effects of higher energy states, but for the sake of the argument, we only consider tunneling processes involving the lowest-energy subgap state. This corresponds to only including elastic cotunning processes through the subgap state. We label the states of the island by (N, N_0), where N is the number of charges and N_0 is the occupation of the subgap state. The two relevant cotunneling processes are

$$(N,0) \to (N+1,1) \to (N,0) \quad \text{and} \quad (N,0) \to (N-1,1) \to (N,0), \tag{9.15}$$

where the state in the middle is the virtual intermediate state. In the first process, an electron first enters the island by occupying the subgap state and afterwards it exits while emptying the subgap state. Both of these single electron tunneling events couple to the electron component $|u|^2$ of the subgap state. For the second process, both single electron processes couple to the hole component $|v|^2$. The first process will thus be proportional to $|u|^4$, while the second to $|v|^4$. The first process dominates in the gate interval N to $N+1$ (with N being even), since the virtual state $(N+1,1)$ has lower energy than $(N-1,1)$. The situation is opposite in the gate interval $N-1$ to N, where the second process will dominate.

With these considerations in mind, we may expect an asymmetry between the electron and hole components, u and v, to be reflected in the differential conductance around the center of the Coulomb valleys at gate tunings N_G = even. If $|u| > |v|$, we expect an asymmetry with larger differential conductance on the right side of the valley, and vice versa.

In making these arguments, we neglected higher energy states. This is not a good assumption when there is no gap between these states and the lowest-energy state, or the gap is small and the higher energy states form a dense spectrum. Especially since the higher energy states may therefore wash out the effect of asymmetric u and v components of the subgap state.

When searching for potential MBSs, the case where $E_0 < E_C$ is of greater interest. Here we have both even and odd parity ground states, and we expect the higher energy states to have a smaller effect, since they are separated from the lowest-energy subgap state by the induced gap. The relevant cotunneling processes are the two discussed above for the even ground states and

$$(N+1,1) \to (N,0) \to (N+1,1) \quad \text{and} \quad (N-1,1) \to (N,0) \to (N-1,1), \tag{9.16}$$

for the odd ground states. The first process involves two single electron tunneling processes that both couple to the electron component. The second process is likewise composed of two single electron tunneling processes, but these couple to the hole component. The picture is hence the same as before, *i.e.* cotunneling processes in the gate interval N to $N+1$ (N being even) scale with $|u|^4$ while those in the interval $N-1$ to N scale with $|v|^4$. An asymmetry between $|u|$ and $|v|$ should thus also give rise to an asymmetry in the Coulomb valleys in this case, but there are both even and odd parity Coulomb valleys. For $|u| > |v|$ we expect that the even valleys will be asymmetric with higher differential conductance on the right side of the valley and opposite for the odd Coulomb valleys.

In the case of a zero energy MBS, we have $|u| = |v|$ and expect all valleys to be symmetric. In the case of an oscillating MBS, we expect the asymmetry of the Coulomb valleys to oscillate with the same frequency as the MBS energy splitting. That is, the Coulomb valley asymmetry is correlated with the energy splitting in the same manner as the ratio Λ, such that the Coulomb valley asymmetry is greatest when the energy splitting is zero and Coulomb valley is symmetric when the energy splitting is maximal.

Explicit calculations are needed to investigate how this effect may depend on the relative strength of the tunnel couplings to the leads and whether it is possible to extract more quantitative information about the electron-hole components of the subgap state. However, it appears to be possible to identify trivial ps-ABS of the kind we discussed in Sec. 9.2.2, by comparing the energy splitting with the Coulomb valley asymmetry in the same manner as the energy splitting and the ratio Λ.

Chapter 10

Conclusion

> “Harry thought over his collected experimental data. It was only the most crude and preliminary sort of effort, but it was enough to support at least one conclusion: “Aaaaaaargh this doesn’t make any sense!”
>
> Harry Potter
>
> - *Harry Potter and the Methods of Rationality*, Eliezer Yudkowsky

We will briefly summarize the findings of chap. 4, 5, 6, 8, and 9 and give a perspective on the current status of the search for MBSs in SC-SM nanowires.

Summary

The second part of this thesis was centered around studying the SC-SM nanowire in a grounded setup, where the scattering formalism was used to simulate the differential conductance in a one-end ETS measurement.

In Chap. 4, we discussed a proposal for identifying MBSs in a SNS setup by tuning the phase difference between the two superconductors. In the topological case we found that the differential conductance measured at the end of the nanowire exhibits a period of 2π as a function of the phase difference between the superconductors. This effect is absent in the topologically trivial phase. The phase difference may be controlled by threading a magnetic flux through a superconducting loop that connects the superconductors. We also discussed the how deviations from an ideal system may affect this signature and found that it is important to have control over the potential in the normal part of the SNS junction. This setup may still be relevant in the context of searching for indirect signatures of MBS, but it will be necessary to investigate whether trivial MBS-look-alike states, such as ps-ABS[Moore *et al.*, 2018b] and quasi-Majorana modes[Vuik *et al.*, 2018], can be distinguished from true MBSs.

In the work presented in Chap. 5, we were concerned with understanding data from an ETS experiment in a coupled quantum dot-nanowire system using a theoretical model and numerical simulations. The numerical simulations qualitatively reproduced the experimental data. Specifically, data from the experiment showed a splitting of the ZBP when a dot level came into resonance with the nanowire, which is consistent with the numerical simulations where the ZBP originated from a MBS. Further studies of the numerical model found that the splitting of the MBS ZBP is due to hybridization between the MBS in the

nanowire and the dot levels. The MBS wavefunction leaks into the quantum dot upon resonance, which in turn alters the wavefunction overlap with the second MBS at the other end of the nanowire and leads to a change in the MBS energy splitting.

In Chap. 6, we discussed a possible explanation for some of the discrepancies between what is observed in experiments and what is predicted by theory. Here we focused on the lack of MBS energy oscillations and the non-$2e^2/h$ quantized conductance peaks seen in experiments. We investigated the effect of the normal metal drain on the parent superconductor of the SC-SM hybrid nanowire. It was found that the normal drain results in a softening of the parents superconductor gap, where a below-gap DOS leaks into the superconductor from the SN-interface. Depending on the coherence length of the superconductor, this below-gap DOS may provide a leakage channel for one or both of the MBSs in the nanowire. If only one MBS is coupled to the drain, the differential conductance remains quantized at $2e^2/h$, but the amplitude of the energy splitting oscillations as a function of the magnetic field is quenched. If the drain couples to both MBSs, the differential conductance is smaller than $2e^2/h$ and all features of the spectrum are suppressed.

In the third part of this thesis, we studied electron transport in Coulomb blockaded SC-SM nanowires, using a master equation model.

In Chap. 8, we modeled quasiparticle poisoning in a CBMI in comparison with experimental observations. In addition to the main Coulomb blockade diamonds, data from experiments exhibited "shadow" diamonds, shifted by 1e in gate voltage, which are consistent with transport through an excited (poisoned) state of the island. Comparison with simulated transport using the master equation model yielded an estimate of parity lifetime for the strongly coupled island ($\sim 1\,\mu s$) and sets a bound for a weakly coupled island ($> 10\,\mu s$).

In Chap. 9, we studied ZBC in the sequential tunneling regime in a CBMI. We found that the Coulomb peaks at the even-to-odd (odd-to-even) charge degeneracy are proportional to the electron (hole) component of the subgap state wavefunction at the position of the two lead interfaces. The relative size of the electron and hole components is therefore accessible by taking the ratio of experimentally measured even-to-odd and odd-to-even conductance peaks. We proceeded to study how this ratio is correlated with the energy splitting of the lowest-energy state in a uniform SC-SM nanowire in the topological and trivial cases. We found that the ratio oscillates with the same frequency as the energy splitting, but phase shifted by $\pi/2$, both as function of Zeeman field and chemical potential. We then investigated two cases of non-uniform SC-SM nanowires, which host trivial low-energy ps-ABSs that exhibit MBS-like features. We found that these trivial states may be discerned from MBSs in a Coulomb blockaded setup by comparing the ratio with the energy splitting as function of Zeeman field and chemical potential.

Perspectives

The projects presented in this thesis are part of ongoing work on the study of SC-SM hybrid nanowires systems and MBSs. At present, the existence of topologically protected MBSs in these systems is still an open question. A myriad of different indirect MBS signatures have been proposed, of which only some have been tested experimentally. However, it has been shown that most of these signatures are non-exclusive to MBSs and/or the experiments display some discrepancies with the predictions from the initial wave of theoretical models.

On the theoretical side, more and more complex models have been developed in order to explain the discrepancies between experiments and theoretical predictions. Spatially varying potentials, orbital effects of the magnetic field, disorder, quantum dots, barriers, and electrostatics, among others, are being taken into account in different combinations. Although these factors may be necessary to explain experimental observations (and they

have explained some discrepancies), it is difficult to know which are the most important. Experimental studies of SC-SM nanowires which focus on determining and disentangling the effects of these factors may serve both to improve experiments as well as further develop theoretical understanding.

Adding complexity to the theoretical models has also served to find specific topologically trivial explanations for some of the proposed indirect MBS signatures. Examples of such are the ps-ABS [Moore *et al.*, 2018b] and quasi-Majorana modes [Vuik *et al.*, 2018], which exist in the regime of high chemical potential. It is thus important to study these states in parameter regimes comparable to experiments and determine which of the currently accessible indirect signatures cannot distinguish them from MBSs. It is equally important to propose currently accessible tests which could distinguish the trivial state from a MBS, in order to assist in the development of better experiments.

In this thesis, we has focused on describing the SC-SM nanowires using single-band 1D models. These types of models have proven able to explain many aspects of experimental observations. However, it is possible that several transverse bands are occupied in experiments and it may be necessary to consider 2D and 3D models in order to study the effects of multiple bands. These models are already being studied numerically, but the possibility of obtaining analytical results from them is very limited. By identifying and studying specific effects that are only present in 2D and 3D models, it may be possible to include these effects phenomenologically in 1D models, which are more tractable for analytical work.

A demonstration of non-abelian exchange statistics is possibly the only definite proof of topological MBSs. This is still outside reach of current experiments, but great effort is being put into improving the quality of materials as well as developing new experimental setups. In recent years the close tandem work between theory and experiments has lead to great advancements in the field superconductor-semiconductor hybrid systems. The field is progressing faster than ever and many exciting discoveries surely still lie ahead. That said, focusing primarily on realizing the Majorana-based qubit may come at the cost of carrying out only superficial studies of many other interesting phenomena that appear along the way.

Whether the quest for realizing topological MBSs in SC-SM hybrid systems proves to be fruitful or not will hopefully be answered within the next few years. In any case, these systems host many other exciting quantum phenomena that are worth studying.

APPENDICES

Appendix A

Green's Function at a Diffusive Superconductor-Normal Interface

In this section we derive the Green's function of the electrons at a diffusive superconductor-normal interface in Eq. (6.9).

We consider a 1D system consisting of a normal and a superconducting part with the interface of the two parts at $x = 0$ and the normal part at $x > 0$. We consider the diffusive limit $\xi \gg l_e$ where the coherence length of the superconductor ξ is much greater than the elastic mean free path of the electrons l_{el}. The equation of motion for the retarded quasiclassical Green's functions G and F is [Usadel, 1970]

$$\frac{D}{2} G\partial_x^2 F - F\partial_x^2 G = -i\epsilon F - \Delta G, \tag{A.1}$$

where G is the normal (diagonal) and F is the anomalous (off-diagonal) parts of the Green's function, and $D = \frac{1}{3} v_{\text{F}} l_{\text{el}}$ is the diffusive constant. We have neglected inelastic scattering processes which are small at low temperatures. The Green's functions obey the normalization condition $G^2 + F^2$, which we enforce by parametrizing them as

$$F(x, i\omega) = \sin\theta(x, i\omega), \qquad G(x, i\omega) = \cos\theta(x, i\omega), \tag{A.2}$$

where $i\omega = \epsilon$ is a Matsubara frequancy, where we have neglected the customary subscript index. At the SN interface we have the boundary conditions

$$F(0^-) = F(0^+) \tag{A.3}$$

$$\frac{\sigma_S}{G(0^-)} \partial_x F(0^-) = \frac{\sigma_S}{G(0^+)} \partial_x F(0^+), \tag{A.4}$$

where $\sigma_{N/S}$ are the conductivityies of the normal metal and the superconductor. A self-consistent solution can be obtained by iteratively solving for the superconducting order parameter, but we will here use a fixed order parameter

$$\Delta(x) = \begin{cases} -i\Delta & \text{for } x < 0, \\ 0 & \text{for } x \geq 0, \end{cases} \tag{A.5}$$

so the solution should be seen as a lowest order approximation. With the parametrization in Eq. (A.2), the differential equation in Eq. (A.1) takes the form

$$\frac{D}{2}\partial_x^2\theta = \omega\sin\theta - \Delta\cos\theta. \tag{A.6}$$

First we consider the normal part where $\Delta = 0$ and we look for a solution of the form

$$\theta = 4\arctan(ae^{bx}). \tag{A.7}$$

Using this ansatz in the differential equation Eq. (A.6), we obtain

$$\frac{D_N}{2}4ab^2e^{bx}\frac{1-a^2e^{2bx}}{(1+a^2e^{2bx})^2} = 4\omega ae^{bx}\frac{1-a^2e^{2bx}}{(1+a^2e^{2bx})^2}, \tag{A.8}$$

where D_N is the diffusive constant in the normal metal and we have used the trigonometric identity

$$\sin 4y = 4\tan y\frac{1-\tan^2 y}{(1+\tan^2 y)^2}. \tag{A.9}$$

Solving Eq. (A.8) for b we obtain the expression

$$b = \pm\sqrt{\frac{2\omega}{D_N}}. \tag{A.10}$$

The other constant a will be found later using the boundary conditions.

Turning to the superconducting part, we use a solution of the form

$$\theta = \theta_S + 4\arctan(ce^{dx}). \tag{A.11}$$

In Eq. (A.6). After applying the trigonometric identities

$$\sin(\alpha\pm\beta) = \sin\alpha\cos\beta \pm \cos\alpha\sin\beta, \tag{A.12}$$

$$\cos(\alpha\pm\beta) = \cos\alpha\cos\beta \mp \sin\alpha\sin\beta, \tag{A.13}$$

$$\cos 4y = 4\tan y\frac{1-\tan^2 y}{(1+\tan^2 y)^2}, \tag{A.14}$$

and Eq. (A.9), and after some algebra, we get the equation

$$\frac{D_S}{2}4cd^2e^{dx} = 4ce^{dx}(\omega\cos\theta_S + \Delta\sin\theta_S) + (1-c^2e^{2dx})(\omega\sin\theta_S - \Delta\cos\theta_S). \tag{A.15}$$

In order for this to hold for a general x, we require

$$\omega\sin\theta_S = \Delta\cos\theta_S \quad\Rightarrow\quad \theta_S = \arctan\left(\frac{\Delta}{\omega}\right) + n\pi, \tag{A.16}$$

where we take n to be even such that $\mathrm{Re}\,\cos\theta > 0$. With this condition, the rest of Eq. (A.15) becomes

$$\frac{D_S}{2}d^2 = \omega\cos\theta_S + \Delta\sin\theta_S = \sqrt{\omega^2+\Delta^2} \tag{A.17}$$

$$\Downarrow$$

$$d = \pm\sqrt{\frac{2}{D_S}}\sqrt[4]{\omega^2+\Delta^2}. \tag{A.18}$$

We pick the solutions of b and d with decaying exponential function away from the interface, *i.e.* " − " for b and " + " for d. In order to find the two other constants a and c, we use the boundary conditions. From the first boundary condition in Eq. (A.3), we have the equation

$$\sin\theta(0^+) = \sin\theta(0^-) \quad \Rightarrow \quad \theta(0^+) + 2n\pi = \theta(0^-). \tag{A.19}$$

We define $\theta_0 \equiv \theta(0^+)$ and on the left-hand we have

$$\theta_0 = 4\arctan(a) \quad \Rightarrow \quad a \equiv \tan\frac{\theta_0}{4}. \tag{A.20}$$

On the right-hand side we have

$$\theta(0^-) = \theta_S + 4\arctan(c). \tag{A.21}$$

The boundary condition is thus fulfilled for

$$c = \tan\frac{\theta_0 - \theta_S + 2n\pi}{4}. \tag{A.22}$$

Due to $\sin(y+\pi) = -\sin y$, another solution is

$$c = -\tan\frac{\theta_0 - \theta_S + (2n+1)\pi}{4}, \tag{A.23}$$

which can be combined with the previous solution to write

$$c = (-1)^n \tan\frac{\theta_0 - \theta_S + n\pi}{4}. \tag{A.24}$$

Inserting the ansatz Green's function into the second boundary condition in Eq. (A.4) we get the equation

$$\frac{a}{1+a^2}\sigma_N b = \frac{c}{1+c^2}\sigma_N d \tag{A.25}$$

$$\Downarrow$$

$$-\eta\frac{a}{1+a^2} = \frac{c}{1+c^2}, \tag{A.26}$$

where we have inserted the previously found solutions $b = -\sqrt{2\omega/D_N}$ and $d = \sqrt{2/D_S}\sqrt[4]{\omega^2+\Delta^2}$, and defined

$$\eta = \frac{\sigma_N}{\sigma_S}\sqrt{\frac{D_S}{D_N}}\frac{\sqrt{\omega}}{\sqrt[4]{\omega^2+\Delta^2}}. \tag{A.27}$$

We insert the solutions for a and c in Eqs. (A.20) and (A.24), which were obtained with the first boundary condition, into Eq. (A.26) and use the trigonometric identity

$$\frac{\tan y}{1+\tan^2 y} = \sin 2y \tag{A.28}$$

to obtain the equation

$$-\eta\sin\frac{\theta_0}{2} = (-1)^n \sin\frac{\theta_0 - \theta_S + n\pi}{2}, \tag{A.29}$$

which yields

$$-\eta\sin\frac{\theta_0}{2} = \begin{cases} \pm\sin\frac{\theta_0-\theta_S}{2} & \text{for even } n \\ \pm\cos\frac{\theta_0-\theta_S}{2} & \text{for odd } n. \end{cases} \tag{A.30}$$

Using n even and the " $-$ " sign gives solution obtained by Belzig *et al.* [1996]. We pick n even and the " $+$ " sign. Using the trigonometric identity in Eq. (A.12), we get the expression

$$\frac{\theta_0}{2} = \arctan\left(\sin\left(\frac{\theta_S}{2}\right)\left[\cos\left(\frac{\theta_S}{2}\right) - \eta\right]^{-1}\right) \tag{A.31}$$

$$= \arctan\left(-\sin\left(\frac{1}{2}\arctan\frac{\Delta}{i\epsilon}\right)\left[\cos\left(\frac{1}{2}\arctan\frac{\Delta}{i\epsilon}\right) - \eta\right]^{-1}\right) \tag{A.32}$$

$$\equiv \arctan\beta, \tag{A.33}$$

where we inserted $\theta_S = \arctan\frac{\Delta}{i\epsilon}$ with $\omega = -i\epsilon$. We have defined β which is the the same as in Eq. (6.10). Combining this expression with Eqs. (A.20), (A.24), (A.18), and (A.10), we write the full solution

$$\theta(x,\epsilon) = \begin{cases} 4\arctan\left\{ae^{bx}\right\} & \text{for } x > 0, \\ \theta_S + 4\arctan\left\{ce^{dx}\right\} & \text{for } x \le 0, \end{cases} \tag{A.34}$$

$$= \begin{cases} 4\arctan\left\{e^{-(x/\xi_N)\sqrt{-i\epsilon/\Delta}}\tan\left(\frac{1}{2}\arctan\beta\right)\right\} & \text{for } x > 0, \\ -\arctan\frac{\Delta}{i\epsilon} + 4\arctan\left\{e^{(x/\xi_S)\sqrt[4]{1-(\epsilon/\Delta)^2}}\right. & \\ \quad \left.\times\tan\left(\frac{1}{2}\arctan\beta + \frac{1}{4}\arctan\frac{\Delta}{i\epsilon}\right)\right\} & \text{for } x \le 0, \end{cases} \tag{A.35}$$

as written in Eq. (6.9), where we have defined $\xi_{N,S} = \sqrt{\hbar D_{N,S}/2\Delta}$.

APPENDIX B

Distribution Function for odd/even Parity BCS Density of States

In this appendix, we will perform a detailed calculation of the distribution function of quasiparticles with BCS density of state in case of even and odd parity, leading to the Eqs. (7.13) and (7.17).

The partition function for odd (o) and even (e) parity states at the inverse temperature $\beta = 1/k_B T$ can be written as

$$2Z_p = \prod_n (1 + e^{-\beta E_n}) \mp \prod_n (1 - e^{-\beta E_n}), \tag{B.1}$$

where $p \in \{o, e\}$, $\bar{p}$ denotes the opposite of p, and the $-$ $(+)$ applies to the odd (even) case. The energies of the quasiparticles are

$$E_n = \sqrt{\epsilon_n^2 + \Delta^2}, \tag{B.2}$$

as given in Eq. (7.8). Through a few algebraic operation we rewrite the expression of the partition function:

$$\begin{aligned}
2Z_p &= \prod_n (1 + e^{-\beta E_n}) \mp \prod_n (1 - e^{-\beta E_n}) \\
&= \prod_{n \neq i} \{1 + e^{-\beta E_n}\}(1 + e^{-\beta E_i}) \mp \prod_{n \neq i} \{1 - e^{-\beta E_n}\}(1 - e^{-\beta E_i}) \\
&= \prod_{n \neq i} \{1 + e^{-\beta E_n}\} \mp \prod_{n \neq i} \{1 - e^{-\beta E_n}\} + \left(\prod_{n \neq i} \{1 + e^{-\beta E_n}\} \pm \prod_{n \neq i} \{1 - e^{-\beta E_n}\} \right) e^{-\beta E_i}) \\
&= 2Z'_p + 2Z'_{\bar{p}} e^{-\beta E_i}, \\
&\Downarrow \\
Z_p &= Z'_p + Z'_{\bar{p}} e^{-\beta E_i},
\end{aligned} \tag{B.3}$$

where Z'_p denotes the partition function where the state at energy E_i is unoccupied. We have thus written the partition function of parity p as the sum of the partition function of parity p where the state i is unoccupied and the partition function with opposite parity

and state i unoccupied times probability of state i being occupied. Both terms contain only states with parity p. The expression can be reversed to write the partition function Z'_p in terms of Z_p and $Z_{\bar{p}}$,

$$Z'_p = \frac{Z_p e^{\beta E_i} - Z_{\bar{p}}}{2\sinh(\beta E_i)} \tag{B.4}$$

We proceed to consider the thermal distribution function

$$f_p(E) = \frac{Z'_{\bar{p}} e^{-\beta E}}{Z_p}, \tag{B.5}$$

which is the weight factor of having the state with energy E occupied $e^{-\beta E}$, multiplied by the partition function of the opposite parity where the state E is unoccupied $Z'_{\bar{p}}$ and divided by the partition function for parity Z_p. Rearranging a bit, we obtain

$$f_p(E) = \frac{Z'_{\bar{p}} e^{-\beta E}}{Z'_p + Z'_{\bar{p}} e^{-\beta E}} = \frac{1}{e^{\beta E}(Z'_p/Z'_{\bar{p}}) + 1} \approx \frac{1}{e^{\beta E}(Z_p/Z_{\bar{p}}) + 1}, \tag{B.6}$$

and we have used the approximation

$$\frac{Z'_p}{Z'_{\bar{p}}} = \frac{e^{\beta E} Z_p - Z_{\bar{p}}}{e^{\beta E} Z_{\bar{p}} - Z_p} \approx \frac{Z_p}{Z_{\bar{p}}}, \tag{B.7}$$

which is obtained using Eq. (B.4) and the approximation holds for $\beta E \gg 1$. For the superconducting gap parameters we will be considering ($\Delta \approx 200\,\mu\text{eV}$) this is satisfied at temperatures below $\sim 0.5\,\text{K}$. We can then write the thermal distribution function as

$$f_p(E) = \frac{1}{e^{\beta(E \pm \delta F)} + 1}, \tag{B.8}$$

where the $-$ ($+$) applies to the odd (even) case and we have defined the free energy difference between the odd and even parity sector

$$\delta F = F_\text{o} - F_\text{e} = -\frac{1}{\beta} \ln\left(\frac{Z_\text{o}}{Z_\text{e}}\right). \tag{B.9}$$

We proceed to calculate the free energy difference of the BCS density of states using Eq. (B.1) through a series of algebraic operations

$$\begin{aligned}
\delta F_\text{BCS} &= -\frac{1}{\beta} \ln\left(\frac{\prod_{n,\sigma}(1 + e^{-\beta E_n}) - \prod_{n,\sigma}(1 - e^{-\beta E_n})}{\prod_{n,\sigma}(1 + e^{-\beta E_n}) + \prod_{n,\sigma}(1 - e^{-\beta E_n})}\right) \\
&= -\frac{1}{\beta} \ln\left(\frac{\prod(e^{\frac{1}{2}\beta E_n} + e^{-\frac{1}{2}\beta E_n}) - \prod(e^{\frac{1}{2}\beta E_n} - e^{-\frac{1}{2}\beta E_n})}{\prod(e^{\frac{1}{2}\beta E_n} + e^{-\frac{1}{2}\beta E_n}) + \prod(e^{\frac{1}{2}\beta E_n} - e^{-\frac{1}{2}\beta E_n})}\right) \\
&= -\frac{1}{\beta} \ln\left(\frac{\prod\sqrt{(e^x + e^{-x})^2} - \prod\sqrt{(e^x - e^{-x})^2}}{\prod\sqrt{(e^x + e^{-x})^2} + \prod\sqrt{(e^x - e^{-x})^2}}\right) \\
&= -\frac{1}{\beta} \ln\left(\frac{\frac{\prod\sqrt{(e^x+e^{-x})^2} - \prod\sqrt{(e^x-e^{-x})^2}}{\prod\sqrt{(e^x+e^{-x})(e^x-e^{-x})}}}{\frac{\prod\sqrt{(e^x+e^{-x})^2} + \prod\sqrt{(e^x-e^{-x})^2}}{\prod\sqrt{(e^x+e^{-x})(e^x-e^{-x})}}}\right)
\end{aligned}$$

$$
\begin{aligned}
&= -\frac{1}{\beta}\ln\left(\frac{\prod\sqrt{\frac{(e^x+e^{-x})}{(e^x-e^{-x})}} - \prod\sqrt{\frac{(e^x-e^{-x})}{(e^x+e^{-x})}}}{\prod\sqrt{\frac{(e^x+e^{-x})}{(e^x-e^{-x})}} + \prod\sqrt{\frac{(e^x-e^{-x})}{(e^x+e^{-x})}}}\right) \\
&= -\frac{1}{\beta}\ln\left[\tanh\left(\ln\left[\prod\sqrt{\frac{(e^x+e^{-x})}{(e^x-e^{-x})}}\right]\right)\right] \\
&= -\frac{1}{\beta}\ln\left[\tanh\left(\frac{1}{2}\sum_{n\sigma}\ln\left[\coth\left(\frac{1}{2}\beta E_n\right)\right]\right)\right], \qquad \text{(B.10)}
\end{aligned}
$$

where we have omitted the product indices through the calculation and defined $x \equiv \frac{1}{2}\beta E_n$. In the three last lines we have used that

$$
\begin{aligned}
\tanh(\ln y) &= \frac{e^{\ln y} - e^{-\ln y}}{e^{\ln y} + e^{-\ln y}} \\
&= \frac{y - y^{-1}}{y + y^{-1}} \qquad \text{(B.11)}
\end{aligned}
$$

and $\ln\sqrt{y} = \frac{1}{2}\ln y$. We convert the sum into an integral in eq. (B.10)

$$
\begin{aligned}
\delta F_{\text{BCS}} &\approx -\frac{1}{\beta}\ln\tanh\frac{1}{2}\int_{-\infty}^{\infty} dE\ \text{Re}\left[\rho_{\text{BCS}}(E)\right]\ln\coth\left(\frac{\beta E}{2}\right) \qquad \text{(B.12)} \\
&\approx -\frac{1}{\beta}\ln\tanh\int_{\Delta}^{\infty} dE\rho_{\text{BCS}}(E)\ln\coth\left(\frac{\beta E}{2}\right) \qquad \text{(B.13)}
\end{aligned}
$$

where

$$
\rho_{\text{BCS}}(E) = \frac{\rho_D E}{\sqrt{E^2-\Delta^2}}, \qquad \text{(B.14)}
$$

is the BCS density of states with $\rho_D = \rho_{\text{Al}}\mathcal{V}$ being the normal density of states at the Fermi level of the island including spin. ρ_{Al} is the aluminum density of states per volume and $\mathcal{V}$ is the volume of the island. For low temperatures $\beta\Delta \gg 1$ we can approximate

$$
\begin{aligned}
\ln\coth\left(\frac{\beta E}{2}\right) &\approx \coth\left(\frac{\beta E}{2}\right) - 1 \\
&= \frac{e^{\frac{\beta E}{2}} + e^{-\frac{\beta E}{2}}}{e^{\frac{\beta E}{2}} - e^{-\frac{\beta E}{2}}} - 1 \\
&= 2\frac{e^{-\frac{\beta E}{2}}}{e^{\frac{\beta E}{2}} - e^{-\frac{\beta E}{2}}} \\
&= 2\frac{1}{e^{\beta E}-1} \\
&\approx 2e^{-\beta E} \qquad \text{(B.15)}
\end{aligned}
$$

which in the same limit lets us approximate the free energy difference as

$$
\begin{aligned}
\delta F_{\text{BCS}} &\approx -\frac{1}{\beta}\ln\tanh\left[2\int_{\Delta}^{\infty} dE\rho_{\text{BCS}}(E)e^{-\beta E}\right] = -\frac{1}{\beta}\ln\tanh[N_{\text{eff}}e^{-\beta\Delta}] \qquad \text{(B.16)} \\
&\approx \Delta - \frac{\ln(N_{\text{eff}})}{\beta}, \qquad \text{(B.17)}
\end{aligned}
$$

with

$$
N_{\text{eff}} = 2\int_{\Delta}^{\infty}\rho_{\text{BCS}}(E)e^{-\beta(E-\Delta)}\,\mathrm{d}E = 2\rho_{\text{D}}\Delta e^{\beta\Delta}K_1(\beta\Delta), \qquad \text{(B.18)}
$$

where $K_\nu(x)$ is the modified Bessel function of the second kind and $N_{\text{eff}} \approx \rho_D\Delta$ is an effective quasi-particle number.

Bibliography

[Akhmerov *et al.*, 2009] Akhmerov, A. R., J. Nilsson, and C. W. Beenakker (2009), Physical Review Letters **102** (21), 216404

[Albrecht *et al.*, 2017] Albrecht, S. M., E. B. Hansen, A. P. Higginbotham, F. Kuemmeth, T. S. Jespersen, J. Nygård, P. Krogstrup, J. Danon, K. Flensberg, and C. M. Marcus (2017), Physical Review Letters **118** (13), 137701

[Albrecht *et al.*, 2016] Albrecht, S. M., A. P. Higginbotham, M. Madsen, F. Kuemmeth, T. S. Jespersen, J. Nygård, P. Krogstrup, and C. M. Marcus (2016), Nature **531** (7593), 206

[Aleiner *et al.*, 2002] Aleiner, I., P. Brouwer, and L. Glazman (2002), Physics Reports **358** (5-6), 309

[Alicea, 2010] Alicea, J. (2010), Physical Review B - Condensed Matter and Materials Physics **81** (12), 125318

[Altland and Zirnbauer, 1997] Altland, A., and M. R. Zirnbauer (1997), Physical Review B **55** (2), 1142

[Beenakker, 2015] Beenakker, C. W. J. (2015), Reviews of Modern Physics **87** (3), 1037

[Belzig *et al.*, 1996] Belzig, W., C. Bruder, and G. Schön (1996), Physical Review B **54** (13), 9443

[Ben-Shach *et al.*, 2014] Ben-Shach, G., A. Haim, I. Appelbaum, Y. Oreg, A. Yacoby, and B. I. Halperin (2014), Physical Review B **91**, 045403

[Bernevig, 2013] Bernevig, T. L., B. Andrei with Hughes (2013), *Topological Insulators and Topological Superconductors* (Princeton University Press)

[Blonder *et al.*, 1982] Blonder, G. E., M. Tinkham, and T. M. Klapwijk (1982), Phys. Rev. B **25**, 4515

[Bonderson and Nayak, 2013] Bonderson, P., and C. Nayak (2013), Physical Review B **87** (19), 195451

[Brouwer *et al.*, 2011] Brouwer, P. W., M. Duckheim, A. Romito, and F. von Oppen (2011), Physical Review B **84** (14), 144526

[Bruus and Flensberg, 2004] Bruus, H., and K. Flensberg (2004), *Many-Body Quantum Theory in Condensed Matter Physics* (Oxford University Press)

[Cayao *et al.*, 2015] Cayao, J., E. Prada, P. San-Jose, and R. Aguado (2015), Physical Review B **91** (2), 024514

[Chang *et al.*, 2015] Chang, W., S. M. Albrecht, T. S. Jespersen, F. Kuemmeth, P. Krogstrup, J. Nygård, and C. M. Marcus (2015), Nature Nanotechnology **10** (January), 10.1038/nnano.2014.306

[Chiu *et al.*, 2017] Chiu, C.-K., J. D. Sau, and S. Das Sarma (2017), Physical Review B **96** (5), 054504

[Chiu *et al.*, 2015] Chiu, C. K., M. M. Vazifeh, and M. Franz (2015), Epl **110** (1), 10001

[Churchill *et al.*, 2013] Churchill, H. O. H., V. Fatemi, K. Grove-Rasmussen, M. T. Deng, P. Caroff, H. Q. Xu, and C. M. Marcus (2013), Physical Review B **87** (24), 241401

[Clarke, 2017] Clarke, D. J. (2017), Physical Review B **96** (20), 201109

[Danon and Flensberg, 2015] Danon, J., and K. Flensberg (2015), Physical Review B **91** (16), 165425

[Danon *et al.*, 2017] Danon, J., E. B. Hansen, and K. Flensberg (2017), Physical Review B **96** (12), 125420

[Das *et al.*, 2012] Das, A., Y. Ronen, Y. Most, Y. Oreg, M. Heiblum, and H. Shtrikman (2012), Nature Physics **8** (12), 887

[Das Sarma *et al.*, 2016] Das Sarma, S., A. Nag, and J. D. Sau (2016), Phys. Rev. B **94**, 035143

[Das Sarma *et al.*, 2006] Das Sarma, S., C. Nayak, and S. Tewari (2006), Physical Review B - Condensed Matter and Materials Physics **73** (22), 220502

[Das Sarma *et al.*, 2012] Das Sarma, S., J. D. Sau, and T. D. Stanescu (2012), Physical Review B - Condensed Matter and Materials Physics **86** (9), 220506

[Deng *et al.*, 2016] Deng, M. T., S. Vaitiekenas, E. B. Hansen, J. Danon, M. Leijnse, K. Flensberg, J. Nygård, P. Krogstrup, and C. M. Marcus (2016), Science **354** (6319), 1557

[Deng *et al.*, 2017] Deng, M. T., S. Vaitiekénas, E. Prada, P. San-Jose, J. Nygård, P. Krogstrup, R. Aguado, and C. M. Marcus (2017), arXiv:1712.03536

[Deng *et al.*, 2012] Deng, M. T., C. L. Yu, G. Y. Huang, M. Larsson, P. Caroff, and H. Q. Xu (2012), Nano Letters **12** (12), 6414

[Domínguez *et al.*, 2017] Domínguez, F., J. Cayao, P. San-Jose, R. Aguado, A. L. Yeyati, and E. Prada (2017), npj Quantum Materials **2** (1), 13

[Eilenberger, 1968] Eilenberger, G. (1968), **214** (2), 195

[Escribano *et al.*, 2017] Escribano, S. D., A. L. Yeyati, and E. Prada (2017), , 1arXiv:1712.07625

[Flensberg, 2010] Flensberg, K. (2010), Physical Review B - Condensed Matter and Materials Physics **82** (18), 180516

[Fu and Kane, 2008] Fu, L., and C. L. Kane (2008), Physical Review Letters **100** (9), 096407

[Fu and Kane, 2009] Fu, L., and C. L. Kane (2009), Physical Review B - Condensed Matter and Materials Physics **79** (16), 161408

[Gül *et al.*, 2017] Gül, Ö., H. Zhang, F. K. De Vries, J. Van Veen, K. Zuo, V. Mourik, S. Conesa-Boj, M. P. Nowak, D. J. Van Woerkom, M. Quintero-Pérez, M. C. Cassidy, A. Geresdi, S. Koelling, D. Car, S. R. Plissard, E. P. Bakkers, and L. P. Kouwenhoven (2017), Nano Letters **17** (4), 2690

[Hansen *et al.*, 2016] Hansen, E. B., J. Danon, and K. Flensberg (2016), Physical Review B - Condensed Matter and Materials Physics **93** (9), 094501

[Hansen *et al.*, 2018] Hansen, E. B., J. Danon, and K. Flensberg (2018), Physical Review B **97** (4), 041411

[van Heck *et al.*, 2016] van Heck, B., R. M. Lutchyn, and L. I. Glazman (2016), Physical Review B **93** (23), 235431

[Hekking *et al.*, 1993] Hekking, F. W. J., L. I. Glazman, K. A. Matveev, and R. I. Shekhter (1993), Physical Review Letters **70** (26), 4138

[Hergenrother *et al.*, 1994] Hergenrother, J. M., M. T. Tuominen, and M. Tinkham (1994), Physical Review Letters **72** (11), 1742

[Higginbotham *et al.*, 2015] Higginbotham, A. P., S. M. Albrecht, G. Kiršanskas, W. Chang, F. Kuemmeth, P. Krogstrup, T. S. Jespersen, J. Nygård, K. Flensberg, and C. M. Marcus (2015), Nature Physics **11** (12), 1017

[Hunter, 2007] Hunter, J. D. (2007), Computing in Science Engineering **9** (3), 90

[Hützen *et al.*, 2012] Hützen, R., A. Zazunov, B. Braunecker, A. L. Yeyati, and R. Egger (2012), Physical Review Letters **109** (16), 166403

[Ivanov, 2001] Ivanov, D. a. (2001), Physical Review Letters **86** (2), 268

[Jørgensen *et al.*, 2007] Jørgensen, H. I., T. Novotný, K. Grove-Rasmussen, K. Flensberg, and P. E. Lindelof (2007), Nano Letters **7** (8), 2441

[Karzig *et al.*, 2017] Karzig, T., C. Knapp, R. M. Lutchyn, P. Bonderson, M. B. Hastings, C. Nayak, J. Alicea, K. Flensberg, S. Plugge, Y. Oreg, C. M. Marcus, and M. H. Freedman (2017), Physical Review B **95** (23), 235305

[Kells *et al.*, 2012] Kells, G., D. Meidan, and P. W. Brouwer (2012), Physical Review B **86** (10), 100503

[Kitaev, 2003] Kitaev, A. (2003), Annals of Physics **303** (1), 2

[Kitaev, 2001] Kitaev, A. Y. (2001), Physics-Uspekhi **44** (10S), 131

[Kjaergaard *et al.*, 2016] Kjaergaard, M., F. Nichele, H. J. Suominen, M. P. Nowak, M. Wimmer, A. R. Akhmerov, J. A. Folk, K. Flensberg, J. Shabani, C. J. Palmstrøm, and C. M. Marcus (2016), Nature Communications **7**, 12841

[Klinovaja and Loss, 2012] Klinovaja, J., and D. Loss (2012), Physical Review B - Condensed Matter and Materials Physics **86** (8), 085408

[Krogstrup *et al.*, 2015] Krogstrup, P., N. L. Ziino, W. Chang, S. M. Albrecht, M. H. Madsen, E. Johnson, J. Nygård, C. M. Marcus, and T. S. Jespersen (2015), Nature Materials **14** (4), 400

[Kuprianov and Lukichev, 1988] Kuprianov, M. Y., and V. F. Lukichev (1988), Sov. Phys. JETP **67** (June), 1163

[Kwon *et al.*, 2003] Kwon, H.-J., K. Sengupta, and V. M. Yakovenko (2003), The European Physical Journal B - Condensed Matter **37** (3), 349

[Lafarge *et al.*, 1993] Lafarge, P., P. Joyez, D. Esteve, C. Urbina, and M. H. Devoret (1993), Physical Review Letters **70** (7), 994

[Law *et al.*, 2009] Law, K. T., P. A. Lee, and T. K. Ng (2009), Physical Review Letters **103** (23), 237001

[Lee *et al.*, 2012] Lee, E. J. H., X. Jiang, R. Aguado, G. Katsaros, C. M. Lieber, and S. De Franceschi (2012), Physical Review Letters **109** (18), 186802

[Linder *et al.*, 2010] Linder, J., Y. Tanaka, T. Yokoyama, A. Sudbø, and N. Nagaosa (2010), Physical Review Letters **104** (6), 067001

[Liu *et al.*, 2017a] Liu, C.-X., J. D. Sau, and S. Das Sarma (2017a), Physical Review B **95** (5), 054502

[Liu *et al.*, 2017b] Liu, C.-x., J. D. Sau, T. D. Stanescu, and S. Das Sarma (2017b), Physical Review B **96** (7), 075161

[Liu *et al.*, 2017c] Liu, C.-X., F. Setiawan, J. D. Sau, and S. Das Sarma (2017c), Phys. Rev. B **96**, 054520

[Liu *et al.*, 2012] Liu, J., A. C. Potter, K. T. Law, and P. a. Lee (2012), Physical Review Letters **109** (26), 267002

[Lutchyn *et al.*, 2010] Lutchyn, R. M., J. D. Sau, and S. Das Sarma (2010), Physical Review Letters **105** (7), 77001

[Majorana, 1937] Majorana, E. (1937), Nuovo Cim. **14** (RX-888), 171

[Mishmash *et al.*, 2016] Mishmash, R. V., D. Aasen, A. P. Higginbotham, and J. Alicea (2016), Physical Review B - Condensed Matter and Materials Physics **93** (24), 245404

[Moore *et al.*, 2018a] Moore, C., T. D. Stanescu, and S. Tewari (2018a), Physical Review B **97** (16), 165302

[Moore *et al.*, 2018b] Moore, C., C. Zeng, T. D. Stanescu, and S. Tewari (2018b), , 1arXiv:1804.03164

[Mourik *et al.*, 2012] Mourik, V., K. Zuo, S. M. Frolov, S. R. Plissard, E. P. A. M. Bakkers, and L. P. Kouwenhoven (2012), Science **336** (6084), 1003

[Nayak *et al.*, 2008] Nayak, C., A. Stern, M. Freedman, and S. Das Sarma (2008), Reviews of Modern Physics **80** (3), 1083

[Nichele *et al.*, 2017] Nichele, F., A. C. Drachmann, A. M. Whiticar, E. C. O'Farrell, H. J. Suominen, A. Fornieri, T. Wang, G. C. Gardner, C. Thomas, A. T. Hatke, P. Krogstrup, M. J. Manfra, K. Flensberg, and C. M. Marcus (2017), Physical Review Letters **119** (13), 136803

[O'Farrell *et al.*, 2018] O'Farrell, E. C. T., A. C. C. Drachmann, M. Hell, A. Fornieri, A. M. Whiticar, E. B. Hansen, S. Gronin, G. C. Gardener, C. Thomas, M. J. Manfra, K. Flensberg, C. M. Marcus, and F. Nichele (2018), arXiv:1804.09676

[Ojanen, 2013] Ojanen, T. (2013), Phys. Rev. B **87**, 100506

[Oreg *et al.*, 2010] Oreg, Y., G. Refael, and F. von Oppen (2010), Physical Review Letters **105** (17), 177002

[Peng *et al.*, 2015] Peng, Y., F. Pientka, L. I. Glazman, and F. von Oppen (2015), Physical Review Letters **114** (10), 106801

[Pikulin *et al.*, 2012] Pikulin, D. I., J. P. Dahlhaus, M. Wimmer, H. Schomerus, and C. W. J. Beenakker (2012), New Journal of Physics **14** (12), 125011

[Plugge *et al.*, 2017] Plugge, S., A. Rasmussen, R. Egger, and K. Flensberg (2017), New Journal of Physics **19** (1), 012001

[Prada *et al.*, 2017] Prada, E., R. Aguado, and P. San-Jose (2017), Physical Review B **96** (8), 085418

[Prada *et al.*, 2012] Prada, E., P. San-Jose, and R. Aguado (2012), Physical Review B **86** (18), 180503

[Rainis *et al.*, 2013] Rainis, D., L. Trifunovic, J. Klinovaja, and D. Loss (2013), Physical Review B **87** (2), 024515

[Read and Green, 2000] Read, N., and D. Green (2000), Phys. Rev. B **61**, 10267

[Reeg *et al.*, 2017] Reeg, C., D. Loss, and J. Klinovaja (2017), Physical Review B **96** (12), 125426

[Reeg *et al.*, 2018] Reeg, C., D. Loss, and J. Klinovaja (2018), Physical Review B **97** (16), 165425

[Rex and Sudbø, 2014] Rex, S., and A. Sudbø (2014), Phys. Rev. B **90**, 115429

[San-Jose *et al.*, 2012] San-Jose, P., E. Prada, and R. Aguado (2012), Physical Review Letters **108** (25), 257001

[San-Jose *et al.*, 2014] San-Jose, P., E. Prada, and R. Aguado (2014), Phys. Rev. Lett. **112**, 137001

[Sau *et al.*, 2010a] Sau, J. D., R. M. Lutchyn, S. Tewari, and S. Das Sarma (2010a), Physical Review Letters **104** (4), 040502

[Sau *et al.*, 2010b] Sau, J. D., R. M. Lutchyn, S. Tewari, and S. Das Sarma (2010b), Phys. Rev. B **82**, 094522

[Schnyder *et al.*, 2008] Schnyder, A. P., S. Ryu, A. Furusaki, and A. W. W. Ludwig (2008), Physical Review B **78** (19), 195125

[Sengupta *et al.*, 2001] Sengupta, K., I. Žutić, H.-J. Kwon, V. M. Yakovenko, and S. Das Sarma (2001), Physical Review B **63** (14), 144531

[Shabani *et al.*, 2016] Shabani, J., M. Kjaergaard, H. J. Suominen, Y. Kim, F. Nichele, K. Pakrouski, T. Stankevic, R. M. Lutchyn, P. Krogstrup, R. Feidenhans'L, S. Kraemer, C. Nayak, M. Troyer, C. M. Marcus, and C. J. Palmstrøm (2016), Physical Review B **93** (15), 155402

[Sherman *et al.*, 2017] Sherman, D., J. S. Yodh, S. M. Albrecht, J. Nygård, P. Krogstrup, and C. M. Marcus (2017), Nature Nanotechnology **12** (3), 212

[Stanescu *et al.*, 2011] Stanescu, T. D., R. M. Lutchyn, and S. Das Sarma (2011), Physical Review B **84** (14), 144522

[Stanescu *et al.*, 2013] Stanescu, T. D., R. M. Lutchyn, and S. Das Sarma (2013), Physical Review B **87** (9), 094518

[Stanescu *et al.*, 2012] Stanescu, T. D., S. Tewari, J. D. Sau, and S. Das Sarma (2012), Physical Review Letters **109** (26), 266402

[Stenger and Stanescu, 2017] Stenger, J., and T. D. Stanescu (2017), Phys. Rev. B **96**, 214516

[Stern, 2010] Stern, A. (2010), Nature **464** (7286), 187

[Tewari and Sau, 2012] Tewari, S., and J. D. Sau (2012), Physical Review Letters **109** (15), 150408

[Tuominen *et al.*, 1992] Tuominen, M. T., J. M. Hergenrother, T. S. Tighe, and M. Tinkham (1992), Physical Review Letters **69** (13), 1997

[Usadel, 1970] Usadel, K. D. (1970), Physical Review Letters **25** (8), 507

[Vuik *et al.*, 2018] Vuik, A., B. Nijholt, A. R. Akhmerov, and M. Wimmer (2018), , 1arXiv:1806.02801

[Wimmer *et al.*, 2011] Wimmer, M., A. R. Akhmerov, J. P. Dahlhaus, and C. W. J. Beenakker (2011), New Journal of Physics **13** (5), 053016

[Zhang *et al.*, 2017] Zhang, H., Ö. Gül, S. Conesa-Boj, M. P. Nowak, M. Wimmer, K. Zuo, V. Mourik, F. K. De Vries, J. Van Veen, M. W. De Moor, J. D. Bommer, D. J. Van Woerkom, D. Car, S. R. Plissard, E. P. Bakkers, M. Quintero-Pérez, M. C. Cassidy, S. Koelling, S. Goswami, K. Watanabe, T. Taniguchi, and L. P. Kouwenhoven (2017), Nature Communications **8** (May), 16025

[Zhang *et al.*, 2018] Zhang, H., C.-x. Liu, S. Gazibegovic, D. Xu, J. A. Logan, G. Wang, N. van Loo, J. D. S. Bommer, M. W. A. de Moor, D. Car, R. L. M. Op het Veld, P. J. van Veldhoven, S. Koelling, M. A. Verheijen, M. Pendharkar, D. J. Pennachio, B. Shojaei, J. S. Lee, C. J. Palmstrøm, E. P. A. M. Bakkers, S. Das Sarma, and L. P. Kouwenhoven (2018), Nature **556** (7699), 74

[Zirnbauer, 1996] Zirnbauer, M. R. (1996), Journal of Mathematical Physics **37** (10), 4986.